Image analysis and computational modelling of Activity-Dependent Bulk Endocytosis in mammalian central nervous system neurons.

Donal Stewart

Doctor of Philosophy
Laboratory for Foundations of Computer Science
School of Informatics
University of Edinburgh
2017

Abstract

Synaptic vesicle recycling is the reuse of synaptic membrane material and proteins after vesicles have been exocytosed at the pre-synaptic terminal of a neuronal synapse. The discovery of the mechanisms by which recycling operates is a subject of active research. Within small mammalian central nervous system nerve terminals, two studied mechanisms of recovery are clathrin-mediated endocytosis and activity-dependent bulk endocytosis. Research into the comparative kinetics and mechanisms underlying these endocytosis mechanisms commonly involves time-series fluorescence microscopy of *in vitro* cultures. Synaptic proteins are tagged with fluorescent markers, or the synaptic vesicles are labelled with fluorescent dye. The change in fluorescence levels of individual synapses over time in response to stimuli is used to understand synaptic activity. The image analysis of these time-series images frequently requires substantial manual effort to extract the changing synaptic fluorescence intensity levels over time.

This work focusses on two closely interlinked areas, the development of improved automated image analysis tools to facilitate the analysis of microscopy image data, and computational simulations to leverage the data obtained from these experiments to gain mechanistic insight into the underlying processes involved in synaptic vesicle recycling.

The imaged properties of synapses within the time-series images are characterised, in terms of synapse movement during the course of an experiment. This characterisation highlights the properties which risk adding error to the extracted fluorescence intensity data, as analysis generally requires segmentation of regions of interest with fixed size and location. Where possible, protocols to optimise the manual selection of synapses in the image are suggested.

The manual selection of synapses within time-series images is a common but time consuming and difficult task. It requires considerable skill on the part of the researcher to select synapses from noisy images without introducing error or bias. Automated tools for either general image segmentation or for segmentation of synapse-like puncta do exist, but have mixed results when applied to time-series experiments. This work introduces the use of knowledge of the experiment protocol into the segmentation process. The selection of synapses as they respond to known stimuli is compared against other current segmentation methods, and tools to perform this segmentation are provided. This use of synapse activity improves the quality of the segmented set of synapses over existing segmentation tools.

Finally, this work builds a number of computational models, to allow published individual data points to be aggregated into a coherent view of overall synaptic vesicle recycling.

The first is FM-Sim, a stochastic hybrid model of overall synapse recycling as is expected to occur during the course of an experiment. This closed system model handles the processes of exocytosis and endocytosis. It uses Bayesian inference to fit model parameters to experimental data. In particular, it uses the experimental protocol to separate the mechanisms and rates that may contribute to the observed experimental data.

The second is a mathematical model of one aspect of synaptic vesicle recycling of particular interest - homoeostasis of plasma membrane integrity on the presynaptic terminal. This model provides bounds on efficiency of the studied endocytosis mechanisms at recovery of plasma membrane area during and after neuronal stimulus.

Both the image analysis and the computational simulations demonstrated in this work provide useful tools and insights into current research of synaptic vesicle recycling and the role of activity-dependent bulk endocytosis. In particular, the utility of adding time-dependent experimental protocol knowledge to both the image analysis tools and the computational simulations is shown.

Acknowledgements

I'd like to thank my excellent supervisors, Prof. Stephen Gilmore and Prof. Mike Cousin for their outstanding support and guidance during the course of my studies.

Thanks to the members of the Cousin laboratory past and present; Karen, Sarah, Andrew, Jamie, Jess, Alex, Darryl, Katherine, Robyn, Callista, Giselle, Liz and Rona; for helpful discussions, and provision of experimental data. I enjoyed observing research in action in the laboratory. Thanks also for being captive test users of my software.

Thanks to my examiners Prof. Geraint Thomas and Prof. J. Douglas Armstrong. Their insightful questions and comments during the defence of this thesis were a great help in improving the publication version.

Thanks to the DTC executive committee for their support and guidance. It was good to know they were looking out for us students.

Finally, thanks to my parents for encouraging academic achievement after all these years at university.

This work was supported in part by grants EP/F500386/1 and BB/F529254/1 for the University of Edinburgh School of Informatics Doctoral Training Centre in Neuroinformatics and Computational Neuroscience (`www.anc.ac.uk/dtc`) from the UK Engineering and Physical Sciences Research Council (EPSRC), UK Biotechnology and Biological Sciences Research Council (BBSRC), and the UK Medical Research Council (MRC). The work has made use of resources provided by the Edinburgh Compute and Data Facility (ECDF; `www.ecdf.ed.ac.uk`), which has support from the eDIKT initiative (`www.edikt.org.uk`).

Declaration

I declare that this thesis was composed by myself, that the work contained herein is my own except where explicitly stated otherwise in the text, and that this work has not been submitted for any other degree or professional qualification except as specified.

Chapter 8 includes parts which appeared in Stewart et al. (2014, 2015).

The microscopy image data and manually segmented region of interest gold standard datasets were kindly provided by members of the Cousin laboratory.

(*author*)

Lay Summary

Synaptic vesicle recycling is an important area of neuroscience research. It is key to the efficient operation of chemical synapses, and therefore neural function. It has been a subject of active research for over 50 years. The primary means of synaptic membrane recovery in small CNS neurons in mammals has been Clathrin Mediated Endocytosis (CME). This was first proposed as a mechanism in 1976 (Pearse, 1976) and has been extensively studied since then. More recently, a mechanism to cope with sustained high levels of neural activity was discovered. This mechanism is triggered under conditions of heavy load, when the standard CME would be unable to cope with the transient load. It involves the recovery of large areas of plasma membrane from the surface of the synapse, rather than one vesicle at a time, and so has been called Activity-Dependent Bulk Endocytosis (ADBE).

The research of this field uses a range of investigatory technologies, with time series fluorescent microscopy being a popular choice. Here, the synapses are labelled with fluorescent markers, either in the fluid contained within the vesicles, or in protein embedded in the surface of the membrane. These fluorescent markers may change their fluorescence brightness in response to external electrical or chemical stimulus, or as the normal recycling processes take place. By recording the changes in brightness of synapses over time, it is possible to infer some of the mechanisms taking place, and their levels of activity in different scenarios.

Starting with a time series image, there is a substantial amount of post-experiment analysis work to be performed. Individual synapses appear as small regions of brightness which may vary in intensity over the individual frames of the time-series, along with many other sources of brightness. The researcher must identify which of the bright areas are most likely to be synapses, and mark them for analysis by placing small circular markers, called regions of interest (ROI) around the potential synapses. The fluorescence intensity of the ROI over the time series can then be measured. This task is complicated by error sources such as the synapses moving with respect to the image frame during the course of the experiment.

My work has two parts. The first is to quantify some of the sources of error in selecting and measuring ROIs, along with enhancements to tools designed to identify these ROIs automatically. This has considerable benefit to the researcher, by simultaneously increasing the number of ROIs discovered per experiment, and greatly reducing the time required during the analysis stage. The other segment of my work has been to create simulation models of current understanding of the synaptic vesicle recycling process. These models integrate existing experimentally derived rate information, and allow experimental protocols to be simulated. If experimental data is available the modelling tools can estimate process rates which are likely to produce the experimental observations. Overall my work has use within synaptic vesicle research, and some of the software tools have more general use in any areas where time series traces require manual filtering.

Table of Contents

Glossary

Computational and statistics terms

ANOVA	Analysis of Variations
CTMC	Continuous Time Markov Chains
DDE	Delay Differential Equation
DSSA	Delay Stochastic Simulation Algorithm
LOOCV	Leave One Out Cross Validation
MCMC	Markov Chain Monte Carlo
ODE	Ordinary Differential Equation
PMMH	Particle Marginal Metropolis-Hastings
SBGN	Systems Biology Graphical Notation
SBML	Systems Biology Markup Language
SDE	Stochastic Differential Equation
SEM	Standard Error of the Mean
SMC	Sequential Monte Carlo
SSA	Gillespie Stochastic Simulation Algorithm, Direct Method

Biological and biological image processing terms

ADBE	Activity-Dependent Bulk Endocytosis
Akt	Protein kinase B (also called PKB)
AP-1 / AP-2 / AP-3	Adaptor protein 1/2/3
ATP	Adenosine Triphosphate
BS	Background Subtraction
Ca^{2+}	Calcium ions
CDK5	Cyclin-Dependent Kinase 5
CME	Clathrin-Mediated Endocytosis
CNS	Central Nervous System
DNA	Deoxyribonucleic Acid
EM	Electron Microscopy
EPSC	Excitatory Postsynaptic Current
FM	Fluorescence Microscopy
FM1-43 / FM2-10	FM styryl dye
GSK3	Glycogen Synthase Kinase 3
HRP	Horseradish peroxidase
KCl	Potassium Chloride
NH_4^+	Ammonium ions (usually in the form of ammonium chloride)
PKB	Protein kinase B (also called Akt)
RNA	Ribonucleic Acid
RNAi	RNA interference
ROI	Region Of Interest
RP	Reserve Pool (of synaptic vesicles)
RRP	Readily Releasable Pool (of synaptic vesicles)
Ser-774 / Ser-778	Serine residues on Dynamin I
SV	Synaptic Vesicle
SynaptopHluorin	Synaptobrevin II (also called VAMP2) fused to pHluorin
SypHy	Synaptophysin fused to pHluorin
VAMP2	Vesicle-associated Membrane Protein 2
VAMP4	Vesicle-associated Membrane Protein 4
VAMP4-pHluorin	VAMP4 fused to pHluorin
V-ATPase	Vacuolar-type H^+-ATPase

Chapter 1

Introduction

Activity-dependent bulk endocytosis (ADBE) is one of a small number of identified types of endocytosis of synaptic vesicles within the pre-synaptic terminal of neurons. It is activated under conditions of high neural stimulation as an additional means of synaptic vesicle recycling in addition to the more common clathrin-mediated endocytosis (CME). The mechanism of operation and chemical and kinetic pathways of ADBE are substantially different to those of CME. Chapter 2 covers the biology of the synaptic vesicle cycle as currently understood, and describes the experimental tools available in current research.

The main aim of this work is to increase understanding of ADBE and its role in synaptic vesicle recycling. As vesicle recycling is identified as a target in the occurrence and potential treatment of a number of neurological disorders including Huntington's disease and Alzheimer's disease, the results of this research have potential uses in the development of these treatments. The addition of a more computational approach to the existing experimental research assists with the discovery of ADBE mechanisms, with the same potential therapeutic benefits as are currently targeted by the experimental research.

Current experimental research provides large quantities of noisy data. Existing procedures for analysis of the raw image data are robust in that these remain stable and easily taught to new laboratory members. The end results are repeatable and provide reasonable measures of activity occurring during experimental protocols.

Assay protocols such as S1/S2 and normal control experiments (discussed in Chapter 2) provide solid scientific procedure. The analysis makes use of standardised and readily available tools with robust and well-characterised behaviour.

However some pragmatic assumptions are made about the base image data, as getting perfect analysis of noisy image data is both prohibitive in cost, and prone to bias. The more detailed the user interaction with the image analysis, the more prone to selection bias the data can be. Perfect analysis of the image data is technically demanding, and in some cases may not be possible with the microscopy tools available, so current practice is close to best effort. Chapter 3 describes the later stages of experiment results analysis of time-series fluorescence microscopy image data, a common output of laboratory experiments in this field. Part of this work has been to characterise the properties of the analysis and the underlying image data, identify the sources of error, and how current analysis procedures mitigate the effects of these errors.

The automated segmentation of regions of interest (ROI) in image data both helps reduce bias introduced during human segmentation of data, and reduces the standard error of a data set, as automated segmentation allows the capture of many more regions of interest per imaging assay; manual segmentation being a very labour intensive task. Chapter 7 describes development of improvements on existing automated segmentation techniques, as applied to synapse fluorescence microscopy.

Automated analysis of ROI drift over the time-series of the assay allows both a concrete measure of the quality of the ROIs selected, and additional criteria by which to eliminate problematic ROIs, thus improving the overall quality of experimental data analysis. Chapter 6 discusses the evaluation of ROI drift in time-series image data, and based on this characterisation, recommends methods to increase the accuracy of the analysed data.

All of these steps, even if individually automated are tedious to perform per experiment and its multiple assays. Software created as part of this work automates the individual early image analysis stages to present an easy-to-view overview common to most experiments in this field. The end user still needs to perform the more varied higher level analysis manually, as these analyses depend on the individual experiments, but they can do so on a robust and repeatable set of basic analyses. Chapter 5 discusses this automation of image processing, and details its use in preparing usable test assay data for later projects.

The end goal of this segment of the work is to allow better measurement of kinetic rates and synapse behaviour to be possible given the available image data.

The other part of the work incorporates this observed behaviour of synapses into computational models of the underlying mechanisms behind the observed behaviour. Chapter 4 gives an overview of computational modelling and simulation tools of potential relevance to this area of neuroscience, and describes some of the existing work in the area.

Two projects were completed in this area:

- The first is a stochastic model of the complete vesicle cycle, tuned to the time-scale and behaviour of available experiments. Each assay has protocols designed to elicit specific behaviour of a synapse population, and the image data produced is linked with the experimental protocol. The modelling of the mechanisms behind this behaviour should reflect this specificity.

  Existing modelling tools are either generic programming languages, somewhat opaque to the researcher, specialised tools hand tuned to a specific problem, or more generic simulation tools only capable of handling a subset of the data.

FM-Sim is a simulator of a single model of the underlying synaptic vesicle recycling behaviour, but capable of representing the various stimuli of an experimental protocol. Given these stimulus events, it attempts to set rate parameters for each stimulus and thus provide inferred rate parameters under each regime which most closely matches the provided experimental data. Chapter 8 describes the development of FM-Sim.

- The second computational model of this work is a more detailed model of plasma membrane at the pre-synapse and its behaviour in response to pre-synaptic events; exocytosis and endocytosis. The goal is to demonstrate the effects of these stimulus driven events on the overall morphology and stability of the presynaptic membrane. This includes how exocytosis affects the growth of membrane area, and how well the pre-synapse recovers from these events with and without activity-dependent bulk endocytosis. Chapter 9 describes the development of this plasma membrane model.

Overall this work has shown that the image analysis and experimental computational modelling fit well together to give a more accurate understanding of the observed synaptic behaviour *in vitro* and bounds on the plausible mechanisms driving the presynaptic behaviour.

The artefacts of this work are the created image processing tools, and the computational models to be used as a framework to structure the available data. The bounds placed on possible plasma membrane area behaviour can be used to drive further experimental work in activity-dependent bulk endocytosis discovery.

Chapter 2

Biological background - the synaptic vesicle cycle

Chemical neural synapses within animals facilitate the transmission of signals from one neuron to the next. The locus of transmission between two neurons is the synaptic terminal, having a pre-synaptic and post-synaptic side. Transmission of a signal occurs when an incoming action potential on the pre-synaptic neuron triggers the release of chemical neurotransmitter into the gap between the neurons at the synaptic terminal; the synaptic cleft. There are a variety of common neurotransmitters, with glutamate being predominant within excitatory neurons of the central nervous system. This neurotransmitter is detected by receptors on the surface of the post-synaptic neuron, which triggers the generation of a signal on the post-synaptic neuron, thereby propagating the signal. A more detailed introduction into the overall biology of the synapse can be found in Chapter 5: Synaptic Transmission of Purves et al. (2008).

In detail, the process is substantially more complex than described above, involving the interaction of a host of complex molecules, ion gradients and transfers, and changes in the internal geometry of the neurons connected at the synapse. The process is highly dynamic and adaptive, both in the short and long term.

2.1 Exocytosis

On the pre-synaptic side, neurotransmitter is released in quanta, because it is contained in synaptic vesicles (spheres of membrane containing the transmitter molecules). When triggered, these vesicles merge with the plasma membrane at the active zones of the synaptic terminal and release the transmitter molecules into the synaptic cleft (Figure 2.1). These vesicles are classed as being within pools denoting their availability for release via exocytosis: the *readily releasable pool* consists of vesicles ready to be released immediately, while the *reserve pool* consists of vesicles filled with neurotransmitter, but not close enough to the plasma membrane for immediate release, and mobilised only during high levels of stimulus.

In one form of exocytosis the synaptic vesicle maintains its integrity, merging with the plasma membrane just enough to release the neurotransmitter through a pore. It then detaches from the plasma membrane intact to be reused (Harata et al., 2006). This is termed ‘fast’ or ‘kiss-and-run’ exocytosis. The other form of exocytosis has the vesicle merge completely with the plasma membrane. This work concentrates on the latter full fusion exocytosis (see Section 2.9).

2.2 Endocytosis

The exocytosis of synaptic vesicles must be balanced by a compensatory recovery to be sustainable over time. There is a contribution of synaptic vesicle membrane components constructed in the soma of the neuron and transported along the axon to the synaptic terminal. This transport takes time and is not sufficient to replenish the available synaptic vesicles after normal levels of stimulation. Rather, it is a longer term means of providing the components of chemical synaptic transmission to the nerve terminal. Over time full exocytosis would cause depletion of the pool of synaptic vesicles in the nerve terminal. The large increase in surface area of the plasma membrane would also damage the structural integrity of the nerve terminal. The short term balancing mechanism in response to stimulus is synaptic vesicle recycling via plasma membrane endocytosis.

Endocytosis within the pre-synaptic terminal is the invagination and retrieval of areas of the plasma membrane containing synaptic vesicle proteins back into the neuron, complementing the process of exocytosis. There are many forms of endocytosis, but the two primary forms studied in the context of pre-synaptic terminals in small CNS neurons are Clathrin-Mediated Endocytosis (CME) and Activity-Dependent Bulk Endocytosis (ADBE) (Figure 2.1). Other endocytosis mechanisms have been reported and are discussed in Section 2.9.

2.2.1 Clathrin-Mediated Endocytosis (CME)

CME retrieves areas of the plasma membrane the size of synaptic vesicles. An area of the plasma membrane is selected for retrieval based upon its surface proteins, and a series of sorting and adaptor proteins forms around the growing structure, which in turn may cluster surface proteins required in functional vesicles. One notable protein is clathrin, which forms a regular geometric cage around the structure. This is the distinguishing feature of this form of endocytosis. Once the vesicle has formed, it is separated from the plasma membrane. The clathrin cage then disassembles, releasing the clathrin and other proteins for reuse (Figure 2.2).

CME is considered the predominant means of endocytosis under low levels of stimulation in small central nervous system neurons in mammals (Granseth et al., 2006). In such situations it is adequate to cope with the normal physiological rates of exocytosis occurring.

CME has been well studied over the years, with nearly 200 papers discussing it in the context of synaptic vesicle recycling (Scopus search, Nov 2016). A good review of the mechanism and functions of CME can be found in McMahon and Boucrot (2011).

The stages of CME begin with nucleation and cargo selection where a cascade of interacting adaptor proteins cause the start of invagination and concentration of the desired membrane proteins. Then coat assembly further stabilises the collection of proteins around the forming

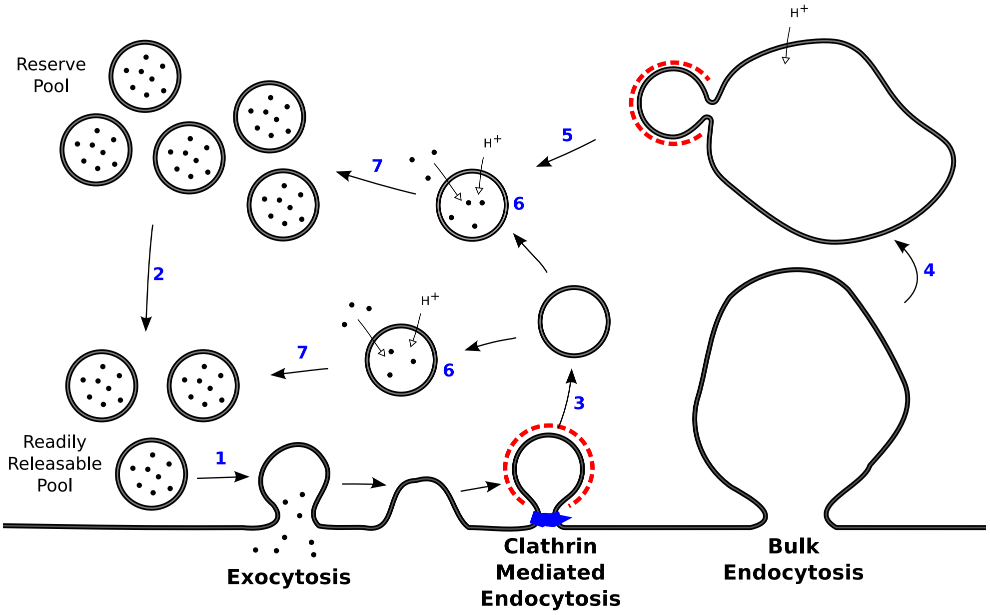

Figure 2.1: The synaptic vesicle cycle. Vesicles containing neurotransmitter reside in the presynaptic terminal. When stimulated, exocytosis of a vesicle from the readily releasable pool releases neurotransmitter (1); Activity causes mobilisation of reserve pool to repopulate readily releasable pool (2); Endocytosis allows recovery of plasma membrane via CME (3) and ADBE (4); Endosomes recovered via ADBE bud vesicles (5); Reacidification and refilling of regenerated vesicles (6); Repopulation of the vesicle pools with recovered vesicles (7). Clathrin cages formed around vesicles shown in red, dynamin ring around the neck of a fissioning vesicle shown in blue.

vesicle. The polymerisation and action of dynamin around the neck of the vesicle causes its scission from the plasma membrane. Once the vesicle is free within the cytoplasm of the nerve terminal, the clathrin coat and adaptor proteins disassociate from the vesicle, and are free to be reused. However, this simple description hides the complexity of the interactions of many proteins involved in the process, not all of which are fully understood to date.

2.2.2 Activity-Dependent Bulk Endocytosis (ADBE)

Under high levels of activity, a second mechanism activates. Here, rather than retrieving the plasma membrane one vesicle at a time, large areas of the plasma membrane are taken in as larger endosomes (Figure 2.1). These tend to have a volume significantly larger than that of a typical synaptic vesicle, estimated at approximately equivalent to fifty synaptic vesicles on average (Cheung et al., 2010; Nicholson-Fish et al., 2016). These endosomes are later decomposed into smaller vesicles. This mechanism is commonly called ‘Activity-Dependent Bulk Endocytosis’ (ADBE). The overall mechanism and its properties are reviewed in Cousin

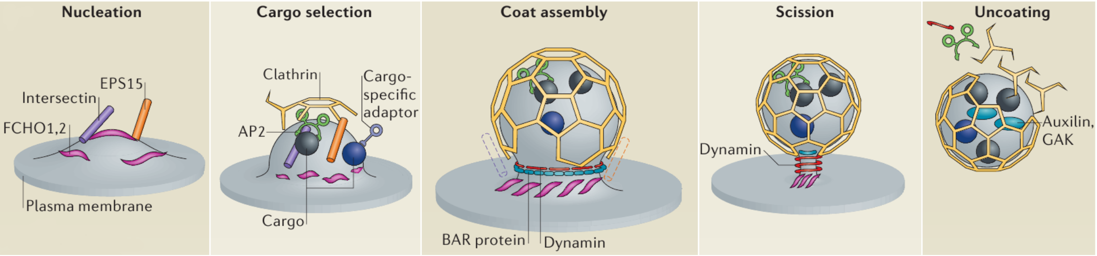

Figure 2.2: The clathrin-coated vesicle cycle. *Nucleation* - proteins bind to areas of the plasma membrane and recruit a sequence of other proteins to initiate clathrin-coated pit formation; *Cargo selection* - cargo-specific adaptors are recruited to the growing structure which select specific cargo proteins in the plasma membrane and enrich their presence in the forming vesicle; *Coat assembly* - clathrin proteins are recruited and polymerise around the structure; *Scission* - dynamin is recruited to the neck of the forming vesicle where it polymerises and induces scission of the vesicle from the plasma membrane; *Uncoating* - the clathrin and adaptor proteins disassemble, leaving a vesicle with embedded cargo proteins. From McMahon and Boucrot (2011), Figure 2.

(2009); Kokotos and Cousin (2015).

CME and ADBE have different triggers, pathways and kinetics. While CME has been studied for many years, ADBE is relatively new as a focus of study. It was first demonstrated in the frog neuromuscular junction in a study by Miller and Heuser (1984). It is fortunate that one of the labs specialising in the study of ADBE is here at Edinburgh University (the Cousin laboratory at the Centre for Integrative Physiology) providing ready access to significant expertise and archives of research data.

2.3 Post endocytosis events

After vesicles have been produced from endocytosis, either directly through CME or indirectly through vesicle budding from endosomes created by ADBE, the vesicles must then become competent for neurotransmitter release.

The vesicles and endosomes contain extracellular media (*in vitro*, or cerebrospinal fluid *in vivo*) when first endocytosed. This is chemically different from the content of a functional synaptic vesicle. In preparation for re-release the vesicle content is reacidified. This is accomplished by the inclusion of at least one vacuolar-type proton ATPase (V-ATPase) in the membrane of the vesicle. Its function is to pump H^+ ions into the vesicle. This drop in pH then causes neurotransmitter to flow into the vesicle via neurotransmitter transporters embedded in the vesicle membrane. As demonstrated in Cheung and Cousin (2013); Nicholson-Fish et al. (2016), this reacidification also occurs in ADBE generated endosomes.

Independently of this preparation of vesicle contents, there are studies suggesting the constituents of the membrane of a vesicle are also modified and sorted (Cheung and Cousin, 2012). This is suggested to occur via sorting endosomes so that the appropriate protein complement of a synaptic vesicle is produced.

There are also theories suggesting that non-fully competent vesicles may exist. These may lack the ability to bind to the plasma membrane and be triggered on stimulation, or may release correctly, but may not be filled with neurotransmitter (Daniels et al., 2006; Wojcik et al., 2004).

It is known that vesicles within the presynaptic terminal do maintain a stable number of the required proteins, suggesting that a significant amount of cargo sorting takes place during vesicle construction - either directly from the plasma membrane, or using sorting endosomes. Work into characterising the membrane components of a typical synaptic vesicle has included the influential paper Takamori et al. (2006) and the more recent refinements supplied by the work Mutch et al. (2011); Wilhelm (2013); Wilhelm et al. (2014).

Even within this well-delineated comparatively small section of neuroscience, there is a vast range of both complexity and variation. Synaptic vesicle recycling is behaviourally diverse across various cell types and species. Different neurons can have varying sizes of vesicle pools and various release probabilities and recycling kinetics. The complexity of the biological domain can be due to the complex chemical interactions of the proteins involved, geometric complexity of selection of vesicles for release, the interplay of the *in vivo* process and its alterations during the capture of *in vitro* experimental observations.

2.4 Kinetic properties of ADBE

This section discusses the discovered kinetic properties of ADBE, highlighting the results published by the Cousin laboratory and associates. Other research groups have also made significant advances in ADBE research, both supporting the work described below, and providing alternative views on the process, some of which are discussed in Section 2.9. The chemical and protein interactions involved in these processes are discussed in Section 2.5.

Figure 2.1 summarises the process flow of the stages of synaptic vesicle recycling of interest. Each stage where research within the Cousin laboratory and associates has yielded published results is discussed.

2.4.1 High stimulation levels trigger ADBE & CME; Mild stimulation levels trigger mainly CME

The initial stage of ADBE based recycling is the creation of bulk endosomes following presynaptic nerve stimulation. Clayton et al. (2008) established that high levels of stimulation (either physiologically with electrical stimulation of 400 action potentials at 40Hz or non-physiological chemical depolarisation of the nerve terminal membrane with KCl) are required to trigger ADBE. Lower levels of stimulation do not cause ADBE, and CME appears to be the main mechanism of endocytosis at these lower levels. The paper also showed that at high stimulation levels, the initial endosome formation in ADBE occurs rapidly. The process was mostly complete by the time the triggering stimulus had finished (approx. 10s). In contrast, CME was shown to have a slower initial vesicle formation time, with only 25% of the process complete by the end of stimulation (approx. 10s). This supports prior work by Balaji and Ryan (2007); Granseth et al. (2006) which established that CME occurs with a time constant of approximately 15 seconds at room temperature in rat hippocampal neurons.

2.4.2 ADBE derived vesicles are created from ADBE endosomes

Cheung and Cousin (2013) provided additional insight into the mechanisms of vesicle budding from ADBE endosomes. One difference from CME is that acidification begins before vesicles are formed from the endosome, and acidification is required for the vesicle budding to take place.

The same study established the generation of vesicles from endosomes after ADBE had taken place was demonstrated to be nerve terminal stimulus independent.

2.4.3 ADBE derived vesicle preferentially replenish the reserve vesicle pool

Cheung et al. (2010) showed that vesicles created through ADBE preferentially replenish the reserve pool of synaptic vesicles, as opposed to the readily releasable pool. This is conjectured to be due to timing of replenishment; the readily releasable pool may be mostly repopulated by the time ADBE derived vesicles are created.

2.5 Chemical and protein interactions of ADBE

Given the overall framework of ADBE kinetics described above, the Cousin laboratory and associates have also made progress in discovering some of the chemical and protein interactions required for this process. This section covers the main interactions and illustrates the complexity of the process at the molecular level.

2.5.1 Dynamin I - Syndapin I cycle

The proteins Dynamin I and Syndapin I are essential for the creation of the endosomes in ADBE (Clayton et al., 2009; Smillie and Cousin, 2005). The cycle these proteins follow is shown in Figure 2.3.

Dynamin I in its resting state has two phosphorylated serine residues (Ser774 and Ser778). Upon high levels of nerve terminal stimulation, the phosphatase calcineurin is activated (Clayton et al., 2009). Active calcineurin dephosphorylates both serine residues of Dynamin I. The now active Dynamin I then binds with Syndapin I, and the Dynamin I - Syndapin I complex in turn triggers ADBE (Anggono et al., 2006).

To restore Dynamin I to its resting state, two separate kinases rephosphorylate the serine residues (Clayton et al., 2010; Evans and Cousin, 2007; Tan et al., 2003). First, CDK5 rephosphorylates the Ser778 residue. Only after this has happens can GSK3 rephosphorylate Ser774.

The action of GSK3 was shown to be modulated by the protein kinase Akt (also known

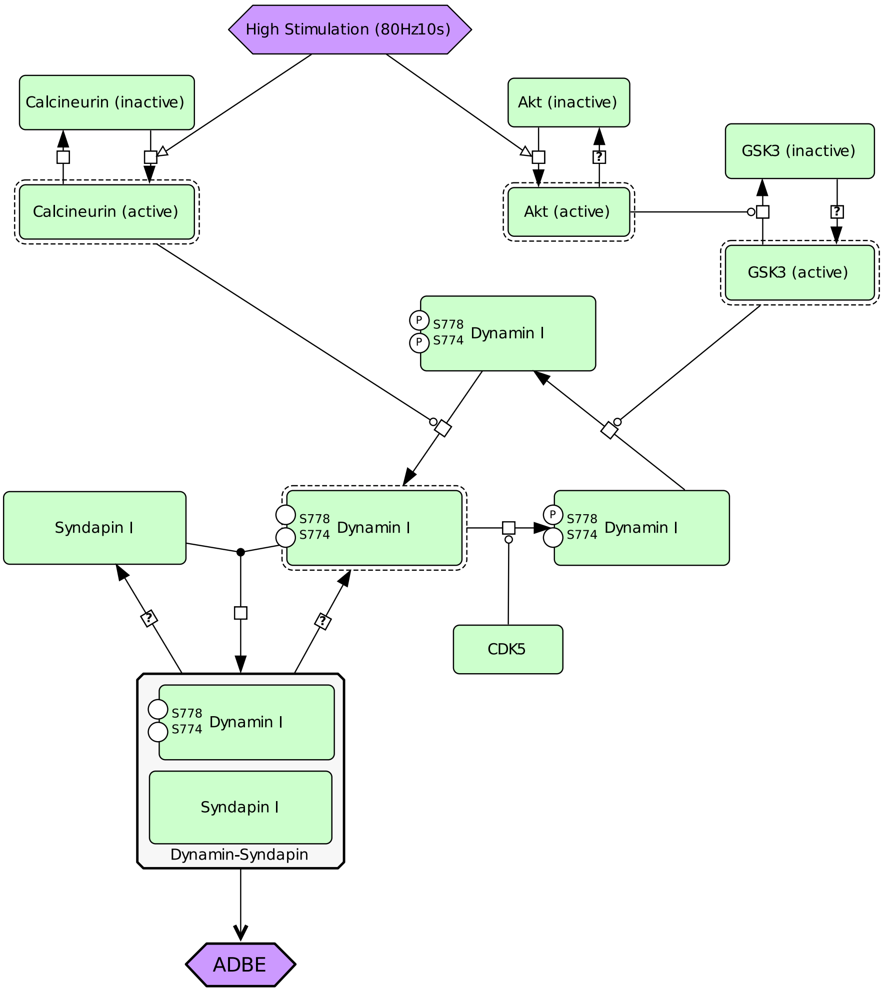

Figure 2.3: Phosphorylation-dependent Dynamin I - Syndapin I cycle. High levels of electrical stimulation activates Calcineurin, which dephosphorylates Dynamin I. Dephosphorylated Dynamin I binds to Syndapin I, leading to ADBE. In the recovery phase after endocytosis has occurred, Dynamin I dissociates from Syndapin I, and its two phosphorylation sites Ser-778 and Ser-774 are rephosphorylated in turn. First, CDK5 rephosphorylates Ser-778, then active GSK3 rephosphorylates Ser-774, priming Dynamin I for reuse. High levels of stimulation also activates Akt, which then inactivates GSK3. In the short term, this is thought to increase the efficiency of Dynamin I dephosphorylation during high levels of stimulus. Systems Biology Graphical Notation (SBGN, Le Novère et al. (2009)).

as PKB - protein kinase B) (Smillie and Cousin, 2011, 2012). Upon high levels of stimulation, phosphorylated Akt phosphorylates GSK3, which in turn inhibits the ability of GSK3 to rephosphorylate Dynamin I. This increases the net efficiency of Dynamin I dephosphorylation during high stimulation, which in turn increases the acute activity of ADBE.

However, if constitutively activated, the effect of Akt on GSK3 causes inhibition of ADBE as the Dynamin I rephosphorylation recovery part of the cycle is impaired.

GSK3 controls the second of two rephosphorylation steps, after CDK5 has been active.

2.5.2 Calcium and calcineurin required for vesicle creation from ADBE endosomes

Cheung and Cousin (2013) demonstrated that both calcium and its interaction with calcineurin are required for vesicles to bud from ADBE endosomes. The calcium is contained within the endosomes themselves, having been taken up by the cell from the extracellular media during endocytosis.

2.5.3 Proteins AP-1 and AP-3 are both required for vesicle creation from ADBE endosomes

Cheung and Cousin (2012) demonstrated that both adaptor proteins AP-1 and AP-3 are required for vesicles to bud from ADBE endosomes, but are not required for either CME or the initial creation of ADBE endosomes. This is in contrast to the requirement of protein AP-2 for CME to take place (Kim and Ryan, 2009).

2.6 Pathologies

Incorrect functioning of synaptic vesicle recycling has been linked to a number of diseases and developmental disorders of the nervous system, such as Huntington's disease (Rozas et al., 2010) and Alzheimer's disease (Arendt, 2009). This adds weight to the need for understanding exactly how these mechanisms work. Recent work has established links between genetic mutations of known recycling proteins and certain disorders. Recent work in Gordon and Cousin (2013) as demonstrated mutations in the presynaptic protein synaptophysin in patients with X-linked intellectual disability interfere with the retrieval kinetics of synaptobrevin II.

2.7 Laboratory tools and protocols

There are a number of experimental tools and protocols available to elucidate *in vitro* properties, some developed locally at the Cousin laboratory. This section is a brief overview of the techniques available. It is important to consider what observations can be made for a particular experimental assay, and what are the limitations of these techniques. The detailed protocol for some of the techniques discussed is beyond the scope of this review.

2.7.1 Fluorescence microscopy

Adding fluorescent markers of various kinds to neurons allows time-series imaging to be performed. This makes it possible to see the effects of stimuli on individual nerve terminals. There is flexibility on the level of magnification (x20 and x40 are common), and on the frequency of images captured during the course of the experiment (0.25Hz is common). The commonly used fluorescence markers are discussed in Section 2.7.6.

The technique has some inherent limitations. First, the resolutions in use allow detection of entire nerve terminals as a small region of pixels, commonly falling within a circle 5-10 pixels in diameter. At this low resolution it is difficult to obtain information on anything other than the nerve terminal as a whole. More detailed analysis of areas within the nerve terminal is challenging. Ingenuity in experimental design is required to de-construct this single measure per nerve terminal to highlight the mechanisms of the synaptic vesicle cycle.

Second, for most of the fluorescent markers in use, photo-bleaching of the marker is a significant issue. This limits the useful duration of the experiment, and the frequency at which individual images can be taken. Also, fluorescence signal decay must be taken into account when performing the image analysis.

Finally, the specificity of fluorescent markers is variable. The signal from the nerve terminals can be difficult to discern from the fluorescent noise in the image. This noise can be caused by marker being accumulated in other areas of the neuron, or visible in dead or unhealthy neurons.

Time-series fluorescence microscopy image analysis is discussed in more detail in Chapter 3.

2.7.2 Electron microscopy

Electron microscopy (EM) images are of much higher resolution, and with the use of appropriate markers, can be used to highlight specific features within individual nerve terminals.

The primary weakness of EM is that it provides only a single time-point for a given nerve terminal. The sample preparation process is destructive and the nerve tissue used is no longer viable. Finally, the most common form of imaging in recent literature is transmission electron microscopy in which individual thin slices are imaged. This is adequate for analysis work concerned only with 2D metrics. However, it is difficult to extrapolate to 3D volumes as population-averaged 2D data introduces a significant source of error during analysis.

Three-dimensional slice reconstruction is possible, and has appeared in the literature (Holderith et al., 2012; Marra et al., 2012; Schikorski and Stevens, 1997; Wilhelm, 2013; Wilhelm et al., 2014), but is considerably more expensive and technically challenging than 2D imaging.

2.7.3 Immunoblot and similar gel electrophoresis techniques

These techniques allow estimation of protein quantities within a tissue sample. As with electron microscopy, this is a destructive technique which can only be performed once on a nerve tissue sample. The process requires considerable skill to perform correctly and reliably. The protein levels are usually normalised against a ubiquitous protein, allowing comparison of samples to determine the increase or decrease of protein levels under varying conditions. Recent work has combined gel electrophoresis with mechanical separation of endosomes and synaptic vesicles from synaptic terminals to provide organelle specific protein levels (Nicholson-Fish et al., 2015, Figure 6).

2.7.4 Electrophysiology

Electrophysiology is commonly used to detect the propagation of signals to the postsynaptic neurons. By measuring the excitatory or inhibitory postsynaptic current (EPSC or IPSC) triggered after stimulating a presynaptic neuron, estimates can be made of the quanta of neurotransmitter released through synaptic vesicle exocytosis. Other electrophysiological techniques include measuring the changes in capacitance of the plasma membrane of a neuron (Gillis, 2000; Wölfel and Schneggenburger, 2003), which would be affected by the area of plasma membrane added or lost through synaptic vesicle recycling, however this is challenging to perform on small CNS neurons as the diameter of a typical synaptic terminal is in the order of 1μm.

One interesting experimental technique is the creation and use of autapses. These are synapses formed when neurons form synapses with themselves (Ikeda and Bekkers, 2006). As both pre and postsynaptic parts of the synaptic terminal are the same cell, electrophysiology of synaptic activity becomes much easier. Autapses can be induced to form in neural cell cultures as described in Bekkers (2005).

2.7.5 Neuron types and preparations

Given the range of synapse structures, and the wide variety of synaptic recycling behaviour due in part to that varying structure, research tends to fragment into pursuing a subset of possible experimental models. Rizzoli and Betz (2005) have given a good comparative overview of the range of presynaptic structure shown in animal models, ranging from small central nervous system neurons containing a few hundred vesicles per presynaptic terminal, to the large terminals of the frog neuromuscular junction which may contain over 500,000 vesicles.

This work concentrates on small mammalian central nervous system neurons, in particular hippocampal neurons and cerebellar granule neurons from mouse and rat. These are the animal models most frequently studied for ADBE research at the Cousin laboratory (Tan et al., 2003).

There is also variability in synaptic vesicle counts depending upon the preparation of the neurons. As mentioned in Rizzoli and Betz (2005), based upon observations made in Harris and Sultan (1995), vesicle counts are different depending upon whether the neurons (hippocampal in this case) are taken from slice preparations (~450 vesicles in medium sized synaptic terminals) or from cultures (100-200 vesicles per terminal, Granseth et al. (2006); Schikorski and Stevens (1997)). The majority of analysis in this work was based on image data taken from isolated cultured neurons forming synapses *in vitro*. The preparation methods of these cultures are detailed in Anggono et al. (2008); Cousin (2008) when using FM dye (see Section 2.7.7.1), and the preparation of cultures using VAMP4-pHluorin (see Section 2.7.7.2) is detailed in Nicholson-Fish et al. (2016).

Finally, an alternative vehicle for studying synaptic vesicle recycling are synaptosomes.

These are isolated nerve terminals obtained by centrifugation and fractionation of homogenised nerve tissue (Whittaker, 1993). They provide a good vehicle to study presynaptic behaviour with less noise from other parts of neurons, and have been used in a number of studies in collaboration with the Cousin laboratory (Anggono et al., 2006; Xue et al., 2011), and in other works (Wilhelm, 2013; Wilhelm et al., 2014).

2.7.6 Reagents and modified expressed proteins

A range of reagents are used in experimentation on cultured neurons. These are either markers to allow visualisation of nerve terminals in certain states, or chemical activators to force activation, or inhibitors to switch off parts of the vesicle recycling machinery. In addition, genetic modifications can be made to the proteins involved in vesicle recycling. These modifications can switch off protein function, or add markers to allow visualisation of behaviour within the nerve terminal (Kavalali and Jorgensen, 2014; Lin and Schnitzer, 2016). Some of the commonly used reagents and proteins are discussed in the following sections.

2.7.7 Fluorescent markers

2.7.7.1 FM styryl dyes

These dyes embed in the outer leaflet of the plasma membrane. They fluoresce considerably more when embedded than they do when in free suspension (Betz et al., 1992, 1996). It is possible to create fluorescent vesicles and endosomes by first flooding the extra-cellular media of cultured neurons with the dye, then stimulating the nerve terminals to internalise plasma membrane via endocytosis, and finally washing the excess FM dye off the plasma membrane (Cheung and Cousin, 2011; Cousin, 2008). Monitoring the decline in fluorescence during subsequent triggered exocytosis allows analysis of exocytosis rates, vesicle pool mobilisation rates, and the sources of vesicles for the various vesicle pools. Their kinetics and membrane affinities were more fully characterised in Wu et al. (2009), showing the behaviour of the dyes under a range of experimental conditions. While a wide range of these styryl dyes exist, two commonly used types in research are FM1-43, and FM2-10 (Figure 2.4). One property of the dyes is that under certain experimental protocols, in particular depending on the dye concentrations used, FM1-43 can be internalised by both CME and ADBE, while FM2-10 can be internalised by CME only. This differential labelling is characterised in Clayton and Cousin (2008), and has been used extensively in ADBE kinetic assays within the Cousin laboratory, for example Cheung et al. (2010); Clayton et al. (2008).

During typical imaging of FM dyes, fluorescence decrease corresponds to a synaptic vesicle containing the FM dye being exocytosed, and the FM dye dissociating from the membrane of the vesicle (and immediately reducing in fluorescence intensity), and then being washed away in the flow of extracellular media. This reports levels of exocytosis, but not information about endocytosis. FM dye assay protocols allow for near complete depletion of FM tagged vesicles

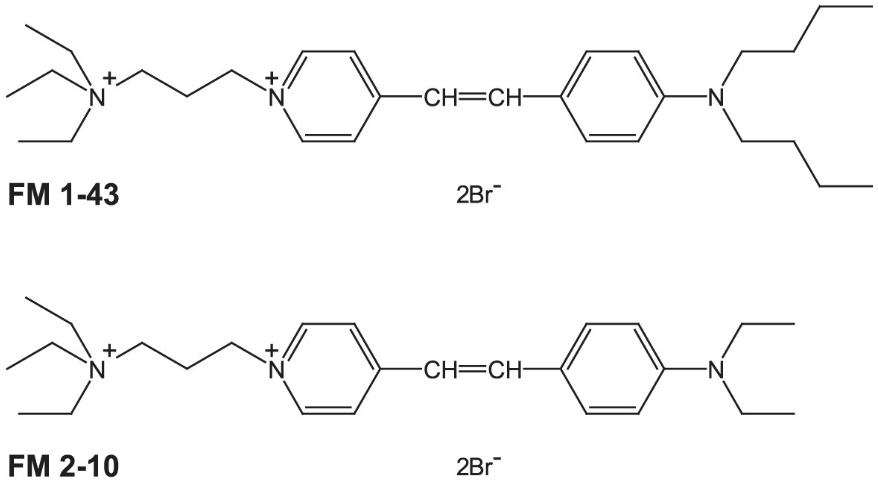

Figure 2.4: Chemical structure of two FM styryl dyes. Note the different lengths of the lipophilic tails on the right of the structure schematics, conferring different affinities for the lipid plasma membrane. From Wu et al. (2009), Figure 1.

in the nerve terminal, which allows calibration of exocytosis over time as a ratio of overall starting vesicle pool size.

2.7.7.2 pH-sensitive fluorescent marker proteins

These are transmembrane vesicle proteins fused to a pH-sensitive fluorescent marker protein. There are now many varieties. The basic principle of operation remains the same however, as they directly indicate the level of acidity of the fluid in contact with the membrane in which they are embedded (for example, Figure 2.5 shows the operation of pHluorin based marker proteins). There is a difference in pH between the lumen of synaptic vesicles at resting state within synaptic terminals (pH $\approx$ 5.5), and the extracellular media (pH $\approx$ 7.4). These marker proteins are engineered to fluoresce in response to part of this pH range. pHluorins for example are modifications of the already pH-sensitive green fluorescent protein (GFP) engineered to increase their fluorescence response to pH changes (Miesenböck et al., 1998). As membrane is exocytosed, endocytosed, and the lumen of internalised structures reacidified, time-series microscopy can record the changes in fluorescence levels as local pH levels change.

The variety of marker proteins allows recording of behaviour of different transmembrane vesicle proteins with different localisation properties. The choice of fluorescent marker fused to the protein determines the fluorescence properties as markers may respond to different pH ranges.

SynaptopHluorin is constructed of a fluorescent protein fused to synaptobrevin (Miesenböck et al., 1998; Sankaranarayanan et al., 2000; Sankaranarayanan and Ryan, 2000), while sypHy is constructed from the same fluorescent protein fused to synaptophysin (Granseth et al., 2006).

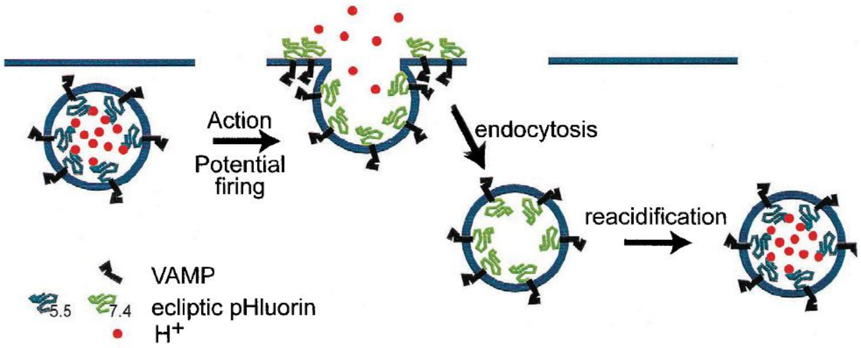

Figure 2.5: The pHluorin marker proteins fused to VAMP transmembrane proteins are non-fluorescent in an acidified vesicle within the pre-synaptic terminal (*left*). Exocytosis of a vesicle in response to an action potential exposes the pHluorin to pH-neutral extracellular media, causing fluorescence (*centre*). Endocytosis of the plasma membrane into a vesicle with pHluorins has continued fluorescence, which is gradually quenched by the reacidification of the vesicle (*right*). From Sankaranarayanan et al. (2000), Figure 1.

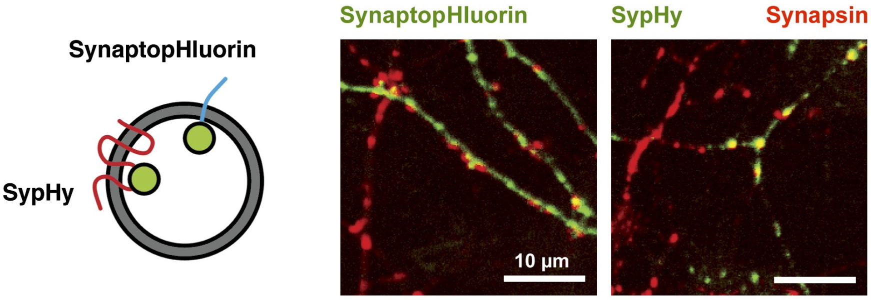

Figure 2.6: (Left) Schematic illustration of differing topology of sypHy and synaptopHluorin. (Right) Confocal images of neurons expressing pHluorins. Note the more punctate localisation of sypHy. From Granseth et al. (2006), Figure 2.

Key features here are that the markers are fairly stably embedded in the membrane, and unlike FM dyes, cannot be washed away. Changes in fluorescence level can be used to monitor both endocytosis (as the fluorescence decreases with pHluorins) or exocytosis (as the fluorescence increases when the acidic vesicle contents mix with the less acidic extracellular media).

SypHy has been shown to have less lateral movement through the synaptic (and plasma) membranes than synaptopHluorin (Figure 2.6), and therefore is more likely to remain localised within the synaptic terminal. This improved localisation gives a cleaner fluorescent signal (Granseth et al., 2006).

While the FM dyes in the previous section can be added to neurons by adding the dyes to the extracellular media and stimulating uptake into the cell, transmembrane marker proteins such as synaptopHluorin and sypHy must be manufactured within the cell to be correctly localised to synaptic vesicle membranes. DNA constructs coding for the novel proteins are transfected into the cells to be imaged, causing expression of the proteins. The studies characterising the fluorescent proteins cited above do show the proteins localised to synaptic terminals visible as fluorescent puncta. One drawback of this method is that the overexpression of the carrier proteins synaptobrevin or synaptophysin may have physiological consequences to the neuron. Gordon et al. (2016) demonstrated that a balance of expression levels of synaptobrevin II and synaptophysin were required to prevent synaptobrevin II from being dispersed along the axon of expressing neurons. Careful experiment design should take these potential effects into account, generally using DNA titration to obtain DNA concentrations which do not negatively impact cell viability.

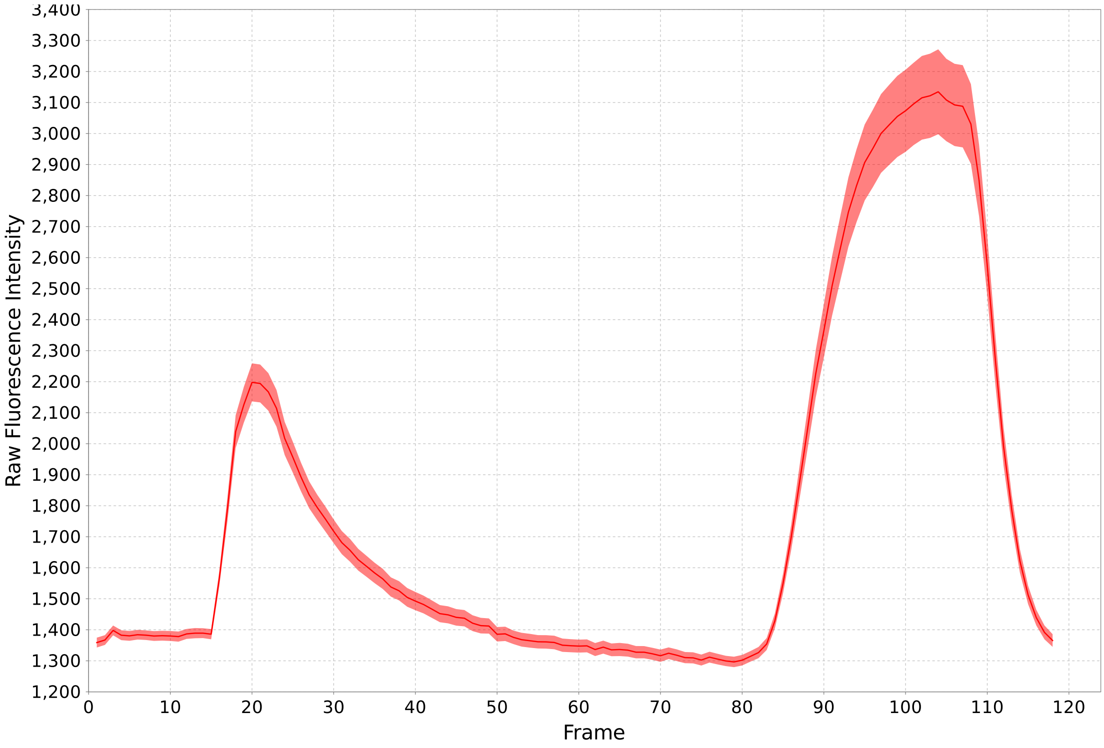

Figure 2.7: Example ROI set intensity trace from a pHluorin assay with 92 ROIs, showing the raw mean fluorescence intensity (with standard error) in arbitrary fluorescence units. Note the stimulus response on the left, and the NH_4^+ response on the right. Original data collected by Katherine Bonnycastle.

A typical pHluorin trace is constructed from a set of individual ROI traces from a single assay, or a number of assays with some time adjustment to line up the traces (Figure 2.7). There are a number of phases:

- Static phase: Usually a straight line. It is assumed there are low levels of spontaneous vesicle recycling taking place here, but not to the level where there is a noticeable change in fluorescence, as exocytosis and endocytosis are in balance. Generally any reduction in fluorescence during this time period is deemed due to photo-bleaching, and the decay during this phase is used to establish baseline values of photo-bleaching decay.

- Stimulus phase: Exocytosis occurs and is shown by a rapid increase in fluorescence. Under low levels of stimulus, CME also occurs with a defined delay. There is some debate as to other forms of exocytosis and endocytosis occurring concurrently (see sections 2.9.2, 2.9.3). Under high levels of stimulation, activity-dependent bulk endocytosis occurs. Depending on the duration of the stimulus phase, some reacidification may have occurred and had an effect on the fluorescence trace.
- Recovery phase: Exocytosis has returned to spontaneous levels, while CME continues. ADBE has been shown to end soon after the end of stimulation (Clayton et al., 2008). Internalised vesicles and endosomes continue reacidification, quenching the fluorescence over time.

2.7.7.3 Dextran

Large fluorescent-tagged dextran molecules can be used to tag endosomes formed by ADBE (Clayton and Cousin, 2009; Clayton et al., 2008). As the molecules are too large (usually 10 kDa or 40 kDa) to be endocytosed within single CME vesicles, they are taken up within the larger ADBE endosomes. This provides another means of selectively quantifying ADBE activity during fluorescence microscopy experiments.

2.7.8 Temporary fluorescence modifiers

As pHluorins and similar marker proteins are pH sensitive, modifying the pH of the environment in contact with the marker proteins alters the fluorescence. Adding acid or base to a cell culture is a common means of temporarily doing this.

2.7.8.1 pHluorins with acid

Adding impermanent acid to the extracellular media quenches fluorescence from all pHluorins on the plasma membrane, and not fully internalised (i.e. partially formed) endosomes and vesicles (Figure 2.8). When applied immediately after endocytosis, this shows the remaining partially reacidified vesicles and endosomes. When applied after sufficient time for all vesicles and endosomes to be fully reacidified, this provides a base fluorescence level for calibration.

2.7.8.2 pHluorins with NH_4^+

NH_4^+ ions cause all (or most) pHluorins anywhere in a nerve terminal to fluoresce, by unquenching any pHluorin that is in an acidic environment. The application of an ammonium pulse at the end of an assay is a common means of calibrating the fluorescence levels; the fluorescence should show all vesicles, endosomes, and membrane of the vesicle recycling machinery.

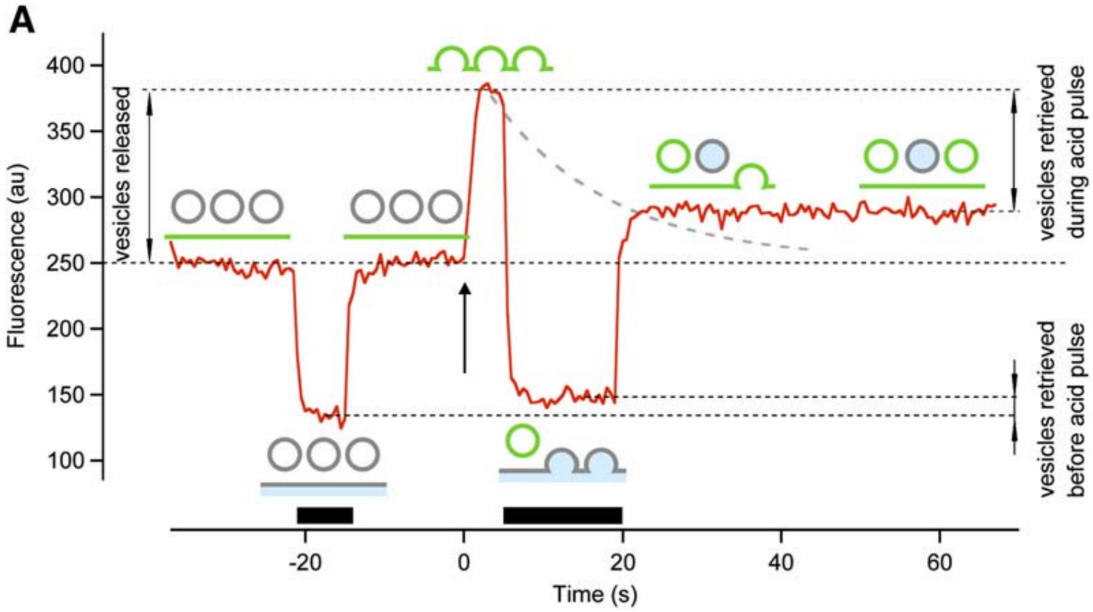

Figure 2.8: Example intensity trace showing effects of acid pulses (red line). In this experiment acid pulses were used to quench fluorescence on surface exposed proteins (first black bar), and to quench fluorescence on vesicles undergoing endocytosis (second black bar) after stimulation with 40 action potentials at 20Hz (black arrow). Normal reacidification of vesicles after endocytosis was prevented using bafilomycin A1. The differences in height of the fluorescence trace are then used to quantify the ratios of exocytosed vesicles retrieved before and during the second acid pulse. From Granseth et al. (2006), Figure 4.

2.7.9 Biological process inhibitors

Certain reagents disrupt parts of the synaptic vesicle recycling process. This can be performed either by using genetic knock-out animals, reducing normal levels of expression of key proteins (knock-down), or chemically disrupting the normal function of key proteins. The last of these includes techniques such as adding antagonists to block protein function, or making use of genetic techniques which allow acute removal of proteins from the area of interest (knock-sideways) (Robinson et al., 2010).

2.7.9.1 Bafilomycin A1

Bafilomycin A1 inhibits the refilling of neurotransmitter into newly formed synaptic vesicles by blocking the action of the V-ATPase proton pump, thereby preventing reacidification of the vesicle (Cousin and Nicholls, 1997; Roseth et al., 1995). It is used in electrophysiological studies wishing to record the release of existing vesicles from vesicle pools, discounting newly created vesicles formed during vesicle recycling (Ikeda and Bekkers, 2009; Xue et al., 2013).

With fluorescence microscopy, the blocking of reacidification of endosomes and vesicles prevents the internal quenching of fluorescence (Atluri and Ryan, 2006). In this situation fluorescence increase during stimulus shows the membrane that has been exocytosed only. Under intense stimulation, this can show cumulative vesicle exocytosis and vesicle pool depletion (Figure 2.9).

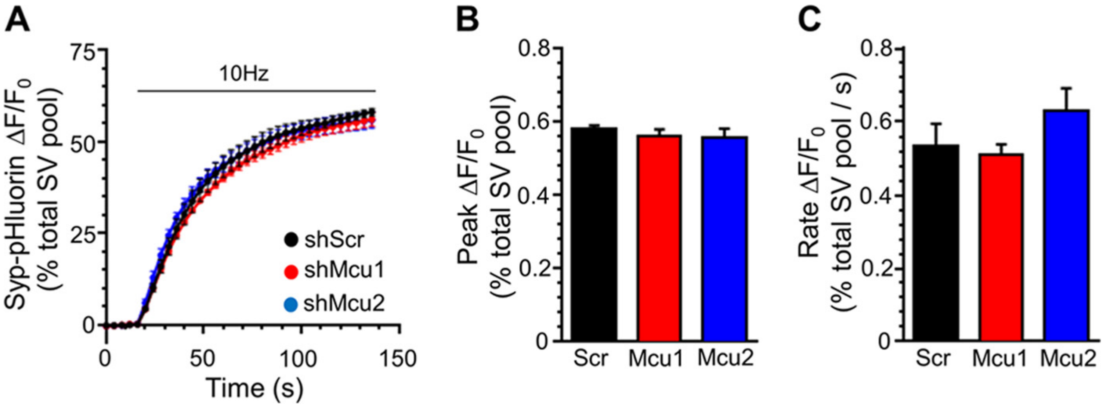

Figure 2.9: Example pHluorin traces showing the effect of Bafilomycin A1. In this case, the effect was used to demonstrate the knockdown of the protein mitochondrial calcium uniporter (MCU) had no effect on synaptic vesicle exocytosis as the traces did not vary significantly between conditions. In this figure the fluorescence levels of Syp-pHluorin (SypHy) during sustained 10Hz stimulation are shown for cultures transfected by one of two shRNA targeting MCU or a scrambled control (shScr). From Marland et al. (2016), Figure 2.

If reacidification is inhibited, then the application of acid quenches all surface fluorescence, leaving only the internalised vesicles and endosomes to fluoresce. Depending on the timing of acid application and stimulus, this may be used as a marker of endocytosis in response to stimulus (Figure 2.8).

2.8 Experimental research issues and caveats

Determining the mechanism and behaviour of synaptic terminals is extremely difficult. The development of the existing tools and their use demonstrate impressive dedication on the part of experimental researchers. The current procedures, while state of the art, have a number of assumptions and caveats which must be accounted for during experimental research. This section details some of those issues relevant to fluorescence microscopy. The first section details biological issues, followed by information extraction issues

2.8.1 Environmental issues

In vitro imaging of cultured neurons allows a wide range of direct manipulation of synapse behaviour, much more than would be possible using *in vivo* models or *in vitro* slice preparations. This does come at the cost of increasing the differences between the experimental model and the cells in their natural state. These differences must be taken into account when determining mechanism.

Cultured neurons are considerably less densely packed than slice preparations, and lack many of the supporting cell structures, such as glia, present *in vivo*. Environmental conditions including temperature must be taken into account during imaging. Cell processes including vesicle endocytosis and reacidification operate more slowly at room temperature than at physiological temperature, as characterised in Granseth and Lagnado (2008). There has been robust debate in the last few years that the performance of imaging at room temperature introduces mechanistic artefacts (CME) into the recycling process that would not occur *in vivo* (see Section 2.9.3).

2.8.2 Overexpression and reagent toxicity

Addition of tagged membrane proteins to cells requires transfection. This means the cells contain a mixture of both tagged and untagged versions of the protein in question, and the protein is usually substantially over-expressed. This change in the biology of the cell needs to be taken into account. Generally assays are performed to show that the recycling kinetics of the cell are not significantly affected. Also, some genetic variants have the endogenous protein in question absent (knock-outs).

Central nervous system neurons are remarkably robust. With care, it is possible to culture cells *in vitro* such that they spontaneously form synapses, allowing experimental work. This is a remarkable feat when one considers the complexity of what is occurring. These cells can tolerate a substantial amount of genetic and chemical manipulation and still function. However there are limits to their ability to tolerate manipulation.

Culture and manipulation of the cells used in an assay cannot be assumed to have no effects on the mechanism being studied. It is common for assay cultures to return noisy data as the cells themselves tend to become unhealthy and die. Many of the reagents used to prepare the cells for testing are toxic, and their concentration must be carefully calibrated to ensure enough cells remain healthy for long enough to be imaged.

2.8.3 Partial effects

The described genetic and chemical modifiers may not have 100% efficacy. For example RNAi knockdown of protein expression can vary substantially, and the level of knockdown must be experimentally quantified using immunofluorescence or similar assays.

What is more difficult to determine however is what effect the remaining active protein has during an assay. Can a linear correlation between fraction of protein removed or chemically deactivated and its effect on behaviour be established? In most cases this cannot be assumed. For example, if the application of Bafilomycin A1 during an assay blocks 90% reacidification, it requires care to correctly interpret observations when the remaining 10% activity can influence pHluorin fluorescence during a recycling assay.

2.8.4 Off-target effects

Endogenous proteins may have multiple functions within a cell, or even within a presynaptic terminal. Modifying levels of protein expression or protein structure to highlight a particular recycling step may also have unintended consequences elsewhere in the cells' metabolism. This in turn may indirectly affect the assay results. Similarly, chemical modifiers to trigger or inhibit a particular operation may have more wide ranging effects within the cell, besides the potential toxicity effects described above.

Careful construction of control and calibration assays are usually required to demonstrate that off-target effects are not confounding the results of the intended assay.

2.8.5 Event and imaging time resolution

Synaptic vesicle recycling events occur over a wide ranging time-scale, from milliseconds for action-potential triggering of exocytosis, seconds for ADBE and CME events, minutes for endosomal budding and re-population of vesicle pools, to longer time periods for vesicle pool modifications, vesicle degradation and arrival of new vesicles from outside the synaptic terminal.

Individual assays can target only part of this range, and with variable resolution. Static images of particular time-points can be fast, in the order of tens of milliseconds for flash-and-freeze (Watanabe et al., 2014) experiments. Time-series imaging by necessity must balance assay duration against frame rate during imaging.

2.8.6 Individual inferences from population measures

Using fluorescence microscopy time-series data there is not sufficient time or visual resolution to follow the cycle of individual structures within synapses. The behaviour of individual structures must be inferred based on their suspected contribution to the overall population measure.

Time-series imaging does provide many samples of these population measures, but the inferences are still based on mean activity rather than direct observation. For example a vesicle budding from an endosome and migrating back to the plasma membrane cannot be observed in real time. Much of the variation in behaviour between synapses, and all of the sub-synapse variation is not captured with these population measures.

2.8.7 Photo-bleaching

Fluorescent markers are prone to bleaching over time and under excitation, with variable severity depending on the marker in use. This interferes with the synapse fluorescence signal of fluorescence markers. Bleaching is mitigated by both designing experiments to minimise the bleaching likely to occur, and by compensating for the effects of bleaching on the resulting image data.

Experiment design constraints may include limiting the duration of experiments, limiting the imaging frame rate to the minimum necessary to reliably show behaviour, not imaging during rest and other periods where image data is not required by the experiment design, and restricting the excitation of the sample to the minimum required to reliably perform the imaging.

Even with these measures, there may still be a significant level of bleaching. This must be compensated for in the processed image data to obtain accurate estimates of synapse activity. This is normally done by applying a bleaching correction to the fluorescence intensity information extracted from the time-series image, described in Section 3.4.2.

2.8.8 Inference from 2D cross-sections in electron microscopy

As previously mentioned, 2D cross-sections are frequently produced with electron microscopy based analysis. If an unbiased selection of images are chosen and the assumption is made that a cross-section is representative of the whole synapse, then some measurements can be made. These are usually structure counts and 2D measurements of structure dimensions.

The researcher is limited to using structure counts as relative measures, i.e. counts of tagged versus untagged structures within an image, or mean counts of structures in control versus test condition images (for example Figure 2.10, Clayton et al. (2008)). It is not possible to reliably extrapolate total counts of structures within a synaptic terminal based on a single 2D cross-section, rather serial sections reconstructed into a 3D image would be required.

Similarly, trends in structure dimensions can be quantified within and between images as performed for example in the endosome budding characterisation in Cheung et al. (2010), but absolute determination of structure dimensions in 3D cannot be reliably inferred from 2D images.

2.9 Research process & ongoing debates

Using the tools described above among others, research has teased apart the mechanisms of synaptic vesicle recycling. As it is currently beyond our capability to directly observe these processes happening, published research had relied on secondary observations, and designed experiments to relate these observations back to the mechanisms theorised to have caused them.

This research process has not been without debate, with conflicting evidence and theories appearing in the literature over the years. There have been a number of reviews attempting to integrate the apparently conflicting results in the literature (Kononenko and Haucke, 2015, for example). Three relevant areas of discussion over the years have been the ratio of available synaptic vesicles which take part in synaptic vesicle recycling, the evidence for kiss-and-run exocytosis in small central nervous system terminals, and the recent debate on the role of ultrafast endocytosis in small central nervous system terminals.

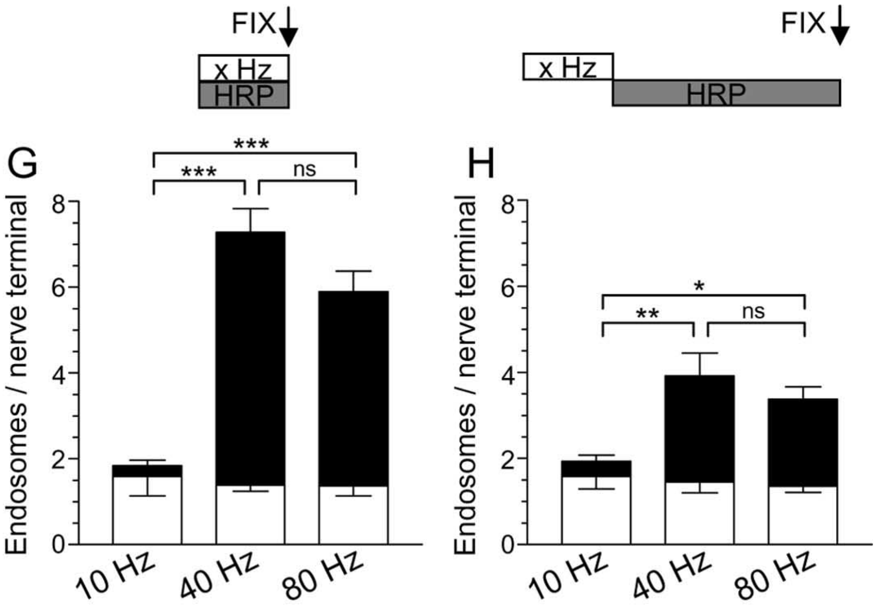

Figure 2.10: Quantification of ADBE derived endosomes (black bars) at different stimulus levels. Nerve terminals were electrically stimulated for trains of 200 (10Hz), 400 (40Hz) or 800 (80Hz) action potentials. Horseradish peroxidase (HRP) was applied to the cultures either during (G) or for 5 minutes after stimulus (H). The cultures were then fixed and prepared for 2D electron microscopy. Endosomes present in nerve terminals were then counted, differentiating between non-HRP containing (white bars) and HRP containing (black bars). The mean counts of endosomes of each type per nerve terminal are shown. From Clayton et al. (2008), Figure 3.

2.9.1 Synaptic vesicle pool active use

The standard models of geometry of vesicles within nerve terminals places the vesicles in distinct pools. These pools are not spatially separated however, but merely a means of classifying the functional characteristics of vesicles within a nerve terminal.

There is debate between research groups both on the terminology used to describe these vesicle pools, and their proportions within synaptic terminals. In rat hippocampal neurons, a number of groups agree on a model consisting of the *readily releasable pool* (RRP) of vesicles available to be released immediately, and the *reserve pool* (RP) consisting of vesicles which are mobilised under conditions of intense stimulation as the readily releasable pool is depleted. Together these pools make up the *recycling pool* of vesicles. An additional pool of vesicles exists not releasable under physiological stimulation called the *resting pool*, which may have a role in spontaneous vesicle exocytosis (Fredj and Burrone, 2009). The recycling pool makes up approximately 50% of the total vesicle count of a total of around 100-200 vesicles per synaptic terminal (Granseth et al., 2006; Schikorski and Stevens, 1997), although there is considerable variability between synapses (Fernández-Alfonso and Ryan, 2008; Kim and Ryan, 2010).

Alternate models of vesicle pools and their proportions are discussed in the reviews by Denker and Rizzoli (2010); Rizzoli and Betz (2005), retaining similar features; multiple pools with the reserve pool sequestering vesicles away from release during mild physiological stimulation. Additions to the model allowed for exchange of reserve pool vesicles between nerve terminals within a neuron.

However, these models have been challenged by electrophysiological studies showing that the bulk of the available vesicles in a synaptic terminal are released under mild physiological stimulation. This was shown for hippocampal neurons by Ikeda and Bekkers (2009), and subsequently for neurons in the Calyx of Held by Xue et al. (2013).

Additionally, Sara et al. (2005) showed evidence for an additional 'reluctantly releasable' pool from which spontaneously released vesicles recycle after regeneration through endocytosis.

2.9.2 Kiss-and-run exocytosis in CNS nerve terminals

Here, exocytosis of synaptic vesicles does not cause the vesicle to fully integrate with the plasma membrane, but rather merge just enough to allow the neurotransmitter to diffuse out of the cell through a pore in the plasma membrane. Then the vesicle separates from the plasma membrane mostly intact and is ready to be refilled with neurotransmitter quickly.

While the evidence for this mechanism in neuroendocrine secretory cells such as chomaffin cells (Zhou et al., 1996) was compelling, less evidence was available for the mechanism occurring in small CNS nerve terminals. For example, studies claiming to prove its existence, including Gandhi and Stevens (2003); Harata et al. (2006); Klingauf et al. (1998), were contested in subsequent papers (Balaji and Ryan, 2007; Granseth et al., 2006). Granseth *et al.* in particular provided compelling evidence in favour of CME being the only retrieval mechanism at the tested experimental conditions: inhibiting CME stopped all vesicle recovery. Recently published papers however provide more evidence for Kiss-and-run existence in CNS nerve terminals (Alabi and Tsien, 2013).

Given the lack of consensus on this aspect of vesicle recycling the computational modelling in this work excludes the effects of Kiss-and-run.

2.9.3 Ultrafast endocytosis in CNS nerve terminals

Recently, another form of endocytosis active at small CNS neurons has been proposed (Watanabe et al., 2013a,b), making use of new optogenetic techniques coupled with high speed capture of events by flash-and-freeze electron microscopy imaging (Watanabe et al., 2014). This endocytosis takes on the order of 100ms to recover plasma membrane, hence the term ultrafast.

The characterisation of the mechanism is still under debate. It has currently been reported as detectable at low stimulus intensities and physiological temperatures, and so has not appeared in the existing corpus of research which fall outside these environmental parameters.

Further research will uncover the place it has in the overall synaptic vesicle recycling process.

As ultrafast endocytosis is still under active debate, and as none of the available image data provides kinetic characterisation of its behaviour, it has been excluded from the modelling work.

2.10 Conclusions

The synaptic vesicle cycle is complex and not yet fully understood. Research groups are actively discovering the underlying mechanisms using the tools and methods described here. The experimental methods described above allow the creation of imaging (and other) data. The steps required to process this imaging data are the subject of Chapter 3.

Chapter 3

Image analysis of fluorescence microscopy experiments

The object of imaging and analysing fluorescence microscopy time-series data is to record the changes in fluorescence intensity of individual synapses within the image field, and from there infer behaviour of the synapses during the course of an experiment as depicted in Figure 3.1. This chapter discusses the steps required to obtain this synapse behavioural data from time-series images with the highest accuracy and least bias.

The types of information that can be extracted from time-series fluorescence microscopy images vary by experiment protocol, but the basic properties of the image data and the common processing steps are discussed in this chapter.

A commonly used analysis technique with time-series fluorescence microscopy assays investigating synaptic vesicle recycling is the segmentation of synapses within the image data. Regions of interest (ROIs) are centred on synapses in time-series images. The purpose is to ideally record the total fluorescence of each synapse across the whole time-series while attenuating the signal as little as possible by including the least amount of non-synaptic fluorescence.

3.1 Properties of fluorescence microscopy time-series image data

A fluorescence microscopy time-series image for both FM dye and pHluorin experiments shows a population of neurons. This image usually contains a mix of healthy neurons, sick or dead neurons, other cell types and perhaps cellular debris.

Fluorescence microscopy data is commonly imaged at resolutions in the region of 4.5μm × 4.5μm per pixel and an effective objective magnification of 20x to 40x, with a emission wavelength in the region of 500-600nm depending on the fluorescent marker used. At these resolutions a central nervous system synaptic terminal can be about five pixels in diameter. This means that structures within synaptic terminals such as vesicles and endosomes cannot be individually imaged, but rather the fluorescence signal is a population measure of all activity within the synapse. A typical image field from fluorescence microscopy data has many neurites each containing many synapses. Many of these are out of focus. However a subset are suitable for image analysis.

The imaging of synaptic terminal behaviour is complicated in most assays by a number of

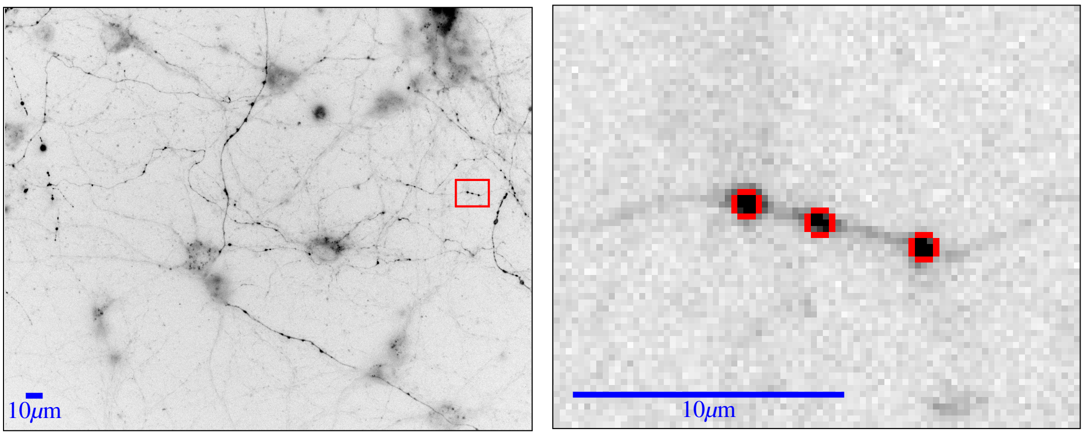

(a) Full image. (b) Zoomed area.

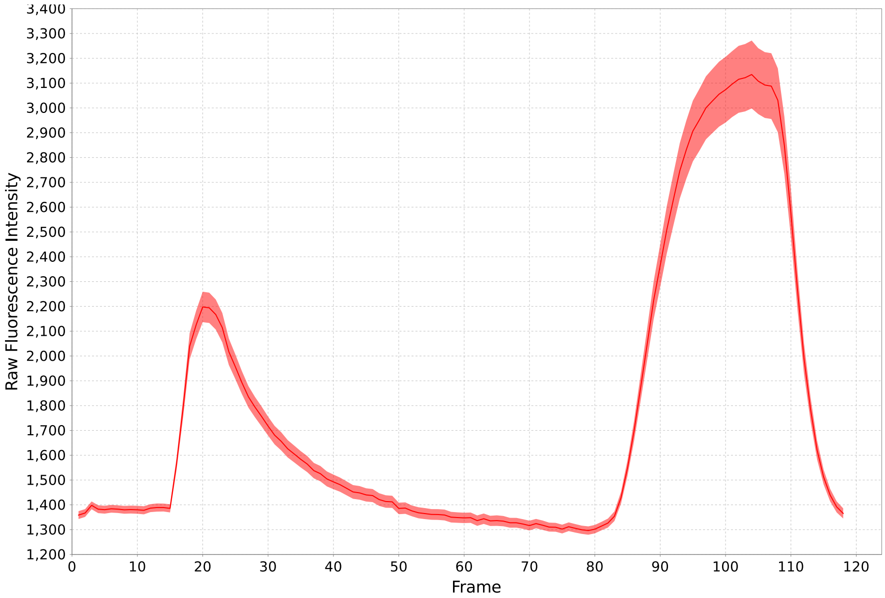

(c) Mean fluorescence intensities of all ROIs (with SEM).

Figure 3.1: Overview of the image analysis process. (b) shows the highlighted region of (a). Regions of Interest (ROI) shown as red circles in (b) are selected from time-series fluorescence microscopy images to produce intensity profiles (c). The intensity profile shown is the mean fluorescence intensity (with SEM) over all ROIs in a single assay (usually in the region of 50-100 ROIs), in arbitrary fluorescence units. Original data collected by Katherine Bonnycastle.

factors:

- Background fluorescence, coming from a number of extra-synaptic sources. Sick, dying or dead neurons tend to have fluorescence properties which obscure the fluorescence signals of nearby healthy neurons.
- Marker proteins or molecules being trafficked in or out of synapse within the cytoplasm.
- Exocytosed marker protein moving laterally along plasma membrane.
- Optical issues such as synapse moving in or out of focus, i.e. movement in the z-axis

with respect to the imaging plane.
- Movement of entire image plane along x- or y-axes.
- Movement of individual synapses along x- or y-axes relative to the rest of the neuron.
- Multiple closely packed synapses being difficult to differentiate.
- Variability in how localised the fluorescent marker is to synaptic nerve terminals, i.e. how punctate the fluorescent signal is.

It is a challenge to consistently measure the fluorescence of a single synaptic terminal over the course of an experiment.

There are multiple applications for synapse detection, depending on experiment requirements:

- Accurate counts of differentiated synapses, either within the field of view, or as a measure of synapse density along a neurite length.
- Measures of punctateness or localisation of fluorescent markers.
- Measures of change in fluorescence in defined areas of the image over time.

It is also possible to image at different fluorescence wavelengths within a single assay. Fluorescence markers can differ in their emission wavelengths. Co-localisation and other interactions between the markers can be analysed by imaging multiple markers within the same assay. These different wavelengths are recorded in different channels within time-series images.

3.2 Image data formats

Time-series image data files exist in a variety of file formats, either proprietary formats specified by the microscope vendor (such as ZVI, CZI, CXD), or general purpose image file formats (usually TIFF). The image data usually consists of 16-bit grayscale images (or occasionally 8-bit grayscale). Time-series images are multi-frame, and may be multi-channel where images taken at different fluorescence wavelengths are interleaved.

The image files may also contain metadata including timing information of the individual frames and information about the microscopy hardware and its settings at the time of imaging. Image processing and conversion may lose some of this metadata, and this issue is addressed in Chapter 5.

A typical time-series image may consist of 50-100 frames, each of usually 1.5-6 Megapixel resolutions, giving file sizes commonly in the range 100-500 Mb per assay.

3.3 Image processing stages

The first processing steps modify the time-series image data to obtain fluorescence intensity values over time for synapses present in the image field.

These processing stages are performed using image processing software; either proprietary tools supplied by microscope vendors, or general purpose image processing applications. This work uses ImageJ/FIJI (Schindelin et al., 2012; Schneider et al., 2012) for the bulk of the image processing as it is in common use both within the Cousin laboratory, and the wider neuroscience community. ImageJ is the core imaging platform, and FIJI is a distribution of ImageJ with a set of scientifically useful plugins. In the rest of this work, the term ImageJ refers to ImageJ and/or FIJI.

3.3.1 Registration

Registration corrects movement of the image field in the *xy*-plane between frames of the time-series. It is a necessary step if there has been movement of the image field and synapses are to be identified reliably across the entire time-series. The individual image frames are transformed to align with each other on the *xy*-plane. This is limited to lateral translation and rotation transformations on individual frames of the image series. Stretch, scale and shear image transformations are not valid in this context as they deform the synapse intensity signals. The commonly used tool for this stage is the StackReg/TurboReg plugin for ImageJ (Thevenaz et al., 1998). This plugin attempts to minimise the difference in pixel-wise fluorescence levels between frames of the time-series images. Local enhancements added during the course of this work have also allowed for comparison of all frames of the image against a single reference frame selected by the researcher from the time-series, in addition to the standard method of aligning each frame against the preceding one. Figure 3.2 shows the effects of applying registration to time-series image data. In practice, image frame drift rarely exceeds 20 pixels over the course of the time-series.

Registration can track the movements of a single rigid body in the image frame. However it does not cope with individual neurites moving or changing shape independently of each other. Registration in this situation cannot track the individual neurite movements and instead just provides a best-effort transformation to minimise the changes of the whole image.

An assessment of movement of individual synapses within a registered image is the subject of Chapter 6. In practice, a researcher would avoid selecting synapses with excessive movement during the segmentation stage described below, as this would introduce error in the measurement of fluorescence intensity over the time-series. Depending on the analysis techniques used, a few pixels movement of a synapse during the course of a time-series assay could be enough to cause intensity measurement error.

3.3.2 Background subtraction

As described earlier, there are many non-synapse sources of fluorescence in the image field. This can include cell nuclei, membrane from dead or unhealthy neurons, or debris in the image field. Some markers are not exclusively localised within synapses. Differentiating the signal produced by synapses from the other sources of fluorescence is a common requirement.

Image features larger than synapses are removed from the image by background subtrac-

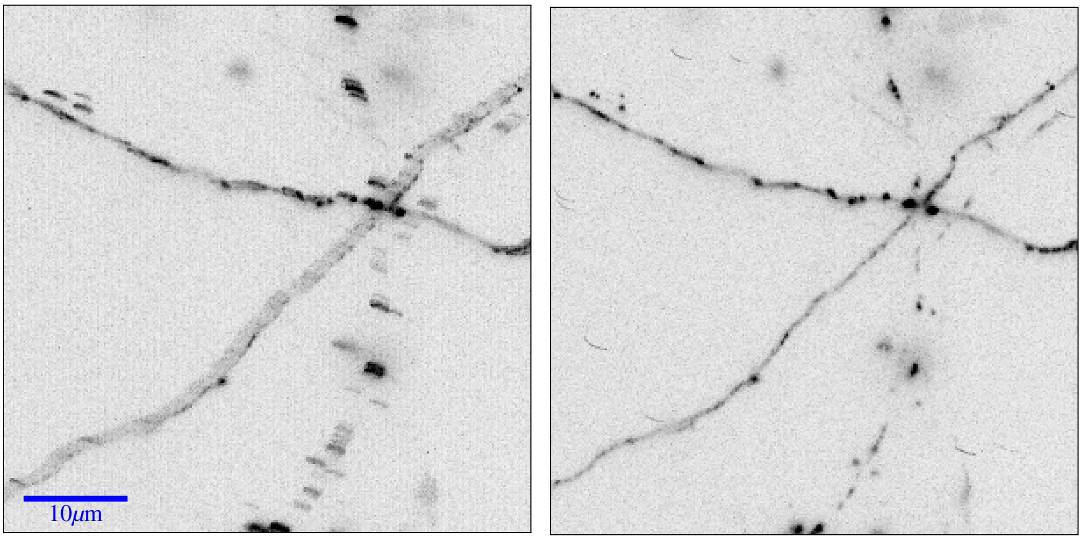

(a) Original time-series image.

(b) Registered image.

Figure 3.2: Example registration of a time-series image. Images are maximum intensity z-projections of a time-series image. Image (a) shows the drift in the xy-plane of the original data. Image (b) shows improved clarity of neurites and synapses after applying registration to the time-series. Original data collected by Darryl Low.

tion. Ideally the larger background components are subtracted from the image, leaving only synapses and other smaller features. In reality, this operation is rarely fully effective and has side effects which must be taken into account.

Background subtraction has two purposes; to aid identification (segmentation) of synapses in the image by removing larger obscuring features, and to isolate the fluorescence signal coming from the synapse as opposed to fluorescence coming from other features in the same region as the synapse. Common automated segmentation algorithms perform background subtraction prior to segmentation.

Background subtraction is a more delicate process when used prior to intensity trace generation. For pixels forming part of a synapse, some of the signal comes from the background, and some from the synapse itself. Partitioning the signal between background and foreground is difficult to do with accuracy. Most of the common subtraction operations subtract part of the synapse signal, which must be considered in later processing.

The background subtraction algorithm in common use in ImageJ is the rolling ball algorithm (Sternberg, 1983). There are alternatives available, described in Chapter 7.

3.3.2.1 Rolling ball algorithm

The rolling ball algorithm removes larger features from an image. Conceptually, the algorithm works as follows. A source image is treated as a 3D surface, with the height of each xy-coordinate being the intensity of the image pixel at that coordinate. A ball of a predefined radius is then rolled over the underside of this surface. At each pixel the intensity level at which the ball can “fit” is subtracted from the source image, producing the target image. The ball can fit into features which are sufficiently large compared to the ball radius, so these larger features are removed from the image. The ball does not fit into features smaller than the ball, so these features are retained, with a small amount of intensity loss. The effect is illustrated in 2D in Figure 3.3 by applying a rolling circle to a single row of pixels. Figure 3.4 demonstrates the effect of applying the algorithm to a sample microscopy image frame.

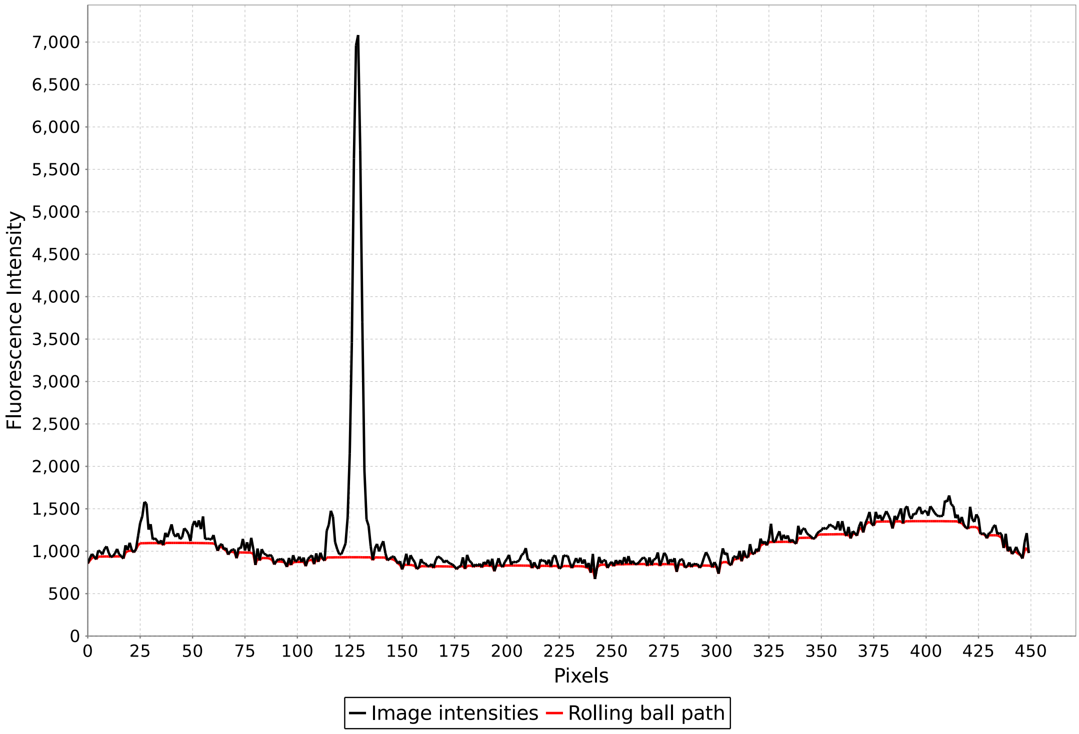

Figure 3.3: Illustration of the 2D equivalent of the rolling ball algorithm. The black line shows the intensity profile of a single row of pixels. A circle of radius 20 pixels is rolled along the underside of this profile, following the path shown as the red line. The remaining area between the black and red lines is the target intensity profile after background subtraction.

The sensitivity of the algorithm to selecting features and how much intensity of those features is lost depends on the chosen ball radius. Smaller radii are better for removing more background features, but remove more of the pixel intensity which could be attributable to the remaining features of interest. Optimal radii therefore depend on whether the background subtraction is being performed for image segmentation or ROI intensity measurement. Ball radii between 10 and 50 pixels are commonly used with the microscopy data used in time-series fluorescence microscopy experiments (Morton et al., 2015). In Chapter 6 a radius of 10 pixels was used for ROI drift analysis, while in Chapter 7 a radius of 20 pixels was used for automated ROI segmentation. A smaller radius in the ROI drift analysis study allowed better tracking of

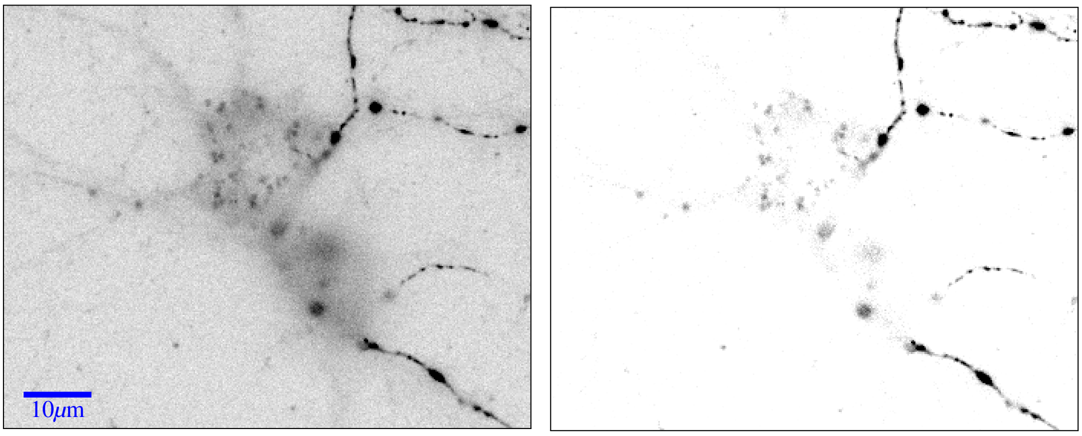

(a) Original frame from time-series image.

(b) Result background subtracted frame.

Figure 3.4: Example background subtraction of a time-series image frame. Image (a) shows an image frame with features of varying sizes visible. Image (b) shows the result of applying the rolling ball algorithm with a ball radius of 20 pixels. The larger features have been removed from the image, leaving the smaller features of interest Original data collected by Katherine Bonnycastle.

the brightest ROI centres, whereas the larger radius used during automated segmentation provided a more detailed overall ROI feature with which to determine feature size and circularity. The studies were independent, and the use of the rolling ball algorithm was to determine the effect of presence or absence of background subtraction.

3.3.3 Segmentation

Segmentation is the term for selecting regions of interest (ROI) from the image. Generally, ROIs are manually segmented on a single frame of the time-series. If the synapse remains within the boundaries of this ROI in all frames of the times series, then the sum of the pixel intensities of all pixels within the ROI for each frame of the time-series is a measure of how the synapse changes in fluorescence intensity over time. For this reason, it is desirable to select as few non-synapse pixels as possible during synapse segmentation to avoid attenuating the activity signal of the synapse.

The common method of performing manual ROI segmentation is to pick an image frame of the time-series corresponding to a time in the experimental protocol when the synaptic terminals are expected to be at their most visible. For FM styryl dye imaging, this is usually when the terminals are fully loaded with dye, generally at the start of the experiment. For pHluorin imaging, this would be when the synapses have been electrically or chemically stimulated to fluoresce.

The researcher manually selects ROIs within the image. The criteria for selection depend on the experiment, but usually ROIs are circles of a fixed diameter (5, 8 or 10 pixels for example), on neurites which are in focus and appear healthy. Tools such as the Time Series Analyser plugin (`https://imagej.nih.gov/ij/plugins/time-series.html`) can assist with the generation and naming of ROIs within ImageJ, but it is still a manual task to place the ROIs over potential synapses (Figure 3.5).

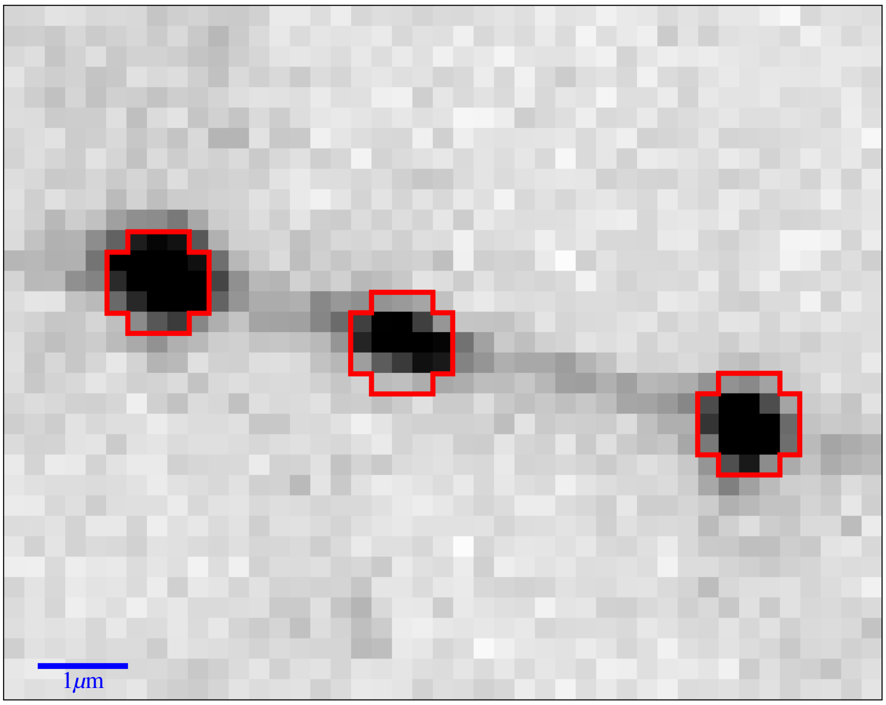

Figure 3.5: Example 5x5 circular ROIs placed over potential synapses. All pixels within the solid red boundary line are part of the ROIs. Image data collected by Katherine Bonnycastle.

The number of ROIs selected per image is dependent on the individual assay, but usually $>$100 ROIs are selected prior to intensity trace filtering (discussed in Section 3.4.1). Factors affecting selected ROI count can include fluorescence brightness of synapses during stimulation, neurite density in the image field, and amount of background noise in the image field.

3.3.4 Intensity trace creation

Given a set of ROIs and a registered time-series image, total raw fluorescence intensity is measured for each ROI for each frame of the time-series. This is simply the sum of the brightness level of each pixel within the ROI in a single frame. These ROI intensities are recorded as either the total or the arithmetic mean of the intensities of pixels within the ROI. In practice, if ROIs of fixed size and shape are used consistently throughout an experiment, these two values are equivalent during later processing.

This data is usually exported in CSV format for processing by other applications.

3.3.5 Other image processing operations

There are many image processing operations available to the researcher to assist in cleaning the raw image data, and segmenting ROIs from the image field. ImageJ for example comes with a multitude of built-in and plugin provided filtering, processing and analysis functions. This section describes three operations which are used in later chapters of this work.

3.3.5.1 Z-projection

It is possible to combine frames from a time-series into a single image. This projection along the z-axis of the image data can take a number of forms. The two most commonly used are maximum and average intensity. As the names suggest, each pixel at location (x,y) in the result image is either the maximum or the average of the pixels at location (x,y) in each of the frames being projected. The operation can be applied to the entire time-series or any subset of the frames. Average intensity z-projection of a subset of frames can be used to remove transient pixel noise from images. Figure 3.2 demonstrates maximum intensity z-projection of a time-series image.

The most common use of z-projection is during automated segmentation, with the assumption that the feature being segmented does not move significantly in the xy-plane for the frames being projected. Image registration may be required first to assist this.

3.3.5.2 Thresholding

Thresholding in the context of this work is the creation of a binary image from a grayscale image. All pixels with intensities within a user defined threshold intensity levels become 1, and all other pixels become 0. This operation and the resulting created binary image is commonly used in automated segmentation in combination with particle detection, described below. However, it can be used in manual segmentation to assist in highlighting ROIs.

While it is possible to set minimum and maximum threshold levels to select pixels with intensities falling between these limits, it is more common to use just a minimum threshold level.

3.3.5.3 Particle Detection

Particle detection takes as input a binary image as produced by thresholding, and identifies the individual regions of 8-connected pixels of value 1 (i.e. two pixels of value 1 are connected if one is any of the 8 pixels immediately surrounding the other). These regions may then be filtered to return only the particles which fit size or shape constraints. The built-in Analyse Particles function in ImageJ allows filtering by minimum and maximum pixel area, and by an estimate of the circularity of the particle, calculated as

$$\text{circularity} = \frac{4\pi \times \text{area}}{\text{perimeter}^2}$$

where the area and perimeter of the particle are measured in pixels. Figure 3.6 demonstrates the calculation on an example particle.

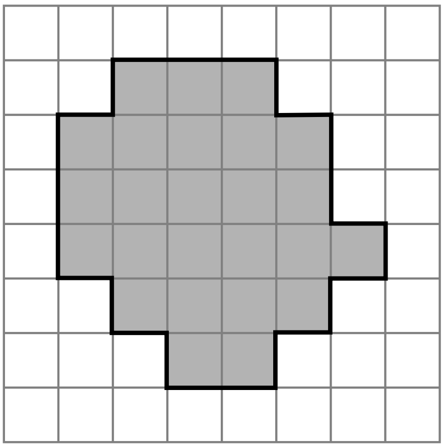

Figure 3.6: Example particle circularity measurement. The area of the particle shown as shaded region is 25 pixels, while the perimeter of the particle shown by the solid black line is 24 pixels, giving a circularity of $(4\pi \times 25)/(24^2) = 0.55$.

All synaptic terminals will not appear perfectly circular in the image field, but a minimum level of circularity will filter out some non-punctate image noise features.

3.4 Intensity trace processing stages

At this point, the time-series image data has been used to produce a set of ROI intensity traces for the time-series, which are now filtered and processed.

3.4.1 Trace filtering

Some of the ROIs selected in the single static image may not be healthy, actively-behaving synapses. The ROIs could be centred on unhealthy synapses or image artefacts, or the synapses may not stay in focus or within the ROI for the full time-series. This is a difficult determination to make in most circumstances. Each ROI intensity trace is subject to significant noise, and may respond only partly to stimulus. Filtering, or screening, the ROI set is a manual operation requiring considerable skill on the part of the researcher. Avoiding bias while still retaining a ROI set of acceptable quality and number is a difficult task. Depending on the protocol, the features sought in acceptable ROI intensity traces for pHluorin experiments can include:

- Flat baseline traces prior to stimulus.
- Marked increase in fluorescence level upon stimulus.
- Slow return to original fluorescence post stimulus.
- Rise to maximum fluorescence during NH_4^+ addition.
- Sustained maximum fluorescence during NH_4^+ addition.
- Return to baseline levels during recovery phase.

- Exponential return curve during recovery phase.
- No extreme changes in fluorescence at unexpected times, usually indicative of the synapse moving out of the ROI or fluorescent material moving across the ROI in the image field of view.

In practice, ROI intensity traces are usually individually screened to avoid unnecessary bias or inadvertent grouping of traces by the researcher, a feature supported by the ROI trace selection tool described in Section 5.2.1. The end result of the filtering process is a set of usually 50-100 ROIs.

3.4.2 Photo-bleaching correction

The fluorescence signal decays during the course of an experiment. This reduction in fluorescence confounds the activity-dependent fluorescence signal and must be removed by applying a correction to the intensity traces (Figure 3.7). Depending on the experiment protocol, this can take the form of a linear or exponential correction, calibrated either at the start of the imaging or after long gaps in the protocol.

The best form of decay correction for a given experimental protocol is generally chosen by running calibration assays, where the cultures are imaged as in the experiment protocol but are not stimulated, thus giving a measure of steady state behaviour. Royle et al. (2008) provides a more detailed description of correcting photo-bleaching effects in pHluorin data.

3.4.3 $\Delta F/F0$ normalisation

Synaptic terminals vary in size and levels of fluorescent marker. Fluorescence ROI traces may have a large intensity range within a single image. Simple minimum/maximum normalisation may not be suitable for some experiments. In these cases a better normalisation is fluorescence fold change from baseline levels, written as $\Delta F/F0$. $F0$ is an average fluorescence value over a defined set of baseline frames (usually near the start of the assay or start of stage of long running protocol) for each ROI individually.

$$\frac{\Delta F_t}{F0} = \frac{F_t}{F0} - 1$$

$$F0 = \frac{\sum_{i=n}^{m} F_i}{m-n+1}$$

where F_t is the fluorescence intensity of the current ROI at frame t, and n, m are the start and end frames of the baseline frame range. $m-n+1$ is the number of baseline frames used. By convention, 1 is subtracted from the fold change to set the baseline intensity to 0 in plots.

3.4.4 ROI and assay replicate aggregation

Once a photo-bleaching corrected, filtered ROI set and traces have been obtained from an assay time-series image, they are aggregated into a mean trace. Variance within an assay is usually

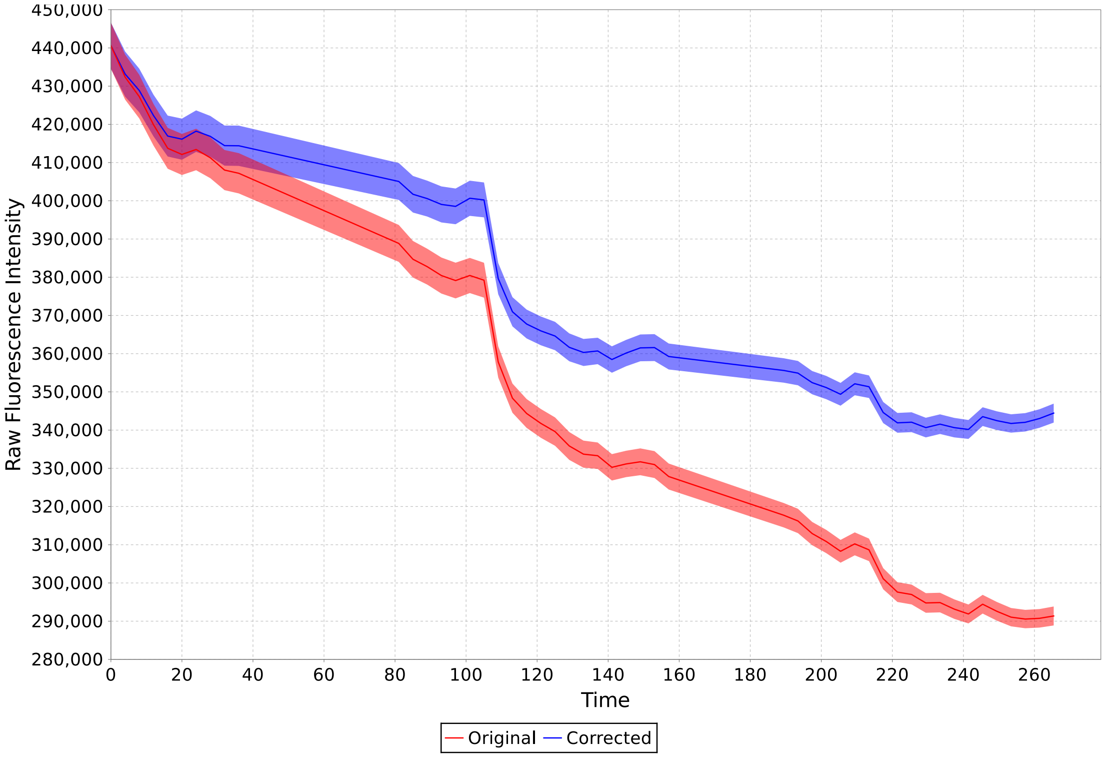

Figure 3.7: Example photo-bleaching correction of an FM dye assay intensity trace with 102 ROIs. Red trace is the original uncorrected raw mean fluorescence intensity (with standard error) in arbitrary fluorescence units, blue trace shows a linear correction of the data at a rate of 200 fluorescence units per frame. Original data collected by Giselle Cheung (Cheung et al., 2010).

discarded, and the mean ROI trace for all ROIs in an assay (usually in the range 50-100 ROIs per assay) is a single data point of the experiment. The traces are usually taken to be uni-modal in their behaviour. However some analyses differentiate behaviour of subsets of ROIs within an assay. Recent work by researchers in the Cousin laboratory have demonstrated bi-modality of the fluorescent marker protein VAMP4-pHluorin under stimulus (Nicholson-Fish et al., 2015, 2016). Handling this bi-modality required additional processing.

There are multiple replicate assays per test condition. These assays are then aggregated to provide a mean and variance for the experiment condition. In this field of research, variance is usually recorded as standard error (SEM) as the statistic of interest is the effect on the population means of experiment conditions.

3.5 Manual processing considerations

Much of the processing described above is performed manually, operating ImageJ and other software per assay. This poses the following problems:

- The work is time consuming - in particular the ROI segmentation and intensity trace filtering require significant researcher input.

- There is a risk of introducing observer bias when selecting or filtering the ROIs, which requires considerable skill on the part of the researcher to avoid.
- Not all parameters of the analysis process may be recorded when doing the analysis, making repeatability of analysis difficult.
- There is the potential for occasional errors in preparing the images for analysis, or creating filtered ROI sets from the image data. These can potentially slip through verification. While the effects of errors in individual ROIs or even assays is not large, it would be better to avoid them if possible.

3.6 Analysis of aggregate intensity traces

The previous stages should provide mean traces for each condition within an experiment with sufficient replicates to give the required confidence in the result. Further analysis can now be performed on this data, including analysis of the shape or time constants of the test condition traces, comparison between test conditions, or comparison of different points within a test condition. The following are analyses common in the literature for pH sensitive fluorescent marker proteins. They are described here as this work makes use of the original image data produced by such experiments, and originally subject to these analyses. Other analysis options are possible, making use of combinations of experiment events to gather further information about synaptic recycling behaviour.

A description of the operation of basic statistical operations such as t-test, ANOVA, post-tests, and their use in effect and significance testing is beyond the scope of this chapter. Works such as Field et al. (2012) provide a good grounding in their derivation and use. Rather, this section describes which features of fluorescence intensity traces are subject to such analysis to highlight the potential use of time-series image data.

3.6.1 Normalisation to peak activity

If multiple test conditions are normalised to their stimulus peaks and compared, then differences become apparent in the rates of fluorescence increase and return to baseline. These can be taken as representative proxies of exocytosis, endocytosis and reacidification activity, depending on the experiment conditions and under given assumptions. Exponential time constants (τ) can be calculated for the recovery to baseline by fitting curves using non-linear regression (Figure 3.8).

Normalisation to stimulus peak can give τ values of exponential decay curves (time to baseline). t-tests or ANOVAs per frame can show time periods within the recovery phase where conditions differ significantly (Figure 3.9).

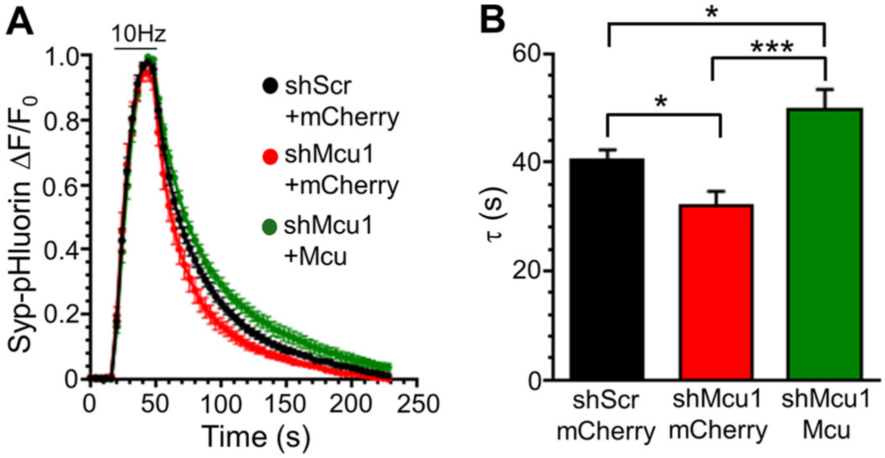

Figure 3.8: Example τ calculation (B) from exponential curves fitted to fluorescence decay traces (A). The results show the effect of overexpression of the protein mitochondrial calcium uniporter (MCU) on endocytosis, as measured by the drop in fluorescence of Syp-pHluorin (SypHy) after 10Hz stimulation. The three test conditions have different expression levels of MCU in the stimulated nerve terminals, and different exponential recovery rates. From Marland et al. (2016), Figure 4.

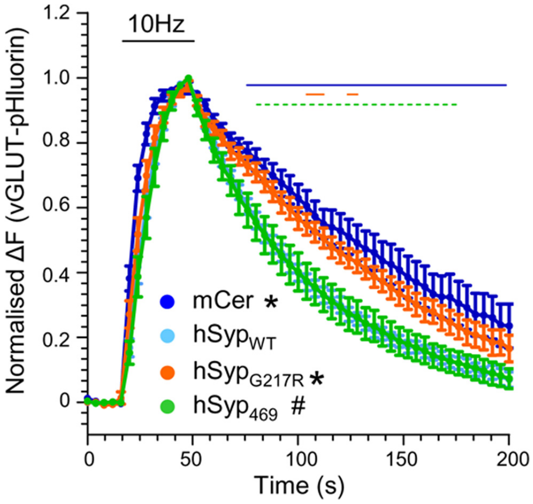

Figure 3.9: Selection of time ranges where conditions differ significantly in value. The coloured over-lines show time ranges when the conditions tested had significantly different normalised fluorescence intensities as calculated by two-way ANOVA. This figure shows the change in fluorescence of vGLUT-pHluorin of stimulated synaptophysin knockout cortical neurons transfected with either mCerulean or mCerulean-hSyp (human synaptophysin) mutants. From Gordon and Cousin (2013), Figure 4.

3.6.2 Normalisation to ammonium peak

Addition of NH_4^+ to a culture causes pHluorin-type pH reporting fluorescent markers to fluoresce, both on the plasma membrane (already fluorescent in normal extracellular media) and within the internal compartments of a neuron. The peak fluorescence recorded is taken to be the total amount of marker protein existing within the ROI. Stimulus peaks earlier in the intensity trace are taken to show the ratio of total amount of marker protein exocytosed in response to stimulus:

$$\text{marker proportion exocytosed during stimulus} = \frac{\text{stimulus peak height}}{\text{NH}_4^+ \text{ peak height}}$$

Normalisation to NH_4^+ gives varying stimulus peak heights. ANOVA or t-tests along with appropriate post-tests can be used to determine the significance of differences in peak height.

3.6.3 Normalisation to acid pulses

Acid pulse protocols are used to determine surface fraction ratios of fluorescent markers. The surface fraction is shown by the drop below baseline of the intensity trace as the normally fluorescent marker protein present on the plasma membrane is quenched by impermeant weak acid (pH 5.5) for 30-60s. By combining this with addition of NH_4^+ later in the experiment, the surface fraction can be converted into a ratio of all marker protein present in the ROI.

Additionally, as acid pulses quench only the surface fraction, remaining fluorescence is taken to be produced by internal marker protein only. Timed acid pulses can then show the reacidification of internal compartments as the internal marker protein is gradually quenched by internal reacidification processes. This technique was recently used to establish the reacidification time constant of ADBE derived endosomes (Nicholson-Fish et al., 2015).

Earlier studies using cytosolic pH-sensitive dyes had established that brief acid pulses had minimal effect on cytosolic pH (Sankaranarayanan et al., 2000).

3.6.4 Normalisation to S1/S2 ratios

An issue with comparing different assays to determine effects is that each assay has a different population of neurons, each with synapses containing different levels of fluorescent marker. This necessitates segmenting many ROIs per assay, and many assay replicates per test condition to achieve confidence in the mean result.

S1/S2 protocols test multiple conditions on the same synapses. If the entire experiment is run within a reasonable time-frame, then differences in behaviour within synapses in an assay can be taken to be primarily due to the test conditions. The output intensities from these assays can then be directly compared (Figure 3.10 for example).

FM dyes have different possible analyses. Their common use is measuring fluorescence drops in response to stimulus events as a fraction of the total fluorescence drop during the experiment.

3.6.5 Differing fluorescence drop behaviour of different FM dyes

Clayton and Cousin (2008) showed that at carefully chosen concentrations, different FM dyes

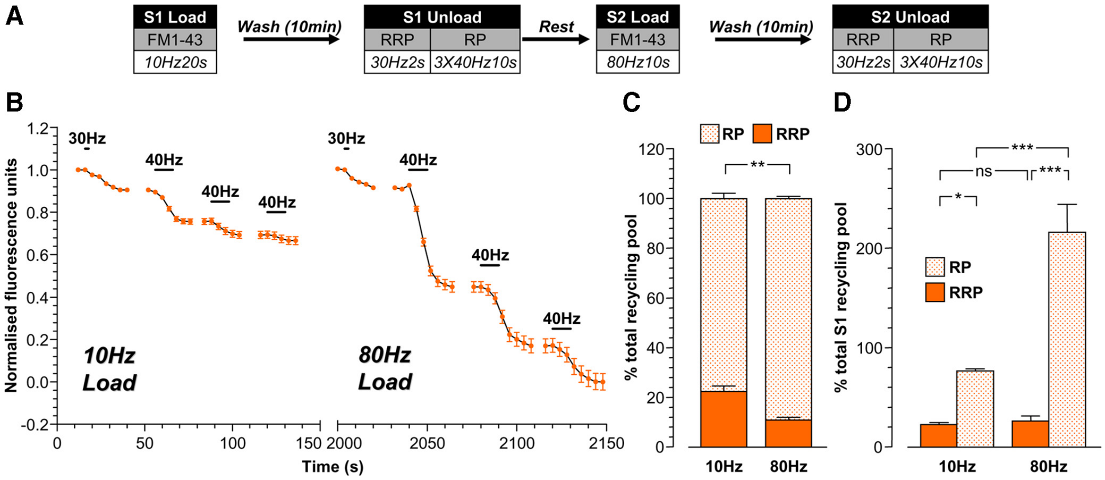

Figure 3.10: Example S1/S2 protocol. Here the FM dye loading stimulation intensity was changed between S1 (10Hz) and S2 (80Hz), and differences recorded in the relative unloading kinetics with both S1 and S2 using the same unloading protocol. Plot (d) is calculated as a ratio of the total recycling pool size from S1. From Cheung et al. (2010), Figure 5.

(FM1-43 and FM2-10) were loaded in different proportions by CME and ADBE. This technique was used to differentially label vesicles generated by the two mechanisms and was used in further study of endocytosis behaviour in Cheung et al. (2010) (Figure 3.11).

3.6.6 Fluorescence drop ratio in response to varying stimuli

By varying the intensity and length of successive stimuli, sequential marker unloading has been used to illustrate the relative sizes for the different vesicle pools within synapses in Cheung et al. (2010) (Figure 3.11).

3.6.7 Fluorescence drop ratios after long delays

Cheung et al. (2010) also used unloading events after a long delay to isolate the unloading of ADBE derived vesicles, and using these results to determine the preferential localisation of ADBE derived vesicles to the reserve pool.

3.7 Analysis of other image data

In addition to the analysis described above, the time-series image data can be used to determine other synaptic properties.

3.7.1 CV analysis of marker localisation to synapses

Some experiments require a measure of how well localised a marker is to synapses, i.e. is the fluorescent signal punctate and mainly within synapses, or more diffuse along the axon being imaged. A standard protocol for estimating this is to calculate the coefficient of variation (CV) of fluorescence intensity of an axonal segment with synaptic terminals (Lyles et al., 2006). The fluorescence intensity of such a segment is recorded on an individual frame of the time-series,

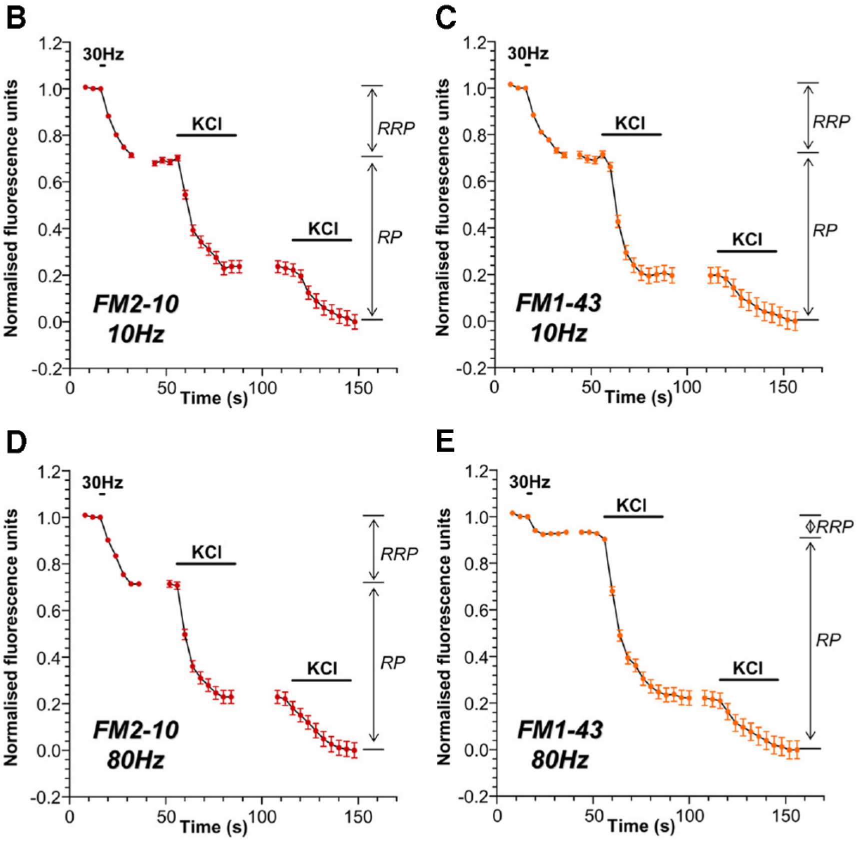

Figure 3.11: Different intensity stimuli used to determine difference in marker content of vesicle pools (from (Cheung et al., 2010, Figure 2)). The unloading differences between (B,C) and (C,E) show the different loading affinities for FM1-43 and FM2-10.

and the CV of individual frames of the time-series is the standard deviation (σ) of the pixel intensities divided by their mean (μ):

$$\mathrm{CV} = \frac{\sigma(\text{pixel intensities along neurite})}{\mu(\text{pixel intensities along neurite})}$$

Lower values indicate dispersion of the marker along the neurite, while higher values indicate punctateness and localisation of the marker to small areas. This localisation may change over the course of a time-series, demonstrating marker diffusion or re-localisation.

This method has been used in the Cousin laboratory to determine localisation of Synaptobrevin II to nerve terminals under different conditions (Gordon and Cousin, 2013; Gordon et al., 2011).

3.8 Conclusions

Time-series fluorescence microscopy is a valuable tool in synaptic vesicle recycling research. However as this chapter has described, the image analysis is complex and requires substantial effort and care on the part of the researcher. Chapters 6 and 7 describe the image analysis research based on the methods described here.

Chapter 4

Computational modelling background

As Chapter 2 highlighted, the biological domain of this work is complex. There are many levels of detail which may be taken into account, and many competing theories and observations to explain the mechanisms of synaptic vesicle recycling. Computational modelling techniques can help structure this complexity, allowing deeper inferences to be made from the available data. This chapter gives an overview of available computational tools and techniques relevant to developing this structured view of the biological domain.

An overview of how to create a good computational model is given in Djurfeldt and Lansner (2007). This report discusses large scale modelling of the nervous system, but the modelling principles discussed are transferable to many other computational modelling domains.

Sections 4.1 and 4.2 discuss modelling principles in abstract, while Sections 4.3-4.6 discuss concrete realisations of these principles and their relation to synaptic vesicle recycling research.

4.1 Computational modelling principles

Computational modelling encompasses a wide variety of techniques, each suited to particular problems. This section is an overview of the distinctive features of the modelling techniques relevant to this project.

4.1.1 Intent of modelling - empirical or mechanistic

Given a domain to be modelled, there are a number of directions the model could take. The first choice is whether the model should just match experimental observations given experimental input parameters. Here, the model does not need to describe how the domain to be modelled works, and is just a black box which gives an appropriate output given a particular input. For many problems this empirical model could be good enough to solve the modelling problem.

In the context of this project however, such a model would be inadequate. To clarify the processes by which ADBE and CME work, a better choice are mechanistic models. These approximate the observed behaviour of the modelled system by internally executing the steps known to occur in the domain being modelled. Here the focus is on the internal mechanism of the system. Given an adequate internal structure and correct parameters for the model, the phenotype of the experimental system is approximated in the final outputs of the model. This may be seen as straightforward cause and effect given the internal workings of the system, or the observed output of the model may appear as emergent behaviour (as sometimes seen when modelling large systems of mostly independent entities).

4.1.2 Level of modelling detail

Another choice in modelling is to determine at what level the experimental system should be modelled. It can range from individual atomic interactions of the material making up the system to a very high level view of a synapse or population of synapses, each one represented by a few representative values (for example total endosome volume or synaptic vesicle count per synaptic terminal).

There are advantages and disadvantages of each level. More detailed modelling down to individual atomic interactions can potentially be more accurate, at the expense of vast computing power required for simulations of reasonable size and duration, whereas higher level models with less detail are more computationally tractable at the expense of detailed behaviour of the model components.

In addition to the computational requirements concern, there is also the question of model realism based on available experimental data. An extremely detailed molecular simulation of synaptic terminal behaviour is hard to verify as accurate if the available experimental observations are only at a very low level of detail.

4.1.3 Level of model abstraction

Given a particular level of modelling detail, there is also the question of level of abstraction of the model. This is slightly different from detail in that it determines the choice of modelling technique depending on level of formalism or abstraction from the system being modelled. At the less abstract end, there are models which attempt to faithfully represent a particular instance of the system being modelled. An example of this would be tracking virtual representations of individual vesicles through their life cycle within the synapse. More abstract modelling techniques remove unnecessary detail (for the purposes of a particular model) to retain only the essential information required for the model to approximate real behaviour. State machines and process calculi are commonly used here.

The loss of model realism is compensated by a usually more tractable model, which tends to be amenable to more complex mathematical analysis techniques. Again, a balance must be struck to achieve the goals of each modelling effort.

4.1.4 Model spatial awareness

Models can have varying levels of representation of space and location. Non spatially aware models have no concept of space or geometry and all species being modelled are implicitly in the same place. Increasing levels of detail of spatial awareness eventually reach full spatial representation, where each element being modelled is aware of its position and movement within the volume being modelled.

4.2 Levels of model detail in problem domain

Given the general modelling principles above, the following are a range of modelling techniques available for the molecular and systems biology fields. They are generally in the order of most detailed and least abstract to least detailed and most abstract, however it is not a simple progression from one end to the other.

4.2.1 Interactions at the atomic or molecular level

Here every molecule in a system is modelled, each with its velocity, orientation and conformation. This type of modelling is implicitly fully spatially aware. A commonly used technique at this level is molecular dynamics simulation. Given the vast numbers of individual molecules required to be modelled for a simple biological system at this level, this type of modelling requires an enormous investment in computing power to simulate very brief time periods. Simulating entire synaptic terminals to the level of seconds or tens of seconds is not feasible.

It is however possible to make use of molecular dynamics tools for certain limited situations, such as modelling the likely static structure of groups of proteins or areas of membrane at single time-points, or modelling a smaller volume for a longer time period.

4.2.2 Approximations of behaviour of individual molecules

Instead of keeping track of every molecule in a system and predicting its behaviour at the atomic level, one can approximate the behaviour of important species such as proteins. For example, using molecular dynamics to predict whether two proteins would interact, the simulation would track their velocities, orientations and conformations. It would then determine if their binding sites are correctly aligned and the proteins make contact at an acceptable relative velocity. An approximation based simulation however would assign a probability of interaction based on the total possible collisions between these two types of proteins. Accuracy is sacrificed for a drastically reduced computational load. This allows large populations of molecules to have simulated interactions within a computational model. The review paper Gillespie (2007) contains a good overview of the balance between performance and accuracy of modelling techniques here.

Within this level there is still the choice of representing space - either individual protein locations can be tracked, or the system to be modelled can be broken up into smaller volumes, each with populations of reacting species. Indeed, space can be ignored altogether, implicitly assuming all species are within interaction range of each other.

4.2.3 Simplification of protein interactions - rule based techniques

One issue with many tools allowing the simulations described above is the difficulty in describing the interactions between species. Proteins can be complex, allowing many simultaneous bindings to different domains within each protein. Rule based modelling is a technique to reduce the combinatorial complexity of model description caused by bindings to different domains. Here individual domains of the proteins can be described, allowing the modeller to ignore the rest of a protein if not considered relevant for a particular interaction.

4.2.4 Modelling membrane behaviour

In the field of fluid or membrane dynamics, the properties of the lipid bilayer of the plasma membrane or vesicle membranes can be modelled. These techniques allow modelling the stresses on the membrane and required forces to make the membrane bend or break, as occurs when vesicles exocytose or endocytose. Such models can also include the structural effects of various transmembrane proteins and the addition of membrane deforming proteins. Section 4.6.2 describes some relevant applications of this technique.

4.2.5 Bond energies and thermodynamics

Related to membrane dynamics is more general modelling of bond energy between model components, to determine the structural stability of complexes and clusters as they form in simulations. Work has already been done in this area with modelling the strength of clathrin bonds during CME (Section 4.6.2).

4.2.6 General vesicle recycling kinetics

At a less detailed level, the kinetics of the entire vesicle recycling system can be modelled. Here, rather than be concerned with the individual protein interactions that cause recycling to occur, the model concentrates on known kinetic rates of overall processes and population counts of vesicles and endosomes within the synaptic terminal. The required kinetic rates to produce such a model are more readily obtained experimentally, and it is computationally less demanding to simulate and analyse such a model. Chapter 8 discusses work so far on this topic.

4.2.7 Spatial aspects

The modelling levels of detail above require varying levels of representation of space. Those dealing with individual instances of proteins within simulated regions of membrane must have adequate geometry built into the model. The techniques dealing with aggregates and populations of components have less need to track each instance of a model component spatially. However, even these may benefit from spatial information. For example rule based modelling of protein interactions can show the effects of Ca^{2+} micro-domains in the coupling of exocytosis and endocytosis by having some means of representing the diffusive flow of calcium. Protein models of CME can show local enrichment of endocytosis proteins near the periactive zones of nerve terminals, affecting the nucleation of vesicles from the plasma membrane. General kinetic models can take into account mobilisation time for a vesicle to come into contact with the plasma membrane and become primed for release.

Many of the techniques listed above have a variety of spatial extensions for this purpose and are discussed further in Sections 4.3.5 and 4.3.6.

4.3 Modelling techniques and tools

Within the framework of the previous sections, there are a range of potentially suitable modelling techniques, and implementations of tools allowing the techniques to be used.

4.3.1 Deterministic mathematical modelling

Deterministic models were one of the most commonly used forms of modelling in the early years of computational systems biology and are still popular in current literature. Model components are related to one another using ordinary differential equations (ODEs). Progression of the system being modelled can then be simulated over time, or in some cases analytically solved for the steady state. ODEs are commonly used for kinetic modelling or chemical reaction modelling. Models can be created using general purpose or ad hoc mathematical programming languages such as Matlab (The MathWorks Inc., Natick, MA) and its many add-on packages, GNU Octave (`http://www.gnu.org/software/octave/`), or may be created in specialised ODE simulators and solvers for systems biology such as Copasi (`http://www.copasi.org`).

ODE based models have the advantages that creation of the system of ODEs is relatively simple (although parameter fitting may not be), and when encoded in a common format, such as Systems Biology Markup Language (SBML, Hucka et al. (2003)), there are a range of simulation, solver and visualisation tools available for such a model.

In addition, there are a large number of existing ODE based models available in various online databases, notably BioModels Database (Li et al., 2010). Such resources assist in development of new models, or new applications of existing models.

The main difficulty with ODE based models is that the biological system being modelled is rarely fully deterministic. When modelling large numbers of species, the noise introduced by random effects averages out, as would occur in chemical simulations with large quantities of reactant molecules (Gillespie et al., 2013). However, in many biological contexts, there are a low number of interacting species. This means that the noise introduced by random events occurring in the system would become significant, and could not be adequately captured by a deterministic model.

4.3.2 Probabilistic mathematical modelling

Different approaches have been developed in an attempt to counter the limitations of ODE modelling of biological systems. One is the use of stochastic differential equations (SDEs). Here, an ODE is extended with a random component, usually represented as a Wiener process, to model the noise of stochastic behaviour of the species involved.

Alternatively, discrete or continuous probability functions allow models to be defined based on various probability distributions (such as exponential, Gaussian or gamma distributions).

Chapter 3 of Wilkinson (2011) provides a good introduction to this area.

4.3.3 Stochastic kinetic modelling

Markov processes are a common tool to model the stochastic kinetics of a biological system. Their distinguishing property is that the system being modelled has no memory, and that the behaviour at any point depends only on the current state of the system. Markov processes can be discrete or continuous time, and can be represented in a variety of forms. There is a large body of work available on Markov processes, and again a good introduction to the field is Chapter 5 of Wilkinson (2011).

While such processes tend to be difficult to solve analytically, there are a range of simple simulation algorithms available, allowing for Markov Chain Monte Carlo (MCMC) solutions to models to be obtained.

A popular simulation algorithm of continuous Markov processes in the field of systems biology is the Gillespie Stochastic Simulation Algorithm, Direct Method (SSA). While originally developed to model chemical interactions (Gillespie, 1977), the algorithm has been widely used in systems biology. There have been many refinements to the original algorithm over the years, as reviewed in Gillespie et al. (2013).

One relevant extension to the SSA has been work to allow for delays in stochastic events. Chemical reactions are seen as instantaneous, whereas biological events may take a finite, non-instantaneous time. One strategy is to let these delays be approximated by having additional states, adjusting entry and exit rates to the introduced states to approximate the event delay. Alternative strategies have been to add delays explicitly into the simulation algorithm, creating delay stochastic simulation algorithms (DSSA) (Barbuti et al., 2009; Barrio et al., 2006; Cai, 2007; Schlicht and Winkler, 2008). These extensions allow events to initiate stochastically, but the event products are not available for use in further events for defined time delays.

The deterministic equivalent, delay differential equations (DDE) is available as a modelling tool. Indeed the process algebra Bio-PEPAd (Caravagna and Hillston, 2010, 2011), can produce output models in DSSA or DDE form.

Spatial extensions to the SSA are more relevant at the protein interaction level, and are described in the Section 4.3.5.

4.3.4 Process algebras

Process algebras are a means of modelling non-deterministic concurrent systems of largely independent agents. In the context of biological systems, the individual communicating processes could represent the individual molecules interacting in a biological pathway. The formal specification of such models is then amenable to analysis and stochastic simulation. There are a number of process algebras currently used in biological research, notably Bio-PEPA (Ciocchetta, 2009) and its derivatives (Ciocchetta and Guerriero, 2009; Ciocchetta and Hillston, 2009). In the case of Bio-PEPA, models may then be converted to ODEs, CTMCs, checked using formal analysis tools such as PRISM (Kwiatkowska et al., 2011), or simulated using a variety of stochastic simulation algorithms.

Ciocchetta and Hillston (2008) gives a comprehensive overview of process algebras and their application to biological contexts.

4.3.5 Protein interaction modelling

A specialisation of stochastic kinetic modelling is to model the behaviour of interacting populations of proteins at a much more detailed level. Similar algorithms are useful here, notably Gillespie's Stochastic Simulation Algorithm (SSA) (Gillespie, 1977). There are a variety of means of describing the model, and in this biological domain, where proteins can have complex interactions, the distinction between reaction and rule based models becomes important.

Reaction based models require all participants in a modelled system to be explicitly enumerated, along with all events or reactions involving each of these participants. As participants include each individual complex of interacting proteins in their many conformations, biological models quickly become intractable as protein complexes and polymers are known to be very large. Reaction based models are better suited to chemical models, with tractable numbers of individual participants and events.

Rule based models on the other hand concentrate on the interactions rather than the complex interacting species. Interactions are described with only enough context to make them biologically valid. Individual protein domains are described in interactions, with other domains of the involved proteins ignored unless the other domains have a modulatory effect on the interaction in question. With such a description, the combinatorial explosion of model rules is avoided.

While many simulation engines for protein interactions assume the modelled volume is homogeneous, a number of tools exist to allow spatial location of the interacting species. Diffusive flow and active transport of species can be simulated, usually at the expense of greater model complexity and much greater computational power needed.

One common method of adding space to models is the next subvolume method as described in Fange et al. (2010).

A more computationally demanding method is explicit tracking of location and movement of each species instance, as is done with the simulation tool STOCHSIM (Le Novère and Shimizu, 2001) for example.

4.3.6 Molecular structure modelling and molecular dynamics

At the extreme end of spatial tracking of species is molecular dynamics. Here the velocities and conformations of individual molecules are tracked at an extremely high time resolution. Thermodynamic interactions between species can then be simulated. Molecular dynamics simulations are extremely computationally intensive, and it is computationally infeasible to simulate a system of the size of a synaptic terminal over the time-scales of synaptic vesicle recycling events.

They have been successfully used however for simulating static packing of large numbers of molecules, for example the packing of transmembrane proteins in lipid membranes, as described in Section 4.6.3, and in the tool BRAHMS (Orsi and W., 2011; Shkurti et al., 2010).

More general structural dynamics models can be created by sacrificing the accuracy of simulating individual molecules. For example, membrane dynamics can simulate the forces holding a plasma membrane together and the effects of stresses on a simulated membrane, demonstrated in Section 4.6.2.

4.4 Model parameter fitting

A detailed model has many parameters, including diffusion rates, binding rates, various kinetic and time constants, and stoichiometries. Some of these parameters are known from experimental work, either exactly or within a distribution of values; others have to be inferred. Parameter fitting is the inference of model parameter values which allow the model to most accurately approximate the observations of the system being modelled.

There are a variety of techniques to perform this parameter fitting. For simple ODE based models, as tend to be found in biological literature, analytical techniques including Runge-Kutta methods allow parameters to be estimated in an iterative process. These are commonly available in mathematical analysis packages such as Matlab (The MathWorks Inc., Natick, MA).

For stochastic models including Markov processes, the process is more complex as such models are less likely to be solvable analytically and must be estimated using Monte Carlo methods.

A good overview of stochastic mathematical and computational modelling techniques are given in Wilkinson (2011), and a comprehensive reference of inference techniques is Bishop et al. (2006).

4.4.1 Cost functions

When fitting a model to experimental observations, a means of gauging how closely observed and simulated data match is required. Cost or fitness functions vary widely between models, depending on which properties of the model are emphasised. For instance, is only the mean value of an observation important, or is the variance of individual data points around this mean also important? Perhaps the mean values are less important than the correlation between the values of different outputs from the model. Commonly used cost functions are described in Bishop et al. (2006).

4.4.2 Parameter fitting techniques

Given a model and cost functions for the outputs of the model against reference data, techniques exist to determine optimum parameters. This is a large research area, particularly in the domain of computational systems biology in recent years.

4.4.2.1 Brute force search

If the number of free parameters is low, and the overall search space of the parameter set is small, it is feasible to simulate all possible choices of parameters (up to a given level of accuracy for each continuous parameter). This approach will give the globally best sets of parameters for the given cost function.

4.4.2.2 Direct search

Given larger parameter search spaces, the brute force approach quickly becomes intractable. For some models, an alternative approach of refining the parameter search space is the Hooke & Jeeves "Direct Search" algorithm (Hooke and Jeeves, 1961). This algorithm explores the parameter space in the vicinity of a starting point. Varying each parameter individually and recording the output of that model gives a contour of costs for the parameters simulated. The best fitting point in the parameter space is then taken as the new starting point and the process repeated. A complete explanation of the algorithm is provided in the original paper.

4.4.2.3 Bayesian inference

A powerful set of model fitting techniques are included here. A substantial body of work exists in the application of Bayesian inference techniques to systems biology MCMC models. In particular the work of Golightly and Wilkinson in recent years have focussed on applying Bayesian techniques to biochemical networks, including a prokaryotic autoregulatory gene network where a protein coded for by a gene represses its own transcription (Golightly and Wilkinson, 2005, 2006a,b, 2008, 2009, 2011; Wilkinson, 2007). These serve as good models from which to handle partially observed data, data with observation error, and further develop methods of Bayesian inference; Particle Marginal Metropolis-Hastings (PMMH) (Andrieu et al., 2010; Golightly and Wilkinson, 2011) has been used in the inference engine described in Chapter 8.

A primer on Bayesian inference is beyond the scope of this chapter. A good starting point are again the books Bishop et al. (2006); Wilkinson (2011).

4.5 Uses of models

Once models have been constructed and parameters fitted to match experimental observations, what can be done with them? This section describes the main uses of constructed models.

4.5.1 Interpolation and extrapolation

A well-fitted model allows the prediction of additional behaviour that was not seen during experimentation, either through interpolation between observed data points, or extrapolation beyond the limits of the experimental observations. For example, fluorescence reductions after stimulation in an FM experiment at low frame rate may yield enough points to fit an exponential decay curve. This curve could then be used to interpolate the rate of vesicle exocytosis at a higher frame rate than experimentally available.

4.5.2 Sensitivity analysis

Here, the effects of individual parameter changes on the overall model are determined. In a kinetic model, such analysis can be used to determine which process rates are critical to the overall model activity, and therefore which are the rate limiting processes within a system. Gillespie et al. (2013) provides a good overview of this topic.

Protein interaction models can be analysed in a similar fashion to determine sensitivity to individual interaction rates. For example Ramanan et al. (2011) modelled the interaction of the proteins AP-2 and clathrin in the generation of simulated clathrin coated pits, a precursor to CME. Additionally, protein expression levels can be modified in simulation to determine the effects of having more or less of a species in the simulated system. In spatial models it is possible to analyse the effects of sequestering proteins away from their binding partners, or modifying their diffusion rates, as would happen through conformation change or addition or removal of protein domains.

4.5.3 Abstract model analysis

Abstract models of protein interactions can be amenable to more general analysis. For example, models generated in process algebras such as Bio-PEPA can be used to determine rate limiting resources within the model. In the context of this project, this would be useful in determining which proteins availability determine the rates of endocytosis steps. Queueing theory applied to these models would help determine the effects of modifying the available expression of these proteins, for example if it was desired to simulate the effect of a rate limiting CME protein being over-expressed.

Temporal logics allow symbolic model checking of developed models, asserting model properties are true (Chabrier and Fages, 2003). Statistical analysis methods such as probabilistic bounded linear temporal logic, as used in the analysis tool BioLab (Clarke et al., 2008), provide the means to explore properties of models by expressing probabilities with which a model has defined properties.

4.5.4 Visualisation

Computational models are powerful tools in explaining a theory. Being able to visualise the behaviour of a system normally beyond our ability to observe experimentally aids in intuitive understanding of how that system (or at least the model representation of it) works.

As the popularity of the Takamori et al. (2006) paper described in Section 4.6.3 shows, theories are more easily explained when their effects can be visualised. This can include static network representations of interacting proteins, for example in the work by Armstrong and Sorokina (2012), and in Bio-PEPA (Smith and Gilmore, 2011) here in the School of Informatics, kinetic time-courses shown as graphs, or computer generated representations of molecular biology structures, either as static images or animations, for example the work of Johnson (`http://www.fivth.com/`, `http://www.youtube.com/grahamj21`), commonly seen on the pages of molecular biology texts and posters.

There are a variety of tools available here, graphing libraries are common, and are included with most modelling tools. Computer generated graphics tools are widely available (for example Autodesk Maya or Cinema4D), and there are an increasing number of computer graphics tools available tailored specifically to molecular biology, for example the molecular dynamics visualisation tools VMD (Humphrey et al., 1996) and NAMD (Phillips et al., 2005), and the tools produced by institutions such as the Olson laboratory at the Scripps Research Institute (`http://mgl.scripps.edu/`).

4.6 Prior computational modelling of synaptic vesicle recycling

There have been a number of studies using computational modelling in the area of synaptic vesicle recycling.

4.6.1 Kinetic modelling (non-spatial)

These studies use computational models to provide kinetic information about vesicle recycling, such as time constants for endocytosis, vesicle reacidification, or vesicle refilling. The bulk of the work in this area has modelled CME and kiss-and-run endocytosis rather than the mechanisms of ADBE, mainly as CME has been known for longer and the subject of more experimental studies.

One relevant study to use ODEs to simulate the endocytosis cycle is by Sara et al. (2005). The system of differential equations was concise, but sufficient to model the spontaneous (as opposed to activity driven) recycling of synaptic vesicles.

Another important work by Granseth and Lagnado (2008) created a system of ODEs to match the vesicle recycling behaviour observed in cultured hippocampal neurons. This study investigated the effects of ambient versus physiological temperature on recycling kinetics.

The paper by Atluri and Ryan (2006) describes the use of ODEs to fit experimental results of vesicle reacidification. The results of the model fitting are detailed kinetics of the reacidification step of vesicle recycling for the experimental model studied. The model illustrated the effects of ambient versus physiological temperature on recycling kinetics.

An extensive model of synaptic vesicle release kinetics is given in work by Gabriel et al. (2011). This paper constructs various ODE models in an iterative fashion to match experimental data showing vesicle release depression over extended stimulation. The paper is a good example of model development and fitting to experimental data.

There are many other studies using similar ODE tools in support of experimental observations, for example by Denker et al. (2011); Klingauf et al. (1998).

4.6.2 Kinetic and spatial modelling

An extension to the previous work also models geometry and movement of entities within the synaptic terminal. Studies in this area include both synaptic vesicle recycling work and more generally trafficking of endosomes and vesicles within cell bodies.

One study by Ramanan et al. (2011) created a cellular Potts model (Graner and Glazier, 1992) to estimate the requirements for clathrin to accumulate and nucleate the formation of a CME vesicle, and to perform the necessary cargo selection of membrane proteins. The same paper and an earlier study by Agrawal et al. (2010) also created elastic fluid membrane bending models to determine the energy required to deform the plasma membrane to form vesicles. This allowed the effects of membrane deforming proteins to be better characterised. This work may have potential extensions in determining similar energy requirements for ADBE.

The localisation of nucleating proteins to hotspots in the nerve terminal plasma membrane, and therefore the spatial organisation of nucleated clathrin-coated pits (a precursor to CME) was studied by Nunez et al. (2011). In this paper, a spatial model of nucleation localisation was created to determine the formation pattern of clathrin-coated pits on the plasma membrane.

A good review of the principles of spatial modelling and general model construction and verification in the context of endocytotic signalling is given by Birtwistle and Kholodenko (2009). This paper is an excellent introduction to the methods of biological modelling. While not specifically dealing with synaptic vesicle endocytosis, parts of the models discussed are still relevant.

4.6.3 Molecular structure modelling and molecular dynamics

These models take the methods of the previous section to a very fine level of detail. Models here are used to predict very low level interactions, and are commonly also used to predict low level structure for visualisation. There has already been some work in this area, significantly with a reconstructed image of a typical synaptic vesicle by Takamori et al. (2006) (Figure 4.1). This virtual reconstruction of the membrane components of a typical vesicle based on estimated protein counts per vesicle gave an intuitive impression of the crowding on the surface of a vesicle. This influential work (cited more than 600 times in Scopus) has subsequently been applied to other fields in biology. The protein count estimates of the work have subsequently been refined (Mutch et al., 2011; Wilhelm, 2013; Wilhelm et al., 2014), leaving scope for updates to the models.

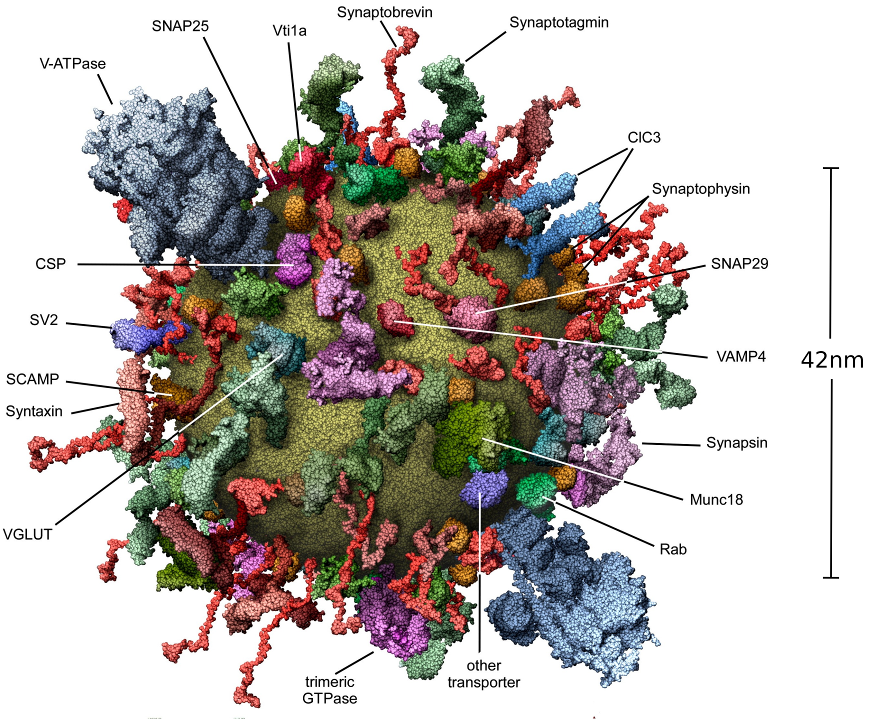

Figure 4.1: Molecular model of a synaptic vesicle. Transmembrane proteins are shown embedded in the membrane of a single vesicle. From Takamori et al. (2006), Figure 4.

The study by den Otter and Briels (2011) simulates the formation of curved clathrin coats from flat clathrin plaques by modelling the geometric properties of populations of self-assembling clathrin molecules. The simulation results look remarkably like the clathrin structures observed on the surface of the plasma membrane of presynaptic nerve terminals.

Chapter 5

Test data preparation and software development

This work required substantial image data curation and filtering, and software development to prepare datasets for testing, running the analyses, and additional tools created to improve image data processing efficiency. These additional tools are in frequent use in the Cousin laboratory.

5.1 Test data preparation

A goal of this work is to leverage the substantial archives of research data available at the Cousin laboratory. This has the benefits of both increasing the value of prior experimental work, and guaranteeing the image analysis has been done to the correct laboratory standards, making it a suitable target for the computational studies.

The image analysis described in Chapters 6 and 7 required a large number of test experimental assay data sets. To be useful for comparative verification of the automated segmentation tool, and to characterise the synapse properties in experimental images, the following were needed at a minimum:

- The registered time-series image data used during ROI segmentation and intensity trace recording, including timing information.
- The manually segmented ROI location set used after manual filtering and rejection of incorrectly behaving ROIs has been completed.
- A description of the assay protocol used, including what experimental events happen at what time or frame.

Unfortunately, few of the available experiment data archives maintain the above information in this format. A substantial amount of filtering of the available datasets and reconstruction of the required data needed to be completed:

- In some cases, the registered image files were not available, rather only the unaligned original microscope image files. As the ROI locations depend on a particular image registration to match their intended target synapses, this image registration needed to be recovered. This could be attempted if the measured ROI intensities were provided along with the ROI locations. The process of image registration parameter discovery is described in Section 5.1.1.

- In cases where the registered or processed image file was provided, it was commonly stored in TIFF format without the timing metadata of the time-series. This was recoverable in many cases by matching the processed file frames to the original microscope image file frames.

- Some of the older datasets used proprietary ROI location file formats (Simple PCI, Compix, Inc.), not compatible with ImageJ. These were converted as necessary.

- In most cases the ROI location file provided was the full set of manually segmented ROIs prior to intensity trace filtering as described in Section 3.4.1. This file along with the filtered ROI intensity file was used to construct a ROI location file of filtered ROIs only.

- Verification checks were done on all of these files to ensure consistency - a registered image (constructed if necessary) combined with a ROI location file of manually segmented and filtered ROIs (constructed if necessary) were used to generate a set of ROI intensity traces which were compared with the provided ROI intensity trace file. Any discrepancy was highlighted to allow the assay data to be removed from the test dataset if necessary.

All these operations were performed on the full set of assay data made available for this project (842 assays), providing a verified subset from which 77 were chosen for ROI drift analysis (Chapter 6) and 36 were chosen for automated ROI detection (Chapter 7).

5.1.1 Image registration metadata recovery

To reliably recreate the ROI intensity data from manually segmented ROI sets requires the registered time-series image which was used for manual segmentation. In many cases, this image was not retained after the original image analysis had been completed due to storage capacity issues, and the registration parameters are not routinely recorded with the assay. Retaining both original and registered images doubles the required storage capacity, which is already substantial in a busy laboratory.

Recreating the image registration manually is difficult as there is substantial flexibility in the parameters and method of registration. This work includes software which attempts to regenerate the image registration originally performed by the researcher given the original image, the manually segmented ROI set, and the original recording of ROI trace intensities.

The registration parameters to be discovered are the base frame chosen for registration and the registration algorithm. The Cousin laboratory primarily makes use of the StackReg plugin for ImageJ, or a local variant with modifications. There are a total of seven algorithm choices expected, with a further six algorithm choices possible using the plugins. These are listed in Table 5.1.

Table 5.1: Time-series registration modes possible using standard registration plugins. The “Not expected” options potentially modify the total intensity value for a given pixel area rather than just changing the pixel area location, and so are not recommended for use.

Plugin	Algorithm	Likelihood
None	None	Expected - unaligned
StackReg	Translation	Expected
	Rigid body	Expected
	Scaled rotation	Not expected
	Affine	Not expected
MBGReg (incremental comparison)	Translation	Expected
	Rigid body	Expected
	Scaled rotation	Not expected
	Affine	Not expected
MBGReg (fixed comparison)	Translation	Expected
	Rigid body	Expected
	Scaled rotation	Not expected
	Affine	Not expected

All of these registration algorithms have one feature in common. There must be at least one frame which has not been changed in position from the original time-series; the ROI intensities are the same for both time-series images. The possibilities are:

- Intensities match in all frames of times-series: registration was not performed prior to manual ROI segmentation.
- Intensities match in a single frame: this is the registration base frame.
- Intensities match in multiple frames: either one of the matching frames is the registration base frame, or the registration operation was incomplete.
- No frames where intensities match: some other operation was performed before or after registration which cannot be determined automatically.

If at least one candidate base frame is found, then the algorithm can be discovered by attempting registration with all twelve possible algorithms until finding one which allowed all intensities to match on all frames. If none are found, the assay is highlighted for manual checking and is removed from the test set used in later chapters.

This is a computationally expensive search process, but only has to be done once per assay, and the results are cached for future use.

5.1.2 Registration artefact removal

Image registration causes the source image to move over the viewport of the target image. The common transformations used in the laboratory for image registration are simple translation and more commonly rigid body transformation which allows both translation and rotation of the source image. There is no scaling or shearing of the image. In the target image, pixels not covered by the source image are set to 0.

When creating a difference image as required in Chapter 7 however, these borders of 0 pixels may generate a non-zero region of pixels, which may then be falsely detected as containing regions of interest during the ROI detection step (illustrated in Figure 5.1). This can cause problems in later ROI intensity analysis as these invalid ROIs are only partly on image data, and this part may change in size as image registration causes the boundary of the viewport to move during successive time-frames.

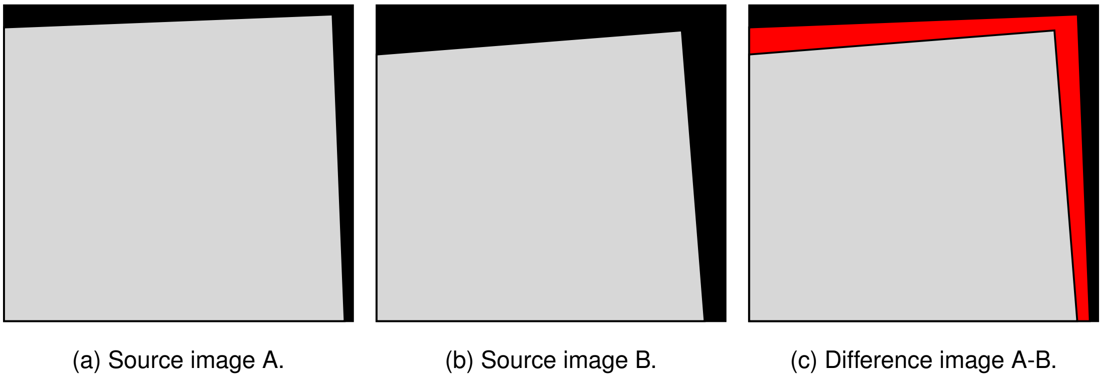
(a) Source image A. (b) Source image B. (c) Difference image A-B.

Figure 5.1: Potential image artefact caused by subtracting two registered images. Registration of images A and B (grey) creates regions of 0 pixels at the borders of the images (black). Subtracting these images may then create artificial regions of intensity where the pixels of image A are subtracted by 0 pixels in image B (red).

To prevent this, these image borders must be removed from the difference image. To do this, the image borders for all frames of the time-series need to be discovered. The ideal algorithm for boundary detection would be to fit straight lines to boundaries between zero pixels and non zero pixels for each frame of a time-series image. This would require scanning of significant areas of each frame because of the options of geometry possible for a registered image, and then fitting lines to match the non-zero areas found.

The goal is find the set of ROIs for which the intensity could be obtained for the full time-series. This required calculation of the area of the image which contained only source image pixels for all frames of the time-series. While this is possible to calculate, the result may be a geometrically complex region to mask.

If the loss of some source extra image pixels around the boundary of the image is acceptable, as there is still a sufficient population of synapses in the remaining image field, the detection process can be simplified. First, obtain the diagonal distance of the zero pixel boundary from each corner of the target image frame, for each frame of the time-series. This is the distance to the first non-zero pixel along the diagonal. From this calculate margins along each edge of the target image which guarantee removal of zero-pixel boundaries. This is less efficient at conserving true pixels than the method above, but requires significantly less reading of each frame, and has simple computation.

The final set of margins are the maximum of the margins for each frame of the time-series. The remaining area inside these margins is guaranteed to be within the zero-pixel boundaries of the registered image for the entire time-series.

5.1.3 Assay indexing and overview

The assay analysis software:

- Recovers image registration metadata and repeats the image registration if necessary.
- Verifies that the ROI intensity traces match those recorded by the user.
- Outputs all generated and potentially missing data files (if it was necessary to recreate them).
- Summarises each assay as a web page (Figures 5.2 and 5.3).

Additionally, at the experiment level, the software:

- Aggregates assays into replicates within experiments.
- Calculates overall time-series graphs for experiments.
- Summarises each experiment as a web page.

The software does its best to cope with unavailable files or metadata, regenerating or inferring where possible.

5.1.4 Final data available for each test assay

Each assay provides some or all of the following files:

- Original microscopy data file - in a number of formats. This usually includes timing information.
- Exported microscopy data file - some of the newer microscopes use proprietary formats not fully supported in ImageJ (although this changes over time). It is necessary to export to a more commonly supported format.

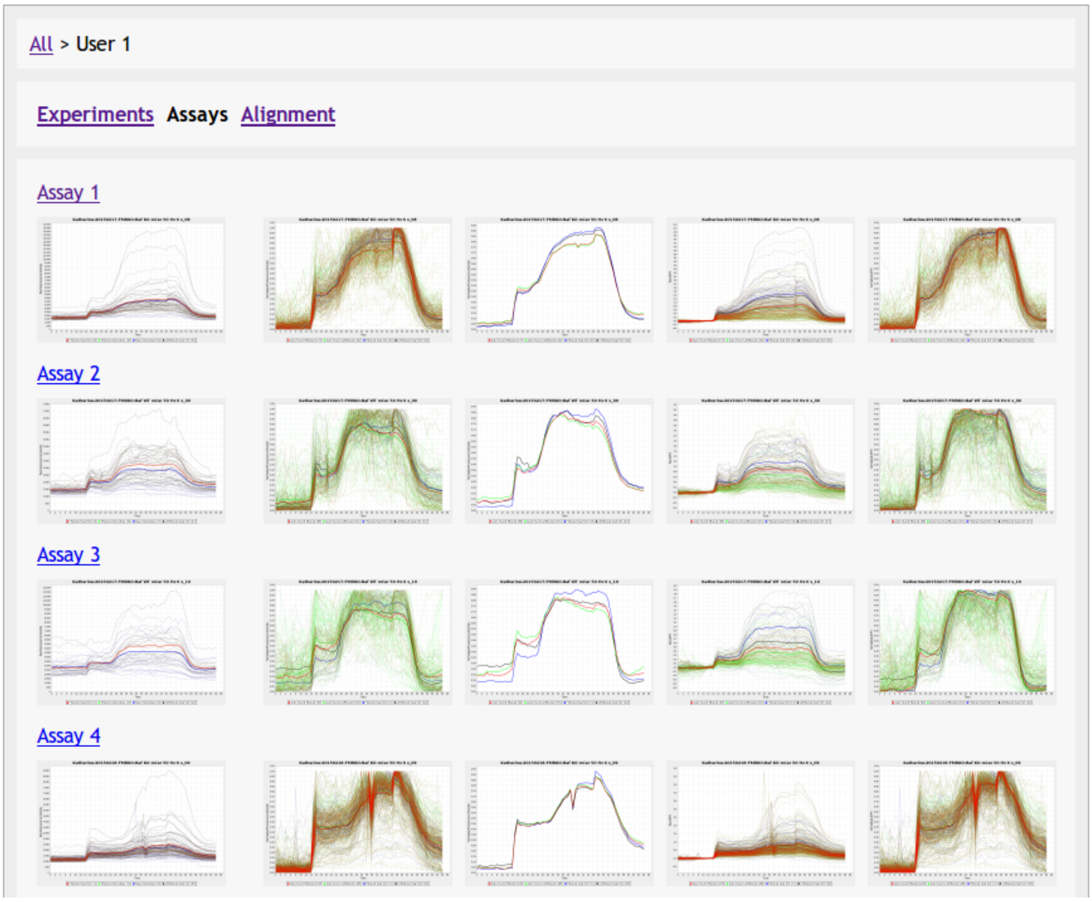

Figure 5.2: User assay index page, providing a quick overview of available assays. Further details for each assay are available by selecting the assay. Assay data originally collected by Katherine Bonnycastle.

- Registered microscopy data file - the result of running image registration. Generally in TIFF format, but usually missing timing data.
- ROI coordinates file - usually in ImageJ format, although some of the older datasets used Simple PCI format converted as necessary. The ROIs are usually the pre-filtered superset of the final filtered ROIs.
- ROI intensity data in CSV format - this is usually after filtering, though pre-filtered intensity data files are sometimes also available.

Additionally, the following metadata is maintained:

- Basic assay identification: User, AssayDate, ExperimentName, AssayName
- Frame range for calculation of baseline fluorescence, required for $\Delta F/F0$ calculation used in Chapter 7.
- Frame ranges for difference frame generation, discussed in Chapter 7.
- (Optional) ReplicateTag to aggregate assays within experiments

All > User 1 > Experiment 1 > Assay 1

User:	User 1	**Experiment:**	Experiment 1
Date:	Feb 17, 2015	**Assay:**	Assay 1
Frames:	67	**ROIs:**	46 screened from 54 unscreened
Duration (s):	Unknown	**ROI type:**	Oval 5x5

Unaligned image
Aligned image
ROI set
Timing file
Unfiltered ROI intensities
Filtered ROI intensities
First difference range
Second difference range
F0 calibration range
Replicate tag
Timing available
Alignment mode: RIGID_BODY_FIXED_BASE
Alignment base frame: 16
Aligned image correct

Figure 5.3: Single assay details page, showing information extracted from the assay data files and summary illustrative graphs for the assay. The ROI type uses the ImageJ naming convention, where a circular ROI is of type "Oval". Assay data originally collected by Katherine Bonnycastle.

5.1.5 Assay test platform

The same software created to regenerate and curate the test assays is also used in the following chapters to automate the analysis process of ROI drift characterisation and automated ROI segmentation. Additional software to perform these operations was added, and the results integrated with the curation and summary output for each assay. This allows configurable and repeatable analysis of the test assay set.

5.2 Other software development

A number of small applications and ImageJ plugin modifications were created to assist the current image processing work performed by researchers.

5.2.1 ROI trace selection

The existing ROI filtering stage of image analysis requires manual inspection of ROI intensity traces. The ROI trace selection tool (Figure 5.4) was created to speed this process from the previous method using spreadsheets. It allows individual selection of ROI traces, semi-automated selection based on trace properties, and assay aggregate results display for the researcher to assess the quality of the ROI set after selection is complete.

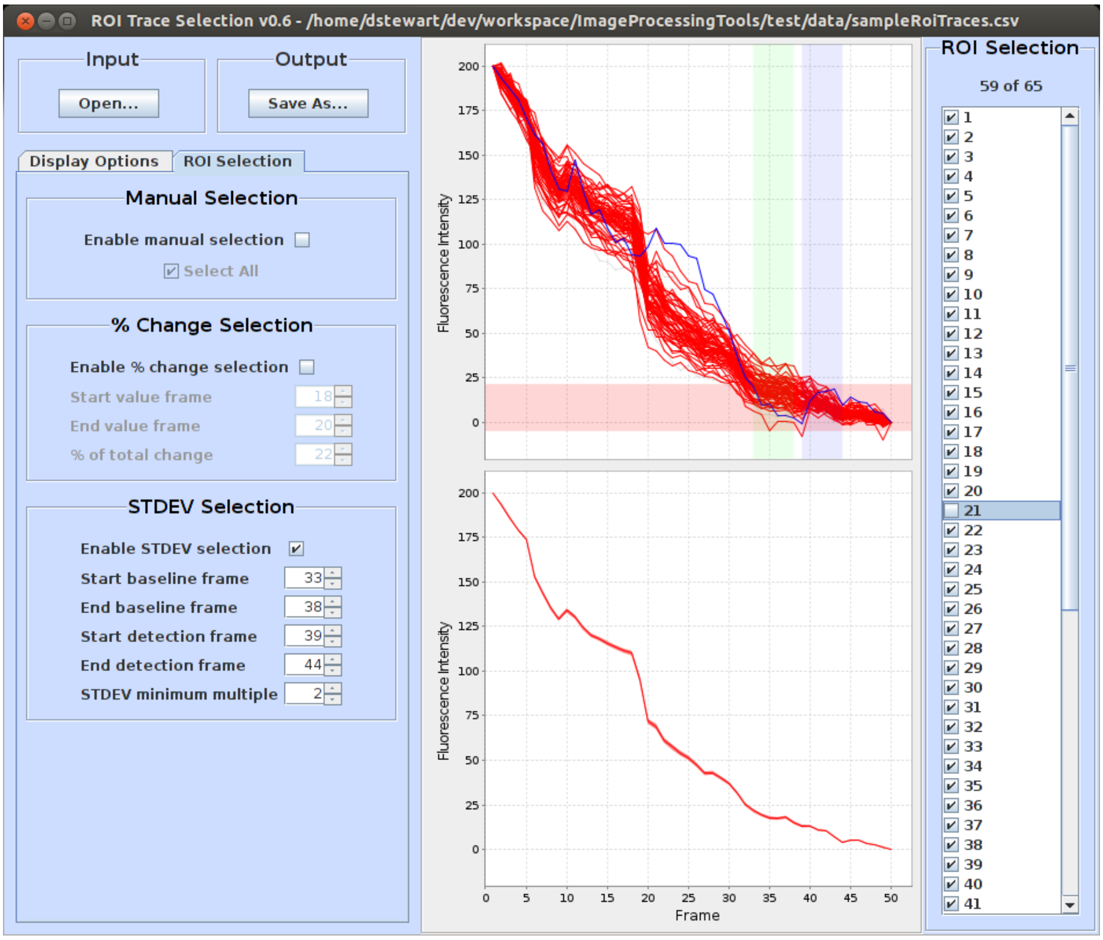

ROI Trace Selection v0.6 - /home/dstewart/dev/workspace/ImageProcessingTools/test/data/sampleRoiTraces.csv

Manual Selection

Enable manual selection ☐
☑ Select All

% Change Selection

Enable % change selection ☐
Start value frame 18
End value frame 20
% of total change 22

STDEV Selection

Enable STDEV selection ☑
Start baseline frame 33
End baseline frame 38
Start detection frame 39
End detection frame 44
STDEV minimum multiple 2

ROI Selection

59 of 65

☑ 1
☑ 2
☑ 3
☑ 4
☑ 5
☑ 6
☑ 7
☑ 8
☑ 9
☑ 10
☑ 11
☑ 12
☑ 13
☑ 14
☑ 15
☑ 16
☑ 17
☑ 18
☑ 19
☑ 20
☐ 21
☑ 22
☑ 23
☑ 24
☑ 25
☑ 26
☑ 27
☑ 28
☑ 29
☑ 30
☑ 31
☑ 32
☑ 33
☑ 34
☑ 35
☑ 36
☑ 37
☑ 38
☑ 39
☑ 40
☑ 41

Figure 5.4: ROI Trace Selection in use, showing automatic ROI selection mode.

The ROI Trace Selection application, and other created image processing tools, are available at `https://demonsoft.org/neuroscience/`.

Chapter 6

Image analysis: ROI drift analysis

ROI segmentation of time-series fluorescence microscopy experiments requires selection of the synapses which are active and behaving under stimulus. The synapse should stay within the same ROI boundary for the duration of the time-series. If the synapse were to move partially or wholly outside the boundary of the ROI, then intensity changes would be mistakenly attributed to the synapse losing fluorescence intensity.

Time-series images may be subject to image plane drift during the course of the experiment. Either the segmented ROIs must track the synapses of interest in the image at each frame, or the overall image frame is adjusted to minimise the overall movement of synapses. Current experiment analysis protocols and the main widely available tools used within neuroscience labs use a fixed ROI. There are multiple reasons for this:

- Manual segmentation is commonly used. Manual selection of ROIs is a tedious process for a single static image. To extend that work to selection of an individual ROI over each frame of a time-series would be both time-consuming and error prone.
- ROI segmentation capability and storage in the commonly available tools has therefore been biased towards fixed ROIs. Multi-frame ROI tracking tools do exist, for example Particle Track and Analysis (PTA2, `http://www.sanken.osaka-u.ac.jp/labs/bse/ImageJcontents/frameImageJ-en.html`), but are not in common use for synapse intensity quantification over time.
- Automated ROI segmentation has also primarily favoured static images. When using automated segmentation, users pick either a representative frame from a time-series, or construct a projection of the time-series to a single image.

This study quantifies the movement of synapse intensity centres from the fixed centre of a static ROI. The effect of using a fixed ROI compared with a moveable tracking one on ROI trace intensity is also measured. Three methods of automated tracking of synapse centres given time-series images and fixed ROIs are provided, along with a sample tool to demonstrate their use.

6.1 Methods

6.1.1 Image data sets

The performance of the tracking heuristics are shown using a variety of time-series fluorescence images conducted on mammalian central nervous system cultured neurons, over a number of fluorescent marker molecules. 77 time-series images along with their respective manually segmented ROI sets were selected for processing as described in Chapter 5. The test criteria were:

- Time-series images of image format 16-bit grayscale (file format is not relevant).
- Matching filtered manual ROI sets using only 5x5 pixel circular ROIs (i.e. of ImageJ ROI type “Oval”).
- Confirmation of the registration mode used for the manual ROI selection.

The first two criteria allow simplifications to be made to the processing, while not significantly reducing the available test data. The last criterion ensures the calculated ROI drift matches that which would have been obtained during the original use of the image data.

To determine the effect of background subtraction on the detection of ROI drift, both original and background subtracted time-series images were used. The background subtraction algorithm used was a standard rolling ball subtraction with a radius of 10 pixels as described in Section 3.3.2.1.

6.1.2 ROI drift measurement

Intensities of ROIs were recorded using the existing fixed ROI centre. Then the ROI centre was allowed to move in the neighbourhood of its current position. The neighbourhood was a 13x13 pixel area centred on the original ROI. These dimensions limit any moved ROI to be within one ROI diameter of the x and y co-ordinates of the original ROI. To determine any effect attributable to the choice of search area size, the processing was repeated for neighbourhoods of area 11x11 and 15x15 for comparison.

Three methods of selecting a new ROI centre were chosen.

- Neighbourhood centre of mass (denoted as *Centre of Mass* for the rest of this chapter): the total intensity of the neighbourhood centred on the existing ROI was taken, and the pixel corresponding to the location of mean intensity in x and y directions was chosen as the new ROI centre (Figures 6.1a,6.1b).

- Maximum ROI intensity (*ROI Maximum*): a ROI of the same dimensions as the original ROI was tested at all locations within the 13x13 neighbourhood, and the ROI location where the ROI intensity was highest was chosen (Figure 6.1c).

- Local maximum ROI centre (*Pixel Maximum*): local maxima pixels within the neighbourhood were found, constrained to an inner boundary so that a mask would still fit within the 13x13 region. These were then weighted for goodness of fit and the lowest value weight chosen as the ROI centre. The weight measure at frame t was:

  $$w_t = d_1(c_t, o)^2 + d_2(c_t, c_{t-1})^2$$

  where o is the original ROI centre location, c_t is the candidate ROI centre location at frame t, and $d(a,b)$ is the Euclidean distance between points a and b. This weight encourages (i.e. $w_t \to 0$) candidate choices which both stay in the vicinity of the original ROI centre (d_1), and do not have large changes in position from one frame to the next due to transient fluctuations in local maxima (d_2). Squaring the distances rapidly increases the weight as the distances increase (Figure 6.1d).

The mean Euclidean drift of these centres from the original ROI centre over the whole time-series was recorded. Aggregate mean drift values were calculated for all ROI within each assay ROI set, and an overall mean and standard deviation were taken for all ROIs in all assays together for each test condition.

6.1.3 ROI time-series intensity measurement

With these three movable ROI centres chosen, ROI image intensities over the time-series were recorded for both the original and background subtracted time-series images. An intensity ratio $I_{t,r}$ was calculated for all ROI $r \in R$ and frames $t \in T$ in the current assay:

$$I_{t,r} = \frac{\text{re-centred ROI intensity}_{t,r}}{\text{original ROI intensity}_{t,r}}$$

It is reasonable to expect the re-centred ROI intensity$_{t,r}$ to be higher than the original ROI intensity$_{t,r}$ if the synapse centre has drifted away from the original ROI centre. Therefore as the amount of drift increases from the original ROI centre, $I_{t,r}$ is likely to also increase.

The mean intensity ratio per assay was calculated, and an overall mean of the assay values was calculated for each test condition.

$$\text{Assay mean intensity} = \sum_{r \in R} \sum_{t \in T} I_{t,r}$$

$$\text{Overall mean intensity} = \sum_{a \in A} \sum_{r \in R_a} \sum_{t \in T_a} I_{t,r}$$

where A is all assays of the test set, T_a and R_a are the frames and ROIs in assay a.

6.1.4 Separation of ROI drift into component elements

There are two components to ROI drift from manually segmented ROIs:

- Fixed component: The centre of manually segmented ROI may not be ideal for the synapse image data it contains. This could be due to mis-targeting of the synapse centre

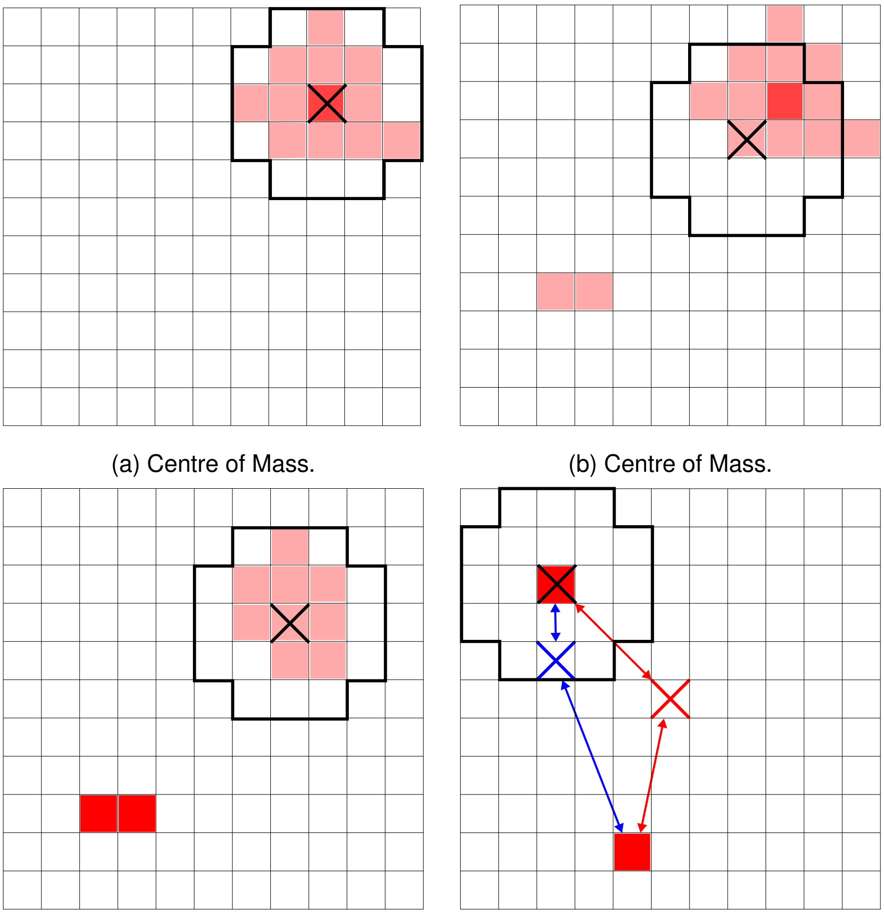

(a) Centre of Mass.

(b) Centre of Mass.

(c) ROI Maximum.

(d) Pixel Maximum.

Figure 6.1: Illustration of ROI centre finding algorithms. Brighter red represents more intense fluorescence in the pixel grid area, black outline shows 5x5 circular ROI positioned at algorithm choice. (a) Centre of Mass takes intensity mean location in x and y. (b) Multiple regions of fluorescence can pull Centre of Mass away from optimal location. (c) ROI Maximum picks the area where the total ROI intensity is largest, which may not include the brightest individual pixels. (d) Pixel maximum finds the local maxima, then calculates distances (arrows) from each local maximum to the original fixed ROI centre (red cross) and previous frame ROI centre (blue cross). The ROI is positioned to minimise the sum of squares of these distances.

when creating the ROI. It is not uncommon for the user to create a ROI with a small offset (generally a single pixel) from the ideal ROI centre when clicking on the image on-screen.

Also the visible image has a wide dynamic intensity range, which makes it hard to distinguish the lower intensity synapse boundaries, and therefore to centre the ROI to include as many of these boundary intensities as possible.

- Mobile component: This is due to actual fluorescence signal movement over the course of the time-series.

It is useful to separate these components in a replicable manner for ROI drift analysis. This work uses z-projections of the time-series to accomplish this.

1. Create a z-projection of the registered time-series. There are two reasonable options here; maximum intensity and average intensity. Results of image analysis using each are shown.

2. For each tracking algorithm, run the tracking centre detection on the single z-projected image. This centre represents the fixed drift component, when measured from the recorded fixed centre.

3. Record the ROI drift from this fixed centre, rather than the original user-selected centre. This is the remaining mobile drift component.

A problem with this approach is that the Pixel Maximum algorithm does not have a previous frame to assist in the weighting. This flaw is reflected in the results, but is unavoidable using single selection frames.

6.2 Results

Running the search algorithms on the test set described in Section 6.1.1 provided results both about the efficacy of the chosen drift algorithms, and general ROI drift characteristics of the test set.

6.2.1 Search area size effect on mean ROI drift

Table 6.1 shows the effects of increasing the search area on mean ROI drift as calculated by the three test algorithms. Centre of Mass drift shows a modest increase in mean drift as the search area increases, for both BS and original image data. ROI Maximum shows a more substantial increase as search area increases, caused by an increased likelihood of another fluorescence peak, perhaps another synapse, appearing on the boundary of the search area. Finally, Pixel Maximum shows a reduction in ROI drift. This is due to some boundary local maxima from other synapses moving location to brighter adjacent pixels exposed by increasing the search area. These local maxima have increased weight, which reduces their likelihood of being selected as the ROI centre.

These results indicate that Pixel Maximum centres are the most stable in response to changes in search area. Figure 6.2 also illustrates the effect of increasing search area on ROI drift.

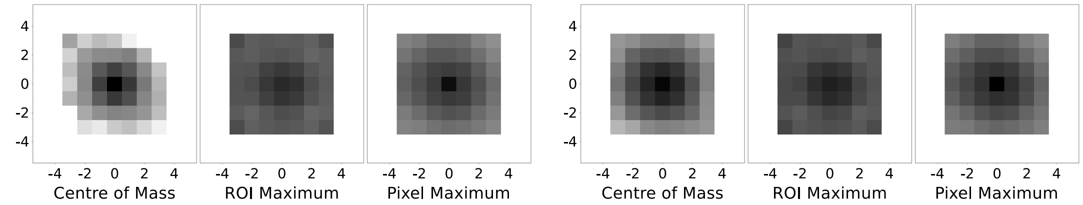

(a) Area: 11x11. Not background subtracted.

(b) Area: 11x11. Background subtracted.

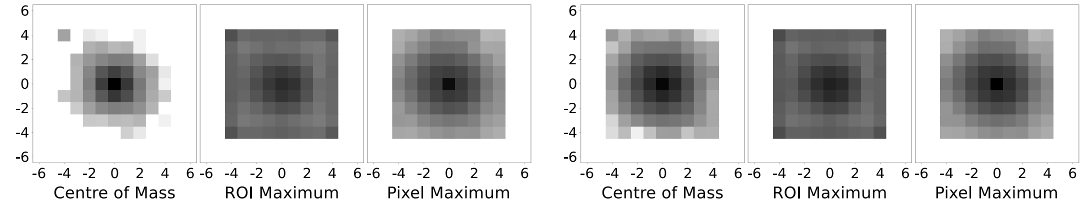

(c) Area: 13x13. Not background subtracted.

(d) Area: 13x13. Background subtracted.

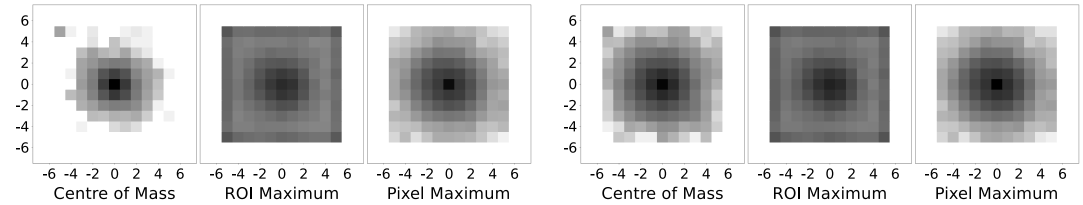

(e) Area: 15x15. Not background subtracted.

(f) Area: 15x15. Background subtracted.

Figure 6.2: Aggregate ROI drift heat-map - each plot shows drift of ROI centres from the original ROI location at (0,0). Darker areas represent larger numbers of ROI centres at that location. Data is aggregated over all ROIs (3594) and all time frames of all assays in the test set (77). Plots (a,c,e) are not background subtracted, plots (b,d,f) have background subtraction using rolling ball of radius 10 pixels. Plots (a,b) have a search area of 11x11 pixels, (c,d) 13x13 pixels, and (e,f) 15x15 pixels.

6.2.2 Background subtraction effect on mean ROI drift

Differences in drift means between background subtracted and original time-series images are shown in Table 6.2. Applying background subtraction has negligible effects on drift means aggregated over all ROIs calculated by ROI Maximum or Pixel Maximum. However, Centre of Mass has substantially higher drift with background subtracted images. This is understandable as synapse pixels make up a larger proportion of the total image intensity after background subtraction, and the general dampening effect of background pixels is reduced. Figures 6.2c and 6.2d also illustrate the difference in ROI drift with the mean peak algorithm between original and background subtracted image data.

6.2.3 ROI drift of test data sets

Pixel Maximum has stable mean ROI drift values as search area increases. It is also stable with and without background subtraction. The mean ROI drift for Pixel Maximum and Centre of

Table 6.1: Euclidean distance of centre from fixed ROI centre, measured in pixels. Results shown for background subtracted (BS) and not background subtracted images of multiple search area sizes. Differences in ROI drift are shown between search area sizes. Values are aggregate mean and (standard deviation) for all test ROIs (3594) over all image frames. A lower distance value means the movable ROIs and original fixed ROIs are closer together, i.e. there is less ROI drift, with a distance value of 0 meaning the original fixed ROIs produce the same result intensity profiles as the movable ROIs.

Image	Search area	Distance from fixed ROI centre in pixels					
		Centre of Mass		ROI Maximum		Pixel Maximum	
BS	11x11	0.964	(0.820)	1.909	(1.197)	1.024	(1.056)
	difference	*0.074*	(*0.122*)	*0.300*	(*0.384*)	*-0.014*	(*0.028*)
	13x13	1.038	(0.942)	2.209	(1.581)	1.009	(1.084)
	difference	*0.055*	(*0.127*)	*0.325*	(*0.407*)	*-0.005*	(*0.004*)
	15x15	1.092	(1.070)	2.535	(1.988)	1.005	(1.088)
Non BS	11x11	0.299	(0.544)	1.929	(1.209)	1.031	(1.060)
	difference	*0.027*	(*0.040*)	*0.314*	(*0.396*)	*-0.013*	(*0.031*)
	13x13	0.326	(0.584)	2.242	(1.605)	1.018	(1.091)
	difference	*0.020*	(*0.038*)	*0.344*	(*0.424*)	*-0.006*	(*0.005*)
	15x15	0.346	(0.621)	2.586	(2.029)	1.012	(1.096)

Table 6.2: Difference in ROI drift mean between original and background subtracted image data, measured in pixel distances from original fixed ROI centre. Values are aggregate mean and (standard deviation) for all test ROIs (3594) over all image frames with a search area of 13x13 pixels. The Centre of Mass difference (in bold) is notably larger than the other two algorithm differences, demonstrating increased mobility of Centre of Mass ROIs in background subtracted images.

Centre type	Not BS - BS	
Centre of Mass	**-0.712**	(-0.359)
ROI Maximum	0.033	(0.025)
Pixel Maximum	0.009	(0.007)

Mass for background subtracted image data in a 13x13 search area is approximately 1 pixel with a standard deviation of 1 pixel (from Table 6.1).

6.2.4 ROI intensity values of test data sets

Table 6.3: Intensity increase as a percentage over fixed ROI centre intensities. Results shown for background subtracted (BS) and not background subtracted images of multiple search area sizes. Differences are shown between search area sizes. Values are aggregate mean and (standard deviation) for all test ROIs (3594) over all image frames. Values in bold are those most suitable for evaluating the effects of ROI drift on ROI intensities.

Image	Search area	Intensity increase as % of fixed ROI centre intensity					
		Centre of Mass		ROI Maximum		Pixel Maximum	
BS	11x11	17.1	(39.7)	25.6	(45.0)	12.8	(32.4)
	difference	*1.5*	(*9.6*)	*4.7*	(*13.6*)	*-0.6*	(*1.5*)
	13x13	**18.5**	(**49.3**)	30.3	(58.6)	**12.2**	(**33.9**)
	difference	*1.0*	(*9.9*)	*4.6*	(*14.1*)	*-0.2*	(*0.8*)
	15x15	19.5	(59.2)	34.9	(72.8)	12.0	(34.6)
Non BS	11x11	3.6	(12.1)	8.6	(16.3)	5.4	(14.1)
	difference	*0.1*	(*1.1*)	*1.1*	(*2.9*)	*-0.1*	(*0.8*)
	13x13	3.7	(13.2)	9.7	(19.3)	**5.3**	(**14.9**)
	difference	*0.0*	(*0.5*)	*1.2*	(*2.8*)	*-0.1*	(*0.3*)
	15x15	3.7	(13.6)	10.9	(22.1)	5.1	(15.2)

Recentering the ROIs to brighter regions in the immediate neighbourhood results in increased mean intensity over the assay, and over the test set overall (as shown in Table 6.3).

- ROI Maximum: this method has the highest intensity increase as it selects the best possible location for the ROI mask for each frame. This is the upper bound possible within an 13x13 neighbourhood centred on the original ROI. However this method may not follow a single synapse. If multiple possible synapses are visible within the neighbourhood, then the brightest is chosen in each frame. This may not be the synapse intended to be targeted, and indeed may not remain the same synapse for all frames of the time-series. The larger the size of the neighbourhood, the more the centre is likely to target other synapses.

- Centre of Mass: when there is a single synapse with a Gaussian 2D intensity profile, this method performs as well as ROI Maximum. However, if the intensity distribution is non symmetric and the synapse signal is larger than the selected ROI diameter then this method records less intensity than that recorded by ROI Maximum. When there are multiple potential synapses in the sampling region, this method centres on a point between them, losing part of the signal from each synapse.

- Pixel Maximum: this method works best when selecting a synapse that fits a 2D Gaussian, with the pixel of highest intensity in the middle of the synapse. However if there are multiple local maxima within the sampling region this method has difficulty selecting the best one, as would be selected by an experienced researcher. The weighting measures alleviate this issue by penalising ROI centre jumps in location from one frame to the next.

The increases in mean intensity over original ROI intensity for the search area 13x13 range from 3.7% to 9.7% in non background subtracted images, and 12.2% to 30.3% in background subtracted images (from Table 6.3). If we choose to discard the intensity increases for ROI Maximum and non background subtracted Centre of Mass based on their mean ROI drift behaviour, the intensity increase ranges are 5.3% (non BS) and 12.2% to 18.5% (BS).

The standard deviations of these values are high, at 14.9% (non BS) and 33.9% to 49.3% (BS). This shows that there is significant variability in potential ROI drift across all of the ROIs in the test set (3594).

Taken together with the mean ROI drift estimates, this means that on average, ROI centres are at least 1 pixel off their ideal potential centre, and that on average, the intensity traces would be 5% higher (with non BS images) if the ROI potential centres were used instead.

The effect this has on the analysis of intensity traces is complex. The following factors must be considered:

- Is the intensity loss a fixed value across the time-series? If yes, then the potential error introduced may be largely removed by normalisation, for example in Figures 6.3 and 6.4.
- If the intensity loss is not a fixed value, does it change at a fixed rate? If yes, then the potential error may be removed by photo-bleaching correction.

It is worth remembering also that there is already significant noise in the intensity traces due to fluctuations in fluorescence. Experiment design already takes that into account by having many replicates of test conditions.

To determine whether a fixed drift is responsible for a significant part of the overall drift and intensity loss, fixed ROI centres were found as described previously.

6.2.5 Fixed and mobile ROI drift components

Table 6.4 shows the effects of compensating for fixed drift by moving the fixed ROI centre based on the z-projections on the intensity traces. As previously mentioned, the Pixel Maximum fixed drift selection is not ideally suited to single frame selection, and this is reflected in the results. After re-centring each ROI, the mobile drift marginally *increases* for both BS and non BS images using both z-projection types. However, using the BS Centre of Mass, which was also considered to be a stable measure of ROI drift, there is a reduction in mobile drift of approximately 30%.

Also worth noting that using the average intensity z-projection to recentre the ROIs gave a consistently higher reduction in mean mobile drift than using maximum intensity z-projection, across both BS and non BS data and all three algorithms for determining ROI drift.

6.3 Conclusions

ROI drift does occur to a small extent in the test sets used, though the estimation measures here put it at a mean of one pixel between the existing fixed ROI centre location and ideal tracking location. Correcting this offset would potentially increase the fluorescence signal in non BS data by about 5% on average (about 12% - 18% in BS data).

The effects of this potentially lost signal are hard to establish without going through each assay individually, along with its statistical analyses, as much of the difference is handled by subsequent processing. The results do however suggest two approaches that may be taken.

First, correct the fixed drift of ROIs within an assay. The results show that it is reasonable to expect a 30% reduction in residual drift if any detected fixed offset is corrected. There already exist tools to do this for ImageJ. For example, the Time Series Analyser plugin (`https://imagej.nih.gov/ij/plugins/time-series.html`) has a centre of mass based ROI relocation function. The following post-selection processing steps accomplish the task:

1. Create an average intensity z-projection of the time-series image data.
2. Use this image to recentre the ROIs using the `Recenter` function of the Time Series Analyser plugin for ImageJ.
3. Use the new ROIs with the registered time-series image to obtain corrected ROI intensity data.

Second, running the analysis software described in this chapter on experiment assay data provides an overall measure of potential ROI drift, and measures per assay. Assay results exceeding a set threshold of potential ROI drift could be flagged for inspection by the researcher. At that point, the image data could be reprocessed if necessary to produce a more stable ROI set.

To assist here, the software produces ROI drift heat-map plots per assay. Asymmetrical distribution of drift in an assay drift heat-map plot shows a general trend for ROIs to drift in the same direction (Figure 6.5). This is a good indicator of image plane drift, and could potentially be corrected by image realignment.

Table 6.4: Euclidean distance of centre from re-centred ROI, measured in pixels. Results shown for background subtracted (BS) and not background subtracted images and both z-projection types used to detect fixed centre. Differences are shown between original ROI drift and remaining mobile drift after ROIs were re-centred. Values are aggregate mean and (standard deviation) for all test ROIs (3594) over all image frames with a search area of 13x13 pixels. A low mobile drift value demonstrates a more stable ROI location after the recentering step. The Centre of Mass difference value in bold shows an increase in fixed ROI centre stability after recentering.

Peak type	Component distance from fixed ROI centre in pixels			
	Fixed drift	Original drift	Mobile drift	*Original-Mobile*
BS, Maximum intensity z-projection				
Centre of Mass	1.095 (0.829)	1.038 (0.942)	0.734 (0.754)	***0.304*** (***0.189***)
ROI Maximum	1.840 (1.383)	2.209 (1.581)	1.427 (1.721)	*0.783* (*-0.140*)
Pixel Maximum	1.340 (0.888)	1.009 (1.084)	1.186 (1.076)	*-0.177* (*0.008*)
BS, Average intensity z-projection				
Centre of Mass	1.095 (0.832)	1.038 (0.942)	0.630 (0.685)	*0.408* (*0.258*)
ROI Maximum	1.867 (1.439)	2.209 (1.581)	1.230 (1.590)	*0.979* (*-0.010*)
Pixel Maximum	1.386 (0.987)	1.009 (1.084)	1.101 (1.090)	*-0.092* (*-0.006*)
Non BS, Maximum intensity z-projection				
Centre of Mass	0.549 (0.676)	0.326 (0.584)	0.407 (0.593)	*-0.081* (*-0.009*)
ROI Maximum	1.881 (1.412)	2.242 (1.605)	1.448 (1.748)	*0.795* (*-0.142*)
Pixel Maximum	1.354 (0.894)	1.018 (1.091)	1.194 (1.080)	*-0.176* (*0.012*)
Non BS, Average intensity z-projection				
Centre of Mass	0.347 (0.560)	0.326 (0.584)	0.250 (0.480)	*0.075* (*0.104*)
ROI Maximum	1.907 (1.470)	2.242 (1.605)	1.211 (1.572)	*1.031* (*0.033*)
Pixel Maximum	1.391 (0.999)	1.018 (1.091)	1.103 (1.096)	*-0.085* (*-0.005*)

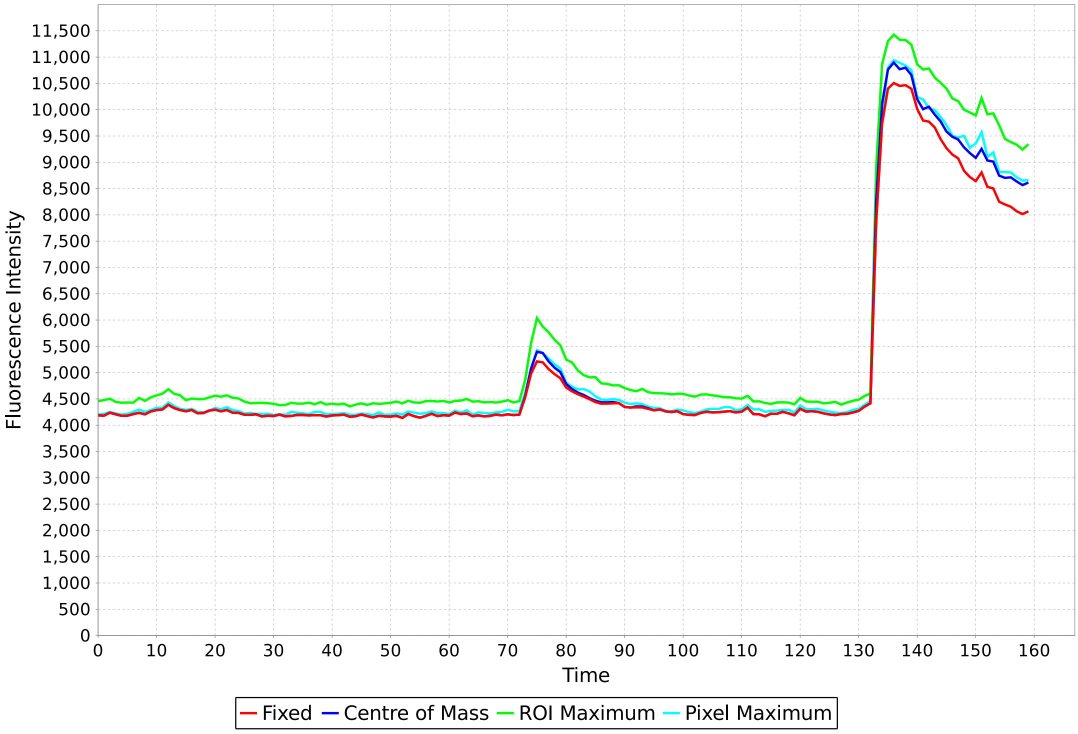

(a) Not background subtracted. Original intensities.

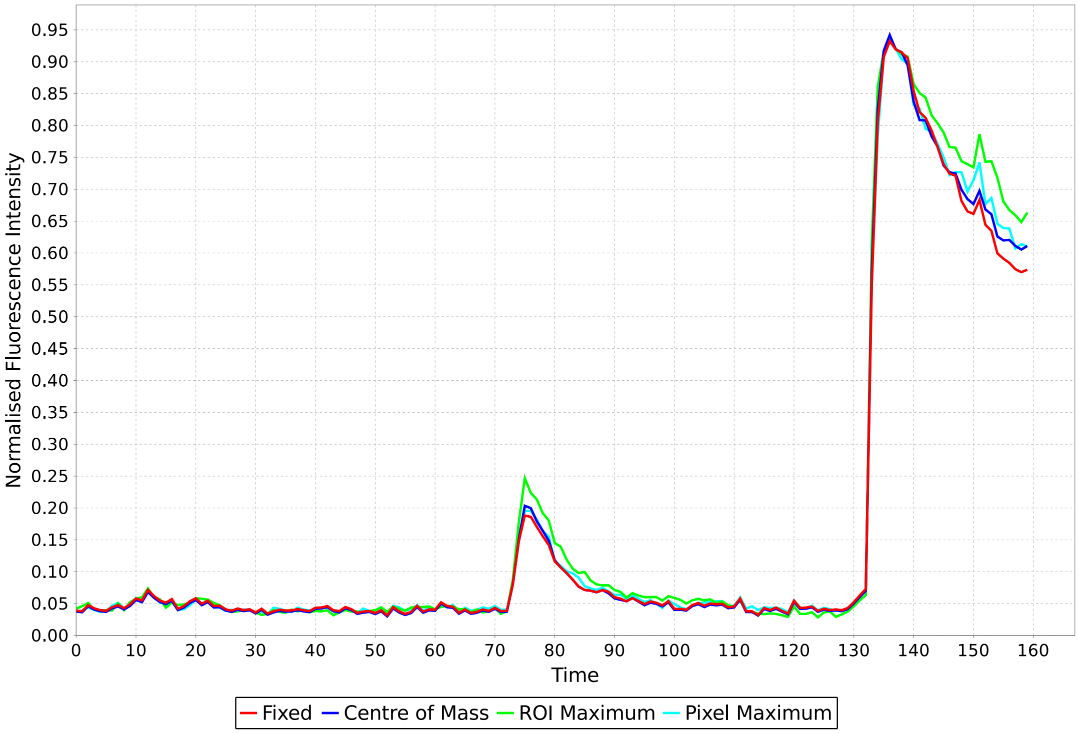

(b) Not background subtracted, min-max normalised intensities.

Figure 6.3: ROI Drift Intensities aggregated over all ROIs (15) and all time frames (160) of an example assay. Plot (a) shows the raw intensity values, plot (b) is normalised min-max for each ROI individually. Plots are not background subtracted.

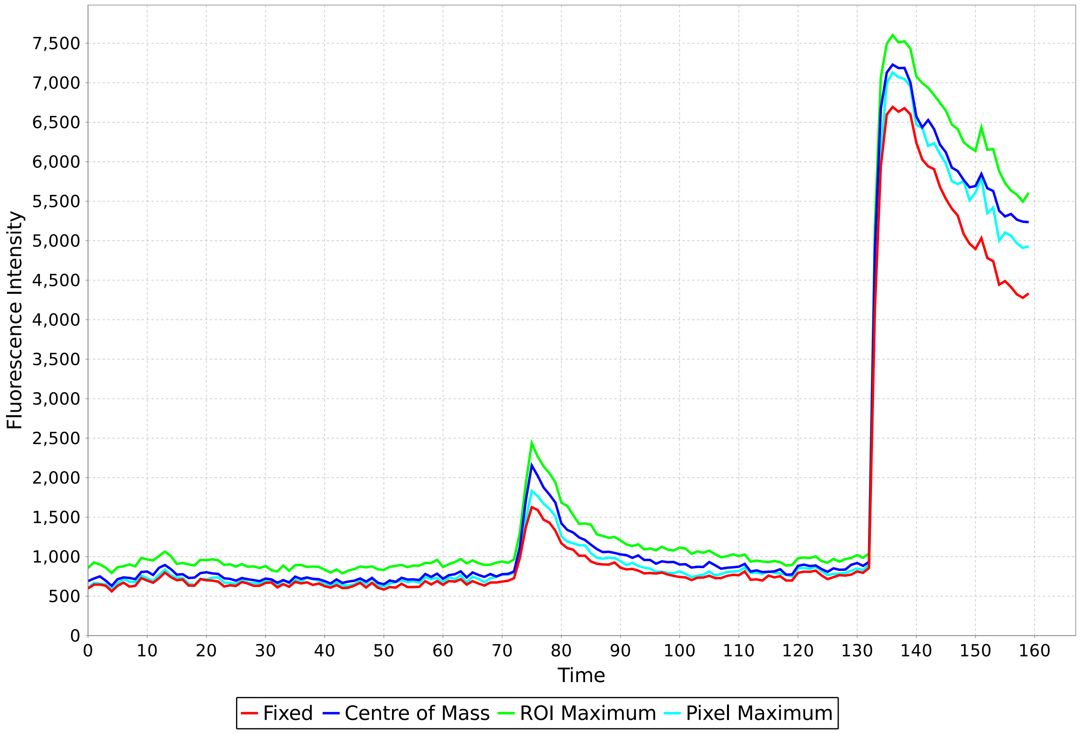

(a) Background subtracted. Original intensities.

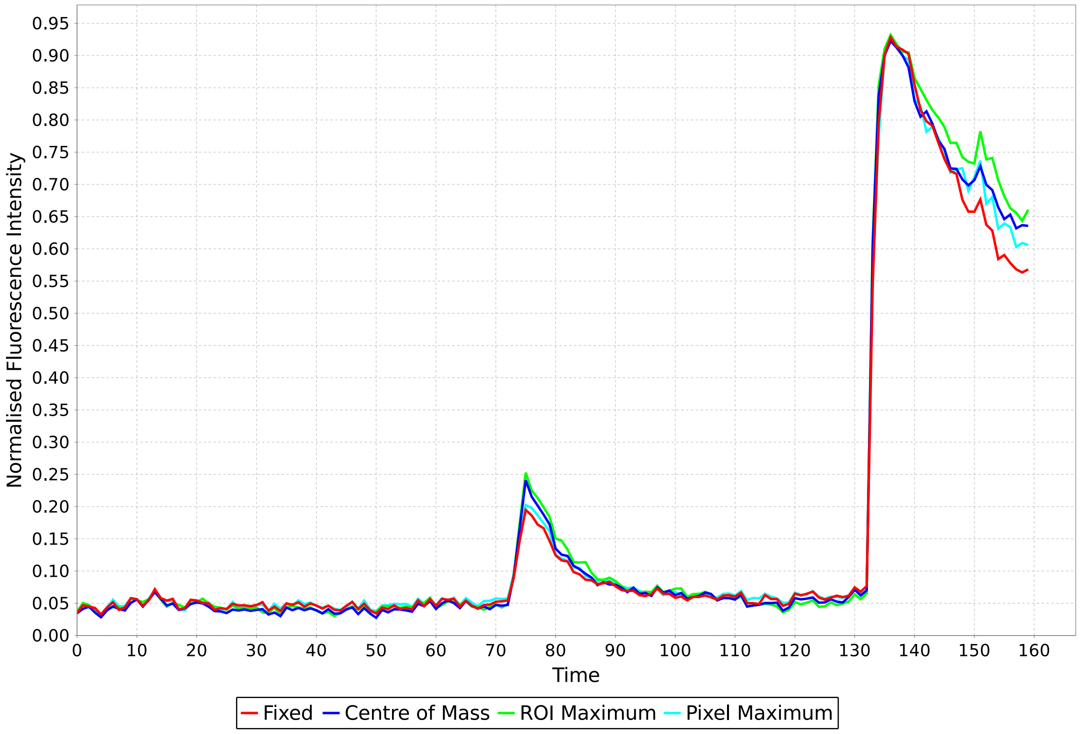

(b) Background subtracted, min-max normalised intensities.

Figure 6.4: ROI Drift Intensities aggregated over all ROIs (15) and all time frames (160) of an example assay. Plot (a) shows the raw intensity values, plot (b) is normalised min-max for each ROI individually. Rolling ball background subtraction with a radius of 10 pixels was applied.

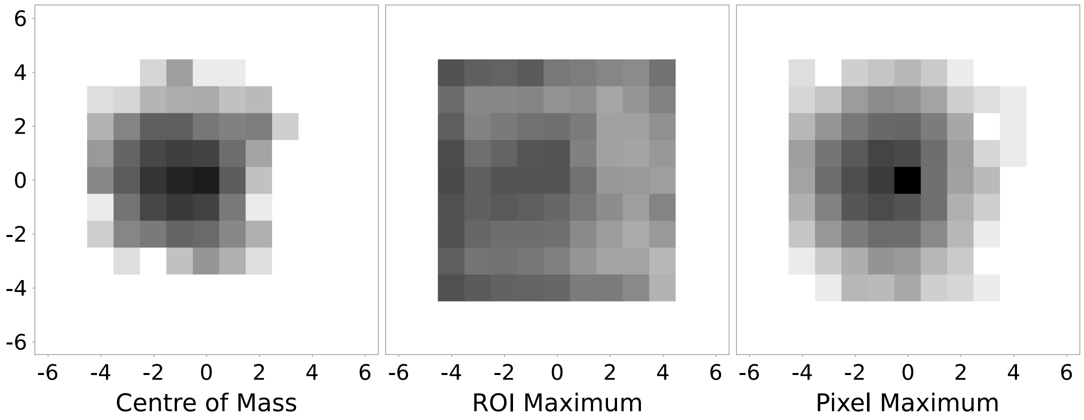

Figure 6.5: Example ROI assay heat-map showing asymmetric drift. This is a good visual indicator that image registration should be checked before continuing with ROI intensity data processing. These cases already would have a large ROI drift value to flag the assay for attention.

Chapter 7

Image analysis: Automated ROI detection

Chapter 3 discussed the ROI segmentation process commonly used for fluorescence time-series images. To recap, the goal of segmentation is to identify the locations of the ROIs (and perhaps their boundaries) through the image noise and non-synapse image features, and quantify the intensity changes over time attributable only to these ROIs. Some error or approximation may be allowable if shown to be not significant.

Manual segmentation is time-consuming and requires considerable skill on the part of the researcher. Automated segmentation has been used in some synapse studies (Billings et al., 2012; Collado-Alsina et al., 2014; Verstegen et al., 2014, for example). However, the description of such use does not always describe the process by which the optimum segmentation was discovered, or include the configuration used to segment the final ROI sets.

The work described in this chapter evaluates a number of existing automated ROI segmentation methods, adapted to suit this study where necessary, along with a number of novel extensions targeted specifically to experiments investigating synaptic vesicle recycling.

7.1 Existing automated segmentation approaches

There have been three segmentation algorithms or tools cited specifically for use in synapse segmentation; Bergsman (Bergsman et al., 2006), Fish (Fish et al., 2008) and Yona (Yona et al., 2011). While all are not exactly suited to the time-series image data that forms the core of this work, they are sufficiently adaptable that they can be used at least in part. The algorithms and tools are named in this work after the respective first authors of the papers for convenience.

Other algorithms or tools which have not been used in the evaluation are also described. These are SynD (Schmitz et al., 2011) and using difference of Gaussians (Iwabuchi et al., 2014). While these have been used in the synapse image segmentation domain, they are not suitable for this study.

7.1.1 Selected algorithm: Bergsman

Bergsman et al. (2006) describes a plugin for Igor Pro (WaveMetrics, Lake Oswego, OR, USA) which performs automated segmentation of synapses on fluorescence microscopy time-series data. The plugin can perform the full sequence of background subtraction, image registration, and ROI segmentation operations. Background subtraction uses a custom algorithm, which the authors describe as superior to the more generally used options.

Image registration is done after background subtraction, using a built-in custom registration routine which can perform translations in the *xy*-plane. An interesting choice, as image registration is commonly performed prior to background subtraction. Commonly used image registration tools such as StackReg (Thevenaz et al., 1998) for ImageJ make use of the larger features of the image to aid registration.

The algorithm uses an iterative threshold and detect stage to handle the high intensity range of fluorescent puncta. The selection of acceptable fluorescence levels, step size, and frames used for detection are left to user input.

The algorithm makes use of time-series image data in two ways. First, potential ROIs are selected from an average z-projection of a number of frames. This reduces transient point noise visible in individual image frames. Second, the algorithm uses time-series information for ROI quality filtering. The intensity trace of the ROI over the course of the time-series is analysed to determine a quality measure of each ROI. This quality is composed of three measures; the slope of intensity change, the fractional destaining between defined frames, and the baseline coefficient of variation (CV) for each ROI. The measure as described in the paper is intended for FM dye experiments, where stimulation causes dye and fluorescence loss. However the authors claim the heuristics are adaptable for pHluorin based experiments too.

The user defined weights allow reordering of the detected ROI list, and the quality threshold allows selection of a variable top fraction of that reordered list. The required parameters are left to the user to determine per assay or group of assays of similar characteristics.

7.1.2 Selected algorithm: Fish

Fish et al. (2008) operates on 3D fluorescence images at a single time point. The basic sequence of operations is deconvolution, background subtraction, and iterative thresholding and particle detection at multiple threshold intensity levels with merging of particles of each threshold level with the previous ones. The deconvolution is notable as it causes some Gaussian smoothing of the original image data and so reduces transient point noise.

The authors describe their non-linear approach to selecting threshold levels, favouring a greater proportion of levels targeting the lower part of the intensity range to detect the maximum number of features.

Combining detected particles from multiple threshold levels can cause overlapping objects to be created. Objects are merged only when completely overlapping. The authors suggest using ROI diameters smaller than the features to be detected to avoid this. This makes their algorithm more suitable for synapse counting rather than synapse intensity recording, although the ROI set could be adapted after segmentation to be suitable for intensity recording also by increasing ROI diameter and merging overlapping ROI.

7.1.3 Selected algorithm: Yona

Yona et al. (2011) takes a different segmentation approach than thresholding and particle detection. After background subtraction using a custom algorithm, the algorithm uses a combination of local maxima pixel detection, shape filtering and quality filtering. The user may then pick a selection quality threshold.

Local maxima within the image are selected. Each local maximum is then checked to see if it appears as the peak in a bell curve in at least one of four directions cutting through the local maximum; horizontally, vertically or diagonally in both directions. If at least one of these curves is bell shaped, then the local maximum is taken to be the peak of a suspected synapse.

Quality filtering is based on the intensity variance in the region around the maximum. Synapses are expected to have a high regional variance, as opposed to synapses out of focus, or other sources of fluorescence such as cell nuclei. This variance measure is expressed as the variance of the region around the synapse divided by the sum of the intensities in the region to cope with regional intensity differences remaining after background subtraction. The scores are normalised to linearise the quality measures between potential target synapses to generate a more user friendly score.

Local maxima may potentially be combined as local maxima may come from the same synapse due to local fluctuations in brightness within the synapse. The algorithm uses a combination of contour finding and filtering formulae to classify maxima originating in the same synapses.

Finally the algorithm uses the same contour information to delimit the size and shape of each synapse.

7.1.4 Alternative tool: SynD (Schmitz)

SynD (Schmitz et al., 2011) is a Matlab based tool which, among other functions, can detect synapses from images of *in vitro* neurons. It uses similar methods of synapse detection to the above algorithms, but additionally filters synapse selection by proximity to previously identified neurites. The neurite identification and location requires soma of the neurons to be identified. This approach works well for the examples given in the original paper, and the studies citing the tool as part of their image analysis methodology (Kannan et al., 2016; Luchkina et al., 2017, for example). However it is not suitable for the bulk of the image data in this work as soma are not readily identifiable in the images used. This prevents the correct execution of the SynD algorithm. Therefore, this tool was not among those used for comparison.

7.1.5 Alternative algorithm: Difference of Gaussians (Iwabuchi)

Iwabuchi et al. (2014) is a good discussion of using difference of Gaussians with synaptic fluorescent puncta as a means of background subtraction to improve the signal from the synapses. The method is covered in some detail, and there are interesting automated and semi-automated heuristics for parameter estimation and verification.

The authors note that in practice a more commonly used algorithm, rolling ball, produces better results in some circumstances than difference of Gaussians.

As this work does not focus on the choice of background subtraction algorithm, the algorithm remained out of scope for this study.

7.1.6 Summary of algorithm features

At an abstract level all of these approaches have similarities, summarised in Table 7.1. There is generally a requirement for background subtraction before particle segmentation. The approaches which explicitly deal with time-series data also have a frame registration step.

There is a low level feature detection stage, either using thresholding and particle detection, or finding local maxima within the image frame.

After potential ROIs are discovered, there may be a further quality filtering step to discard poor ROIs (either not features of interest, or with excessive noise) from the ROI set. Depending on the algorithm, this filtering is based on local features within the segmentation frame, or using the intensity trace of the ROI over the time-series of the data.

Table 7.1: Original segmentation algorithm feature summary.

	Bergsman	Fish	Yona
General features			
Base data type	2D time-series	3D single time-point	2D single time-point
Background subtraction	Yes (custom algorithm)	Yes (unspecified)	Yes (custom algorithm)
Time-series registration	Yes (translation only)	No	No
Low level detection			
Threshold and analyse particles	Yes linear thresholds	Yes non-linear thresholds 3D particle detection	No
Local maxima	No	No	Yes
Quality filtering			
Single frame features	No	No	Yes
Time-series features	Yes	No	No

The detection and quality filtering stages have input parameters which must be correctly fitted to the image data. These parameters are summarised in Table 7.2. Note that for the purposes of this comparative study additional parameters in the background subtraction and image registration stages are not included. As shown in the table, the Bergsman algorithm in particular requires careful calibration to work with image data. While some of these parameters are readily available given knowledge of the experimental protocol (the quality time point selection and particle dimensions), and others are advised to leave constant (the threshold level count), some parameters require manual intervention to set effectively (the quality weights and thresholds). This is a time consuming process, prone to missing the optimal settings.

Table 7.2: Original segmentation algorithm parameter summary.

	Bergsman	Fish	Yona
Low level detection			
Min/max threshold	Yes	No	No
Min/max particle size	Yes	No	No
Quality filtering			
Frame indices	Baseline and destain frames	No	No
Quality score weights	CV, Slope and Destain weights	No	No
Quality threshold value	Yes	No	Yes

7.2 Opportunities for improvement

The goal of this work is to evaluate the effectiveness of the existing algorithms in processing sample test datasets covering a range of fluorescence markers and experiment protocols. The ROI sets generated by automated segmentation were scored against pre-existing manually segmented ROI sets.

The various possibilities for algorithm tuning were tried with all of the segmentation implementations, including choice of source image, algorithm parameters, and quality thresholds if used by the algorithm.

The outcome of the work is to supply a choice of algorithm, source image and parameter set which produce high quality ROI sets for a given experimental protocol. Where this is not possible, for example when segmenting a new experimental protocol, the work provides software to determine the best choices for a group of assays if provided with manually segmented ROI sets of a subset of the assays.

7.2.1 Static image frames for segmentation

Of the methods discussed above, only Bergsman explicitly discusses segmentation of time-series image data, and does not specify which frame or frame range is best for segmentation. The example given in the paper chooses the start frames of an FM dye imaging dataset, where the dye concentration is highest.

There are a number of choices of frames in a time-series which could potentially give the best quality segmented ROI set. Options include maximum or average intensity z-projections of either the entire time-series or a subset of the frames. Bergsman takes the approach of using an average z-projection of a number of contiguous frames to suppress transient noise.

7.2.2 Activity-dependent image frames for segmentation

In addition to choosing arbitrary frame ranges or projections of the full time-series, this study adds frame ranges where activity has been known to take place. This is a choice of images where the synaptic puncta are expected to be fluorescing more brightly in response to stimulus. This can be either electrical or chemical stimulus, with electrical stimulus expected to be more localised to synapses. This of course depends on the fluorescent marker and the experiment protocol in effect.

For FM dye based imaging experiments the best frame range would be the time of peak dye content in the image, usually at the start of the experiment, as shown in the example in the Bergsman study. For pHluorin and similar markers, the best activity response is expected immediately after an electrical stimulus or an ammonium pulse.

This is the common approach taken during manual segmentation. The researcher chooses ROIs on an image frame where the synapses are most clearly visible. The activity recording frame ranges are frequently the same for all assays within an experiment, so are easy to add to the assay metadata for batch processing.

7.2.3 Activity-dependent difference images for segmentation

Existing segmentation methods look primarily for static features at the image analysis stage; bright spots of the correct size and shape. This process should detect the synapses in the image if an appropriate frame or z-projection from the time-series is used. However there are also a lot of non-active synapse features included. These additional features must be filtered out using methods including those described previously to increase the quality of the mean trace intensity from the created ROI set.

However, adding knowledge of the timing of stimuli also allows the use of difference images. These are images created by subtracting averaged images prior and post stimulus. The difference in intensity between these frame ranges should be primarily caused by reaction to the stimulus, so the difference image should therefore highlight the active synapses with other fluorescing features less visible. There may be other reasons for the change, including simple noise and perhaps bleaching effects. However the remaining difference should be activity driven, and given the morphology of synapses, the signals of interest should still be punctate, and therefore amenable to the same detection methods as used for synapses in the static images. This should make difference frames a good choice for physiologically relevant ROI segmentation, and has been used in the past as a base image for manual segmentation in some studies (Granseth et al., 2006). Ideally, the interval between the before and after stimulus ranges should be small to reduce the effect of non-stimulus caused fluorescence change.

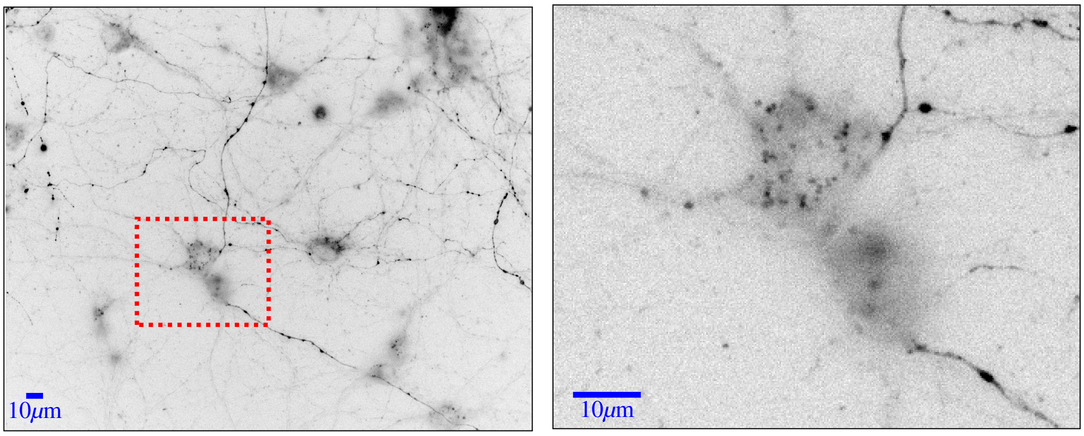

(a) Full image. (b) Zoomed area.

Figure 7.1: Frame from original time-series data. (b) shows the highlighted region of (a). Original data collected by Katherine Bonnycastle.

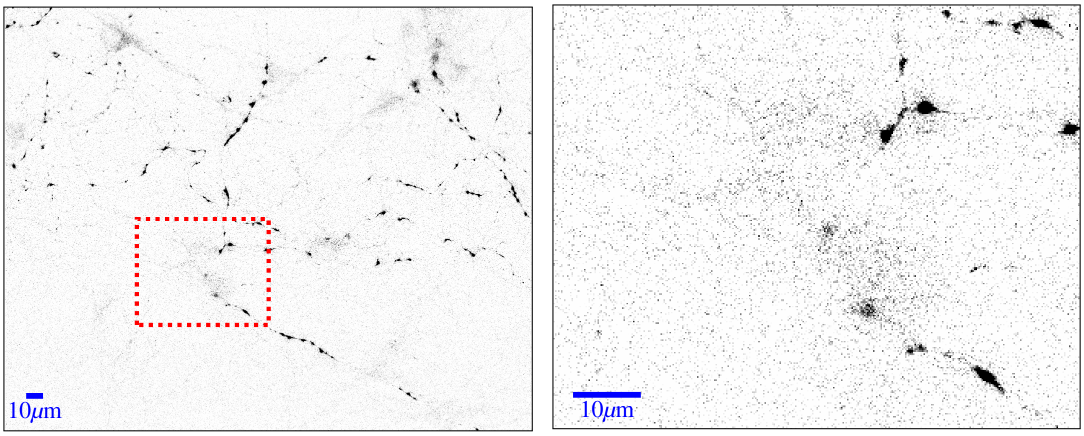

(a) Full image. (b) Zoomed area.

Figure 7.2: Difference of base and peak average images. (b) shows the highlighted region of (a). Original data collected by Katherine Bonnycastle.

If two such difference regions can be identified in an experimental protocol, which is a common experimental approach when the magnitude of stimulus response must be normalised against another stimulus type, then the work allows for a second difference image.

This work tests the usefulness of difference images as the source images for segmentation using the described algorithm. In addition, the use of pairs of difference images are tested; perhaps unions or intersections of two ROI sets generated from the same time-series image have higher quality than the other possibilities for automated segmentation (Figure 7.3).

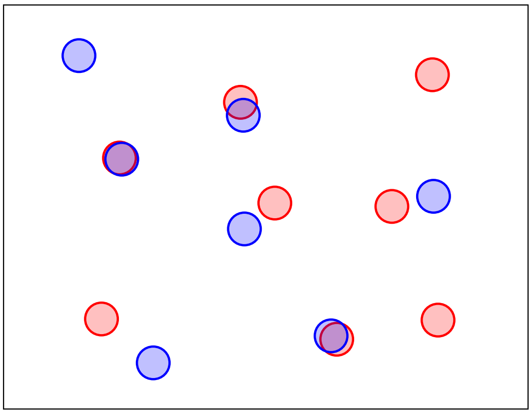

(a) Two ROI sets (Red and Blue) with some overlapping ROIs.

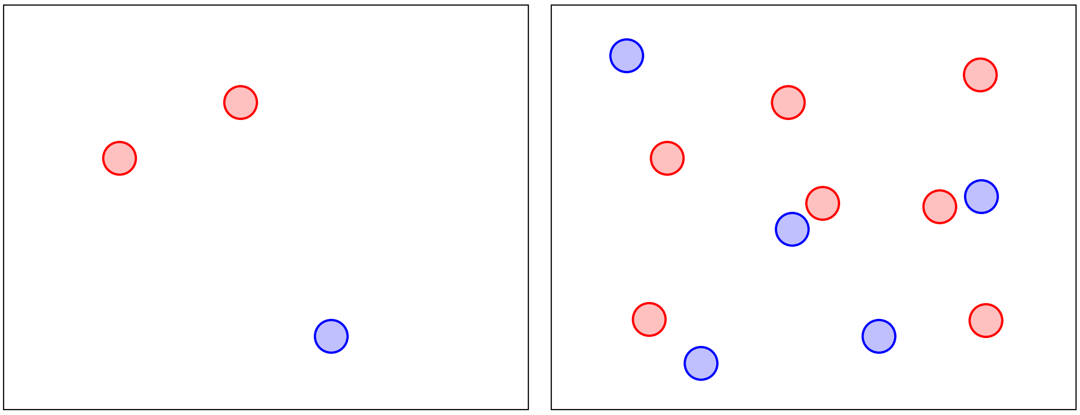

(b) Intersection of ROI sets (Red ∩ Blue) - only the overlapping ROIs are selected.

(c) Union of ROI sets (Red ∪ Blue) - all ROIs are selected.

Figure 7.3: Given two sets of ROIs (Red and Blue), the intersection Red ∩ Blue contains only the ROI locations common to both sets, and the union Red ∪ Blue contains the ROI locations in either set. In the case of overlapping ROIs, only the ROI with the highest intensity is retained.

7.2.4 Summary of segmentation images available

There are potentially eight images of interest that could be used for ROI segmentation for a time-series image:

1. **Overall Max**: Z-projection of the entire time-series to record maximum intensity per pixel
2. **Overall Mean**: Z-projection of the entire time-series to record average intensity per pixel

3. **Diff1 Start**: Z-projection of the region just before the stimulus to record average intensity per pixel
4. **Diff1 End**: Z-projection of the region just after the stimulus to record average intensity per pixel
5. **Diff1**: Difference image of the z-projections before and after the stimulus

Where a secondary stimulus is available in the time-series:

6. **Diff2 Start**: Z-projection of the region just before the second stimulus to record average intensity per pixel
7. **Diff2 End**: Z-projection of the region just after the second stimulus to record average intensity per pixel
8. **Diff2**: Difference image of the z-projections before and after the second stimulus

Having two stimuli also allows two additional aggregate ROI sets to be constructed as described above.

1. **Diff1** $\cup$ **Diff2**: Union of ROI sets from difference images of first and second stimuli
2. **Diff1** $\cap$ **Diff2**: Intersection of ROI sets from difference images of first and second stimuli

Overall, this allows ten potential ROI sets to be constructed per time-series dataset. The choice of which is better in which circumstances is evaluated. The image names listed above are those shown in the results later in this chapter.

7.2.5 Algorithm input parameters and quality thresholds

As shown in Table 7.2, the algorithms have a number of input parameters, each with the potential to affect the quality of the generated ROI set. Performing an exhaustive search covering the entire parameter space is prohibitive, and the effects of dependence between the parameters is difficult to predict.

However, Metropolis-Hastings sampling of the parameter space per assay and segmentation image could potentially uncover some general constraints on the parameter choices. This process is further described in Section 7.3.3.

7.3 Methods

7.3.1 Image data sets

A test data set from the same source as used in the ROI drift study in Chapter 6 was reused. To recap, a number of experiment types with image data fitting certain criteria were chosen, each with at least $n = 4$ assays (Table 7.3). The criteria were chosen to ensure a fair and consistent trial of the algorithms, and the experiment types were chosen to test a variety of fluorescence markers and experimental protocols. The test criteria were:

- Time-series images of image format 16-bit grayscale (file format is not relevant).
- Matching filtered manual ROI sets using only 5x5 pixel circular ROIs.
- Confirmation of the registration mode used for the manual ROI selection.

The first two criteria allow substantial performance optimisations to be made to the processing. The last criterion ensures the automated segmentation is working to the same registered time-series as was used for manual selection of ROIs.

Assays for both control and tested experimental conditions were chosen. The segmentation would be used to compare both assay types without bias, so the automated segmentation should be able to handle both test and control assays equally within an experiment. Subject to the segmentation possible given the actual experiment, as an experiment designed to inhibit vesicle recycling may show fewer active synapses.

Table 7.3: Test image data sets used in the study. A range of fluorescent markers were included to provide 20 FM dye assays and 16 pHluorin assays.

Category	Experiment	Marker	Assay count
FM dye	FM dye 1	FM1-43/FM2-10	8
	FM dye 2	FM1-43	12
pHluorin	pHluorin 1	sypHy	4
	pHluorin 2	VAMP4-pHluorin	4
	pHluorin 3	sypHy	4
	pHluorin 4	sypHy	4

7.3.2 Re-implementations of selected algorithms

The segmentation algorithms presented in the papers discussed above were reimplemented to run using the features available in ImageJ, within a custom batch assay processing application. This allows direct comparison of each method using the test set. Preprocessing steps not directly part of the segmentation process, such as the custom image registration stage of Bergsman were left out, as all methods would start with the same preprocessed image data, in this case, already registered images.

The re-implementations were necessary as the described algorithms were either not published as tools, or published as tools for non-ImageJ systems, such as Igor Pro. Again, the implementations are named after the first authors of the respective papers for convenience, although the implementations may have some changes to the original described algorithms to be suitable for this study.

For simplicity, and to reduce the sources of variability between the algorithms, each segmentation image is segmented by each algorithm in either its original format, or with rolling ball background subtraction of a fixed radius of 20 pixels applied. The custom background subtraction algorithms described in the source papers are not used.

7.3.2.1 Yona

The implementation makes use of the local maxima selection and filtering parts of the Yona algorithm. The contour mapping and area determination parts of the algorithm are not required as the target ROIs are circles of 5x5 pixel fixed size to match the manually segmented ROIs. This means that the original handling of multiple nearby maxima was replaced with the same overlap handling code as used in the other implementations below, with higher quality local maxima getting priority in the case of overlap.

The authors did not describe the details of the bell-like filter for synapses. The implementation in this study has taken it to mean that the curve is monotonically decreasing as it moves away from the local maximum peak for a minimum distance.

The original algorithm used a normalisation power to linearise the distribution of ROIs over the quality range 0-1, rather than have the majority occupying only a small part of that range. This normalisation power was dependent on the image data being segmented. To avoid adding another parameter to tune for each segmentation image, the implementation here just uses the parameter value $n = 6$ as suggested in the paper. Quality selection is instead based on a simple fraction of the segmented ROI. For example, a quality threshold of 0.8 selects only the highest quality 20% of the available ROIs.

7.3.2.2 Bergsman

The image registration stage in Bergsman was not used, as the segmentation must work with the same image registration as used for the manual segmentation.

The segmentation stage was implemented using code based on the `ParticleAnalyser` class of ImageJ. This provides the choice of minimum and maximum pixel areas of each segmented particle. Additionally, the class provides a minimum circularity measure to filter based on the shape of the particle. This parameter was added to the parameter set for this algorithm.

The segmentation minimum threshold was replaced by the similar brightness fraction of the image. The threshold level count was fixed at 30 to match the other threshold based segmentation algorithm. The threshold levels were linearly equidistant as in the Bergsman paper. A range of different maximum particle cut-offs per level including unlimited particles were tested.

Rather than having an additional set of parameters for the destain frame indices, these were taken to be the midpoint of the difference image start ranges, as for FM dye based assays that would be the appropriate destain frame to use.

The quality score was implemented as described in the source paper. The quality threshold selects a ratio of available quality ordered ROIs as described for Yona above.

7.3.2.3 Fish

This implementation is a hybrid of the original Bergsman and Fish algorithms. The segmentation stage is similar in operation to the Bergsman implementation above, with the difference that the threshold levels are not linearly but log equidistant. This differs from the original algorithm described in the paper which uses a geometric spacing between threshold levels. The end results are similar, with more of the threshold levels at the lower end of the intensity range. As with the Bergsman implementation above, a range of maximum particle cut-offs per threshold level were tested.

The segmentation size parameters were fixed values in the original Fish implementation, but their values were designed for 3D features. This implementation leaves them as configurable parameters.

There is no quality filtering stage.

7.3.3 Optimum parameter selection

For a fair comparative evaluation of the capabilities of the algorithms, those with parameters are scored at their optimal parameter values for each assay, as much as is practical with sampling. There are three groups of parameters: those required for low level detection of potential ROIs within the segmentation image; those used to determine quality scores using the time-series intensity traces of each potential ROI; and a final quality threshold to select a subset of the potential ROIs.

The first group have values selected using a random walk Metropolis-Hastings sampling algorithm. In brief, a set of parameter values $\mathbf{x}'$ for the segmentation algorithm is selected from the proposal distribution $q(\mathbf{x}'|\mathbf{x})$ where $\mathbf{x}$ is the previous set of parameter values. The initial parameter value set is taken largely from Bergsman et al. (2006). The proposal distribution samples each of the parameters in turn using a symmetric Gaussian distribution for each centred on their current value (Table 7.4).

$$q(\mathbf{x}'|\mathbf{x}) = \mathcal{N}(\mathbf{x}'|\mathbf{x}, \sigma^2)$$

The test image is then segmented with the chosen algorithm and the resulting ROIs scored as described in Section 7.3.4 to produce $\mathrm{Score}(\mathbf{x}')$. The proposed parameter set $\mathbf{x}'$ is accepted as the current parameter set $\mathbf{x}$ stochastically with an acceptance probability r

$$r = \min\left(1, \frac{\mathrm{Score}(\mathbf{x}')}{\mathrm{Score}(\mathbf{x})}\right)$$

So $\mathbf{x}'$ is accepted if $\mathrm{Score}(\mathbf{x}') > \mathrm{Score}(\mathbf{x})$ with probability 1, and with decreasing probability as $\mathrm{Score}(\mathbf{x}')/\mathrm{Score}(\mathbf{x})$ tends to 0.

The process is repeated selecting the next parameter in the set to modify. The algorithm is run for 100 iterations on each assay-algorithm-image combination.

Table 7.4: Proposal distribution value ranges. The standard deviation (σ^2) used for the Gaussian distribution $\mathcal{N}(\mathbf{x}'|\mathbf{x},\sigma^2)$ was taken to be a tenth of the full parameter range. Minimum and maximum particle sizes are linked to prevent invalid inputs to the particle detection algorithm.

Parameter	Minimum value	Maximum value	σ^2
Brightest Image Fraction	0	0.9	0.1
Minimum particle size	1	current maximum particle size	10
Maximum particle size	current minimum particle size	100	10
Minimum particle circularity	0	1	0.1

The second group (within the Bergsman algorithm) is again selected using random walk Metropolis-Hastings sampling for each sample generated by the first Metropolis-Hastings sampler above. Again, 100 iterations are used to survey the parameter space. The proposal distribution parameter ranges are given in Table 7.5, and again the initial proposal distribution is taken from Bergsman et al. (2006).

Table 7.5: Bergsman weighting proposal distribution value ranges for the Bergsman quality score weights: Slope, Coefficient of Variation (CV) and Destain. The standard deviation (σ^2) used for the Gaussian distribution $\mathcal{N}(\mathbf{x}'|\mathbf{x},\sigma^2)$ was taken to be a tenth of the full parameter range.

Parameter	Minimum value	Maximum value	σ^2
Slope	-50	50	10
CV	-50	50	10
Destain	-50	50	10

Finally, the quality threshold is simply scanned over its full range for each of the iteration outputs above. Rather than having an arbitrary quality threshold, as both Yona and Bergsman have non-linear quality distributions, the implementation selects quality thresholds to produce 20 ROI subsets of linearly increasing size.

The relatively low iteration count of the Metropolis-Hastings samplers is offset in part by the fairly broad proposal distributions used, giving a broad coverage of the parameter space. Each iteration is computationally intensive, and each segmentation source image produces over 200,000 samples (Table 7.6). Even with the performance optimisations included in the implementation, a larger number of iterations would not be practical.

In addition, the algorithms using particle detection (Bergsman and Fish) have limits on particles detected per threshold level, as used by Bergsman. Threshold and detect ends as soon as a threshold level exceeds a defined number of detected particles. The evaluation is run for seven limit values; 50, 100, 200, 500, 1000, 5000 and unlimited particles per threshold level.

Table 7.6 summarises the parameter sets required by the algorithm test implementations.

Table 7.6: Adapted segmentation algorithm parameter summary with value ranges.

	Bergsman	Fish	Yona
Low level detection (as Metropolis-Hastings sampling)			
Threshold minimum	Yes	Yes	No
(brightest fraction of image)	(0.0 - 1.0)	(0.0 - 1.0)	
Min/max particle size	Yes	Yes	No
(pixels)	(1 - 100)	(1 - 100)	
Min particle circularity	Yes	Yes	No
(described in Section 3.3.5)	(0.0 - 1.0)	(0.0 - 1.0)	
Threshold particle limit	Yes	Yes	No
(particles)	(50-unlimited)	(50-unlimited)	
Quality weighting (as Metropolis-Hastings sampling)			
Frame indices	Baseline and destain frames	No	No
(frame indices)	(fixed from existing metadata)		
Quality score weights	CV, Slope and Destain weights	No	No
(arbitrary units)	(-50.0 - 50.0)		
Quality thresholding (as iterative sampling)			
Quality threshold value	Yes	No	Yes
(fraction of detected ROIs)	(0.0 - 1.0)		(0.0 - 1.0)
Total parameter count	8	4	1
Total samples per image	200,000	100	20

7.3.4 Score metrics

The following metrics were used both for scoring the individual methods, and providing the Metropolis-Hastings acceptance probability during parameter inference. The choice of metrics was designed to favour automated segmentation results which were similar in content to the manually segmented ROI sets. Multiple scores were used to target different properties of the manual ROI sets, and a weighted sum of the component scores was used as the final quality score. Each of the component scores had values in the range from 0 to 1, with higher values signifying better quality segmentation.

- Score 1: fraction of ROIs in manual ROI set discovered by auto segmentation.

  $$\text{Score1} = \frac{\text{matched manual ROIs}}{\text{total manual ROIs}}$$

  ROIs are considered matched if an auto ROI centre is within the radius of a manual ROI. As the work in Chapter 6 discovered, the ROI centres following ROI drift are on average one pixel from the manually segmented ROI centre. Centres of manual and automated segmentation of the same synapse are likely to be within one ROI radius of each other. The score is a linear measure from 0 to 1.

- Score 2: difference between the mean $\Delta F/F0$ intensity traces of the manual and automated ROI sets. This is the difference between manual and automated mean trace values for each frame of the time-series, averaged over the full time-series. To normalise the score within 0 and 1, the mean difference is divided by the full range of both time-series.

  $$\begin{aligned}\text{mean difference} &= \frac{\sum_{t=1}^{T}|x_t - y_t|}{T} \\ \text{max range} &= \max_{t=1}^{T}(\max(x_t, y_t)) - \min_{t=1}^{T}(\min(x_t, y_t)) \\ ||\text{mean difference}|| &= \frac{\text{mean difference}}{\text{max range}} \\ \text{Score2} &= 1 - ||\text{mean difference}||\end{aligned}$$

  where T is the number of frames in the time-series image, x_t, y_t are the values at frame t for the manual and automated mean intensity traces respectively.

- Score 3: ROI count. Score 1 without correction rewards an algorithm which picks a very large number of ROIs, as each segmented ROI may potentially match a manually segmented ROI. To prevent this, large numbers of ROIs are penalised. Automated ROI counts between one and five times that in the manual ROI set are considered ideal, and automated ROI counts outside this range are penalised.

  $$\text{Score3} = \begin{cases} \frac{N_x}{N_y} & N_x < N_y \\ 1 & N_y \leq N_x \leq 5N_y \\ 1 - \frac{N_x - 5N_y}{5N_y} & 5N_y < N_x < 10N_y \\ 0 & 10N_y \leq N_x \end{cases}$$

  where N_x and N_y are the numbers of ROIs from automated and manual segmentation respectively.

The three score metrics favour auto segmentation which is a superset of the manual ROIs, with similar overall intensity trace profiles.

An additional score metric was considered, the variance of the intensity traces of the segmented ROI set. On the assumption that the data distribution for good ROI is uni-modal, the variance of the result time traces should be small for a good ROI set. However, evaluation of the existing manually segmented ROI traces shows high levels of variance within some ROI sets, and indeed some recent work has revealed bimodal intensity trace results in some instances (Nicholson-Fish et al., 2015).

The final score metric is the weighted sum of the individual scores, with additional weight given to finding the manually segmented ROIs, balanced with additional weight given to penalising excessive numbers of segmented ROIs.

$$\text{Score} = 2 \times \text{Score1} + \text{Score2} + 2 \times \text{Score3}$$

This gives a final score in the range 0 to 5, with higher scores signifying better automated segmentation results.

7.3.5 Test image processing

For each assay of the test set, the 8 types of images described in Section 7.2.4 were generated, along with background subtracted versions (using a rolling ball algorithm with a radius of 20 pixels). For each of these images, the three segmentation algorithms were attempted using parameter sampling as described in Section 7.3.3. When two difference images were available, the ROI set aggregations described in Section 7.2.4 were also created. Each sample result was scored and recorded.

7.3.6 Results processing

For each assay/algorithm/image combination, the result with the highest score is retained. These results are then aggregated over all assays in the assay group, giving an $n \geq 4$ assays for each category. These represent the near optimal results per experiment for each algorithm and image type. Results tables then compare the scores across segmentation image, algorithm and experiment type. Parameter ranges for these best scores are also aggregated over all assays in each assay group.

An additional step of processing is required for the Bergsman quality weights. The value ranges for Slope, Destain and CV are similar to those presented in the original paper. However as the overall quality score can be scaled without impacting the ordering of ROIs, it is possible to normalise the weights. The normalised weights are

$$(\text{Slope}', \text{Destain}', \text{CV}') = \frac{(\text{Slope}, \text{Destain}, \text{CV})}{\sqrt{\text{Slope}^2 + \text{Destain}^2 + \text{CV}^2}}$$

This places the quality weight tuples on the surface of a sphere of unit radius, making visualisation of trends in parameter choice easier. The centroid of these normalised points is the most reasonable mean weight tuple to use for subsequent testing, as long as it is not at the point $(0,0,0)$. Note that this centroid does not need to be scaled to the surface of the unit sphere to weight Bergsman ROIs.

7.3.7 Testing suggested parameter sets

The mean parameter values of the top scores for each assay-algorithm-image combination were taken per experiment, and segmentation retried for the test datasets using these fixed parameter sets. The segmentation results were also processed as described above.

7.3.8 Implementation constraints

For the purposes of this study, the choice of test data has allowed some optimisations to be made to improve processing speed. In summary:

- ROI size and shape has been fixed as a circle of diameter 5 pixels. This matches the dimensions of the ROI in the manually segmented ROI sets for a large subset of the existing assay data.
- Background subtraction was chosen to be a standard rolling ball algorithm of radius 20 pixels. The test segmentation algorithms were run either with these background subtracted images, or with the original images.
- Image registration was that used for the manual segmentation. This allows for the closest match between automated and manual segmentation environments

Any loss in flexibility of the general image segmentation case was not relevant for this comparative study. A more detailed description of the software implementation is given in Appendix A.

7.4 Results

Tables 7.7 and 7.8 list the parameter, algorithm and particle detection limit combinations of the highest scoring 30 result sets. Figure 7.4 shows the ROIs of a highly scoring pHluorin experiment result.

When interpreting the total score for a particular automated segmentation run, a score > 4.0 is taken to be good, > 3.8 is taken to be reasonable, with 5.0 being the maximum score possible. Results have shown that the means difference score of optimum parameter sets is in the range $0.7 - 1.0$, so a score of $2.7 - 3.0$ is achievable without matching any of the manually segmented ROIs. A score > 4.0 means at least half of the manually segmented ROIs must have been found by automated segmentation, with the total number of segmented ROIs within an order of magnitude of the manual ROI set.

Table 7.7: pHluorin ranked scores of image and algorithm combinations. The '-BS' suffix represents the named algorithm operating on the background subtracted image. Scores are given as mean and (standard deviation) of the highest score of each of the assays in the pHluorin test group for the algorithm/image combination.

Rank	Score	Limit	Algorithm	Image
1	4.37 (0.33)	200	Fish	Diff2
2	4.36 (0.30)	100	Fish-BS	Diff2
3	4.36 (0.31)	100	Fish	Diff2
4	4.35 (0.33)	200	Fish-BS	Diff2
5	4.29 (0.22)	200	Bergsman	Overall Max
6	4.26 (0.43)	100	Fish-BS	Diff1 ∪ Diff2
7	4.26 (0.25)	50	Fish-BS	Diff1 ∪ Diff2
8	4.26 (0.22)	50	Fish	Diff1 ∪ Diff2
9	4.24 (0.50)	100	Fish	Diff1 ∪ Diff2
10	4.23 (0.34)	200	Bergsman-BS	Overall Max
11	4.23 (0.35)	500	Fish-BS	Diff2
12	4.22 (0.42)	200	Fish-BS	Overall Max
13	4.21 (0.20)	100	Fish-BS	Overall Max
14	4.21 (0.37)	200	Bergsman	Diff2
15	4.19 (0.29)	500	Bergsman-BS	Overall Max
16	4.19 (0.37)	100	Fish-BS	Diff2 End
17	4.19 (0.25)	50	Fish-BS	Diff2
18	4.19 (0.45)	200	Bergsman-BS	Diff2
19	4.19 (0.30)	200	Bergsman-BS	Diff2 End
20	4.17 (0.21)	100	Fish	Overall Max
21	4.17 (0.42)	200	Fish-BS	Overall Mean
22	4.17 (0.33)	500	Bergsman	Overall Max
23	4.16 (0.28)	50	Fish	Diff2
24	4.16 (0.45)	500	Bergsman	Diff2
25	4.16 (0.34)	1000	Bergsman	Diff2
26	4.15 (0.56)	200	Fish-BS	Diff2 End
27	4.15 (0.49)	1000	Fish-BS	Diff2
28	4.14 (0.37)	500	Bergsman-BS	Diff2
29	4.14 (0.55)	100	Bergsman-BS	Diff1 ∪ Diff2
30	4.14 (0.27)	100	Bergsman	Overall Max

Table 7.8: FM Dye ranked scores of image and algorithm combinations. The ‘-BS’ suffix represents the named algorithm operating on the background subtracted image. Scores are given as mean and (standard deviation) of the highest score of each of the assays in the FM dye test group for the algorithm/image combination.

Rank	Score	Limit	Algorithm	Image
1	3.67 (0.37)	1000	Bergsman-BS	Overall Max
2	3.65 (0.41)	500	Bergsman	Overall Max
3	3.65 (0.40)	500	Bergsman	Diff1 End
4	3.65 (0.41)	5000	Bergsman	Overall Max
5	3.65 (0.38)	500	Bergsman-BS	Overall Max
6	3.64 (0.39)	1000	Bergsman	Overall Max
7	3.64 (0.38)	200	Bergsman	Overall Max
8	3.63 (0.39)	1000	Bergsman	Diff1 End
9	3.63 (0.36)	500	Bergsman-BS	Diff1
10	3.63 (0.41)	500	Bergsman	Diff1
11	3.63 (0.41)	none	Bergsman	Diff1 End
12	3.62 (0.38)	5000	Bergsman	Overall Mean
13	3.62 (0.40)	none	Bergsman	Overall Max
14	3.62 (0.34)	1000	Bergsman-BS	Diff1
15	3.62 (0.38)	500	Bergsman-BS	Diff1 End
16	3.62 (0.36)	5000	Bergsman	Diff1
17	3.62 (0.40)	5000	Bergsman-BS	Overall Max
18	3.61 (0.42)	500	Bergsman	Overall Mean
19	3.61 (0.40)	200	Bergsman	Diff1 End
20	3.61 (0.38)	1000	Bergsman-BS	Diff1 End
21	3.60 (0.42)	none	Bergsman-BS	Diff1
22	3.60 (0.43)	5000	Bergsman-BS	Diff1 End
23	3.60 (0.40)	5000	Bergsman	Diff1 End
24	3.60 (0.39)	5000	Bergsman-BS	Diff1
25	3.59 (0.34)	1000	Bergsman-BS	Overall Mean
26	3.59 (0.39)	1000	Bergsman	Overall Mean
27	3.58 (0.39)	none	Bergsman-BS	Diff1 End
28	3.58 (0.38)	none	Bergsman	Diff1
29	3.58 (0.36)	1000	Bergsman	Diff1
30	3.58 (0.36)	200	Bergsman	Diff1

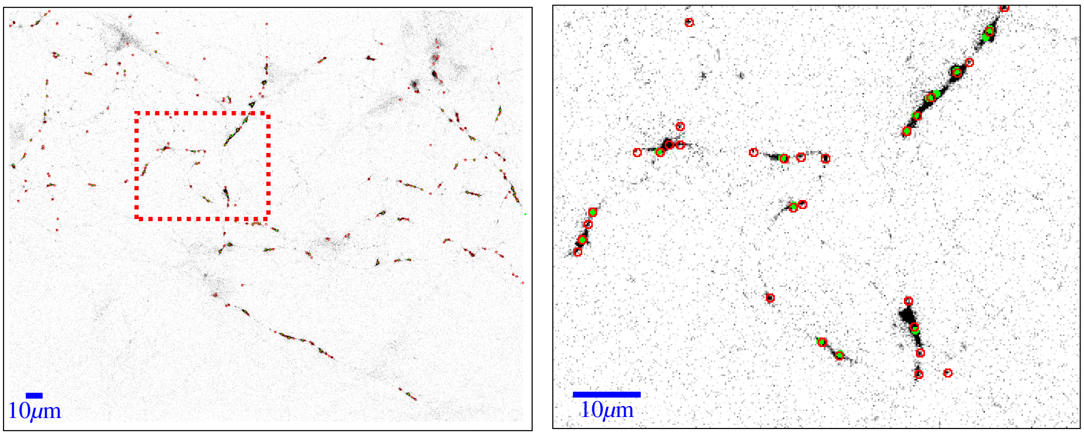

(a) Full image.

(b) Zoomed area.

Figure 7.4: Segmentation result image for a pHluorin assay. (b) shows the highlighted region of (a). Green circles are manually segmented ROIs, red circles are automated segmentation results. Segmentation image was the NH_4^+ difference image, using Fish (particle limit=200). ROI set total score was 4.8. Original data collected by Katherine Bonnycastle.

As can be seen in the ranking tables, the Fish algorithm occurs frequently in the highest ranks for pHluorin experiments, and the Bergsman algorithm appears exclusively in the highest ranking FM dye experiment results. The pHluorin result is surprising as the Bergsman algorithm allows for finer tuning of the output ROI set for each assay with its use of quality weights and threshold. It would have been reasonable to expect Bergsman to rank highly in both experiment types.

However, the low particle detection limits in the highest scoring pHluorin parameter sets offer an explanation. The Fish implementation sets threshold values equally spaced on a logarithmic scale, with more threshold values at the lower end, whereas the Bergsman implementation equally spaces the threshold levels linearly. Lower threshold intensities are likely to cause more particles to be detected, due to the distribution of pixel intensities in the segmentation images. It is likely that the Fish algorithm processes more threshold levels at the lower intensity end of the range before reaching a particle cut-off than the Bergsman algorithm, increasing the quality of the segmented Fish ROI set. This is supported by the optimal mean numbers of ROIs segmented per algorithm shown in Table 7.9.

7.4.1 Automated segmentation performs better with pHluorin experiments

Table 7.10 shows the summary mean total scores for all experiment types, using the particle detection limit that ranks most highly for each experiment type. As can be seen, pHluorin segmentation scores more highly than FM dye segmentation across most algorithm and image choices. In the ranking tables (Tables 7.7 and 7.8) all of the top 30 pHluorin segmentation combinations score above 4.0, whereas the highest scoring FM dye combination has a score of

Table 7.9: ROI Count of pHluorin experiments (particles=200). For comparison, the mean manual ROI count over the same images was 56 (with a standard deviation of 29). Figures in bold show the increased counts for segmented ROIs by Fish over Bergsman algorithms for the highest scoring segmentation image. BS means background subtracted image.

	Bergsman		Fish		Yona	
	Non BS	BS	Non BS	BS	Non BS	BS
Overall Max	162 (68)	157 (76)	243 (99)	227 (111)	172 (124)	168 (120)
Overall Mean	190 (77)	155 (58)	232 (101)	219 (91)	361 (196)	301 (174)
Diff1 Start	176 (60)	157 (48)	269 (99)	202 (71)	172 (127)	174 (129)
Diff1 End	181 (59)	154 (83)	246 (93)	236 (83)	186 (135)	172 (129)
Diff1	128 (66)	135 (62)	185 (90)	181 (94)	2517 (4254)	2517 (4254)
Diff2 Start	176 (77)	141 (64)	242 (91)	223 (113)	173 (135)	169 (131)
Diff2 End	148 (69)	147 (83)	264 (124)	212 (121)	165 (124)	146 (115)
Diff2	**123** (65)	**124** (61)	**208** (109)	**215** (112)	333 (455)	333 (455)
Diff1 $\cup$ Diff2	245 (88)	245 (81)	330 (148)	336 (147)	14307 (13895)	14307 (13895)
Diff1 $\cap$ Diff2	45 (36)	47 (39)	64 (54)	60 (53)	1828 (2923)	1828 (2923)

only 3.67.

This is compelling evidence that when able to optimise parameters for individual assays, the tested segmentation implementations are much more useful for pHluorin based imaging work.

7.4.2 Activity located frame ranges are good choices for segmentation with chosen algorithms

Activity located frame ranges are those showing either chemical or electrical stimulus. In this test set, the images *Diff1 End* and *Diff2 End* for pHluorin experiments, and *Diff1 End* for FM dye based experiments, and excluding the difference images *Diff1* and *Diff2* discussed in the next section. As can be seen from Figures 7.5 and 7.6, there is a consistent trend towards higher scores when these activity located images are used for segmentation. Segmenting images showing the NH_4^+ pulse in pHluorin experiments appears particularly effective.

When ranking the image-algorithm results (Tables 7.7 and 7.8) activity based images rank highly in both experiment types, although more notably for pHluorin experiments.

7.4.3 Difference images are good segmentation choices in some experimental protocols

Difference images of activity located frame ranges are the images *Diff1* and *Diff2* for pHluorin experiments, and *Diff1* for FM dye based experiments. As can be seen from Figures 7.5 and 7.6, there is also a consistent trend towards higher scores when these difference images are used for segmentation. Again, segmenting images showing the NH_4^+ pulse in pHluorin experiments

Table 7.10: Total scores for both FM dye and pHluorin experiment types broken down by algorithm and image. Each value shown is the mean (and standard deviation) of the best scoring segmentation parameter combination for each assay of that category. BS means background subtracted image. No FM dye entries have a score exceeding 4.0 and so are not considered good results, whereas 16 of the pHluorin entries exceed 4.0 and are considered good results, shown in bold.

	Bergsman		Fish		Yona	
	Non BS	BS	Non BS	BS	Non BS	BS
FM dye (particles = 1000)						
Overall Max	3.64 (0.39)	3.67 (0.37)	3.24 (0.54)	3.2 (0.45)	2.79 (0.55)	2.77 (0.53)
Overall Mean	3.59 (0.39)	3.59 (0.34)	3.29 (0.64)	3.13 (0.52)	2.77 (0.53)	2.74 (0.45)
Diff1 Start	3.43 (0.28)	3.42 (0.32)	3.18 (0.58)	3.09 (0.52)	2.74 (0.65)	2.7 (0.59)
Diff1 End	3.63 (0.39)	3.61 (0.38)	3.26 (0.61)	3.14 (0.51)	2.81 (0.55)	2.79 (0.51)
Diff1	3.58 (0.36)	3.62 (0.34)	3.24 (0.65)	3.31 (0.66)	3.06 (0.8)	3.06 (0.8)
pHluorin (particles = 200)						
Overall Max	**4.29** (0.22)	**4.23** (0.34)	**4.12** (0.52)	**4.22** (0.42)	3.81 (0.67)	3.84 (0.69)
Overall Mean	**4.12** (0.2)	**4.13** (0.22)	3.9 (0.61)	**4.17** (0.42)	3.7 (0.73)	3.69 (0.72)
Diff1 Start	3.68 (0.28)	3.73 (0.29)	3.56 (0.73)	3.7 (0.53)	3.36 (0.49)	3.36 (0.49)
Diff1 End	3.8 (0.24)	3.75 (0.3)	3.71 (0.55)	3.86 (0.45)	3.48 (0.5)	3.5 (0.45)
Diff1	3.67 (0.46)	3.51 (1.03)	3.72 (0.45)	3.71 (0.49)	2.48 (0.93)	2.48 (0.93)
Diff2 Start	3.75 (0.37)	3.74 (0.42)	3.67 (0.67)	3.89 (0.42)	3.34 (0.7)	3.34 (0.68)
Diff2 End	**4.1** (0.36)	**4.19** (0.3)	**4.01** (0.74)	**4.15** (0.56)	3.79 (0.63)	3.75 (0.69)
Diff2	**4.21** (0.37)	**4.19** (0.45)	**4.37** (0.33)	**4.35** (0.33)	2.54 (1.45)	2.54 (1.45)
Diff1 ∪ Diff2	**4.03** (0.72)	3.93 (0.72)	3.89 (0.73)	3.84 (0.65)	1.82 (0.42)	1.82 (0.42)
Diff1 ∩ Diff2	2.98 (1.05)	2.94 (1.08)	3.19 (1.01)	3.08 (1.03)	1.69 (0.99)	1.69 (0.99)

appears particularly effective. The difference images work best with the threshold-and-detect based algorithms, Bergsman and Fish. Results show that the Yona implementation is poorly suited to work with difference images.

When ranking the image-algorithm results (Tables 7.7 and 7.8) difference images rank highly in both experiment types, again particularly for pHluorin experiments.

7.4.4 Some aggregations of difference image segmentation results perform well

It was conjectured that aggregating the results of two difference image ROI sets, either by creating a union or an intersection of the two ROI sets, would create a higher quality ROI set

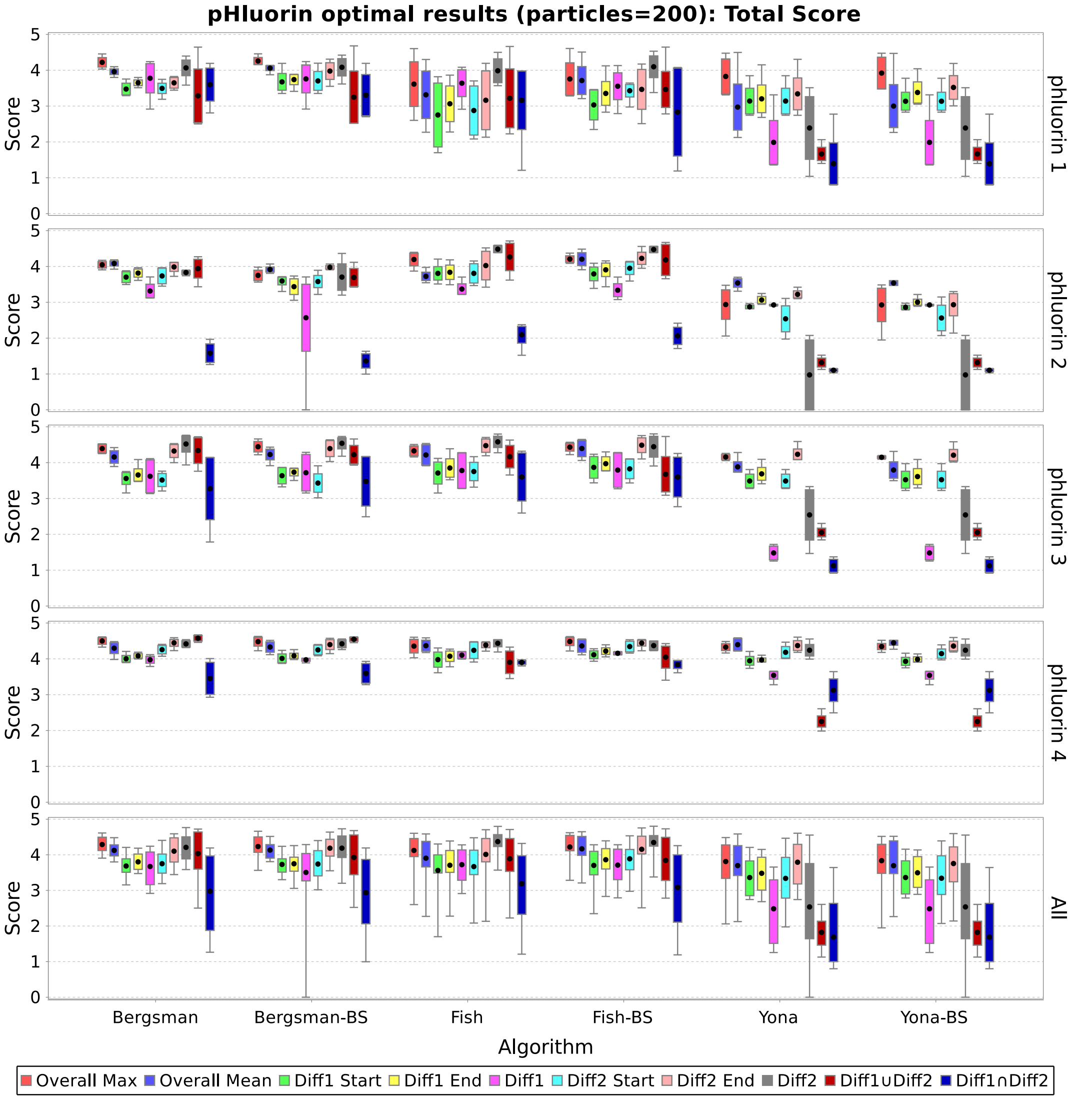

Figure 7.5: Total scores for best parameter choices with pHluorin assays. Boxes show interquartile ranges, lines show maxima and minima, and black dots show mean values for each combination of experiment, image and algorithm. Bergsman and Fish algorithms using difference images and activity located images have good mean scores (> 4.0).

overall. In the case of the pHluorin experiments, the union of difference frames performed well using the Fish algorithm with a particle detection limit of 200 (Figure 7.5). The union of differences choice for segmentation appears a number of times in the top ranked scores. The intersection of differences however does not perform well, as the resulting ROI set count is low for both Bergsman and Fish algorithms (Table 7.9).

Union and intersection of difference images for FM dye experiments were not available as the FM assays had only one defined difference image.

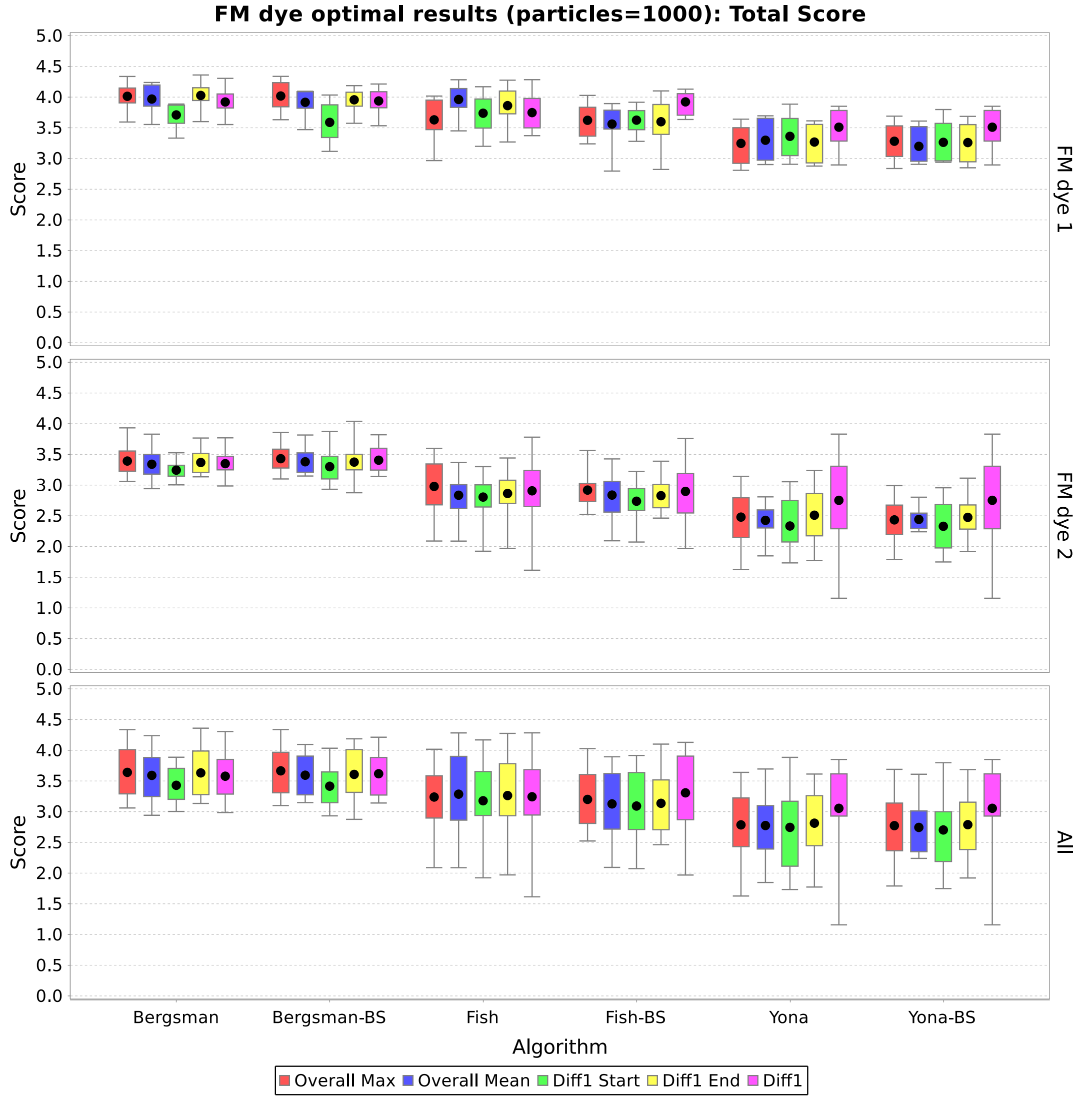

Figure 7.6: Total scores for best parameter choices with FM dye assays. Boxes show interquartile ranges, lines show maxima and minima, and black dots show mean values for each combination of experiment, image and algorithm. Overall, the results do not consistently score as good (> 4.0), for all image types and algorithms.

7.4.5 Optimum algorithm and image choices are dependent on experiment type

There is no clear ideal choice of algorithm and image combination across all experiments. As Figures 7.5 and 7.6 show, there is variability in the results between experiments. While it would be possible to select *good* choices, for example using the overall rank in Tables 7.7 and 7.8, this does not guarantee the *optimal* algorithm and image combination for an experiment.

That said, the use of NH_4^+ difference frames with the Fish algorithm and a particle detection limit of 200 seem a good choice for all of the pHluorin experiments on the test set.

7.4.6 Optimum algorithm parameter choices are dependent on experiment type

The experiment protocol has an effect on the optimum parameter choices for each algorithm, with each experiment type suggesting different parameter value ranges for optimum segmentation (Figures B.1 to B.16). General trends in particle detection parameters for Bergsman and Fish are apparent, but still variable per experiment. This is reasonable to expect as each experimental protocol is different, may use different fluorescence reporters, and may generate different intensity response profiles.

The quality weight parameters of Bergsman however are much harder to predict. There is no clear pattern for parameter choice within an individual experiment or between experiments of the same type, even when limiting attention to the highest ranked image types (*Diff2*, *Diff2 Union* and *Max Intensity*). The interdependence of the three weight parameters adds to this variability. Section 7.4.8 demonstrates the effect this has on reuse of optimal parameters within an experiment.

7.4.7 ROI cut-off limits per threshold improve scores of threshold and detect based algorithms

As seen in the ranking tables (Tables 7.7 and 7.8) limiting the number of particles detected in one threshold level has a positive effect on ROI set quality. This occurs even with the extra Bergsman parameters allowing ROI re-weighting and thresholding, which one would expect to allow a post-detection filtering of the ROIs to choose only those of highest quality.

To illustrate the difference made by applying particle detection limits to the algorithms, Figures 7.7 and 7.8 show the differences in scores between the unlimited particle detection case and the highest scoring particle detection limit for each experiment type; 200 for pHluorin and 1000 for FM dye. Values represent the score gained by limiting particle detection. The improvement by limiting particle detection is particularly apparent with the union of difference images in Figure 7.7.

Note that particle detection limits have no effect on the Yona algorithm results as it is not based on a threshold and detect process.

7.4.8 Testing suggested parameter sets

To determine whether optimum parameter sets discovered by inference would be reusable across assays in an experiment, averaged parameter sets were taken and used to repeat automated segmentation. All algorithms and segmentation images were retried, each with their own parameter set. Each parameter in the set was the mean of the parameter values of all assays in an experiment. Each image-algorithm-experiment combination had a unique set of suggested parameters.

Each of these combinations were re-segmented across the same test set of assays, and the segmentation scores calculated as before. Ranking tables 7.11 and 7.12 show the combination performances with their total score averaged across all assays of the experiment type.

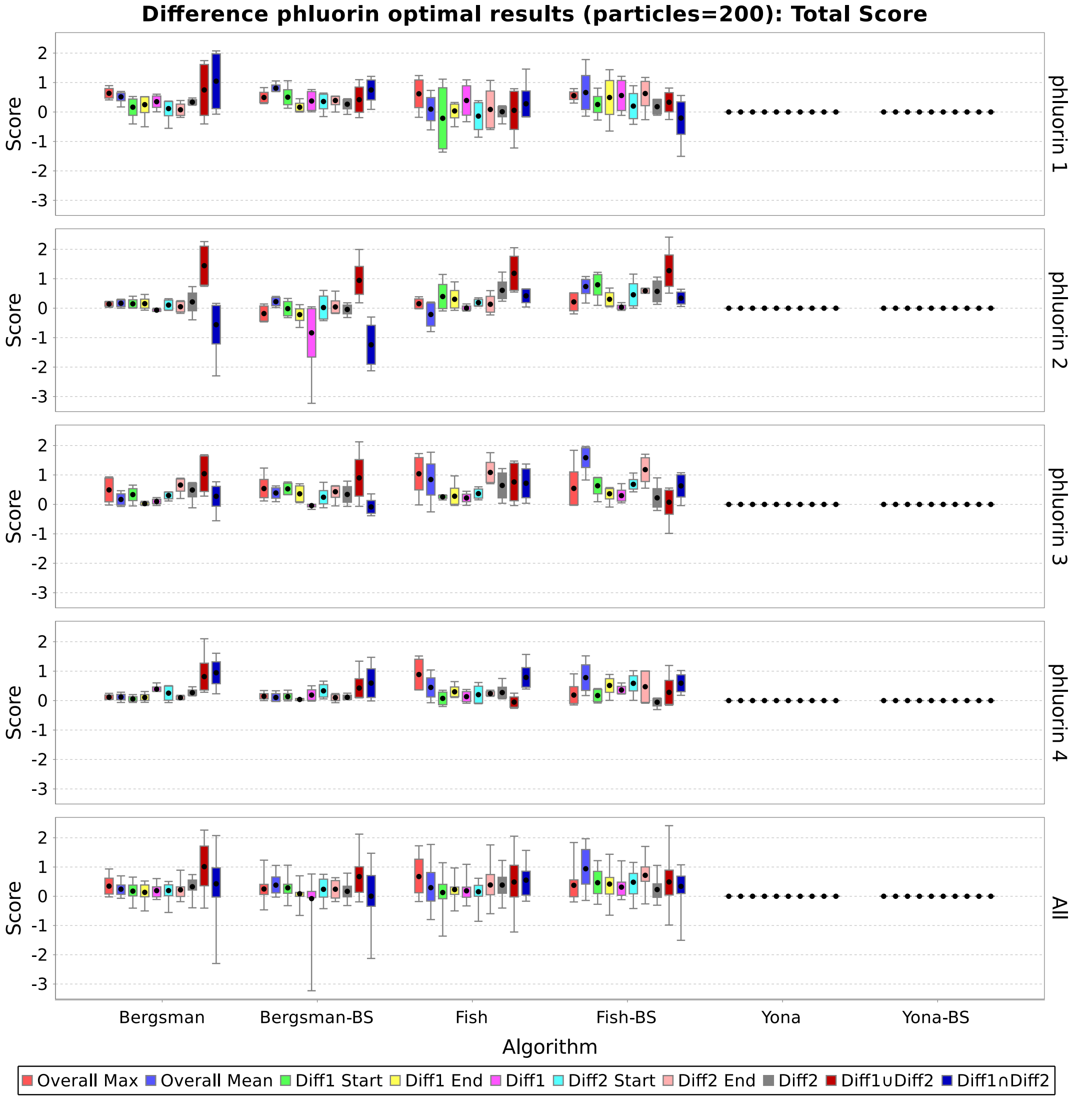

Figure 7.7: Total score differences between unlimited and a particle detection limit of 200 ROIs for best parameter choices with pHluorin assays. Boxes show interquartile ranges, lines show maxima and minima, and black dots show mean values for each combination of experiment, image and algorithm.

As can be seen, there is a drop from this experiment-specific suggested parameter set based segmentation and the previous assay-specific optimum parameter set based segmentation. This is due primarily to the variance in optimum parameter sets between assays of an experiment.

The pHluorin scores show the Fish algorithm continuing to perform best, with the Bergsman scores dropping. The use of the NH_4^+ difference image with the Fish algorithm using a particle limit of 100 appears to be the best choice for the tested pHluorin experiments, with a still good score of 4.22.

The FM dye scores however have dropped significantly below the level of reasonable segmentation at a highest mean score of 2.84. Overall the segmentation performance is not good.

Table 7.11: pHluorin ranked scores of image and algorithm combinations using suggested parameter sets. The '-BS' suffix represents the named algorithm operating on the background subtracted image. Scores are given as mean and (standard deviation) of the highest score of each of the assays in the pHluorin test group for the algorithm/image combination.

Rank	Score	Limit	Algorithm	Image
1	4.22 (0.39)	100	Fish	Diff2
2	4.21 (0.34)	100	Fish-BS	Diff2
3	4.13 (0.45)	100	Fish	Diff1 ∪ Diff2
4	4.03 (0.62)	100	Fish-BS	Diff1 ∪ Diff2
5	4.00 (0.38)	50	Fish-BS	Diff1 ∪ Diff2
6	4.00 (0.74)	200	Fish-BS	Overall Max
7	3.98 (0.36)	100	Fish-BS	Overall Max
8	3.98 (0.33)	100	Fish	Overall Max
9	3.98 (0.86)	200	Fish	Diff2
10	3.98 (0.35)	50	Fish	Diff1 ∪ Diff2
11	3.95 (0.43)	200	Bergsman	Overall Max
12	3.92 (0.42)	100	Fish-BS	Diff2 End
13	3.89 (0.75)	100	Bergsman-BS	Diff1 ∪ Diff2
14	3.89 (0.82)	200	Fish-BS	Diff2 End
15	3.88 (1.01)	200	Fish-BS	Diff2
16	3.87 (0.88)	200	Bergsman	Diff1 ∪ Diff2
17	3.85 (0.81)	200	Fish-BS	Overall Mean
18	3.84 (0.73)	none	Fish-BS	Diff2
19	3.84 (0.33)	100	Fish-BS	Overall Mean
20	3.83 (0.81)	100	Bergsman	Diff1 ∪ Diff2
21	3.81 (0.39)	100	Bergsman	Overall Max
22	3.81 (0.43)	200	Bergsman-BS	Overall Mean
23	3.80 (0.35)	100	Bergsman-BS	Overall Max
24	3.77 (0.66)	5000	Fish	Diff2
25	3.76 (0.81)	200	Bergsman	Diff2
26	3.75 (0.50)	200	Bergsman	Overall Mean
27	3.74 (0.53)	50	Fish	Diff2
28	3.74 (0.69)	200	Bergsman-BS	Overall Max
29	3.73 (0.72)	200	Bergsman	Diff2 End
30	3.73 (0.53)	200	Fish-BS	Diff1 End

Table 7.12: FM Dye ranked scores of image and algorithm combinations using suggested parameter sets. The '-BS' suffix represents the named algorithm operating on the background subtracted image. Scores are given as mean and (standard deviation) of the highest score of each of the assays in the FM dye test group for the algorithm/image combination.

Rank	Score	Limit	Algorithm	Image
1	2.84 (0.90)	100	Fish	Diff1
2	2.84 (0.78)	200	Bergsman-BS	Overall Max
3	2.83 (0.90)	1000	Bergsman-BS	Diff1
4	2.78 (0.30)	50	Bergsman	Diff1
5	2.77 (0.48)	50	Fish	Diff1
6	2.77 (1.00)	5000	Bergsman	Overall Max
7	2.76 (0.96)	5000	Bergsman	Diff1
8	2.76 (1.09)	200	Bergsman	Diff1 End
9	2.74 (0.38)	50	Bergsman-BS	Diff1
10	2.73 (0.99)	1000	Bergsman	Overall Mean
11	2.73 (1.04)	5000	Bergsman	Overall Mean
12	2.73 (0.83)	100	Bergsman-BS	Diff1
13	2.73 (1.01)	none	Bergsman	Diff1 End
14	2.73 (1.09)	none	Bergsman	Overall Mean
15	2.72 (0.91)	1000	Bergsman	Diff1
16	2.72 (0.81)	500	Fish	Overall Max
17	2.71 (1.11)	none	Bergsman	Overall Max
18	2.71 (0.50)		Yona	Overall Mean
19	2.70 (1.02)	200	Bergsman	Overall Max
20	2.70 (0.91)	500	Bergsman	Overall Mean
21	2.69 (0.94)	500	Fish	Overall Mean
22	2.69 (0.92)	none	Fish	Overall Max
23	2.69 (0.53)	1000	Fish-BS	Diff1 Start
24	2.68 (0.93)	200	Bergsman	Diff1 Start
25	2.68 (1.10)	1000	Bergsman	Overall Max
26	2.67 (0.67)	50	Bergsman	Overall Max
27	2.67 (0.80)	100	Bergsman	Diff1 Start
28	2.67 (0.75)	100	Bergsman	Diff1
29	2.67 (0.71)	50	Bergsman	Diff1 Start
30	2.67 (0.77)	50	Bergsman	Diff1 End

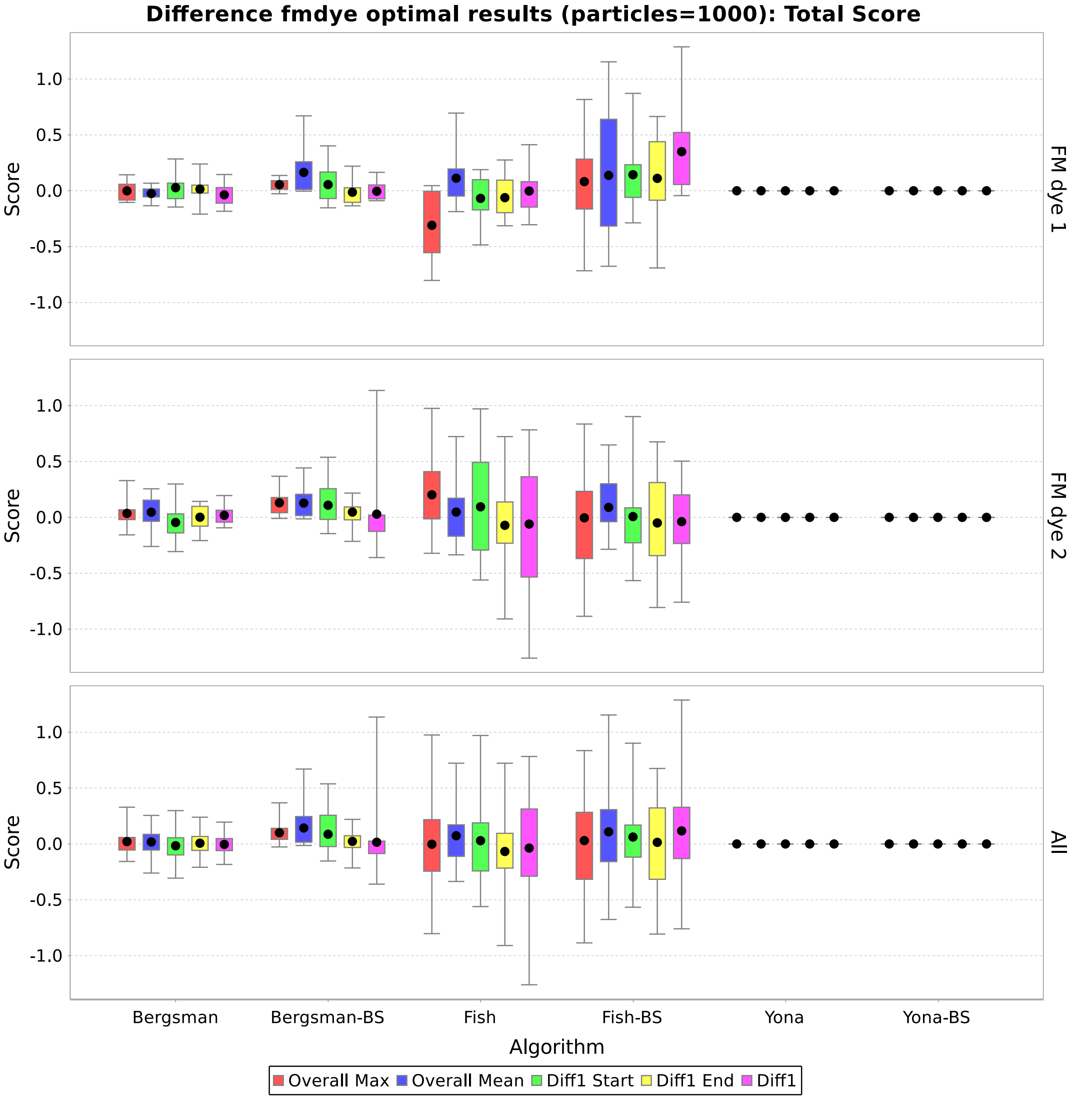

Figure 7.8: Total score differences between unlimited and a particle detection limit of 1000 ROIs for best parameter choices with FM dye assays. Boxes show interquartile ranges, lines show maxima and minima, and black dots show mean values for each combination of experiment, image and algorithm.

An additional unimplemented extension to the parameter set validation would have been to determine average parameter sets and their applicability using leave one out cross validation (LOOCV). In this method, the parameter values for each group of n assays would be calculated by taking mean parameter values from $n-1$ of the assays in the group (the training set), and the automated segmentation scores calculated by segmenting and scoring the remaining assay in the group (the test set). This process would have been repeated n times, each time leaving out a different assay from the training set, and the mean taken of the resulting n scores.

This validation was not performed in this study, but remains an option for future work.

7.5 Conclusions

7.5.1 Automated segmentation performance

For initial parameter inference of pHluorin experiments, the Fish algorithm gives highest total score when optimised for each individual assay with manually segmented training ROI sets. For this algorithm a particle detection limit of 200 appears to be favoured. There is no clear preference in the use of background subtraction. The preferred segmentation images are both the difference image showing the NH_4^+ pulse activity, and the union of difference images (which would include the ROIs found in the NH_4^+ event).

When used to infer parameter sets for use for assays in pHluorin experiments, the Fish algorithm with a particle detection limit of 200 retains good scores, using the same choices of segmentation image.

The results for both initial parameter inference, and the testing of mean parameter sets demonstrate that the use of activity frame ranges, and difference frames improve the performance of the tested algorithms in segmenting ROIs for pHluorin experiments.

For initial parameter inference of FM dye experiments, the Bergsman algorithm dominates the ranking of assay specific parameter inference. However the highest ranked scores are significantly lower than those from the pHluorin assay tests, failing to provide similar quality ROI sets.

This quality drops further when reusing inferred parameter sets at the experiment level. Difference images with the Fish algorithm have the highest ranked scores.

7.5.2 Recommendations for use

For the pHluorin experiment type, it would be reasonable to infer algorithm parameter sets using manually segmented assays of an experiment and use these sets to generate additional ROIs for the same assays, or generate ROI sets for other assays within the same experiment.

For the FM dye experiment type, while the same recommendation as for pHluorin segmentation above holds, it is recommended that these segmented ROI sets be subject to more stringent manual quality control.

In both cases, the automated segmentation can be used as a starting point for manual segmentation. This is not ideal as the manual part of the process still exists, but it is likely to reduce the level of manual work involved.

Chapter 8

Computational modelling: FM-Sim - Protocol definition, simulation and rate inference for neuroscience assays

As described in Chapter 2, synaptic vesicle recycling at the presynaptic terminal of neurons is essential for the maintenance of neurotransmission at central synapses. Among the tools used to visualise the mechanics of this process is time-series fluorescence microscopy. Fluorescent dyes such as FM1-43, or engineered fluorescent versions of synaptic vesicle proteins such as pHluorins, have been employed to reveal different steps of this key process (Cousin, 2008; Miesenböck et al., 1998).

Predictive *in silico* modelling of potential experimental outcomes is a highly informative procedural step prior to making the significant investment of time and expense which is needed to prepare and run an *in vitro* study.

This domain has already been the subject of computational modelling research, as described in Section 4.6.1. Although many general-purpose simulation and analysis packages exist, most do not allow any alteration to the system during the course of an experimental assay. These alterations can include the addition and removal of reagents to extracellular media, and electrical stimulation of neurons being observed. None give a treatment of fluorescence which reflects our current understanding.

Debate is ongoing (Aravanis et al., 2003; Atluri and Ryan, 2006) over which types of endocytosis may be in effect at CNS nerve terminals under different stimuli. A number of published computational models investigate the ability of one or a combination of these models to fit observed experimental data (Granseth and Lagnado, 2008; Granseth et al., 2006). However, these models are created on an ad-hoc basis for particular experimental protocols.

Additionally, different fluorescent markers have different properties and behaviours within these experimental assays. Generally, assays using one or other of these markers are modelled independently.

8.1 FM-Sim

FM-Sim is an easy-to-use hybrid stochastic simulator written specifically for this domain. It is composed of a protocol definition user interface, a stochastic time-series simulation engine, and a Bayesian inference engine (Andrieu et al., 2010; Golightly and Wilkinson, 2011) to infer rate parameters for a protocol based on comparison with supplied experimental observation data from *in vitro* fluorescence microscopy assays.

The simulation and inference engines use a model of vesicle movement within a nerve terminal, and can simulate a number of *in vitro* techniques used to modify the fluorescence output during an experiment.

The main benefit of simulations performed by FM-Sim over those performed by generic stochastic simulators is that FM-Sim manages the effects of nested and overlapping events which impact on the kinetics of vesicle recycling. For example, a chemical inhibitor may be introduced at some time during an experimental protocol, with electrical stimulation applied subsequently for part of the time that the inhibitor is available. These changes in stimulus or experimental conditions during a protocol, termed *regime changes* for the remainder of this chapter, are derived from the protocol definition, managing the effects of nested and overlapping events.

The flexibility of the protocol definition allows the wide variety of potential experiments to be modelled. New experiments can be simulated based upon rate parameters obtained from prior experiments.

8.1.1 FM-Sim Synaptic Terminal Model

At the core of FM-Sim is a stochastic model of vesicle movement, or more specifically the cell membrane making up the surface of vesicles, within a synaptic terminal. The model tracks the movement of cell membrane around the structures of a single synaptic terminal, namely the vesicles, endosomes and the plasma membrane. As a simplification, all membrane movements are tracked in quanta of vesicles as this is a consistent, smallest unit of membrane surface area to move. The plasma membrane is a repository of x vesicles worth of membrane, and endosomes are created with y vesicles worth of membrane and decrease in size as vesicles bud from their surface. Vesicles stored within the synaptic nerve terminal are designated as being part of the reserve pool (RP) or readily releasable pool (RRP).

The initiation of movement of vesicles between the regions (RP, RRP, endosomes, plasma membrane) is stochastic, with propensity defined by rules for each transition, as depicted in Figure 8.1.

However, in contrast to the widely-used convention in the simulation of stochastic chemical kinetics where the reaction events are abstracted as instantaneous, each of the processes moving vesicles from one state to another takes a non-negligible time delay. Therefore the model is extended to include delays. Each pool or region of vesicles has an associated transition state. Vesicles in this transition state take a fixed time to transition from their prior to their current state. This approach is a form of the Delayed Stochastic Simulation Algorithm (DSSA) as discussed in Barrio et al. (2006), with reactants being vesicles in the source region, and products

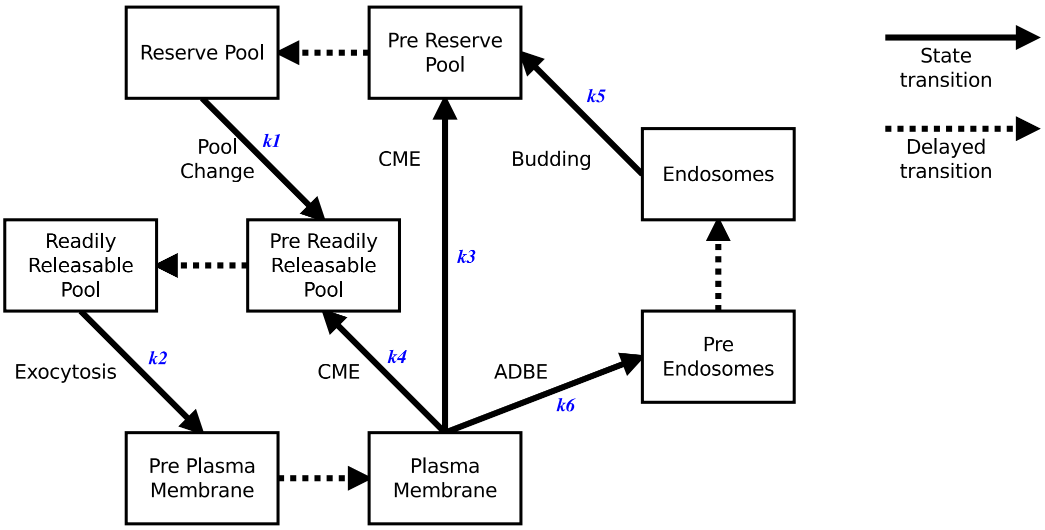

Figure 8.1: FM-Sim synaptic terminal model. The states shown are the four regions where vesicle membrane is held: RP, RRP, endosomes, plasma membrane. The associated *pre*-states are artificial modelling states which exist to allow vesicles to move from one region to another with a time delay, rather than representing particular physiological states of vesicles. The state transition annotations *k1*-*k6* are the rule propensities of the state transitions.

being the vesicles transferred to the target region.

Let $\mathcal{S}$ be the set of states in which a vesicle can exist

$$\mathcal{S} = \{\text{RP, RRP, E, PM, Pre-RP, Pre-RRP, Pre-E, Pre-PM}\}$$

denoting Reserve Pool, Readily Releasable Pool, Endosome, Plasma Membrane, and the associated pre-states respectively.

Define a vesicle as $V_s(D,E,pH,T)$, $s \in \mathcal{S}$ with the following properties:

- D - Presence of FM dye: This determines whether or not the vesicle counts towards the fluorescence level of the nerve terminal. It is treated as a boolean value, as is the convention in current biological experiments. The dye is either present at the concentrations used when first loaded into the terminal (D_{Y}), or completely absent (D_{N}). Partial or low concentration dye loading does not take place.

- E - Endocytosis source: The vesicle is classified as having been produced via recycling by CME (E_{CME}) or ADBE (E_{ADBE}). While it is possible that new vesicles could arrive from the soma of the cell, or be trafficked from neighbouring nerve terminals (Fernández-Alfonso and Ryan, 2008), it is thought that the effect of this possible influx of new vesicles occurs too slowly over the time-frame of an experiment to be detectable. The mechanism of vesicle creation is a factor in determining which vesicles fluoresce under the effect of each FM dye. FM2-10 has been shown to be taken up through CME only, whereas FM1-43 is taken up through both CME and ADBE at the loading concentrations commonly used in the literature. This differential uptake of different dyes was explored experimentally in depth in (Clayton and Cousin, 2008).

- pH: Extracellular media is normally of neutral pH (pH_{neutral}, normalised to 1). Vesicles competent for release are at lower pH (pH_{acid}, normalised to 0). The reacidification process occurs between endocytosis and arrival at the vesicle pool. Experiments using pHluorins are affected by this pH change. Any pHluorins in contact with neutral pH fluoresce strongly, and this fluorescence decreases as the media within the vesicle is acidified. As experimental work has provided evidence that this reacidification process can take between three and five seconds (Atluri and Ryan, 2006; Granseth et al., 2006), pH levels are recorded as continuous values. After endocytosis, these values are reduced linearly over time to reach the target pH.

- T - Time delay for vesicle to remain in pre-pool state as described above, with T_0 representing 0 time delay.

Note: for notational convenience, vesicle properties irrelevant to particular transitions may be omitted, for example $V_s(D_{\text{Y}}) = V_s(D_{\text{Y}}, E_?, pH_?, T_?)$.

8.1.2 Discrete State Changes

The state changes of the model are:

$$\begin{aligned}
\text{Pool change}: &\quad V_{\text{RP}}(T_0) \xrightarrow{k_1} V_{\text{Pre-RRP}}(T_{\text{Pool change}}) \\
\text{Exocytosis}: &\quad V_{\text{RRP}}(D_?, pH_?, T_0) \xrightarrow{k_2} V_{\text{Pre-PM}}(D^*, pH_{\text{neutral}}, T_{\text{Exocytosis}}) \\
\text{CME}: &\quad V_{\text{PM}}(D^*, E_?, T_0) \xrightarrow{k_3} V_{\text{Pre-RP}}(D^*, E_{\text{CME}}, T_{\text{CME}}) \\
: &\quad V_{\text{PM}}(D^*, E_?, T_0) \xrightarrow{k_4} V_{\text{Pre-RRP}}(D^*, E_{\text{CME}}, T_{\text{CME}}) \\
\text{Budding}: &\quad V_{\text{E}}(T_0) \xrightarrow{k_5} V_{\text{Pre-RP}}(T_{\text{Budding}})
\end{aligned}$$

D^* represents that the vesicle is FM dye tagged only if FM dye is present in the extracellular media. There are two CME state changes, one for each destination pool, and each with a different propensity. Each of the rules above apply to individual vesicles for each instance of the rule being executed. The rule below however, operates on N vesicles taken together to represent a single endosome. If N vesicles are not available in the plasma membrane state, the rule is not executed.

$$\text{ADBE}: \quad V_{\text{PM}}(D^*, E_?, 0) \xrightarrow{k_6} V_{\text{Pre-E}}(D^*, E_{\text{ADBE}}, T_{\text{ADBE}})$$

The values $k_1, \ldots, k_6$ are the rule propensities, each the product of the number of vesicles available in the source state, and a rule rate C. Let V denote number of vesicles:

$$\begin{aligned}
k_1 &= V_{\text{RP}} \times C_{\text{Pool change}} \\
k_2 &= V_{\text{RRP}} \times C_{\text{Exocytosis}} \\
k_3 &= V_{\text{PM}} \times C_{\text{CME}} \times C_{\text{CME RP ratio}} \\
k_4 &= V_{\text{PM}} \times C_{\text{CME}} \times (1 - C_{\text{CME RP ratio}}) \\
k_5 &= V_{\text{E}} \times C_{\text{Budding}} \\
k_6 &= V_{\text{PM}} \times C_{\text{ADBE}}
\end{aligned}$$

The values k_3 and k_4 have an additional input, $C_{\text{CME RP ratio}}$. This constant takes values from zero to one and represents the proportion of vesicles produced by CME which go to the RP. The remainder go to the RRP. This work uses 0.7 as the value for the $C_{\text{CME RP ratio}}$, meaning a ratio of 7:3 in favour of vesicle movement to RP over RRP. Similar values are used in the literature (Cheung et al., 2010).

In summary, the input parameters for the model are the rate constants $C_?$ and the time constants $T_?$.

8.1.3 Continuous State Changes

In addition to the above state change rules, there are the following continuous processes:

- Pre-pool delays: A vesicle $T_{\text{delay}} > 0$ reduces as simulated time elapses. Once the T_{delay} reaches T_0, a vesicle in a pre-pool moves into the corresponding pool

$$\begin{aligned}
V_{\text{Pre-pool}}(T) &\to V_{\text{Pre-pool}}(T - dt) \\
V_{\text{Pre-pool}}(T_0) &\to V_{\text{Pool}}(T_0)
\end{aligned}$$

- Reacidification: The pH of a fully internalised vesicle or endosome (i.e. one which is no longer in direct contact with extracellular media) reduces linearly over time from pH_{neutral} to pH_{acid}, at a rate matching current literature (Atluri and Ryan, 2006; Granseth et al., 2006).

$$V(pH) \to V(pH - dpH)$$

8.1.4 Fluorescence Calculation

The model can simulate the fluorescence of each of the three previously described fluorescent markers. Based on the fluorescent marker used in the experiment design, fluorescence is calculated as described below. In all cases fluorescence is scaled from minimum $= 0$ to maximum $= 1$ possible fluorescence by dividing by the total vesicle count in the model $[V]$.

- **FM1-43**: Total fluorescence is the count of all vesicles in states not in contact with extracellular media with FM dye boolean variable true. Vesicles in states {PM, Pre-PM} do not contribute because standard experimental protocols (Wu et al., 2009) have shown FM dye rapidly dissociates from the plasma membrane and is washed away in the extracellular media.

  $$F_{\text{FM1-43}} = [V_s(D_{\text{Y}})]/[V], s \notin \{\text{PM, Pre-PM}\}$$

- **FM2-10**: Total fluorescence is the count of all vesicles in the RP and RRP (and their pre-states) with vesicle source CME. ADBE-derived vesicles do not contribute under standard experimental protocols of 100μM FM2-10 (Cousin, 2008).

  $$F_{\text{FM2-10}} = [V_s(D_{\text{Y}}, E_{\text{CME}})]/[V], s \in \{\text{RP, RRP, Pre-RP, Pre-RRP}\}$$

- **pHluorin**: Total fluorescence is the sum of normalised vesicle pH of all vesicles. A family of pHluorin fusion proteins is commonly used in these experiments. For the purposes of simulation however, they are broadly the same in behaviour. They fluoresce when in contact with neutral pH and not when in an acidic environment. In addition to the normal physiological changes in pH within a nerve terminal, there are two external stimuli used in pHluorin assays.
  - *Ammonium addition*: Ammonium chloride is used to cause all pHluorin in a nerve terminal to fluoresce. When applied, ammonium ions permeate extracellular media, cytoplasm, and vesicle interiors, reducing the acidity of all media (Sankaranarayanan et al., 2000).
  - *Acid addition*: Impermanent acid is used to quench the fluorescence of pHluorin on the plasma membrane, leaving only the pHluorin on fully internalised membrane to fluoresce (Atluri and Ryan, 2006).

$$F_{\text{pHluorin}} = \begin{cases} 1, & & \text{if NH}_4^+ \text{ present} \\ \left(\sum pH\right)/[V], & V_s(pH), s \notin \{\text{PM, Pre-PM}\} & \text{if acid present} \\ \left(\sum pH\right)/[V], & V_s(pH), s \in \mathcal{S} & \text{otherwise} \end{cases}$$

Current experimental data available records fluorescence levels per nerve terminal as relative measures only. It is not commonly feasible to calculate absolute quantities of marker. Therefore, experimental observations are taken to vary from maximum (1) and minimum (0) fluorescence per nerve terminal during the experimental assay.

8.1.5 Protocol Definition and Rate Parameter Specification

FM-Sim allows the user to define an experimental protocol to a sufficient level of detail to be simulated. A protocol consists of a number of events with a defined start time (or frame) and a given duration. Multiple events may be active simultaneously, for example chemical stimulation of nerve terminals while simultaneously inhibiting certain protein functions within the nerve terminal with the application of chemical inhibitors. Figure 8.2 shows a defined example protocol.

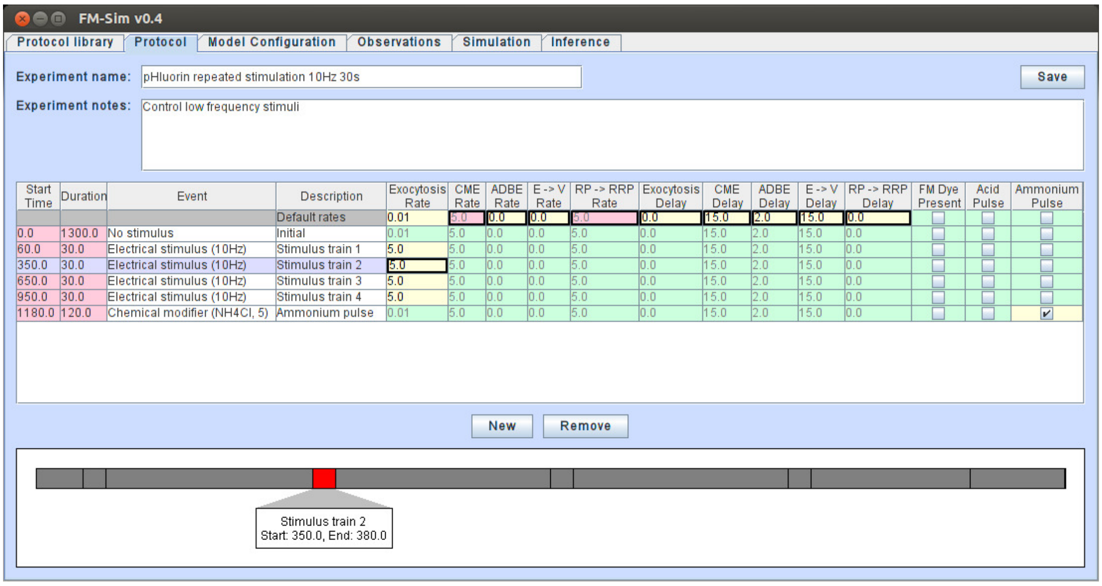

Experiment name: pHluorin repeated stimulation 10Hz 30s

Experiment notes: Control low frequency stimuli

Start Time	Duration	Event	Description	Exocytosis Rate	CME Rate	ADBE Rate	E -> V Rate	RP -> RRP Rate	Exocytosis Delay	CME Delay	ADBE Delay	E -> V Delay	RP -> RRP Delay	FM Dye Present	Acid Pulse	Ammonium Pulse
			Default rates	0.01	5.0	0.0	0.0	5.0	0.0	15.0	2.0	15.0	0.0	☐	☐	☐
0.0	1300.0	No stimulus	Initial	0.01	5.0	0.0	0.0	5.0	0.0	15.0	2.0	15.0	0.0	☐	☐	☐
60.0	30.0	Electrical stimulus (10Hz)	Stimulus train 1	5.0	5.0	0.0	0.0	5.0	0.0	15.0	2.0	15.0	0.0	☐	☐	☐
350.0	30.0	Electrical stimulus (10Hz)	Stimulus train 2	5.0	5.0	0.0	0.0	5.0	0.0	15.0	2.0	15.0	0.0	☐	☐	☐
650.0	30.0	Electrical stimulus (10Hz)	Stimulus train 3	5.0	5.0	0.0	0.0	5.0	0.0	15.0	2.0	15.0	0.0	☐	☐	☐
950.0	30.0	Electrical stimulus (10Hz)	Stimulus train 4	5.0	5.0	0.0	0.0	5.0	0.0	15.0	2.0	15.0	0.0	☐	☐	☐
1180.0	120.0	Chemical modifier (NH4Cl, 5)	Ammonium pulse	0.01	5.0	0.0	0.0	5.0	0.0	15.0	2.0	15.0	0.0	☐	☐	☑

Figure 8.2: A sample defined protocol in the FM-Sim protocol editor.

For each protocol event, the user may choose to enter values for rate parameters. The rate parameters available for modification depend on the configuration of the model to be simulated (discussed below). The user may also leave rate values for individual events unmodified, in which case the values are taken from the enclosing event if any, or a default rate if there are no enclosing events. Finally, the user may choose to mark rate parameters as to be inferred from observed data. This requires the loading of an appropriate dataset of observed fluorescence values for inference to be performed (Figure 8.3).

8.1.6 Simulation

Once defined, the set of protocol events are converted into a sequence of regime change events for simulation (Figure 8.4). At each regime change event, the set of rate values in effect are calculated, accounting for value inheritance. A single value is used for each inferred protocol event parameter when generating Bayesian inference proposals, ensuring consistency if that parameter value is used in multiple regime change events. This simplification of protocol definition entry and automatic regime event generation with inherited rate values is a feature not found in many of the general purpose simulators currently available, such as VCell (Moraru

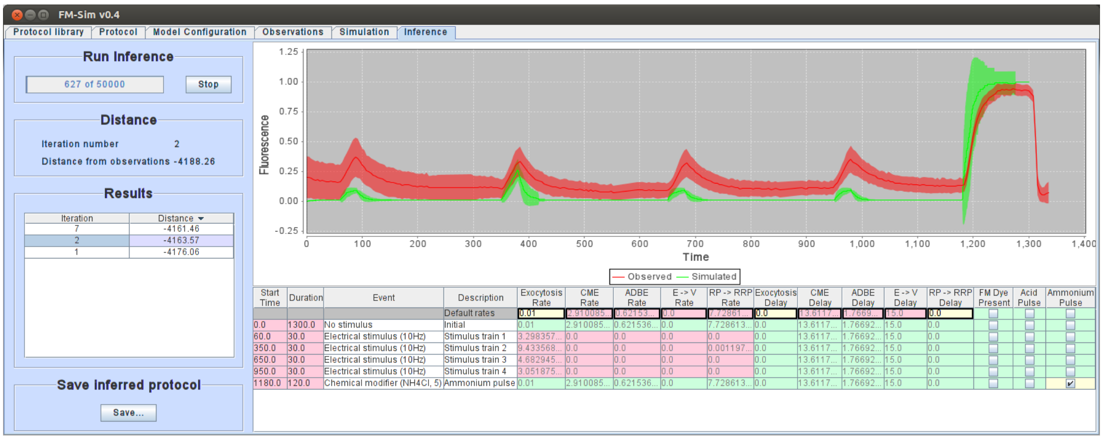

627 of 50000

Iteration number 2

Distance from observations -4188.26

Iteration	Distance
7	-4161.46
2	-4163.57
1	-4176.06

Start Time	Duration	Event	Description	Exocytosis Rate	CME Rate	ADBE Rate	E -> V Rate	RP -> RRP Rate	Exocytosis Delay	CME Delay	ADBE Delay	E -> V Delay	RP -> RRP Delay	FM Dye Present	Acid Pulse	Ammonium Pulse
			Default rates	0.01	2.910085...	0.62153...	0.0	7.72861...	0.0	13.6117...	1.7669...	15.0	0.0	☐	☐	☐
0.0	1300.0	No stimulus	Initial	0.01	2.910085...	0.621536...	0.0	7.728613...	0.0	13.6117...	1.76692...	15.0	0.0	☐	☐	☐
60.0	30.0	Electrical stimulus (10Hz)	Stimulus train 1	3.298357...	0.0	0.0	0.0	0.0	0.0	13.6117...	1.76692...	15.0	0.0	☐	☐	☐
350.0	30.0	Electrical stimulus (10Hz)	Stimulus train 2	9.433568...	0.0	0.0	0.0	0.001197...	0.0	13.6117...	1.76692...	15.0	0.0	☐	☐	☐
650.0	30.0	Electrical stimulus (10Hz)	Stimulus train 3	4.682945...	0.0	0.0	0.0	0.0	0.0	13.6117...	1.76692...	15.0	0.0	☐	☐	☐
950.0	30.0	Electrical stimulus (10Hz)	Stimulus train 4	3.051875...	0.0	0.0	0.0	0.0	0.0	13.6117...	1.76692...	15.0	0.0	☐	☐	☐
1180.0	120.0	Chemical modifier (NH4Cl, 5)	Ammonium pulse	0.01	2.910085...	0.621536...	0.0	7.728613...	0.0	13.6117...	1.76692...	15.0	0.0	☐	☐	☑

Figure 8.3: Example parameter inference of a defined protocol, the parameter values in red are inferred from observed experimental data. The graph shows a sample simulation using these parameter values (green) compared against the supplied experimental data (red).

et al., 2008).

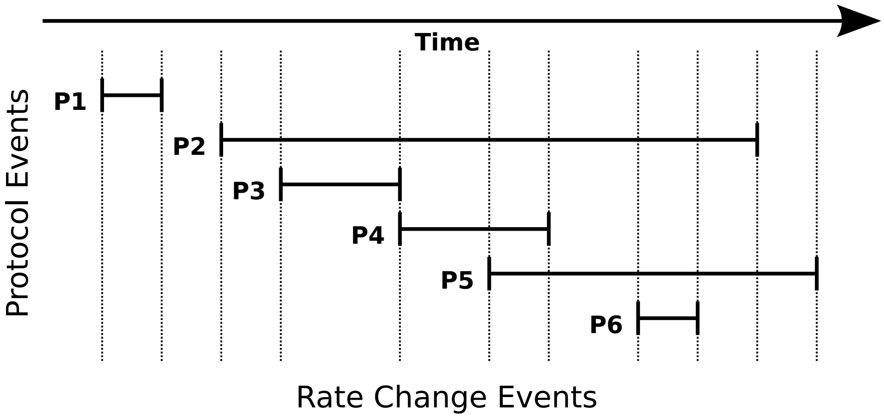

Figure 8.4: Example regime change event generation. Protocol events P1,...,P6 are defined with start times and durations. These protocol events are then used to generate a sequence of events where rate values may change.

These regime change time-points and the associated user-defined rates in effect during each regime are used to stochastically simulate a population of nerve terminals. The result is a trace of mean simulated fluorescence during the experiment.

The simulation engine uses an extended form of the Gillespie Stochastic Simulation Algorithm, specifically, the Direct Method (Gillespie, 1977), keeping track of vesicles and endosomes within a presynaptic terminal. The extensions added allow vesicle movement to be non-instantaneous using an algorithm similar to the DSSA method by Barrio *et al.* (Barrio et al., 2006), and handling of continuous state changes (pH) over time.

8.1.7 Observation Data Handling

Observed experimental data may be input in the form of a comma-separated value (CSV) data file holding fluorescence values across multiple nerve terminal regions-of-interest (ROIs) over multiple imaging frames (usually one frame every few seconds).

Experimental fluorescence levels are known to decay during the time course of the experiment. This is due to photo-bleaching of the dye during image acquisition under the microscope. It is standard practice to compensate for this decay during analysis of experimental data, most commonly with a linear decay function. FM-Sim can apply a similar compensation formula to raw observed data if necessary:

$$\text{Corrected observation} = \text{Observation} - C \times (t_{\text{obs}} - t_0)$$

where C is the linear correction factor, t_{obs} is the time of observation, and t_0 is the time at the start of image acquisition. Generally, the linear correction factor is obtained by the user using calibration assays. If more complex decay correction is required, it is expected that the user performs the preprocessing prior to importing the data into FM-Sim. Once the data has been decay-corrected and scaled, it can be compared with the output of the simulation, or used to infer rate parameters.

8.1.8 Bayesian Parameter Inference

A Bayesian approach to parameter inference was taken, using a standard Particle Marginal Metropolis-Hastings (PMMH) scheme and Sequential Monte Carlo (SMC) estimates of marginal likelihoods (Andrieu et al., 2010; Golightly and Wilkinson, 2011), with the addition of the following mechanism to handle regime changes: a defined protocol is decomposed into rate change events. The minimum set of inference parameters is also calculated over the entire protocol. For each PMMH iteration, a set of proposals are drawn for the set of inference parameters. The SMC scheme is then run, changing the rates in effect as each rate change time is reached in the simulation.

The SMC scheme used in FM-Sim is as described by Golightly *et al.* (Golightly and Wilkinson, 2011). It requires a set of N particles generated by forward simulation for each observed time-point. The weight w of each of these particles contributes to the estimated marginal likelihood $\hat{p}(y_{t+1}|\mathbf{y}_t, c)$ where y_{t+1} is the experimental observation at time $t+1$, $\mathbf{y}_t$ is the set of experimental observations up to time t, and c is the set of simulation parameters.

$$\hat{p}(y_{t+1}|\mathbf{y}_t, c) = \frac{1}{N}\sum_{i=1}^{N} w_{t+1}^{i} \quad \text{where} \quad w_t^i = p(y_t|x_t^i, c)$$

Each particle weight is $p(y_t|x_t^i, c)$, where y_t is the experimentally observed (normalised) fluorescence at time t, x_t^i is the fluorescence of simulated particle i at time t, and c is the set of simulation parameters. In other words, the probability of obtaining values matching the observed y_t given the simulated result x_t, making the assumption that $p(y_t|x_t^i, c) = p(y_t|x_t^i)$.

The calculations also make the assumption that both the experimental and simulated observations at a particular time-point are normally distributed. Experimental observations provide a set of fluorescence values for y_t, from which the mean $\mu(y_t)$ and variance $\sigma(y_t)^2$ are computed. Forward simulation of an individual particle provides a single value for x_t^i. Given that the single particle result has zero variance, $\mathcal{N}(\mu(y_t)|x_t, \sigma(x_t)^2)$ is not useful.

To avoid this problem, the assumption is made that the variance around an x_t^i result is equal to the variance of the observed y_t values. This has the advantage over choosing an arbitrary variance that it provides a variance for each time-point which is tailored to the experimental data. This provides the distribution

$$\mathcal{N}(\mu(y_t)|x_t^i, \sigma(y_t)^2) = \mathcal{N}(x_t^i|\mu(y_t), \sigma(y_t)^2)$$

Finally, the distribution is normalised to the peak probability $\mathcal{N}(\mu(y_t)|\mu(y_t), \sigma(y_t)^2)$ to avoid arithmetic underflow of marginal likelihoods of long time-series, and to provide a more user-friendly distance measure. As PMMH proposal acceptance probability is based on the ratio of proposal marginal likelihood over the previously accepted marginal likelihood, this normalisation of the whole time-series has no effect on proposal acceptance.

$$\begin{aligned} p(y_t|x_t^i, c) &= \frac{\mathcal{N}(x_t^i|\mu(y_t), \sigma(y_t)^2)}{\mathcal{N}(\mu(y_t)|\mu(y_t), \sigma(y_t)^2)} \\ &= \exp\left(-\frac{x_t^i - \mu(y_t)}{2\sigma(y_t)^2}\right) \end{aligned}$$

The overall estimated marginal likelihood of the SMC scheme is the product of the marginal likelihoods of all of the T observed time-points. This marginal likelihood is used to update the PMMH best match for that iteration.

$$\begin{aligned} \hat{p}(\mathbf{y}|c) &= \hat{p}(y_1|c) \prod_{t=1}^{T-1} \hat{p}(y_{t+1}|\mathbf{y}_t, c) \\ &= \prod_{t=1}^{T} \frac{1}{N} \sum_{i=1}^{N} p(y_t|x_t^i, c) \end{aligned}$$

The final result of the inference process is a set of model rate parameters for the whole protocol which best matched the experimental data, from the proposals generated by the inference algorithm. For most applications, it is expected that there are a mix of user-defined and inferred rate parameter values.

8.2 Case Study 1: FM Dye based assay

This case study uses real experimental data from the Cousin neuronal cell biology laboratory in Edinburgh (Cheung et al., 2010). The assay has multiple exocytosis stimuli designed to trigger release of synaptic vesicles from both of the vesicle pools (RP and RRP). The case study demonstrates use of FM dyes, regime changes and a series of protocol events, shown

Table 8.1: Protocol events for the FM dye based assay. A short electrical stimulus is followed by a longer sustained chemical stimulus.

Event	Stimulus	Start time (s)	Duration (s)
Default	None	0	250
RRP Unload	Electrical (20Hz)	12	2
RP Unload	Chemical (KCl, 0.5 mM)	100	30

in Table 8.1. The raw observations are corrected for decay with a linear correction of 200 fluorescence units per second.

This first example shows inferred parameters for a model without ADBE. The inference parameters were Exocytosis, CME, and Pool Change rate, for each of the three protocol events. The remaining parameters were fixed. The final results of inference are shown in Figure 8.5a, leading to the parameters shown in Table 8.2, with a distance measure of -0.35.

Table 8.2: Inference results for CME only, and both CME and ADBE. Values shown are rate constants C (s^{-1}) and time delay constants T (s) for each of the discrete state change rules, with inferred values shown in bold.

Event	Exocytosis		CME		ADBE		Budding		Pool change	
	C	T	C	T	C	T	C	T	C	T
CME only										
Default	**0.03**	0	**0.01**	15	0	2	0	15	**0.00**	1
RRP Unload	**8.81**	0	**1.67**	15	0	2	0	15	**0.92**	1
RP Unload	**8.23**	0	**0.84**	15	0	2	0	15	**1.00**	1
CME and ADBE										
Default	**0.04**	0	**0.01**	15	0	2	**0.07**	15	**0.00**	1
RRP Unload	**10.29**	0	**0.87**	15	0	2	**0.01**	15	**3.50**	1
RP Unload	**4.03**	0	**1.06**	15	**0.58**	2	**0.87**	15	**0.36**	1

Repeating the inference with allowing the parameters ADBE and Budding rate to be inferred under the second stimulus gave the parameters shown also in Table 8.2, with an improved distance measure of -0.22, illustrated in Figure 8.5b.

8.3 Case Study 2: pHluorin Based Assay

This case study is based on current pHluorin experimental work from the Cousin laboratory. The assay demonstrates repeated stimulus and recovery cycles, along with the use of pHluorin

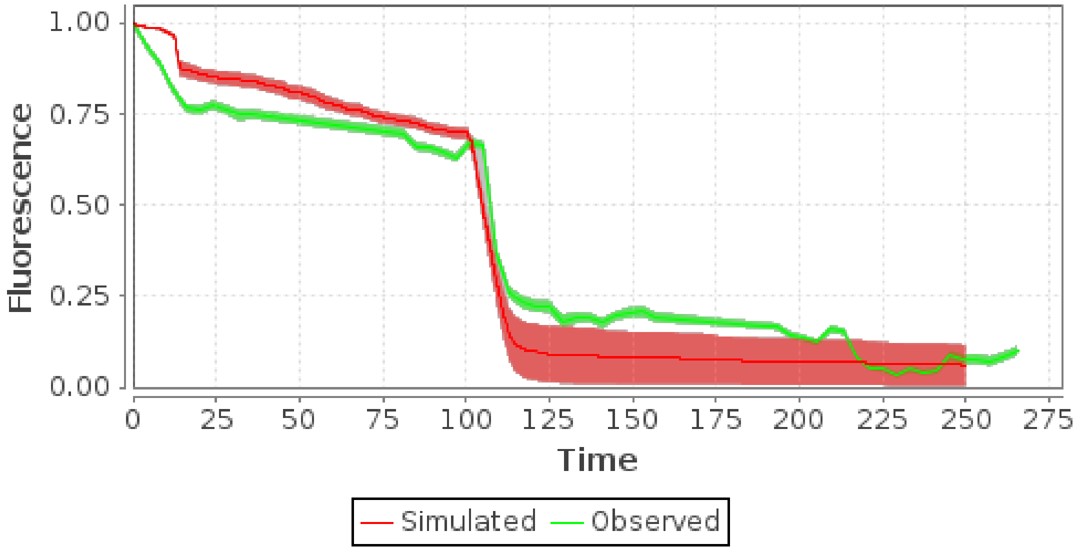

(a) CME only

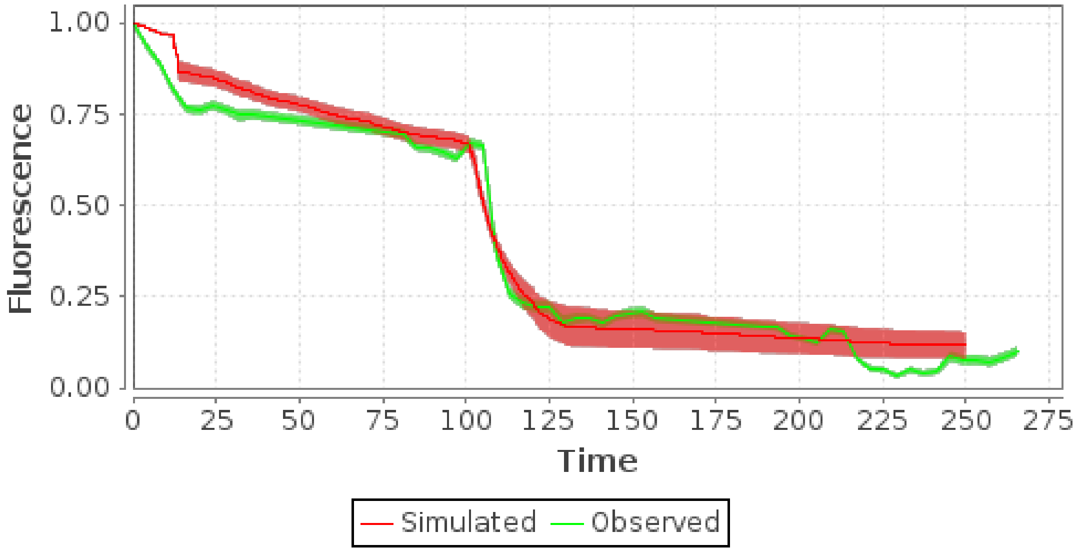

(b) CME and ADBE

Figure 8.5: Simulated fluorescence traces using the inferred parameters shown in Table 8.2, plotted against the real observed data used for parameter inference.

specific stimulus, shown in Table 8.3. Again, real experimental observations have been used.

Final results of inference as shown in Figure 8.6, gave the parameters shown in Table 8.4, with a distance measure of -7.14.

8.4 Conclusions

The FM-Sim application and its computational model of synaptic vesicle recycling has been demonstrated to work for a number of experimental assays. It provides the following benefits to both experimental and theoretical neuroscientists

Table 8.3: Protocol events for the pHluorin Based Assay. Four cycles of sustained low frequency electrical stimulus are followed by the addition of ammonium chloride.

Event	Stimulus	Start time (s)	Duration (s)
Rest	None	0	1300
Stimulus train 1	Electrical (10Hz)	60	30
Stimulus train 2	Electrical (10Hz)	350	30
Stimulus train 3	Electrical (10Hz)	650	30
Stimulus train 4	Electrical (10Hz)	950	30
Ammonium pulse	Chemical (NH_4Cl, 50 mM)	1180	120

Table 8.4: Inference Results for pHluorin Assay. Values shown are rate constants C (s^{-1}) and time delay constants T (s) for each of the discrete state change rules, with inferred values shown in bold.

Event	Exocytosis		CME		ADBE		Budding		Pool change	
	C	T	C	T	C	T	C	T	C	T
Rest	0.01	0	**2.59**	15	0	2	0	15	**10.34**	0
Stimulus train 1	**4.81**	0	**2.59**	15	0	2	0	15	**10.34**	0
Stimulus train 2	**8.12**	0	**2.59**	15	0	2	0	15	**10.34**	0
Stimulus train 3	**3.68**	0	**2.59**	15	0	2	0	15	**10.34**	0
Stimulus train 4	**5.59**	0	**2.59**	15	0	2	0	15	**10.34**	0
Ammonium pulse	0.01	0	**2.59**	15	0	2	0	15	**10.34**	0

- A user-friendly means of cataloguing experimental assays.
- An aid to experimental design by simulating the predicted effects of chemical modifiers on neurons prior to *in vitro* work.
- A means of gaining further insight into the kinetics of vesicle recycling by having numerous sets of observed data compared against a single kinetic model. This allows validation of the model and its rate parameters under a range of environmental conditions.

FM-Sim has been applied to a range of experimental assays within the Cousin laboratory. The research focus of this laboratory includes investigation of the mechanisms involved in synaptic vesicle recycling. Future work includes extending this library of experimental protocols, with supporting experimental data, and cross-validating inferred experimental rates and models between compatible experiments, where environmental factors allow.

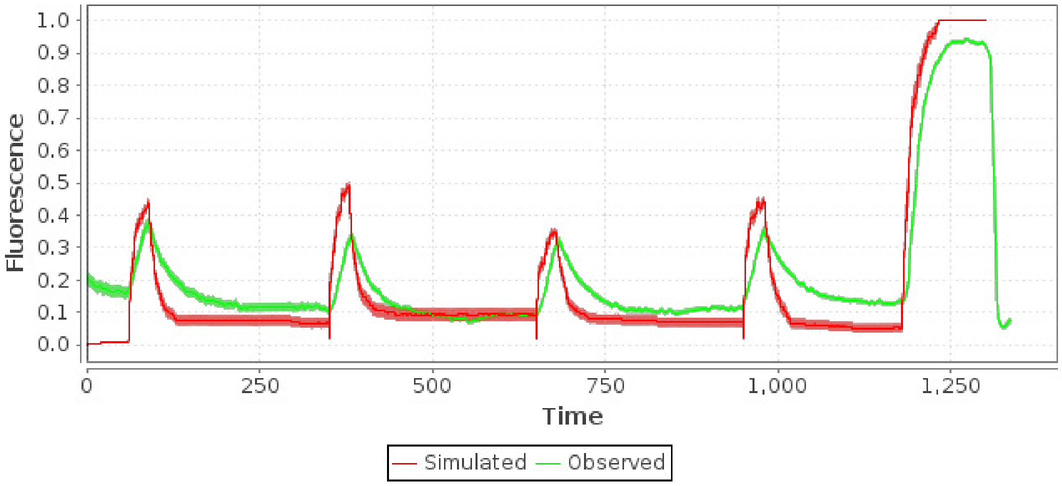

Figure 8.6: Simulated fluorescence trace using the inferred parameters shown in Table 8.4, plotted against the real observed data used for parameter inference.

The structure of the application allows straightforward programmatic extension of the model to incorporate other recycling mechanisms. Future development could easily accommodate the addition of kiss-and-run exocytosis or ultrafast endocytosis. This would require adding new transition rules and rule propensities, while leaving the simulation and inference engine unchanged. The main requirement for such extensions to be useful would be enough experimental datasets from which to infer values for these additional parameters.

Some of the material in this chapter is adapted from two papers published on the project (Stewart et al., 2014, 2015). FM-Sim is available at `https://demonsoft.org/neuroscience/`.

Chapter 9

Computational modelling: Plasma membrane modelling of the synaptic vesicle cycle

As discussed in Chapter 2, a common function attributed to activity-dependent bulk endocytosis is as a fall-back mechanism for plasma membrane recovery under conditions of high activity (i.e. high levels of exocytosis) when the normal mechanism CME is unable to cope with the influx of membrane to the plasma membrane. The implied problem is that rapidly increasing the plasma membrane area at a nerve terminal is an unhealthy event for the terminal.

Under normal physiological levels of stimulation of a nerve terminal, vesicle exocytosis causes an increase in plasma membrane surface area (and potentially a matching decrease in nerve terminal volume). This is balanced by a compensatory reduction in plasma membrane area via CME. This causes not only replenishment of the vesicle pool available to the nerve terminal, but conservation of the overall structure of the nerve terminal (Figure 9.1).

Under conditions of high physiological stimulation (Clayton et al., 2008), a large quantity of vesicles are exocytosed in a short period of time, resulting in a large increase of plasma membrane surface area (and potentially a substantial drop in nerve terminal volume). It is conjectured that this situation is unhealthy for the nerve terminal, as the pre-synaptic membrane will likely become deeply folded which in turn may make the synapse less efficient.

ADBE is considered a necessary mechanism of homoeostasis under times of extreme stress to avoid synaptic terminal destabilisation by conserving synaptic terminal area and volume. The triggers required to initiate ADBE events are worth considering. There are multiple options for the necessary events required to trigger ADBE:

- Total excess plasma membrane area exceeding a threshold level.
- Rate of addition to the plasma membrane area exceeding a threshold level.
- Rate of stimulus events triggering other physiological changes, such as transient increases in Ca^{2+} levels within the synaptic terminal.

Morton et al. (2015) determined experimentally that a combination of vesicle exocytosis and a suitably high level of calcium influx were necessary and sufficient to cause ADBE. The

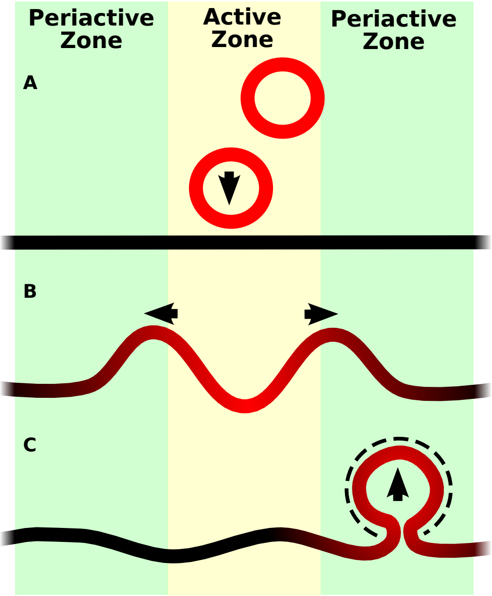

Figure 9.1: Effects of vesicle recycling on plasma membrane of pre-synaptic nerve terminal. Addition of extra membrane to the plasma membrane by vesicle exocytosis at the active zone (A) is compensated for by removal of membrane via endocytosis (C). If the nerve terminal perimeter is constrained by packing of neighbouring cells, then the membrane must fold to accommodate the extra material (B).

proposed mechanism was that calcium influx activates calcineurin to dephosphorylate dynamin I, initiating the dynamin I - syndapin I cycle described in Section 2.5.1 (Clayton et al., 2009)

The following mathematical model provides supporting evidence to this result by demonstrating the low likelihood that excess plasma membrane area alone is sufficient to trigger ADBE.

9.1 Hypothesis

ADBE is not initiated based on excess plasma membrane levels, but requires additional trigger inputs to happen. The calculated levels of membrane added under low and high levels of stimulation, with exocytosis and CME mechanisms operating at reported rates will support this hypothesis.

9.2 Parameter values from experimental work

Experimental work has provided kinetic and timing information related to these processes. As discussed in Chapter 2, these figures are not without some debate, but this model uses the current consensus. These values are based on assays operating at room temperature.

9.2.1 Recycling vesicle pool size

The estimated recycling pool size in a small CNS neuron synaptic terminal is approximately 100 vesicles. This means it is realistic for the entire vesicle pool to be exocytosed at high stimulation (120 vesicles in the following model).

9.2.2 Synaptic vesicle size

This is the surface area of a typical synaptic vesicle which has a fairly constant diameter of 40nm.

9.2.3 Exocytosis response to stimulus

The release rate does vary as a function of available vesicles for release, as the RRP and then the RP become depleted (Gordon and Cousin, 2013).

9.2.4 CME completion time

CME is estimated to take approximately 15 seconds to complete at room temperature (Balaji and Ryan, 2007; Granseth and Lagnado, 2008; Sankaranarayanan and Ryan, 2000). This is the time between initiation of the molecular interactions causing the endocytosis to happen, and the final scission of the vesicle from the plasma membrane. Experimental work has shown that CME slows as stimulus count increases 15s-60s (Sankaranarayanan and Ryan, 2000, Figure 4). This is considered in the model to follow.

9.2.5 CME concurrency

The adaptor proteins and clathrin required for CME are a limited resource. This parameter puts an upper bound on the number of CME events which may complete concurrently. CME concurrency is estimated at approximately 7 vesicles worth of protein (López-Murcia et al., 2014; Wilhelm, 2013; Wilhelm et al., 2014).

9.2.6 ADBE activity in response to stimulus

It has been shown experimentally that CME occurs at both low and high stimulus levels, but ADBE is activated on high intensity stimulation only (Clayton et al., 2008). The same work also demonstrated that most of the ADBE activity occurred during the stimulus train (approximately 70%).

9.2.7 ADBE endosome size

A typical ADBE endosome has the equivalent surface area of 14 vesicles. Based on the observed average diameters of synaptic vesicles and endosomes of 40nm and 150nm respectively (Cheung et al., 2010; Nicholson-Fish et al., 2016) and applying the formula for the surface area of a sphere $A = 4\pi r^2$. Endosomes are calculated as spherical as a simplification of the variance in morphology.

9.3 Bounds on plasma membrane maintenance efficiency

If the assumption is made that the endocytosis clearance mechanisms are continuously working at peak efficiency, limits on plasma membrane area dynamics can be found. While cell level biological processes are stochastic, this model is designed to establish bounds on behaviour, and so is deterministic.

9.4 Assumptions

For this model, the following assumptions are made:

- An exocytosed vesicle is of constant size. The lack of significant variation in vesicle size (and therefore surface area) allows the model to treat one vesicle as the unit measurement of surface area, and not model variable plasma membrane area changes with each exocytosis or CME event.
- An exocytosed vesicle is the same size as one recovered by CME.
- The density of the membrane remains fixed as membrane changes location between vesicle, plasma membrane, endosome and endocytosed vesicle.
- Only activity driven exocytosis occurs. Spontaneous exocytosis is not included.
- There are only two mechanisms of endocytosis; CME and ADBE. It is assumed that other forms of membrane recovery are not taking place (such as kiss-and-run or ultrafast endocytosis).
- CME only starts when all the necessary CME molecules are available. There will be no CME events which fail to complete due to lack of resources.
- CME starts as soon as there is extra plasma membrane material available. The mechanics of the CME trigger are not relevant.
- The CME components are immediately available for the next CME event after scission takes place.
- The plasma membrane synaptic terminal boundary is fixed for the duration of an experimental assay. There is no lateral movement of membrane into or out of the synaptic terminal, and the terminal boundary does not grow in response to membrane addition. This assumption does not hold over longer time-scales. *In vivo* this boundary is thought to be structurally reinforced by packing around the site of the synapse by glia and other neurons.
- The model strives for homoeostasis; in this case that all exocytosed membrane will eventually be endocytosed again.
- The model is valid for *in vitro* room temperature parameters listed in Section 9.2. Different parameter values produce different limits on plasma membrane maintainability (Micheva and Smith, 2005; Ryan et al., 1996).

- Synapses *in vitro* have been shown to recover from the long stimulus trains used, so the synaptic terminal can be expected to handle them effectively.

9.5 Stimulus

The initiation of the cycle is controlled by the stimulus train which evokes exocytosis (and triggers potentially ADBE via calcium influx). This external stimulus has two parameters, frequency and duration. This model uses low frequency stimulus (10Hz for 40s) and high frequency stimulus (40Hz for 10s), with the total stimulus count the same (400).

9.6 Exocytosis

In response to a stimulus train, exocytosis can be simulated with vesicles from both the RRP and RP. At the level of detail of this model, the distinction between the two pools of vesicles is not required, only the overall kinetics of exocytosis is required. For completeness however, the following section discusses possible effects of two-mode kinetics; a fast followed by a slow phase, as may be predicted if the interplay between RRP and RP was modelled.

The parameters of this stage are the total number of vesicles available to exocytose (including recycled vesicles if necessary), the release probability in response to stimulus, and the overall changes in release rate during a stimulus train.

Bounds on the contribution of exocytosis to plasma membrane area over time can be established. Take 10Hz 40s, total stimulus count 400 stimuli. In (Cheung et al., 2010), it was shown that sustained stimulus (40Hz) could continue to cause release after 80s (with FM dye). In (Gordon and Cousin, 2013), pHluorin traces showed a distinct slowing of release after 30s at 10Hz. The conflicting results are due in part to the different markers used; FM dye release is slower than pHluorin response to pH changes. This model will use the faster of the two reports.

There is no evidence of exocytosis speeding up during a stimulus train. Therefore, exocytosis either continues at a steady rate during a stimulus train, or slows down as individual release events become less probable as immediately releasable vesicles reduce in number. This can be modelled as a linear or exponential release rate with a single or multiple modes.

- Single mode linear release (Figure 9.2a). Vesicles are released at a constant release rate of n vesicles per second under constant stimulus.

- Single mode exponential release (Figure 9.2b). Vesicle release rate follows an exponential function with time constant T.

- Two mode linear release (Figure 9.2c). Vesicles are released at a constant release rate of n vesicles per second for the first x vesicles, then at a lower rate of m vesicles per second.

- Two mode exponential release (Figure 9.2d). Vesicle release rate follows an exponential function with time constant T, for the first x vesicles, then at a lower exponential rate of *m* vesicles per second.

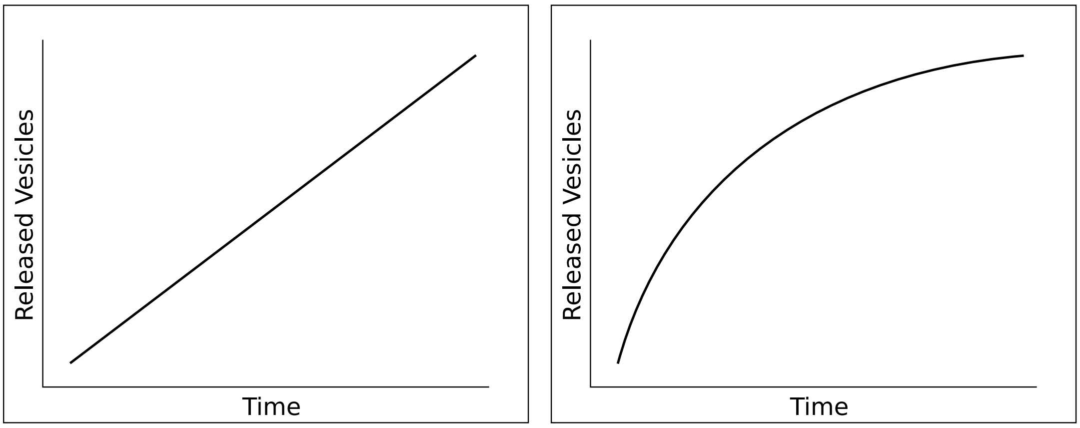

(a) Single mode linear release.

(b) Single mode exponential release.

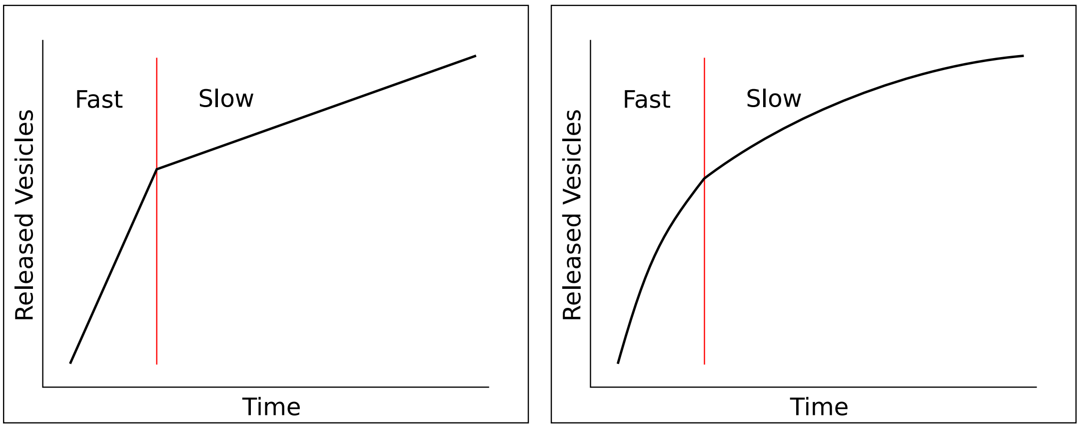

(c) Two mode linear release.

(d) Two mode exponential release.

Figure 9.2: Illustrations of vesicle release rates over time. (a,b) show single mode release. (c,d) show two mode release, a fast initial stage followed by a slow stage.

Taking exocytosis alone, the peak plasma membrane area is simply the total number of released vesicles N.

9.7 Exocytosis and CME

Consider now an ideal form of CME, operating at maximum efficiency. What is the possible ability of CME to recover the excess membrane and reduce the plasma membrane deformation. The available parameters are:

- CME event completion delay (D_{CME}) - the time taken for a single CME event to occur, from initiation through to the vesicle being fully formed and the CME resources released and available for the next CME event.
- CME concurrency (C_{CME}) - the number of CME events which may occur simultaneously, a function of the available CME resources.

To establish bounds on the performance, it is assumed CME works without initiation delay, and never fails due to unavailability of resources in the vicinity of an individual CME event. If it is possible for a single CME event to take place at a particular time (there are sufficient plasma membrane and CME resources), then that CME event initiates immediately. CME events also remove plasma membrane area immediately upon initiation, rather than after scission, again to establish best case bounds on plasma membrane area.

Exocytosis produces N vesicles worth of additional plasma membrane material, so there must be N CME events to return to baseline. The shortest time for CME to complete this is

$$\frac{N - C_{CME}}{C_{CME}} \times D_{CME}$$

where $N - C_{CME}$ endocytic events must occur with concurrency C_{CME} and delay D_{CME}. The last C_{CME} events remove plasma membrane immediately as described above, so do not count towards the overall completion time for the purposes of establishing bounds.

CME at peak operation removes plasma membrane material at a rate of C_{CME}/D_{CME} vesicles per second.

At the start of a stimulus train, there is not enough excess plasma membrane material for CME to operate at full capacity. It takes a short time for exocytosis to add enough membrane to the plasma membrane, and this time depends on the release mode of exocytosis. However this works out to only a small difference in overall CME recovery times. After the initial start delay, CME operates at peak efficiency while there is greater than C_{CME} material on the plasma membrane.

While C_{CME}/D_{CME} is less than the exocytosis rate, the plasma membrane area continues to increase. With single mode linear exocytosis, the peak plasma membrane area occurs immediately after the last exocytosis event N at time T_N. At this point in time, there have been at most $T_N \times C_{CME}/D_{CME}$ complete CME events, and C_{CME} events still in progress. This makes the peak area

$$N - T_N \times \frac{C_{CME}}{D_{CME}} - C_{CME}$$

Using parameter values $C_{CME} = 7, N = 120, D_{CME} = 15$ predicted in the current literature, the peak area is reduced by the introduction of CME only to approximately 94 vesicles at 10Hz 40s stimulus. At 40Hz 10s stimulus, the peak area would be at best, 112 vesicles.

Repeating the above analysis with a single mode exponential exocytosis release rate, the release slows as the stimulus train progresses. This means potentially the point at which exocytosis becomes slower than the peak CME rate (C_{CME}/D_{CME}) may be earlier in the stimulus train (before all N vesicles have been exocytosed). Representing the cumulative number of vesicles exocytosed N_t by time t as an inverted exponential decay function

$$N_t = N\left(1 - e^{\frac{-t}{\tau}}\right)$$

where N is the total number of exocytosed vesicles as before, and τ is the exponential decay constant. Solving for τ and taking the end of stimulation to be the time when the last vesicle is exocytosed, $N_t = N - 1$

$$N - 1 = N\left(1 - e^{\frac{-t}{\tau}}\right)$$

$$\tau = \frac{t}{\ln N}$$

For 120 total vesicles exocytosed, this gives $\tau = 8.355$ for low stimulus train ($t = 40s$), and $\tau = 2.089$ for high stimulus train ($t = 10s$).

The rate of exocytosis over time is

$$\frac{d}{dt}N_t = \frac{1}{\tau}(N - N_t)$$

The relevant time-point here is when the exocytosis rate equals the CME recovery rate (C_{CME}/D_{CME}). At this point, the peak added plasma membrane area has been achieved. Solving for N_t

$$\frac{C_{CME}}{D_{CME}} = \frac{1}{\tau}(N - N_t)$$

$$N_t = N - \tau\frac{C_{CME}}{D_{CME}}$$

Again using parameter values $C_{CME} = 7, N = 120, D_{CME} = 15$ predicted in the current literature, and the τ values calculated above, the peak area occurs when $N_t = 116$ vesicles under slow stimulus, and $N_t = 119$ vesicles under high stimulus. This is not a lot less than the total vesicles endocytosed. Calculating the release times of these N_t by taking the exponential release function and solving for t

$$N_t = N\left(1 - e^{\frac{-t}{\tau}}\right)$$

$$t = -\tau \ln\left(\frac{N - N_t}{N}\right)$$

giving $t = 28$s for slow stimulus and $t = 10$s for fast stimulus. The net peak plasma area is

$$M - T_M \times \frac{C_{CME}}{D_{CME}} - C_{CME}$$

where M vesicles have been added at time T_M. This gives a peak area using an exponential exocytosis function of 95 vesicles under slow stimulus and again 112 vesicles under high stimulus. This is at least as high as that for linear exocytosis.

Using two mode linear or exponential release functions increase the peak plasma membrane area yet again, as the faster initial release of vesicles is not compensated by potentially reaching the exocytosis and CME rate balance point earlier in the stimulus train.

In both linear and exponential exocytosis cases the plasma membrane is significantly perturbed at both low and high stimulus levels. This lends additional weight to the experimental observations that plasma membrane excess area alone is not a sufficient trigger for ADBE (Morton et al., 2015). Low stimulation levels cause a large excess of plasma membrane, yet ADBE has been reported to not occur in this situation (Clayton et al., 2008).

9.8 Exocytosis, CME and ADBE

There are not concrete bounds on the concurrency of ADBE, so there is no limit to what rate it can recover plasma membrane and maintain homoeostasis. In the calculations above an average of 8 endosome events at time-points when sufficient excess plasma membrane was available would suffice to maintain the peak plasma membrane area at < 14 vesicles (14 being the average surface area of an endosome in vesicles).

The shortest time for endocytosis to complete is also highly variable. As the literature notes ADBE is largely completed by the end of a stimulus train (Clayton et al., 2008), so the completion time can reasonably be dependent on the remaining membrane after the last ADBE and exocytosis event has taken place.

9.9 Conclusions

The above results show that it is highly unlikely that the quantity of excess plasma membrane area is sufficient trigger for ADBE. The models show that even if CME is operating at peak efficiency given the model parameter values and assumptions, the difference in peak excess area between low and high stimulus conditions is not large (barely larger than a single bulk endosome). This necessitates the ADBE trigger to require additional inputs such as the calcium trigger described in Clayton et al. (2009); Morton et al. (2015). This is not a novel result, but good supporting evidence for the existing consensus.

Chapter 10

Conclusions and contributions

Synaptic vesicle recycling is an area of neuroscience with many opportunities for collaboration with computational approaches. Experimental data analysis has implicit awareness of the experimental protocols. There are advantages to using this protocol information in computational approaches including refinement of the data analysis result quality.

The project to quantify ROI drift over a time-series provides additional characterisation of experimental data analysis. It gives the researcher the opportunity to check assumptions of ROI accuracy, and provides indicators of when ROI selection may need to be quality controlled more closely. A simple unbiased measure of this movement allows the optimisation of this quality control by checking large numbers of assays rapidly. The correct location of ROIs is crucial to the data analysis in determining synaptic behaviour, improving quality control is therefore an obvious benefit.

Automated segmentation has been in development for some years in the context of synaptic fluorescence imaging. It has variable uptake in neuroscience labs depending on the experimental protocols and image data in use, and the requirements of the analysed data. Manual processing is still common, as a trained researcher manually segmenting ROIs may still generate higher quality results than a semi-automated or automated algorithm. However, manual processing requires substantial training and review of results to control variance in results between researchers.

The work here demonstrates again that protocol information can be used to improve the quality of the automated segmentation process. It shows that using image processing to isolate the active synapses prior to segmentation improves the quality of the resulting ROI set in some experiment types.

Incorporating this processing as a plugin in common image processing software provides extra capabilities to researchers to reduce their workload per assay and improve the quality and size of resulting ROI sets.

FM-Sim demonstrates the benefit of incorporating protocol knowledge into computational models. The novel handling of protocol regime changes in a researcher-targeted simulation application allows easy description of experimental events. The Bayesian inference engine allows determination of model parameters from observed data. It is hoped the rate constants and the provided recycling model will be useful in developing mechanistic theories of synaptic vesicle recycling.

Finally, the mathematical modelling of plasma membrane area behaviour during synapse stimulation demonstrates the utility of modelling in corroborating biological results. Providing hard bounds on CME behaviour under stimulation given current experimentally derived parameters allows possible recycling scenarios to be eliminated.

Overall this work has provided insights into synaptic vesicle recycling from a computational viewpoint, and provided a number of software tools to assist and improve the quality control of data processing in synaptic vesicle recycling research.

Some of the applications developed during the course of this work are in routine use in the Cousin laboratory to assist microscopy image analysis. It is hoped that these applications will see wider use in the future. The ROI trace selection tool for instance is useful for analysis of neuroscience image data, and any other fields where selection of time-series traces is a required laboratory task.

Chapter 11

Future Work

There are many directions the components of this work can be taken:

ROI drift characterisation: Chapter 6 focusses on one aspect of ROI behaviour most directly relevant to output data quality. There are many other aspects of synapse behaviour as reported by time-series imaging which could be characterised. Using the existing time-series information, visible synapse area over time could be characterised. Better knowledge of how closely a ROI of fixed size and location encloses synapses could be used to tune ROI size for individual experiments. It is reasonable to assume that less background information pixels included in the intensity trace improves the signal from the synapses.

The ROI drift knowledge could be used to extend existing tools for ROI motion tracking. The ideal would be fully automated ROI tracking with no need for user input. However, it is debatable if the potential intensity improvement found in Chapter 6 is worth the additional complexity, given the current image noise in the base data. Perhaps improvements in data capture or post-capture filtering will make the intensity gains worthwhile in the future.

Automated ROI segmentation: Automated segmentation of synaptic terminal ROIs currently works well for pHluorin image data. Obtaining similar improvement for FM dye image data would allow effort savings in those experiments too.

The current implementation of the segmentation software is set at a fixed ROI size for performance reasons. A more flexible ROI choice will be of benefit to laboratories. This is largely a software development and verification task, and should not be particularly difficult to manage.

There are possibilities for extending the scope of the study. Comparative evaluation of background subtraction algorithm and parameters is one direction the evaluation could be taken. Applying the algorithms for background subtraction may yield further segmentation quality improvements.

Building up better characterisation of the segmentation parameters; perhaps linking parameter choice to identifiable properties of the source data, for example fluorescent marker protein or cell type specific parameter ranges, could be of use to researchers. The less tuning required per experiment or assay for segmentation the better.

If automated parameter discovery is not feasible, then performance improvements to allow more real-time response to segmentation parameter changes will benefit the researcher. The user experience would be improved if segmentation parameter changes resulted in near immediate results in the segmented ROI set. This feature would have to be implemented and used with care to minimise user bias.

An additional feature would be to combine ROI sets gathered using multiple imaging channels. For example, some of the available time-series datasets also have a single frame mCerulean (a cyan fluorescent protein) image used to identify transfected neurons. Comparing ROI sets over two channels would allow automated partitioning of the time-series data between transfected and non-transfected synapses.

FM-Sim protocol simulator: FM-Sim is currently a good demonstration of the end-user extension to a fixed computational model; allowing protocol definition and rate inference. A library of defined protocols, inferred rate constants and supporting observed data would allow further research into trends on rate constant behaviour across multiple protocols. Increasing this library of protocol data and studying the trends in rates is a good direction for future work. Adding capability for automated sensitivity analysis to the inference engine would also be useful.

Currently the Bayesian inference engine takes time to converge on optimal parameter matches. Any computational approaches to improve the performance or final accuracy of inferred match would be of use.

Plasma membrane modelling: Finally, the plasma membrane model has many opportunities for further development. The basic model could be taken forward as either a deterministic or stochastic model to determine the sensitivity of the model outputs on membrane stability. The domain offers many extensions to the current model, including 3D membrane modelling, incorporating calcium micro-domains affecting ADBE triggering, demonstrating the effects membrane folding has on the efficiency of synaptic signalling during membrane recovery times, and taking into account the synaptic structural proteins and their effects on membrane folding.

Overall, synaptic vesicle recycling research is a rich domain for future computational modelling and data analysis work.

Appendix A

Implementation notes

A.1 Batch image processing - segmentation analysis required optimisation to base ImageJ code.

The default image process type was assumed to be 16-bit grayscale as it suited the bulk of the microscopy data under analysis. The default code then targeted the `short` data type, while allowing fall-back to the more flexible but slower ImageJ code where necessary. This allowed a number of optimisations:

- Most image processing code was converted to integer only, rather than the default floating point processing used by ImageJ to retain flexibility.
- By checking image format at the entry point to the large functions (external API calls only), all of the image type selection complexity could be removed.
- For the ImageJ core classes copied and replaced, all functions not directly required by the ROI characterisation and segmentation code was removed, and the data structures simplified where possible.
- `java.lang.Math` calculations were replaced by Apache Commons `FastMath` equivalents where the optimisation resulted in a significant performance improvement.
- Some data structures (notably `ArrayLists`) were replaced by faster equivalents, or the code restructured to allow the use of different, faster data structures (usually from the Apache Commons Collections package).
- Where feasible, caching of calculations and processing was performed. Notably, image registration data retrieval was performed only once per assay, and the metadata and if necessary the registered images were cached for future runs.
- As Metropolis-Hastings iteration of image ROI segmentation parameters required $dF/F0$ intensity traces for each segmented ROI, and as these intensity traces were independent of the static image, algorithm and segmentation parameters used, but only depended on

the pixel location of the ROI centre and the time-series data used, the traces were cached for all processing/segmentation of each assay, indexed by pixel location.

- ROI size was fixed for the all of the test datasets (after confirming appropriate with ROI characterisation). This allowed ROI analysis operations to be streamlined, with a hard-coded set of pixels to be investigated directly, rather than the more flexible ImageJ approach of mask calculation.
- Similarly, thresholding for particle analysis could be performed in-line rather than creating thresholded images, or using the more complex thresholding and threshold masking routines built into ImageJ.

Rejected optimisation choices:

- Selecting smaller field of view within image - as many of the segmentation operations involve scanning pixel by pixel, selecting a smaller test range within the bounds of the image would speed up processing time. This choice was discarded however, as either the loss of manually segmented ROIs outside the field of view, or the complexity (and potential introduced bias) of concentrating on image areas where manual ROI selections were concentrated was prohibitive.
- A discarded optimisation was replacing the `ParticleAnalyser` ImageJ class with a significantly faster algorithm. The implementation was discarded as it required replacement of the circularity measure of `ParticleAnalyser` with a simpler approximation.

  The `ParticleAnalyser` definition of circularity was defined as

  $$\text{circularity} = 4\pi \frac{\text{pixels in ROI}}{\text{perimeter of ROI}^2}$$

  giving a range of 0 to 1, with 1 being approximately a circle.

  The replacement definition of circularity was defined as

  $$\text{circularity} = \frac{\text{pixels in ROI}}{\text{pixels in ellipse filling same rectangular bounds as ROI}}$$

  giving a range capped from 0 to 1, with 1 being a ROI with at least the same area as ellipse filling the ROI bounds.

  Running the modified algorithm on the test data set showed reduced overall scores for segmentation quality, so the modified algorithm was discarded.

The end result was that for the operations needed to be repeated lots of times (as within the Metropolis-Hastings iteration), the code was heavily optimised - close to the limit of feasible speed improvement. Further significant speed improvements are unlikely. Amdhal's law suggested that was a good time to stop.

The classes copied and modified in whole or part within this implementation are:

- From ImageJ:
    - `ij.plugin.filter.ParticleAnalyzer`
    - `ij.gui.Wand`
    - `ij.Process.PolygonFiller`
- `Time_Series_Analyzer_V2_0_rev1`

Credits to the original authors, and the many contributions by members of the ImageJ and FIJI projects.

A.2 Architecture and data-type size and accuracy

The implementation was run on a 32-bit Java architecture. This has the potential drawbacks of reduced addressable memory of approximately 2.3 Gb, and reduced accuracy and capacity of primitive data-types, compared with 64-bit.

The data-types were not seen to be an issue, as the most common image type was 16-bit, and the largest integer value would be from summation of pixels within ROIs. Taking a ROI of 64 pixels (more than needed) would require a total of 22 bits, so 32-bit `ints` would be fine.

For floating point operations, 64-bit `doubles` are more than sufficient for accuracy in calculations to the extent required for image analysis, given the noise in the initial data input.

The 2.3 Gb memory limit was more of an issue. However the memory constraint in handling and processing large time-series images encouraged good coding practices in being careful with memory management - not creating copies of data structures unnecessarily, and generally being frugal with creation of objects. This had the additional benefit of generally speeding up the processing by avoiding unnecessary object creation and memory copying overhead.

It also made the code more portable for use on laboratory machines.

A.3 Execution platform specifications

All image analysis and simulations were executed on an 4 core Intel i7 CPU 930, running Ubuntu 32-bit 14.04, and Java execution environment 32-bit Java 1.7.0 OpenJDK. Image processing code was based on ImageJ version 1.51b.

Appendix B

Automated segmentation complete results

The following are the detailed results of the automated segmentation evaluation described in Chapter 7.

B.1 Parameter: Brightness Fraction

Table B.1: Brightness Fraction for both FM dye and pHluorin experiment types broken down by algorithm and image. Each value shown is the mean (and standard deviation) of the best scoring segmentation parameter combination for each assay of that category. BS means background subtracted image.

	Bergsman		Fish		Yona	
	Non BS	BS	Non BS	BS	Non BS	BS
FM dye (particles = 1000)						
Overall Max	0.24 (0.13)	0.22 (0.26)	0.34 (0.2)	0.22 (0.22)	0 (0)	0 (0)
Overall Mean	0.41 (0.27)	0.22 (0.18)	0.2 (0.13)	0.19 (0.14)	0 (0)	0 (0)
Diff1 Start	0.3 (0.2)	0.24 (0.26)	0.31 (0.23)	0.26 (0.21)	0 (0)	0 (0)
Diff1 End	0.38 (0.28)	0.24 (0.23)	0.29 (0.21)	0.18 (0.21)	0 (0)	0 (0)
Diff1	0.26 (0.18)	0.33 (0.26)	0.32 (0.29)	0.21 (0.24)	0 (0)	0 (0)
pHluorin (particles = 200)						
Overall Max	0.31 (0.26)	0.29 (0.26)	0.29 (0.22)	0.34 (0.27)	0 (0)	0 (0)
Overall Mean	0.18 (0.13)	0.31 (0.23)	0.27 (0.22)	0.27 (0.19)	0 (0)	0 (0)
Diff1 Start	0.3 (0.22)	0.27 (0.22)	0.24 (0.15)	0.27 (0.24)	0 (0)	0 (0)
Diff1 End	0.31 (0.3)	0.37 (0.22)	0.29 (0.21)	0.31 (0.24)	0 (0)	0 (0)
Diff1	0.26 (0.17)	0.35 (0.21)	0.28 (0.23)	0.3 (0.16)	0 (0)	0 (0)
Diff2 Start	0.23 (0.29)	0.31 (0.19)	0.22 (0.11)	0.28 (0.21)	0 (0)	0 (0)
Diff2 End	0.21 (0.2)	0.24 (0.24)	0.24 (0.2)	0.17 (0.13)	0 (0)	0 (0)
Diff2	0.15 (0.13)	0.37 (0.24)	0.32 (0.23)	0.29 (0.24)	0 (0)	0 (0)
Diff1 ∪ Diff2	0 (0)	0 (0)	0 (0)	0 (0)	0 (0)	0 (0)
Diff1 ∩ Diff2	0 (0)	0 (0)	0 (0)	0 (0)	0 (0)	0 (0)

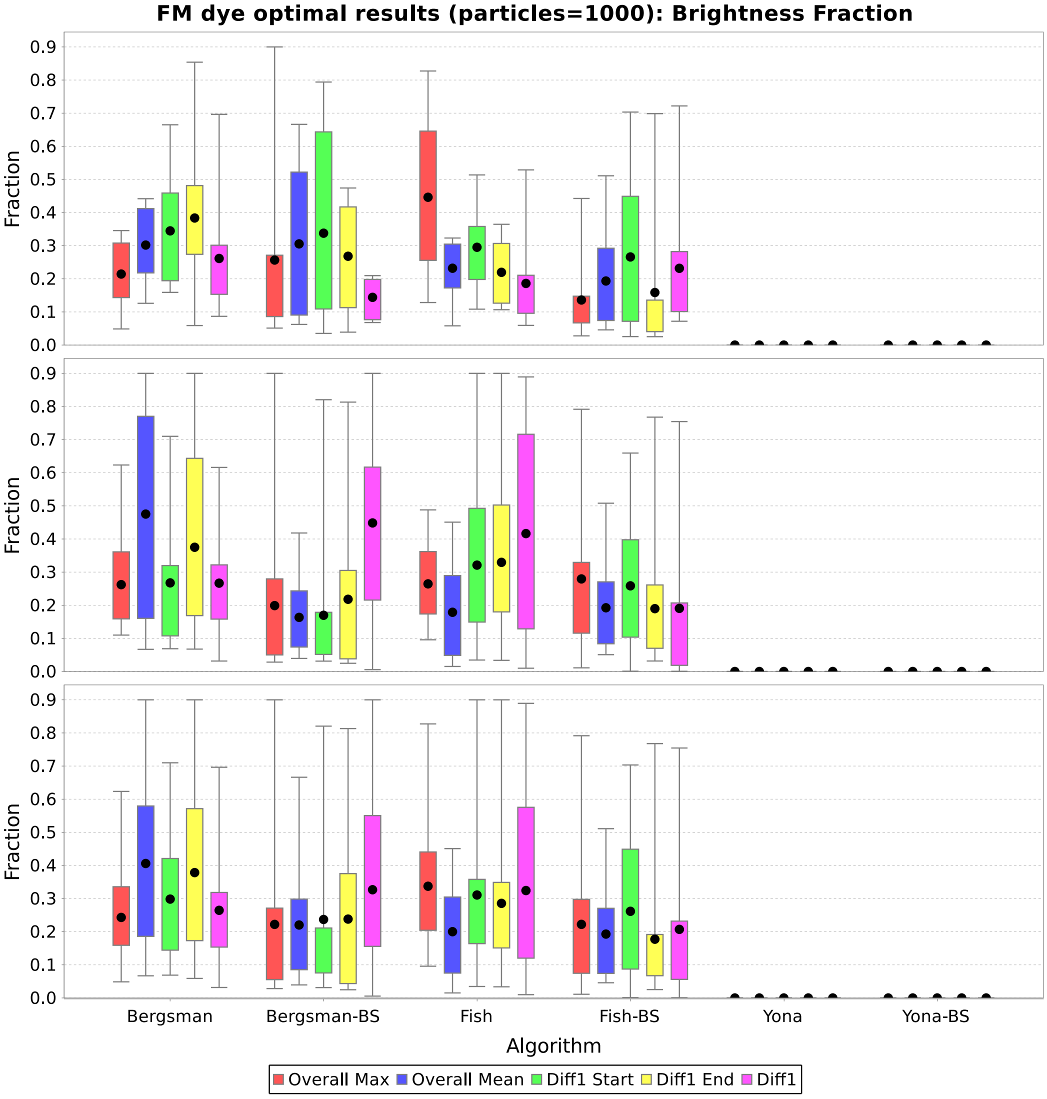

Figure B.1: Parameter Brightness Fraction range values with FM dye assays. Boxes show interquartile ranges, lines show maxima and minima, and black dots show mean values for each combination of experiment, image and algorithm.

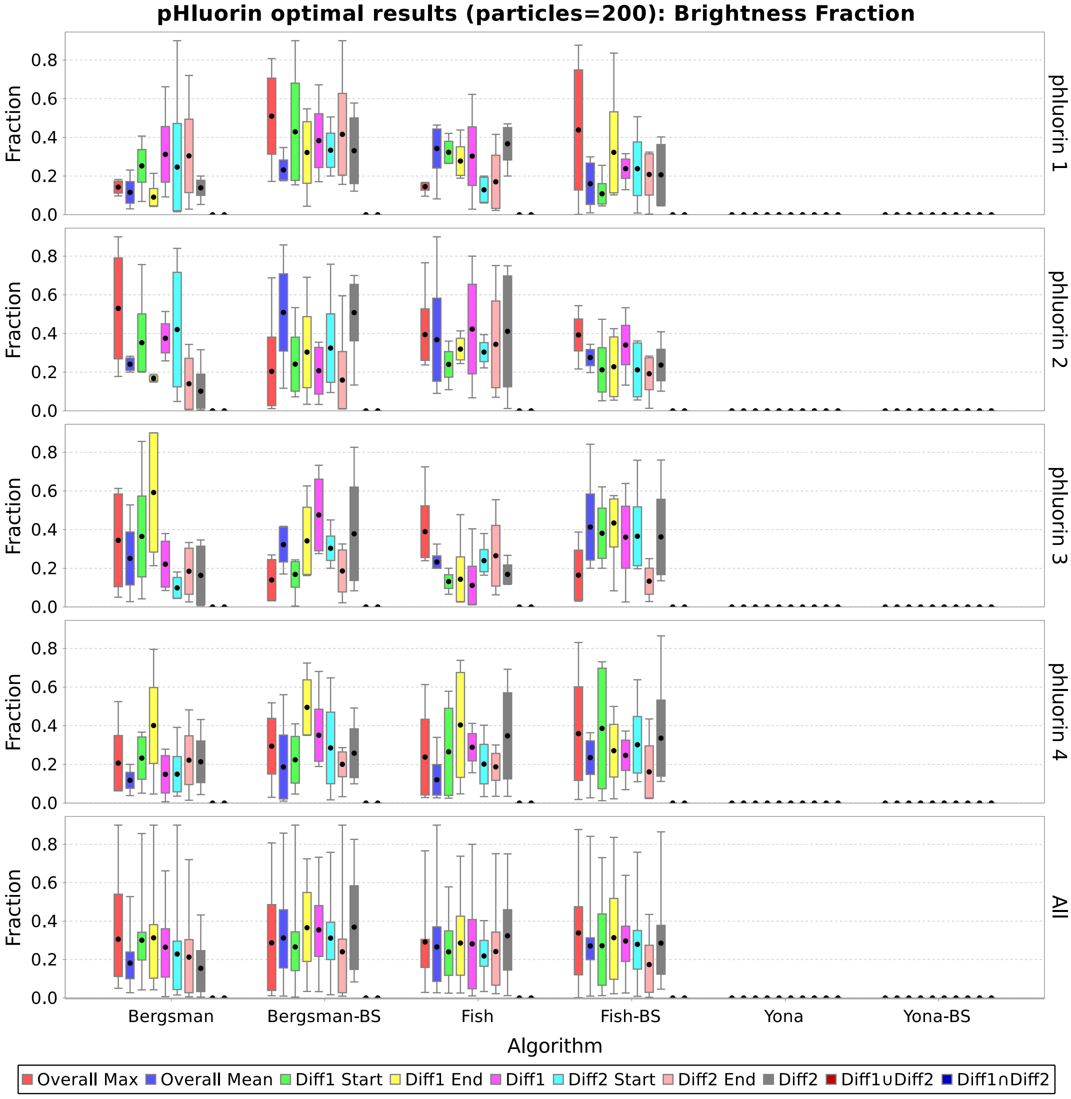

Figure B.2: Parameter Brightness Fraction range values with pHluorin assays. Boxes show interquartile ranges, lines show maxima and minima, and black dots show mean values for each combination of experiment, image and algorithm.

B.2 Parameter: Minimum ROI Size

Table B.2: Minimum ROI Size for both FM dye and pHluorin experiment types broken down by algorithm and image. Each value shown is the mean (and standard deviation) of the best scoring segmentation parameter combination for each assay of that category. BS means background subtracted image.

	Bergsman		Fish		Yona	
	Non BS	BS	Non BS	BS	Non BS	BS
FM dye (particles = 1000)						
Overall Max	12.75 (8.69)	11.1 (10.74)	27.1 (19.26)	29.25 (21)	0 (0)	0 (0)
Overall Mean	16.35 (11.85)	9.35 (11.85)	20.4 (16.95)	24.55 (20.47)	0 (0)	0 (0)
Diff1 Start	18.65 (20.38)	13.9 (10.24)	27.6 (26.28)	16.6 (16.61)	0 (0)	0 (0)
Diff1 End	23.95 (16.29)	15.65 (16.38)	23.8 (20.74)	24.3 (21.14)	0 (0)	0 (0)
Diff1	20.4 (18.2)	20.65 (14.1)	35.5 (22.58)	20.2 (15.29)	0 (0)	0 (0)
pHluorin (particles = 200)						
Overall Max	2.81 (2.46)	3.75 (3.04)	5.19 (6.81)	4.81 (8.9)	0 (0)	0 (0)
Overall Mean	3.25 (2.72)	3.31 (3.59)	5.38 (9.52)	4.62 (6.9)	0 (0)	0 (0)
Diff1 Start	5.75 (5.04)	3.88 (3.01)	6.31 (4.24)	11.12 (14.86)	0 (0)	0 (0)
Diff1 End	4.25 (5.13)	4.44 (6.47)	6.88 (8.11)	3.81 (4.92)	0 (0)	0 (0)
Diff1	5.12 (6.83)	7.25 (17.02)	5.31 (5.1)	6.12 (10.44)	0 (0)	0 (0)
Diff2 Start	5.88 (6.12)	4.12 (3.86)	8.12 (12.3)	11 (13.99)	0 (0)	0 (0)
Diff2 End	4.44 (5.01)	3.88 (5.44)	5.94 (9.42)	3.06 (3.82)	0 (0)	0 (0)
Diff2	2 (1.83)	2.94 (2.79)	3.56 (7.41)	5.56 (9.84)	0 (0)	0 (0)
Diff1 ∪ Diff2	0 (0)	0 (0)	0 (0)	0 (0)	0 (0)	0 (0)
Diff1 ∩ Diff2	0 (0)	0 (0)	0 (0)	0 (0)	0 (0)	0 (0)

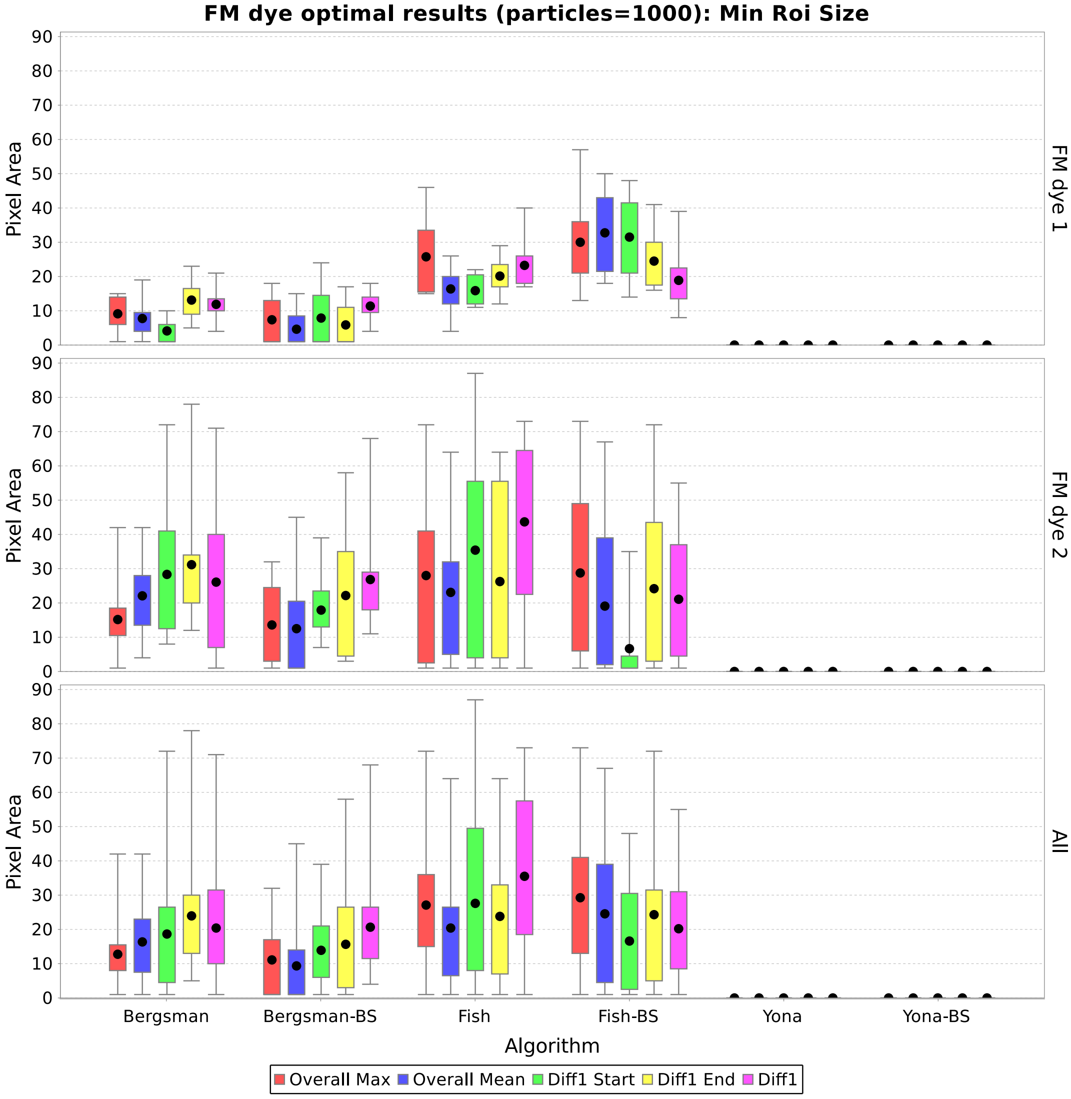

Figure B.3: Parameter Minimum ROI Size range values with FM dye assays. Boxes show interquartile ranges, lines show maxima and minima, and black dots show mean values for each combination of experiment, image and algorithm.

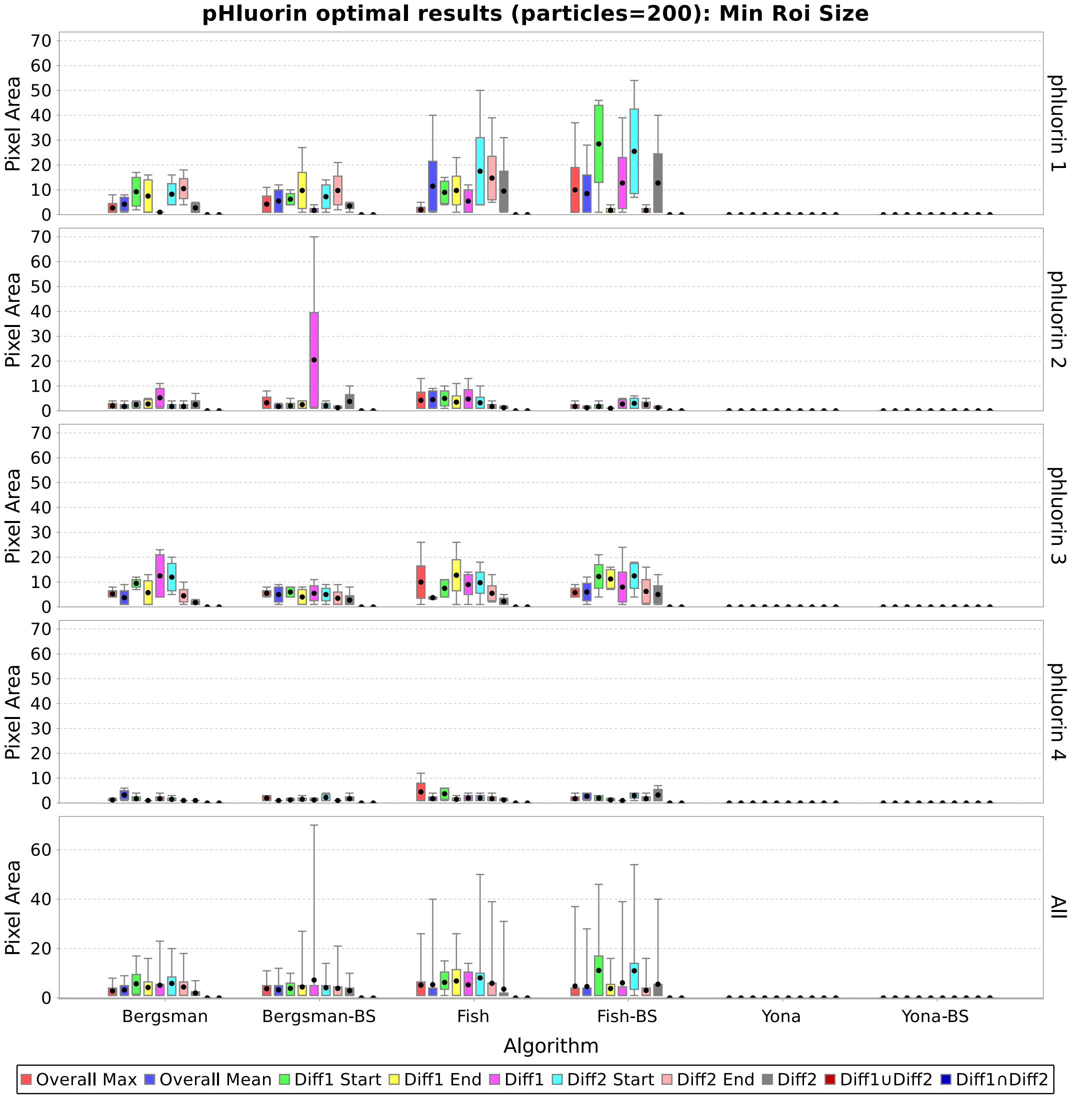

Figure B.4: Parameter Minimum ROI Size range values with pHluorin assays. Boxes show interquartile ranges, lines show maxima and minima, and black dots show mean values for each combination of experiment, image and algorithm.

B.3 Parameter: Maximum ROI Size

Table B.3: Maximum ROI Size for both FM dye and pHluorin experiment types broken down by algorithm and image. Each value shown is the mean (and standard deviation) of the best scoring segmentation parameter combination for each assay of that category. BS means background subtracted image.

	Bergsman		Fish		Yona	
	Non BS	BS	Non BS	BS	Non BS	BS
FM dye (particles = 1000)						
Overall Max	80.1 (25.2)	76.1 (23.74)	65.55 (27.23)	80.2 (17.04)	0 (0)	0 (0)
Overall Mean	77.6 (24.27)	79.55 (17.75)	78.1 (26.15)	82.7 (22.56)	0 (0)	0 (0)
Diff1 Start	91 (12.5)	84.25 (18.98)	81.65 (19.62)	78.75 (27.34)	0 (0)	0 (0)
Diff1 End	81.5 (20.24)	86.45 (14.13)	81.3 (17.84)	78.7 (16.41)	0 (0)	0 (0)
Diff1	84.95 (15.54)	73.2 (24.33)	77.1 (19.92)	73.3 (26.47)	0 (0)	0 (0)
pHluorin (particles = 200)						
Overall Max	85.19 (18.85)	78.88 (23.79)	83.94 (19.36)	77.75 (22.79)	0 (0)	0 (0)
Overall Mean	80.62 (19.74)	88 (18.3)	85.25 (15.6)	91.69 (12.48)	0 (0)	0 (0)
Diff1 Start	79.19 (22.91)	89.69 (13.12)	78.19 (19.15)	77.06 (22.1)	0 (0)	0 (0)
Diff1 End	84.94 (16.87)	82.44 (18.55)	74.75 (28.74)	75.38 (30.4)	0 (0)	0 (0)
Diff1	80.56 (27.8)	79.94 (18.68)	83.56 (17.34)	85.06 (18.46)	0 (0)	0 (0)
Diff2 Start	90.31 (13.97)	74.5 (25.8)	82.88 (25.26)	85.69 (17.78)	0 (0)	0 (0)
Diff2 End	88.56 (15.24)	82.94 (15.83)	86.38 (13.72)	86.81 (19.99)	0 (0)	0 (0)
Diff2	72.75 (27.53)	88.88 (12.87)	84.25 (22.41)	89.75 (17.32)	0 (0)	0 (0)
Diff1 $\cup$ Diff2	0 (0)	0 (0)	0 (0)	0 (0)	0 (0)	0 (0)
Diff1 $\cap$ Diff2	0 (0)	0 (0)	0 (0)	0 (0)	0 (0)	0 (0)

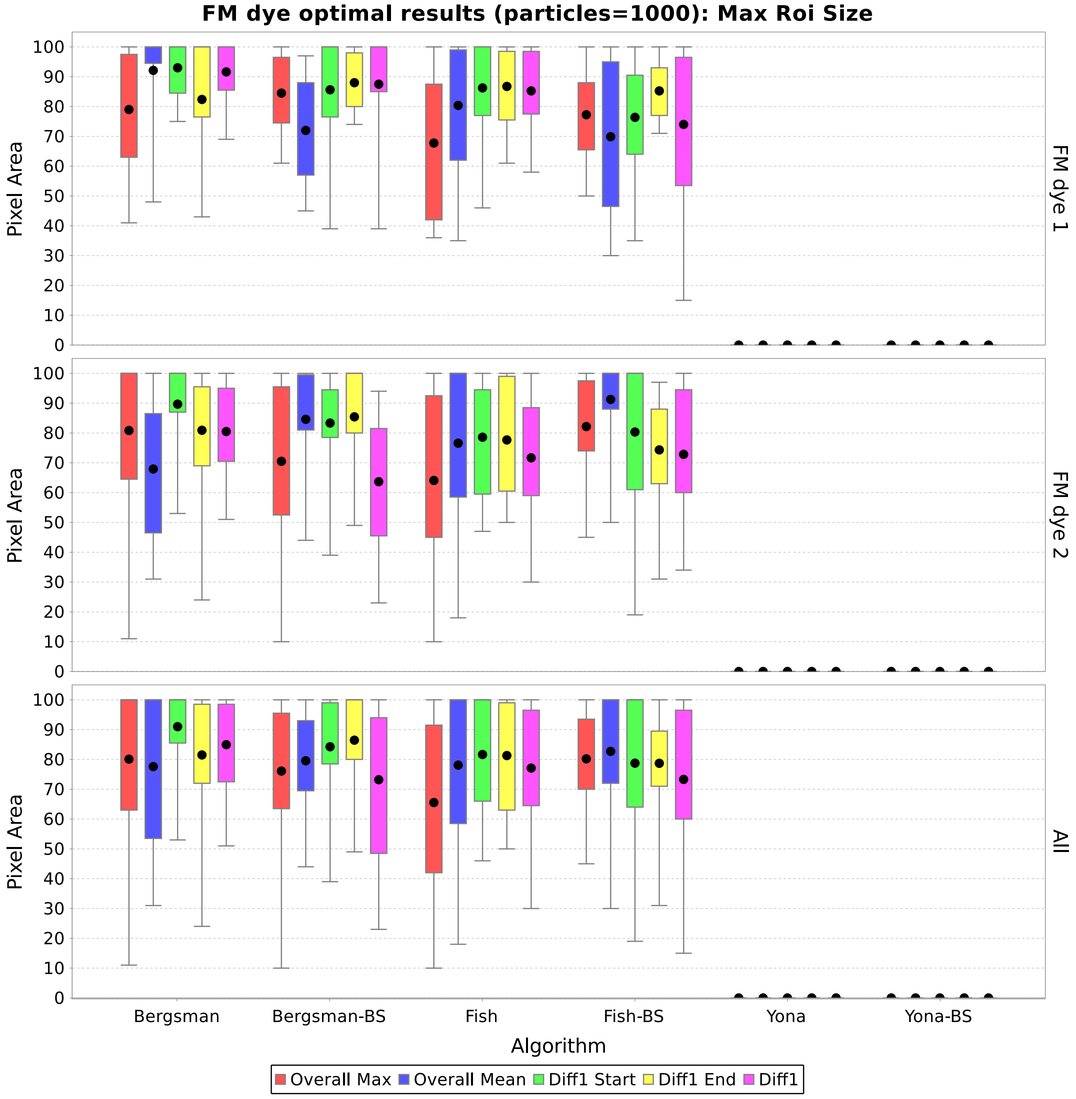

Figure B.5: Parameter Maximum ROI Size range values with FM dye assays. Boxes show interquartile ranges, lines show maxima and minima, and black dots show mean values for each combination of experiment, image and algorithm.

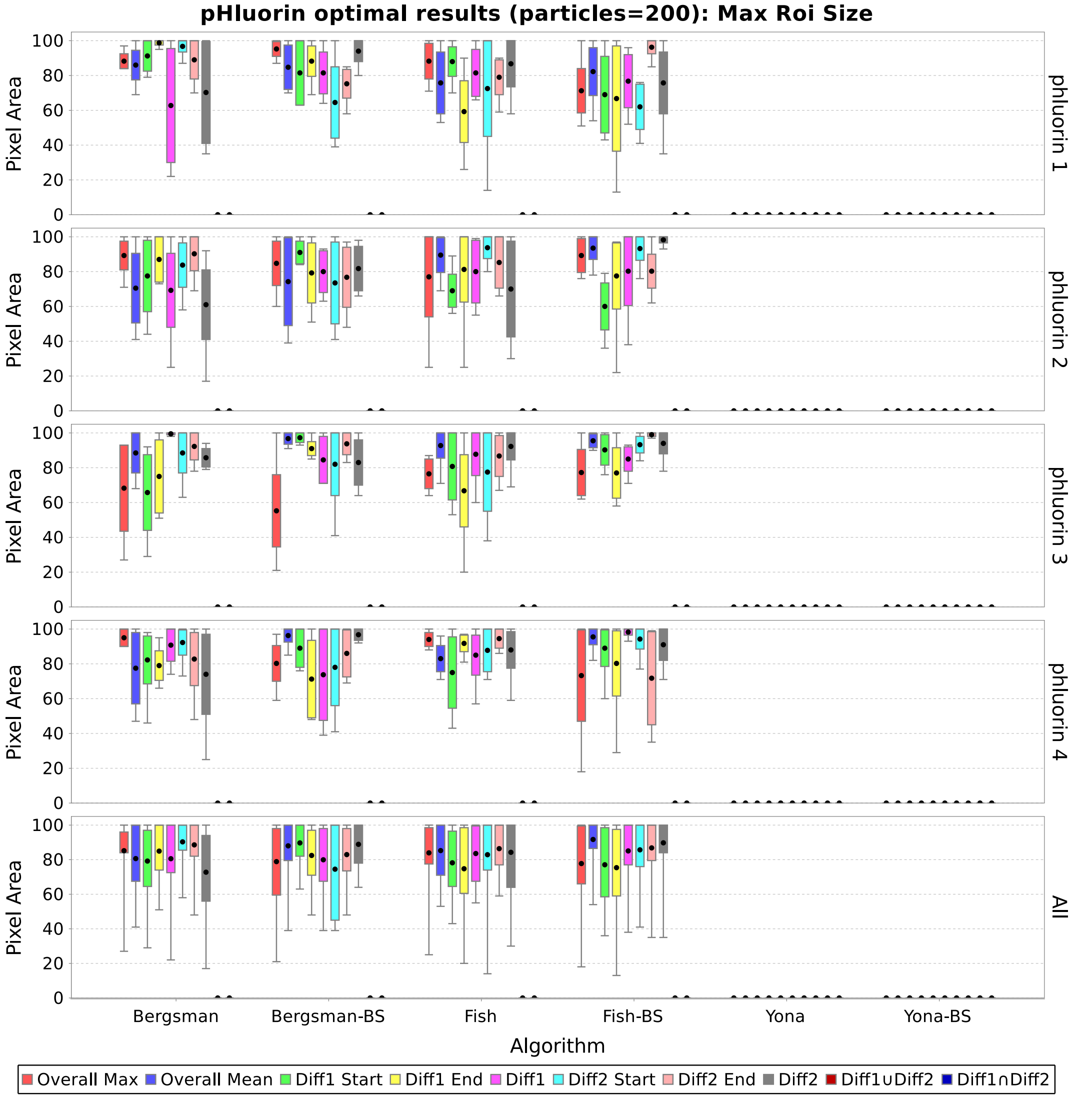

Figure B.6: Parameter Maximum ROI Size range values with pHluorin assays. Boxes show interquartile ranges, lines show maxima and minima, and black dots show mean values for each combination of experiment, image and algorithm.

B.4 Parameter: Minimum ROI Circularity

Table B.4: Minimum ROI Circularity for both FM dye and pHluorin experiment types broken down by algorithm and image. Each value shown is the mean (and standard deviation) of the best scoring segmentation parameter combination for each assay of that category. BS means background subtracted image.

	Bergsman		Fish		Yona	
	Non BS	BS	Non BS	BS	Non BS	BS
FM dye (particles = 1000)						
Overall Max	0.44 (0.23)	0.39 (0.27)	0.43 (0.27)	0.48 (0.28)	0 (0)	0 (0)
Overall Mean	0.27 (0.2)	0.35 (0.3)	0.24 (0.23)	0.47 (0.31)	0 (0)	0 (0)
Diff1 Start	0.29 (0.21)	0.27 (0.23)	0.3 (0.22)	0.33 (0.22)	0 (0)	0 (0)
Diff1 End	0.34 (0.24)	0.34 (0.28)	0.38 (0.27)	0.43 (0.29)	0 (0)	0 (0)
Diff1	0.37 (0.18)	0.38 (0.3)	0.32 (0.19)	0.42 (0.26)	0 (0)	0 (0)
pHluorin (particles = 200)						
Overall Max	0.31 (0.22)	0.33 (0.26)	0.26 (0.15)	0.29 (0.22)	0 (0)	0 (0)
Overall Mean	0.28 (0.2)	0.23 (0.2)	0.27 (0.23)	0.31 (0.24)	0 (0)	0 (0)
Diff1 Start	0.24 (0.17)	0.24 (0.12)	0.32 (0.17)	0.29 (0.19)	0 (0)	0 (0)
Diff1 End	0.23 (0.21)	0.38 (0.19)	0.3 (0.26)	0.33 (0.24)	0 (0)	0 (0)
Diff1	0.3 (0.21)	0.21 (0.16)	0.29 (0.15)	0.29 (0.19)	0 (0)	0 (0)
Diff2 Start	0.3 (0.16)	0.14 (0.15)	0.26 (0.17)	0.26 (0.2)	0 (0)	0 (0)
Diff2 End	0.35 (0.16)	0.32 (0.19)	0.33 (0.24)	0.26 (0.19)	0 (0)	0 (0)
Diff2	0.28 (0.21)	0.25 (0.11)	0.31 (0.2)	0.33 (0.12)	0 (0)	0 (0)
Diff1 ∪ Diff2	0 (0)	0 (0)	0 (0)	0 (0)	0 (0)	0 (0)
Diff1 ∩ Diff2	0 (0)	0 (0)	0 (0)	0 (0)	0 (0)	0 (0)

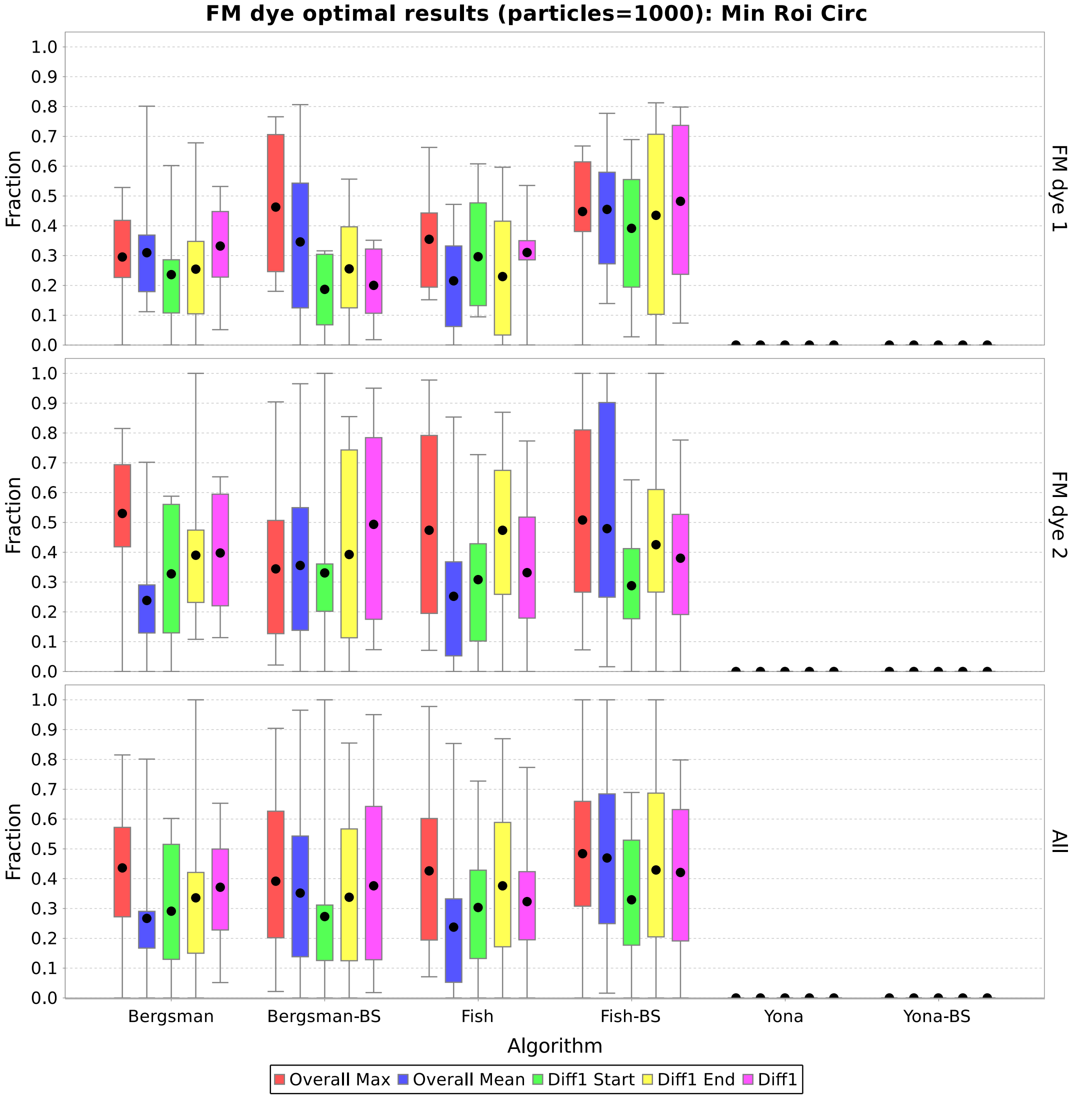

Figure B.7: Parameter Minimum ROI Circularity range values with FM dye assays. Boxes show interquartile ranges, lines show maxima and minima, and black dots show mean values for each combination of experiment, image and algorithm.

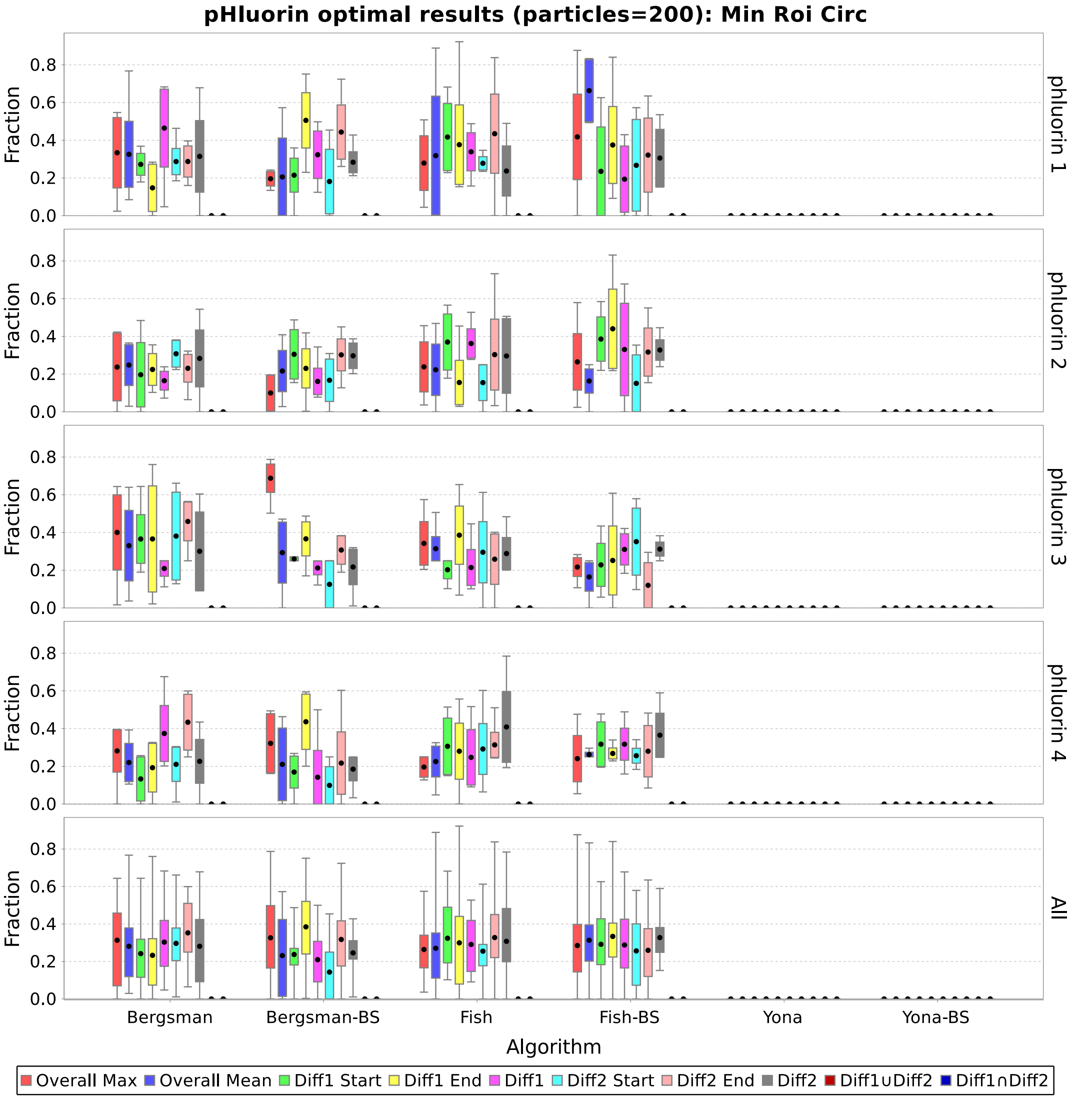

Figure B.8: Parameter Minimum ROI Circularity range values with pHluorin assays. Boxes show interquartile ranges, lines show maxima and minima, and black dots show mean values for each combination of experiment, image and algorithm.

B.5 Parameter: Quality Threshold

Table B.5: Quality Threshold for both FM dye and pHluorin experiment types broken down by algorithm and image. Each value shown is the mean (and standard deviation) of the best scoring segmentation parameter combination for each assay of that category. BS means background subtracted image.

	Bergsman		Fish		Yona	
	Non BS	BS	Non BS	BS	Non BS	BS
FM dye (particles = 1000)						
Overall Max	0.4 (0.29)	0.37 (0.23)	0 (0)	0 (0)	0.29 (0.2)	0.3 (0.18)
Overall Mean	0.46 (0.29)	0.36 (0.26)	0 (0)	0 (0)	0.27 (0.12)	0.24 (0.15)
Diff1 Start	0.52 (0.29)	0.46 (0.33)	0 (0)	0 (0)	0.41 (0.23)	0.41 (0.21)
Diff1 End	0.54 (0.25)	0.38 (0.22)	0 (0)	0 (0)	0.27 (0.16)	0.27 (0.17)
Diff1	0.47 (0.24)	0.54 (0.22)	0 (0)	0 (0)	0.23 (0.19)	0.23 (0.19)
pHluorin (particles = 200)						
Overall Max	0.86 (0.12)	0.85 (0.12)	0 (0)	0 (0)	0.36 (0.26)	0.36 (0.27)
Overall Mean	0.82 (0.18)	0.85 (0.12)	0 (0)	0 (0)	0.21 (0.21)	0.18 (0.23)
Diff1 Start	0.82 (0.17)	0.85 (0.15)	0 (0)	0 (0)	0.45 (0.32)	0.45 (0.31)
Diff1 End	0.8 (0.2)	0.88 (0.11)	0 (0)	0 (0)	0.44 (0.31)	0.41 (0.29)
Diff1	0.84 (0.14)	0.82 (0.24)	0 (0)	0 (0)	0.17 (0.2)	0.17 (0.2)
Diff2 Start	0.8 (0.2)	0.85 (0.13)	0 (0)	0 (0)	0.4 (0.29)	0.38 (0.25)
Diff2 End	0.83 (0.19)	0.88 (0.12)	0 (0)	0 (0)	0.41 (0.25)	0.36 (0.22)
Diff2	0.86 (0.07)	0.87 (0.08)	0 (0)	0 (0)	0.18 (0.26)	0.18 (0.26)
Diff1 $\cup$ Diff2	0 (0)	0 (0)	0 (0)	0 (0)	0 (0)	0 (0)
Diff1 $\cap$ Diff2	0 (0)	0 (0)	0 (0)	0 (0)	0 (0)	0 (0)

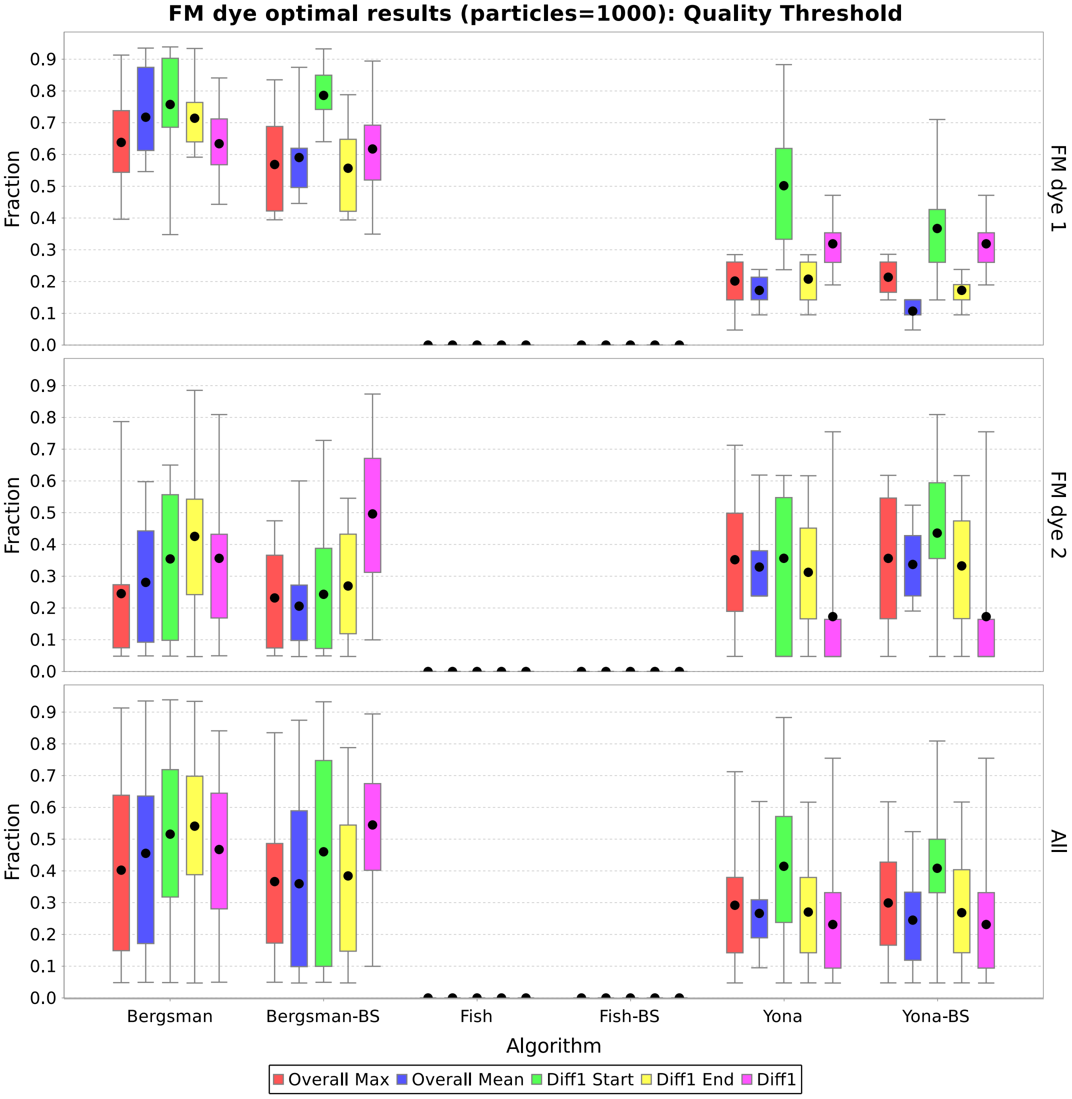

Figure B.9: Parameter Quality Threshold range values with FM dye assays. Boxes show interquartile ranges, lines show maxima and minima, and black dots show mean values for each combination of experiment, image and algorithm.

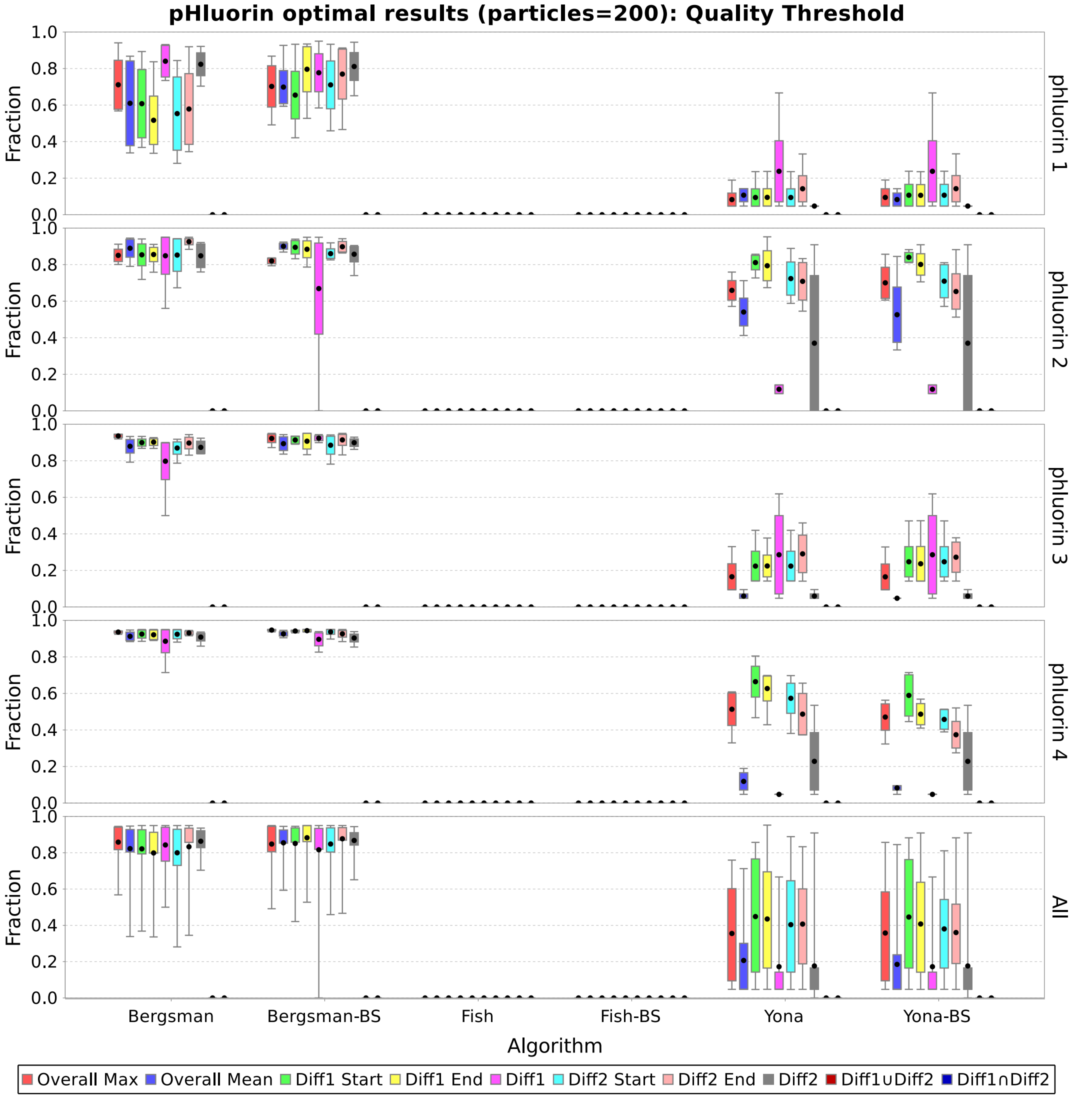

Figure B.10: Parameter Quality Threshold range values with pHluorin assays. Boxes show interquartile ranges, lines show maxima and minima, and black dots show mean values for each combination of experiment, image and algorithm.

B.6 Parameter: Slope

Table B.6: Slope for both FM dye and pHluorin experiment types broken down by algorithm and image. Each value shown is the mean (and standard deviation) of the best scoring segmentation parameter combination for each assay of that category. BS means background subtracted image.

	Bergsman		Fish		Yona	
	Non BS	BS	Non BS	BS	Non BS	BS
FM dye (particles = 1000)						
Overall Max	0.29 (0.63)	-0.04 (0.69)	0 (0)	0 (0)	0 (0)	0 (0)
Overall Mean	-0.17 (0.67)	0.06 (0.55)	0 (0)	0 (0)	0 (0)	0 (0)
Diff1 Start	0.01 (0.64)	0.01 (0.59)	0 (0)	0 (0)	0 (0)	0 (0)
Diff1 End	-0.16 (0.64)	-0.1 (0.76)	0 (0)	0 (0)	0 (0)	0 (0)
Diff1	0.04 (0.62)	-0.31 (0.45)	0 (0)	0 (0)	0 (0)	0 (0)
pHluorin (particles = 200)						
Overall Max	-0.11 (0.79)	0.36 (0.56)	0 (0)	0 (0)	0 (0)	0 (0)
Overall Mean	0.28 (0.63)	0.17 (0.62)	0 (0)	0 (0)	0 (0)	0 (0)
Diff1 Start	0.15 (0.54)	0.1 (0.63)	0 (0)	0 (0)	0 (0)	0 (0)
Diff1 End	0.01 (0.61)	-0.19 (0.54)	0 (0)	0 (0)	0 (0)	0 (0)
Diff1	-0.07 (0.7)	-0.09 (0.58)	0 (0)	0 (0)	0 (0)	0 (0)
Diff2 Start	0.19 (0.67)	0.42 (0.65)	0 (0)	0 (0)	0 (0)	0 (0)
Diff2 End	0.12 (0.53)	0.2 (0.65)	0 (0)	0 (0)	0 (0)	0 (0)
Diff2	0.05 (0.48)	-0.06 (0.64)	0 (0)	0 (0)	0 (0)	0 (0)
Diff1 ∪ Diff2	0 (0)	0 (0)	0 (0)	0 (0)	0 (0)	0 (0)
Diff1 ∩ Diff2	0 (0)	0 (0)	0 (0)	0 (0)	0 (0)	0 (0)

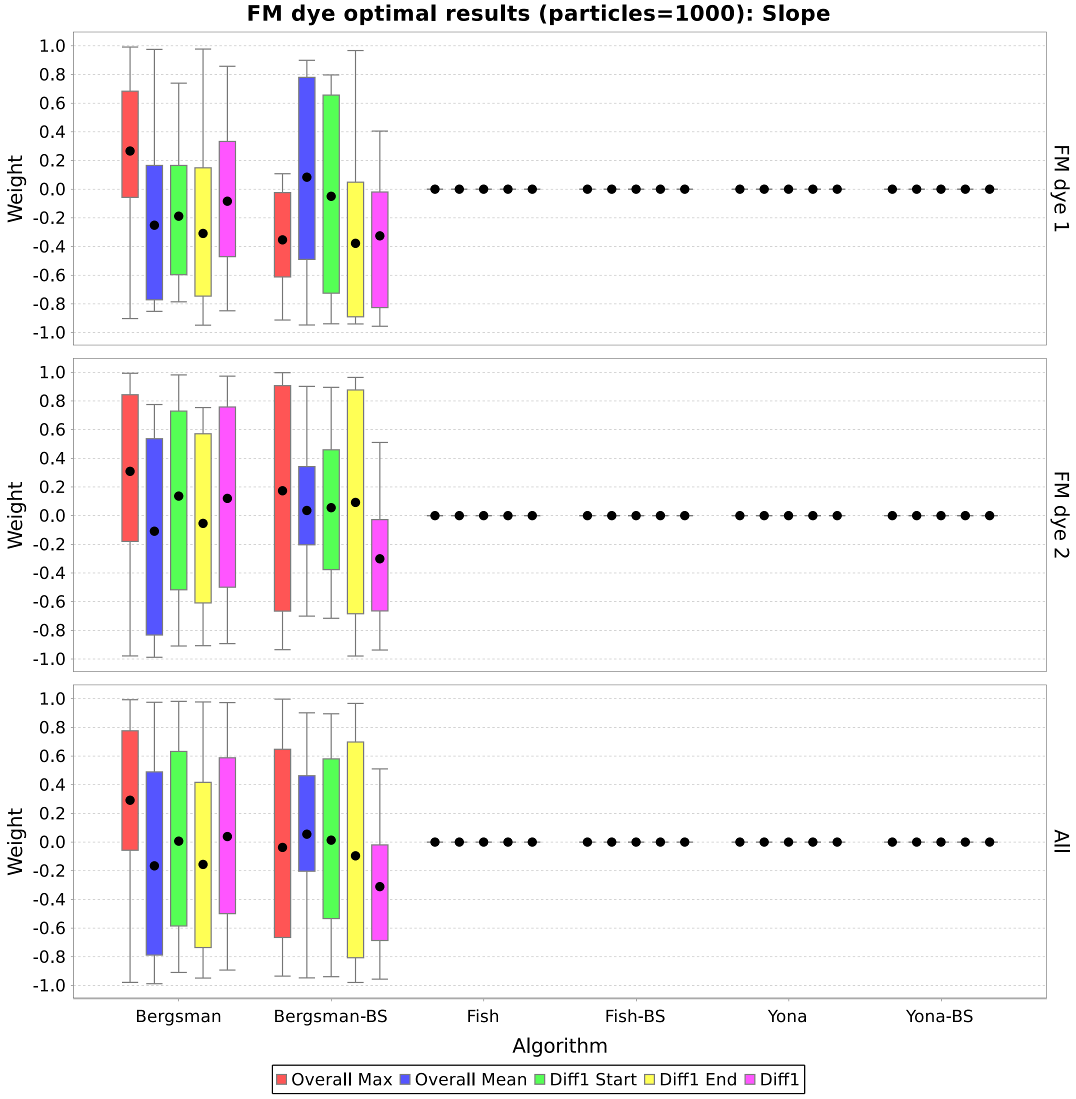

Figure B.11: Parameter Slope range values with FM dye assays. Boxes show interquartile ranges, lines show maxima and minima, and black dots show mean values for each combination of experiment, image and algorithm.

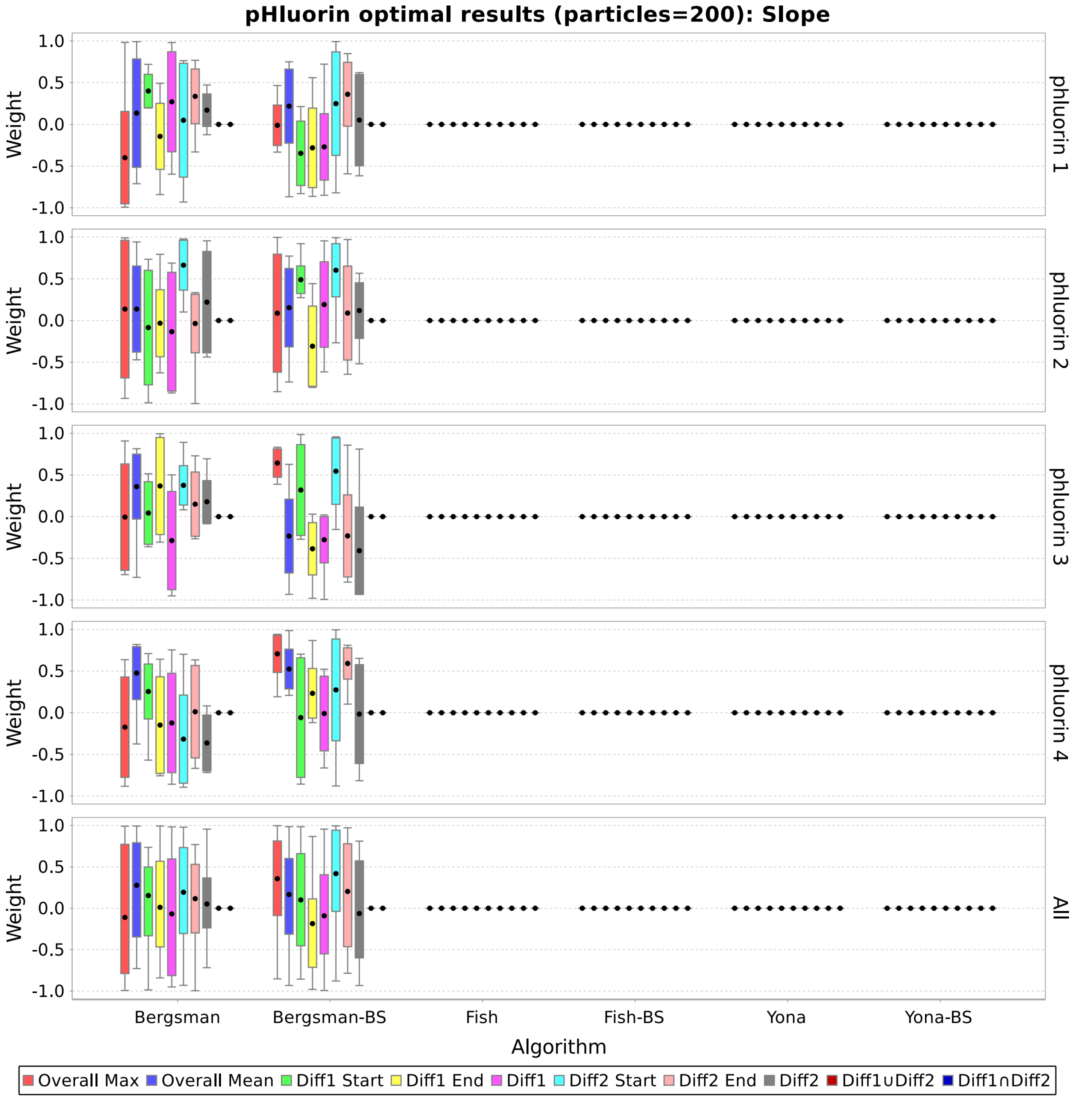

Figure B.12: Parameter Slope range values with pHluorin assays. Boxes show interquartile ranges, lines show maxima and minima, and black dots show mean values for each combination of experiment, image and algorithm.

B.7 Parameter: Destain

Table B.7: Destain for both FM dye and pHluorin experiment types broken down by algorithm and image. Each value shown is the mean (and standard deviation) of the best scoring segmentation parameter combination for each assay of that category. BS means background subtracted image.

	Bergsman		Fish		Yona	
	Non BS	BS	Non BS	BS	Non BS	BS
FM dye (particles = 1000)						
Overall Max	0.03 (0.47)	0.04 (0.42)	0 (0)	0 (0)	0 (0)	0 (0)
Overall Mean	0.13 (0.45)	0.22 (0.6)	0 (0)	0 (0)	0 (0)	0 (0)
Diff1 Start	0.06 (0.5)	0.06 (0.56)	0 (0)	0 (0)	0 (0)	0 (0)
Diff1 End	0.01 (0.45)	0.19 (0.35)	0 (0)	0 (0)	0 (0)	0 (0)
Diff1	0.08 (0.37)	0.09 (0.46)	0 (0)	0 (0)	0 (0)	0 (0)
pHluorin (particles = 200)						
Overall Max	0.01 (0.33)	-0.07 (0.43)	0 (0)	0 (0)	0 (0)	0 (0)
Overall Mean	-0.03 (0.48)	0.02 (0.37)	0 (0)	0 (0)	0 (0)	0 (0)
Diff1 Start	0.01 (0.39)	0.19 (0.48)	0 (0)	0 (0)	0 (0)	0 (0)
Diff1 End	-0 (0.37)	-0.28 (0.56)	0 (0)	0 (0)	0 (0)	0 (0)
Diff1	-0.25 (0.36)	-0.14 (0.5)	0 (0)	0 (0)	0 (0)	0 (0)
Diff2 Start	0.14 (0.32)	-0.08 (0.35)	0 (0)	0 (0)	0 (0)	0 (0)
Diff2 End	-0.23 (0.41)	0.1 (0.49)	0 (0)	0 (0)	0 (0)	0 (0)
Diff2	-0.14 (0.43)	-0.05 (0.54)	0 (0)	0 (0)	0 (0)	0 (0)
Diff1 ∪ Diff2	0 (0)	0 (0)	0 (0)	0 (0)	0 (0)	0 (0)
Diff1 ∩ Diff2	0 (0)	0 (0)	0 (0)	0 (0)	0 (0)	0 (0)

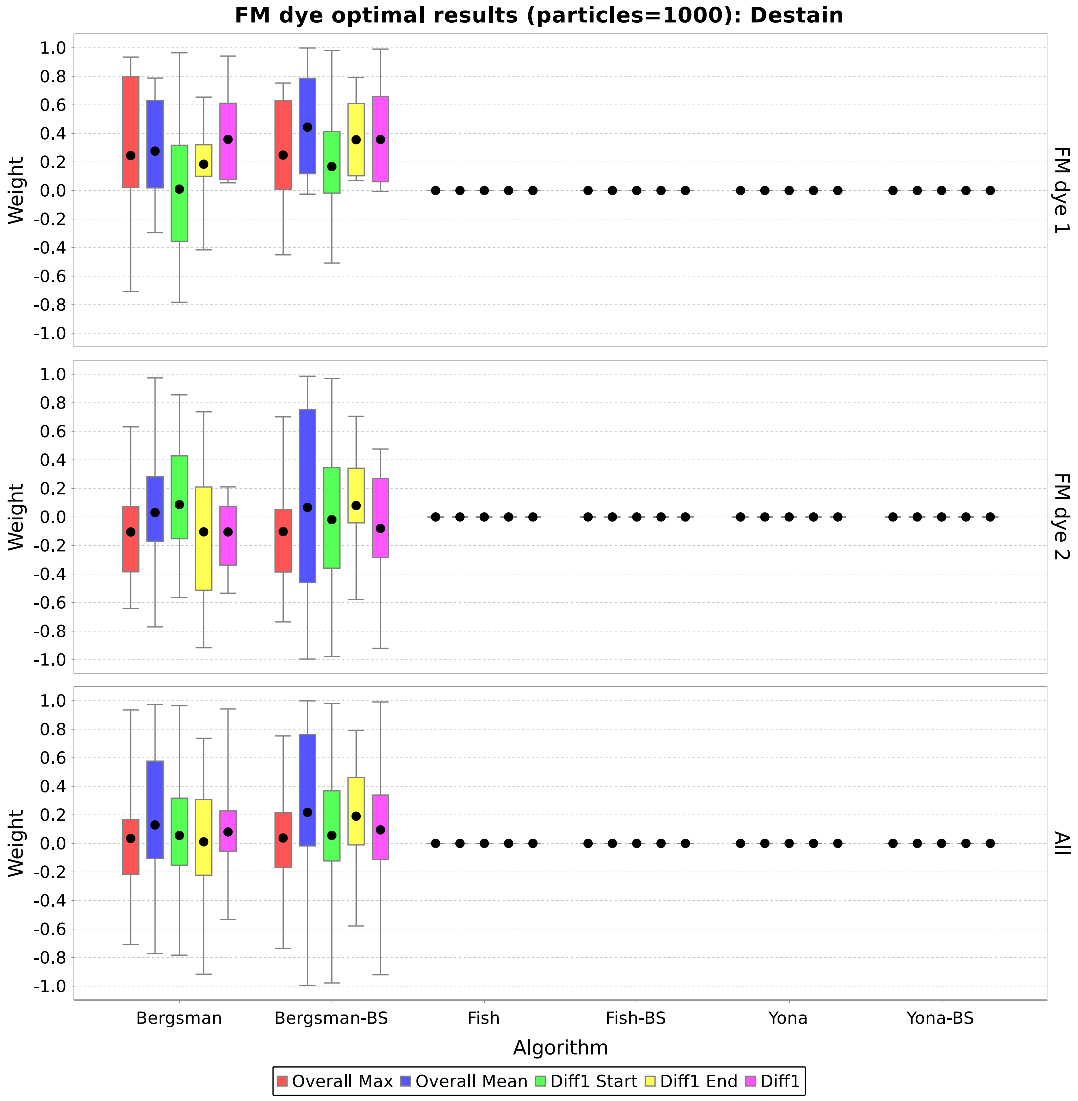

Figure B.13: Parameter Destain range values with FM dye assays. Boxes show interquartile ranges, lines show maxima and minima, and black dots show mean values for each combination of experiment, image and algorithm.

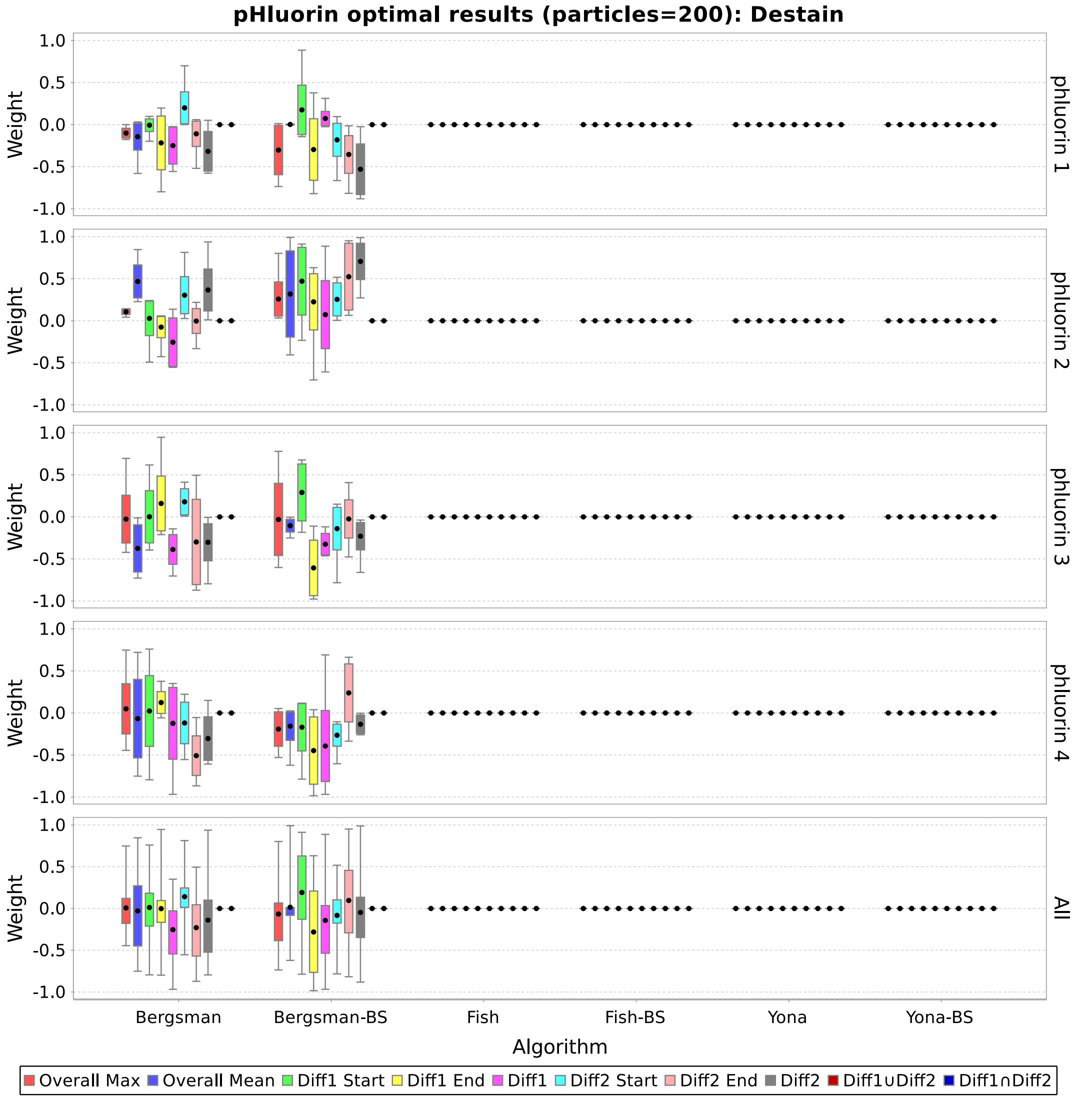

Figure B.14: Parameter Destain range values with pHluorin assays. Boxes show interquartile ranges, lines show maxima and minima, and black dots show mean values for each combination of experiment, image and algorithm.

B.8 Parameter: Coefficient of Variation (CV)

Table B.8: Coefficient of Variation (CV) for both FM dye and pHluorin experiment types broken down by algorithm and image. Each value shown is the mean (and standard deviation) of the best scoring segmentation parameter combination for each assay of that category. BS means background subtracted image.

	Bergsman		Fish		Yona	
	Non BS	BS	Non BS	BS	Non BS	BS
FM dye (particles = 1000)						
Overall Max	0.24 (0.53)	0.38 (0.49)	0 (0)	0 (0)	0 (0)	0 (0)
Overall Mean	0.39 (0.44)	0.34 (0.46)	0 (0)	0 (0)	0 (0)	0 (0)
Diff1 Start	0.41 (0.46)	0.36 (0.5)	0 (0)	0 (0)	0 (0)	0 (0)
Diff1 End	0.24 (0.6)	0.28 (0.47)	0 (0)	0 (0)	0 (0)	0 (0)
Diff1	0.42 (0.57)	0.45 (0.56)	0 (0)	0 (0)	0 (0)	0 (0)
pHluorin (particles = 200)						
Overall Max	-0.17 (0.53)	0.03 (0.65)	0 (0)	0 (0)	0 (0)	0 (0)
Overall Mean	0.07 (0.59)	-0.1 (0.71)	0 (0)	0 (0)	0 (0)	0 (0)
Diff1 Start	0.2 (0.75)	0.2 (0.59)	0 (0)	0 (0)	0 (0)	0 (0)
Diff1 End	0.24 (0.71)	0.16 (0.56)	0 (0)	0 (0)	0 (0)	0 (0)
Diff1	0.04 (0.6)	0.12 (0.67)	0 (0)	0 (0)	0 (0)	0 (0)
Diff2 Start	0.25 (0.63)	0.02 (0.57)	0 (0)	0 (0)	0 (0)	0 (0)
Diff2 End	0.15 (0.72)	-0.1 (0.58)	0 (0)	0 (0)	0 (0)	0 (0)
Diff2	0 (0.79)	0.1 (0.59)	0 (0)	0 (0)	0 (0)	0 (0)
Diff1 $\cup$ Diff2	0 (0)	0 (0)	0 (0)	0 (0)	0 (0)	0 (0)
Diff1 $\cap$ Diff2	0 (0)	0 (0)	0 (0)	0 (0)	0 (0)	0 (0)

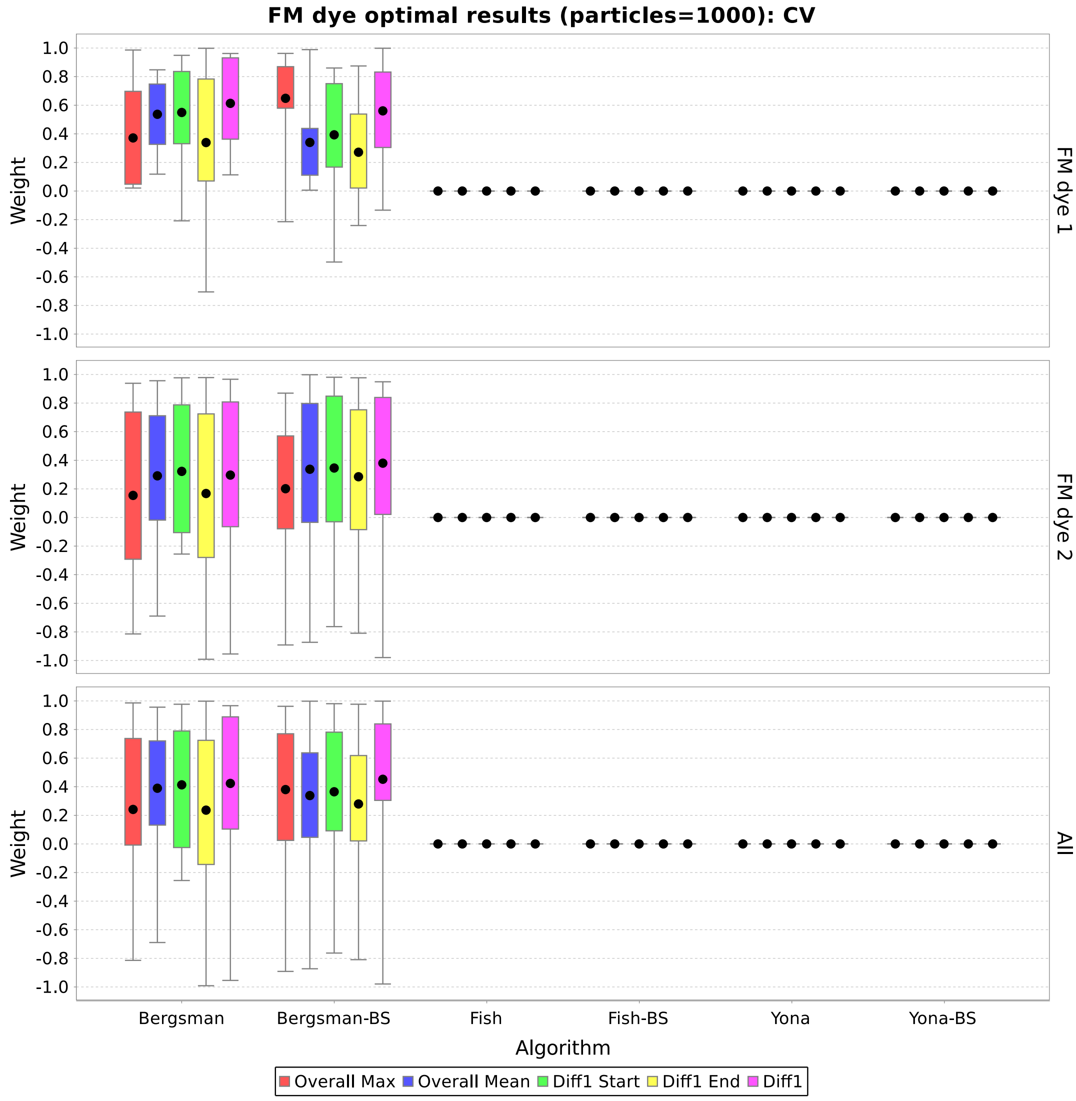

Figure B.15: Parameter Coefficient of Variation (CV) range values with FM dye assays. Boxes show interquartile ranges, lines show maxima and minima, and black dots show mean values for each combination of experiment, image and algorithm.

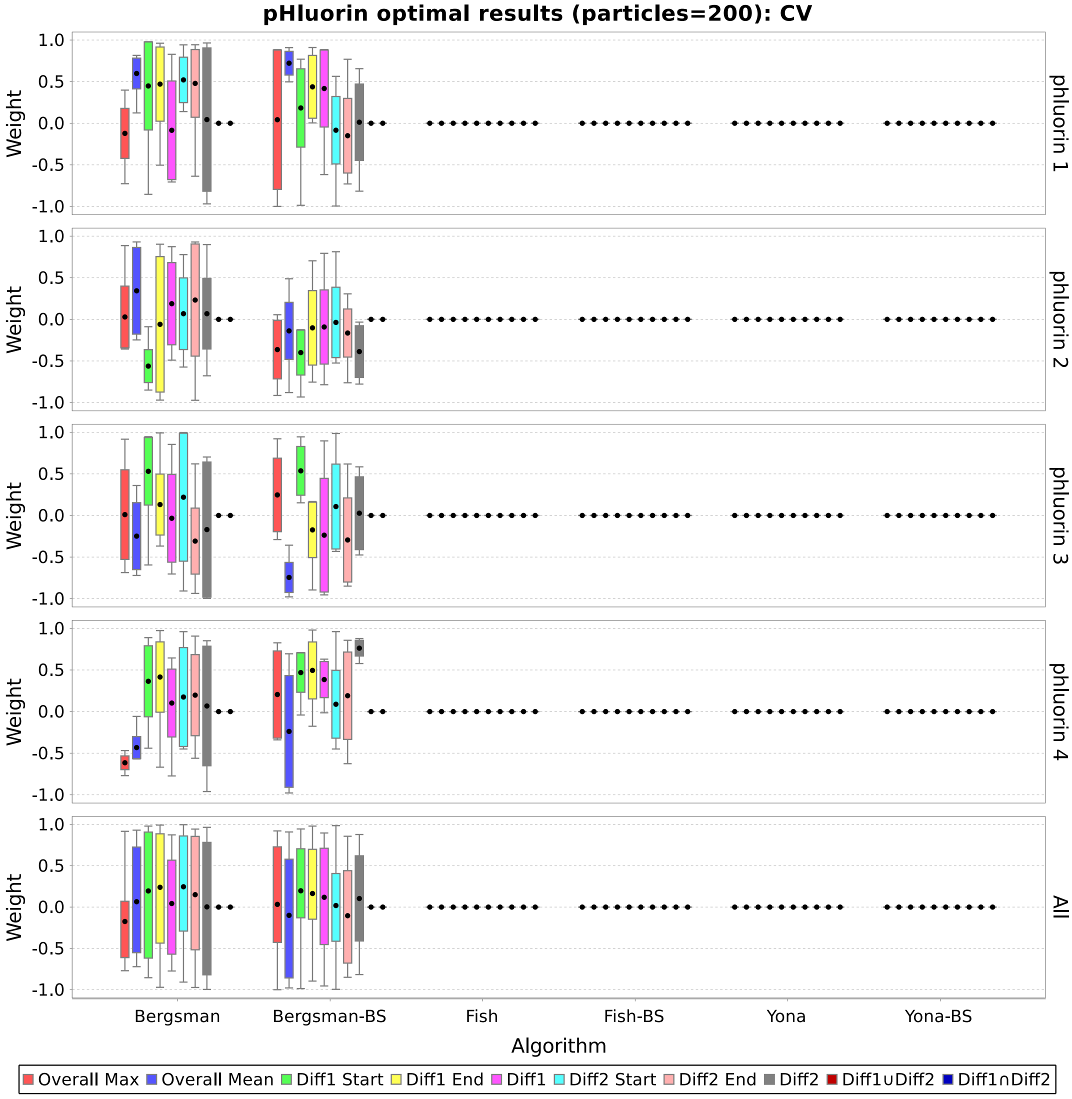

Figure B.16: Parameter Coefficient of Variation (CV) range values with pHluorin assays. Boxes show interquartile ranges, lines show maxima and minima, and black dots show mean values for each combination of experiment, image and algorithm.

B.9 Result: ROI Count

Table B.9: ROI Count for both FM dye and pHluorin experiment types broken down by algorithm and image. Each value shown is the mean (and standard deviation) of the best scoring segmentation parameter combination for each assay of that category. BS means background subtracted image.

	Bergsman		Fish		Yona	
	Non BS	BS	Non BS	BS	Non BS	BS
FM dye (particles = 1000)						
Overall Max	258 (235)	263 (234)	794 (1138)	666 (727)	900 (803)	1048 (802)
Overall Mean	264 (232)	261 (233)	556 (458)	884 (699)	1438 (965)	1976 (1492)
Diff1 Start	259 (226)	247 (210)	511 (594)	1224 (1256)	977 (782)	1349 (1113)
Diff1 End	261 (231)	260 (230)	664 (671)	768 (671)	892 (650)	1116 (880)
Diff1	264 (237)	253 (230)	615 (813)	665 (755)	377 (320)	377 (320)
pHluorin (particles = 200)						
Overall Max	162 (68)	157 (76)	243 (99)	227 (111)	172 (124)	168 (120)
Overall Mean	190 (77)	155 (58)	232 (101)	219 (91)	361 (196)	301 (174)
Diff1 Start	176 (60)	157 (48)	269 (99)	202 (71)	172 (127)	174 (129)
Diff1 End	181 (59)	154 (83)	246 (93)	236 (83)	186 (135)	172 (129)
Diff1	128 (66)	135 (62)	185 (90)	181 (94)	2517 (4254)	2517 (4254)
Diff2 Start	176 (77)	141 (64)	242 (91)	223 (113)	173 (135)	169 (131)
Diff2 End	148 (69)	147 (83)	264 (124)	212 (121)	165 (124)	146 (115)
Diff2	123 (65)	124 (61)	208 (109)	215 (112)	333 (455)	333 (455)
Diff1 $\cup$ Diff2	245 (88)	245 (81)	330 (148)	336 (147)	14307 (13895)	14307 (13895)
Diff1 $\cap$ Diff2	45 (36)	47 (39)	64 (54)	60 (53)	1828 (2923)	1828 (2923)

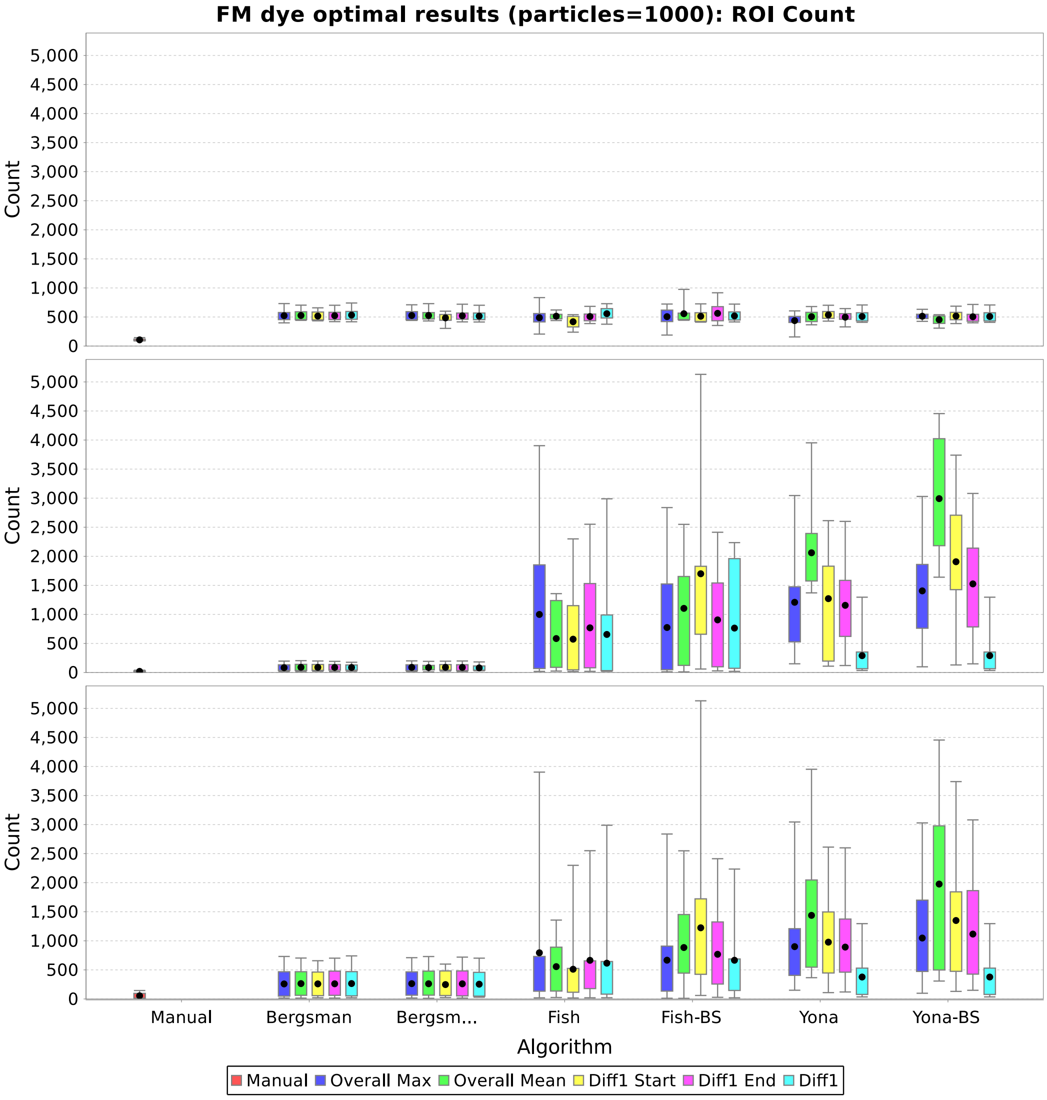

Figure B.17: Result ROI Count range values with FM dye assays. Boxes show interquartile ranges, lines show maxima and minima, and black dots show mean values for each combination of experiment, image and algorithm.

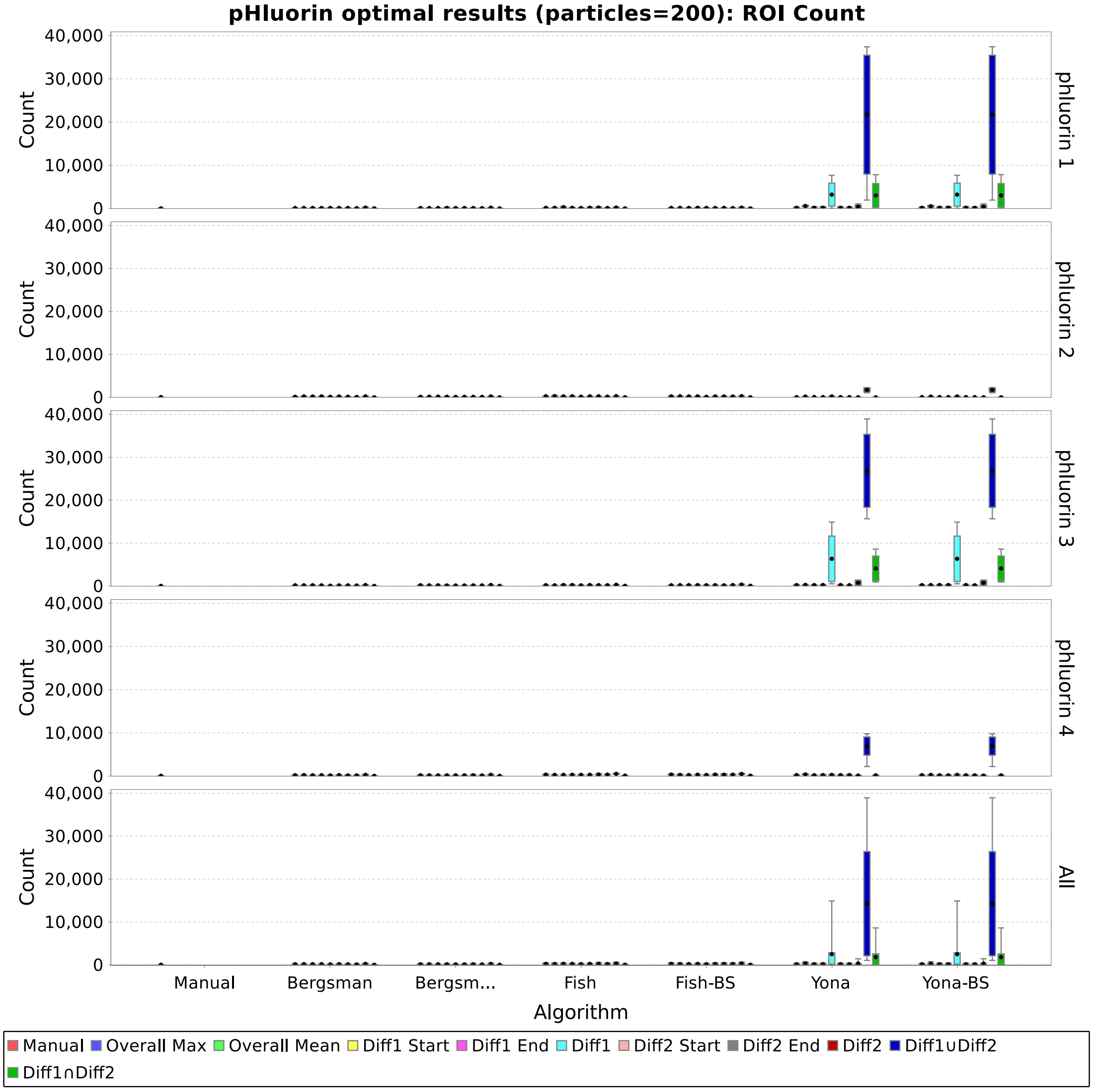

Figure B.18: Result ROI Count range values with pHluorin assays. Boxes show interquartile ranges, lines show maxima and minima, and black dots show mean values for each combination of experiment, image and algorithm.

B.10 Result: Intensity Trace Variance

Table B.10: Intensity Trace Variance for both FM dye and pHluorin experiment types broken down by algorithm and image. Each value shown is the mean (and standard deviation) of the best scoring segmentation parameter combination for each assay of that category. BS means background subtracted image.

	Bergsman		Fish		Yona	
	Non BS	BS	Non BS	BS	Non BS	BS
FM dye (particles = 1000)						
Overall Max	0.47 (0.21)	0.45 (0.21)	0.42 (0.18)	0.43 (0.2)	0.41 (0.19)	0.42 (0.19)
Overall Mean	0.47 (0.19)	0.45 (0.22)	0.45 (0.17)	0.43 (0.17)	0.44 (0.18)	0.42 (0.16)
Diff1 Start	0.42 (0.17)	0.43 (0.19)	0.41 (0.18)	0.42 (0.16)	0.38 (0.18)	0.4 (0.18)
Diff1 End	0.46 (0.19)	0.48 (0.18)	0.46 (0.2)	0.44 (0.18)	0.45 (0.18)	0.45 (0.17)
Diff1	0.52 (0.16)	0.51 (0.17)	0.5 (0.19)	0.51 (0.17)	0.45 (0.19)	0.45 (0.19)
pHluorin (particles = 200)						
Overall Max	0.05 (0.09)	0.07 (0.11)	0.07 (0.11)	0.06 (0.1)	0.06 (0.11)	0.06 (0.11)
Overall Mean	0.06 (0.11)	0.05 (0.1)	0.06 (0.11)	0.06 (0.1)	0.06 (0.11)	0.05 (0.1)
Diff1 Start	0.07 (0.12)	0.06 (0.11)	0.07 (0.12)	0.06 (0.11)	0.08 (0.14)	0.07 (0.13)
Diff1 End	0.06 (0.12)	0.07 (0.13)	0.06 (0.11)	0.06 (0.1)	0.07 (0.13)	0.07 (0.12)
Diff1	0.08 (0.1)	0.05 (0.08)	0.07 (0.11)	0.06 (0.1)	0.08 (0.12)	0.08 (0.12)
Diff2 Start	0.06 (0.11)	0.06 (0.1)	0.06 (0.11)	0.06 (0.1)	0.07 (0.14)	0.07 (0.13)
Diff2 End	0.05 (0.09)	0.05 (0.09)	0.06 (0.11)	0.05 (0.09)	0.05 (0.1)	0.06 (0.09)
Diff2	0.05 (0.09)	0.05 (0.08)	0.05 (0.08)	0.05 (0.09)	0.04 (0.07)	0.04 (0.07)
Diff1 $\cup$ Diff2	0.06 (0.09)	0.05 (0.1)	0.05 (0.09)	0.05 (0.09)	0.13 (0.13)	0.13 (0.13)
Diff1 $\cap$ Diff2	0.1 (0.1)	0.07 (0.05)	0.08 (0.09)	0.09 (0.1)	0.14 (0.16)	0.14 (0.16)

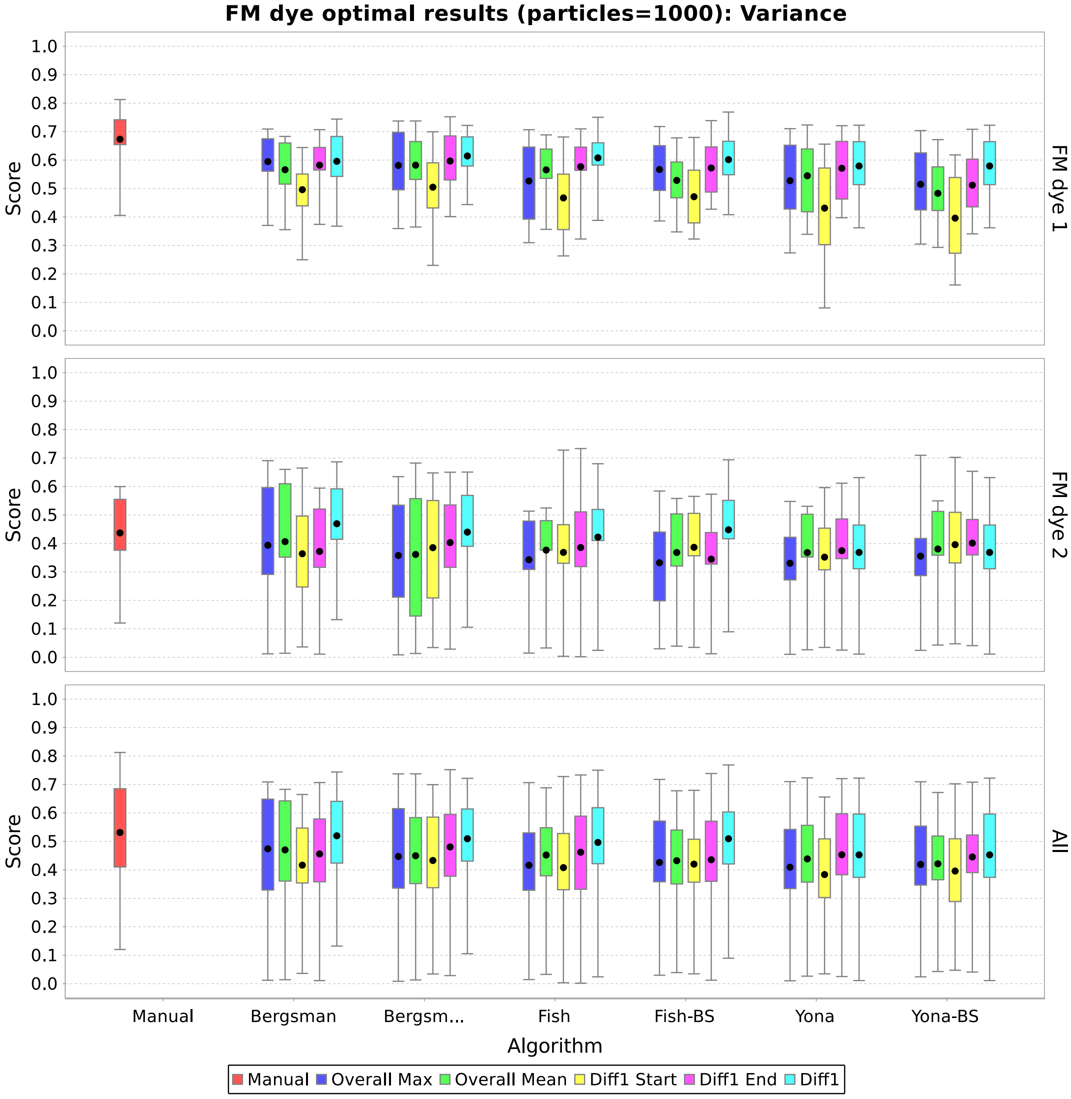

Figure B.19: Result Intensity Trace Variance range values with FM dye assays. Boxes show interquartile ranges, lines show maxima and minima, and black dots show mean values for each combination of experiment, image and algorithm.

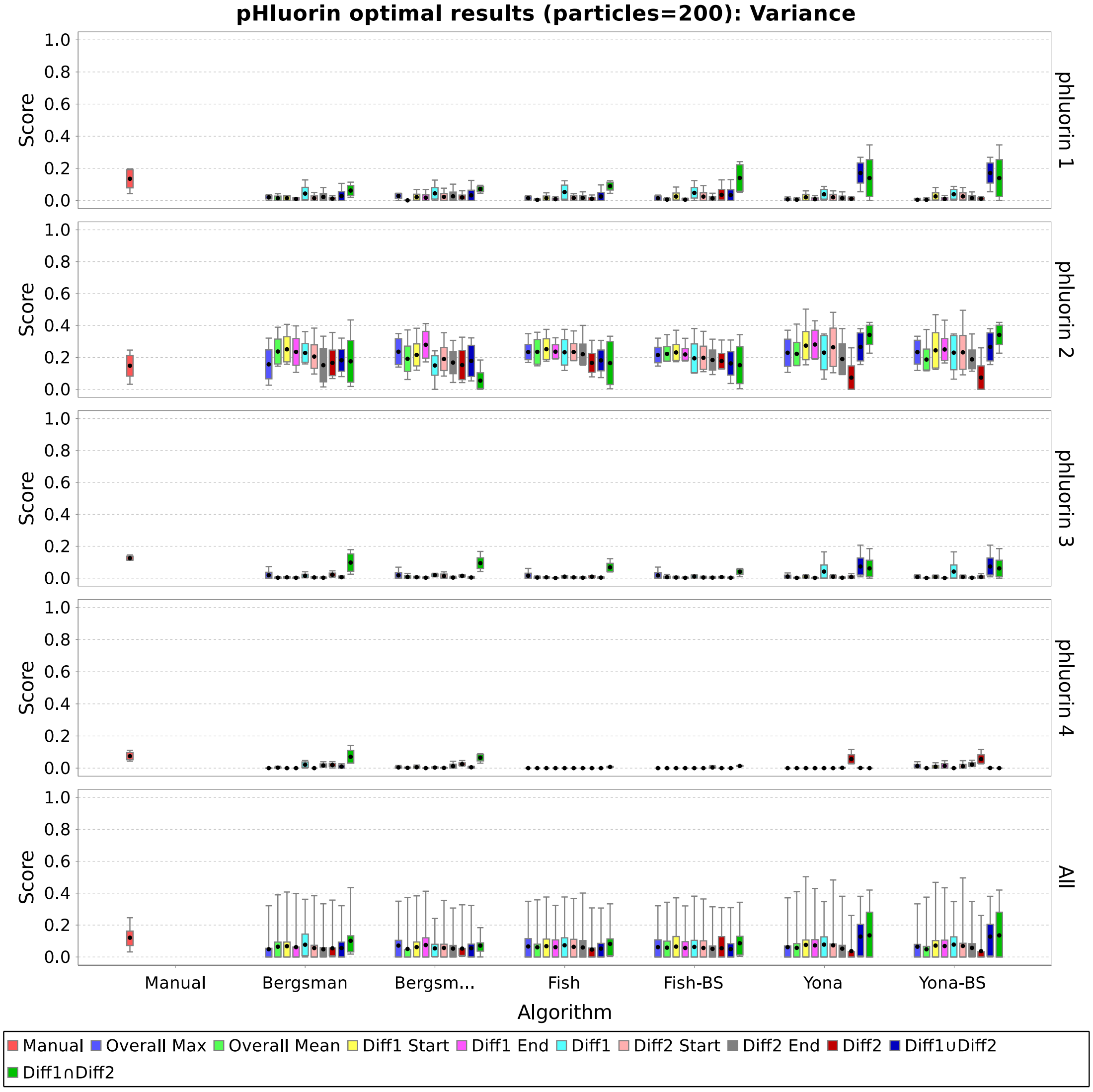

Figure B.20: Result Intensity Trace Variance range values with pHluorin assays. Boxes show interquartile ranges, lines show maxima and minima, and black dots show mean values for each combination of experiment, image and algorithm.

B.11 Result: Means Difference

Table B.11: Means Difference for both FM dye and pHluorin experiment types broken down by algorithm and image. Each value shown is the mean (and standard deviation) of the best scoring segmentation parameter combination for each assay of that category. BS means background subtracted image.

	Bergsman		Fish		Yona	
	Non BS	BS	Non BS	BS	Non BS	BS
FM dye (particles = 1000)						
Overall Max	0.91 (0.07)	0.92 (0.07)	0.89 (0.08)	0.89 (0.08)	0.88 (0.08)	0.89 (0.08)
Overall Mean	0.91 (0.07)	0.91 (0.07)	0.89 (0.1)	0.9 (0.08)	0.88 (0.08)	0.88 (0.08)
Diff1 Start	0.9 (0.08)	0.9 (0.09)	0.89 (0.1)	0.88 (0.1)	0.87 (0.09)	0.88 (0.09)
Diff1 End	0.92 (0.07)	0.92 (0.06)	0.9 (0.08)	0.9 (0.08)	0.88 (0.07)	0.89 (0.07)
Diff1	0.94 (0.04)	0.93 (0.04)	0.92 (0.04)	0.93 (0.05)	0.9 (0.05)	0.9 (0.05)
pHluorin (particles = 200)						
Overall Max	0.91 (0.04)	0.9 (0.05)	0.88 (0.05)	0.88 (0.05)	0.89 (0.05)	0.89 (0.05)
Overall Mean	0.87 (0.05)	0.89 (0.05)	0.86 (0.06)	0.87 (0.05)	0.85 (0.05)	0.86 (0.05)
Diff1 Start	0.84 (0.06)	0.85 (0.07)	0.83 (0.05)	0.84 (0.06)	0.82 (0.07)	0.83 (0.07)
Diff1 End	0.85 (0.06)	0.85 (0.06)	0.84 (0.04)	0.85 (0.05)	0.83 (0.06)	0.85 (0.07)
Diff1	0.89 (0.05)	0.83 (0.22)	0.87 (0.03)	0.87 (0.04)	0.83 (0.06)	0.83 (0.06)
Diff2 Start	0.85 (0.06)	0.85 (0.06)	0.84 (0.06)	0.84 (0.06)	0.83 (0.07)	0.84 (0.07)
Diff2 End	0.89 (0.06)	0.88 (0.06)	0.85 (0.06)	0.86 (0.06)	0.86 (0.06)	0.87 (0.07)
Diff2	0.91 (0.05)	0.91 (0.04)	0.88 (0.03)	0.88 (0.03)	0.76 (0.31)	0.76 (0.31)
Diff1 $\cup$ Diff2	0.89 (0.04)	0.88 (0.04)	0.87 (0.03)	0.87 (0.03)	0.81 (0.05)	0.81 (0.05)
Diff1 $\cap$ Diff2	0.92 (0.06)	0.92 (0.05)	0.92 (0.05)	0.92 (0.05)	0.83 (0.06)	0.83 (0.06)

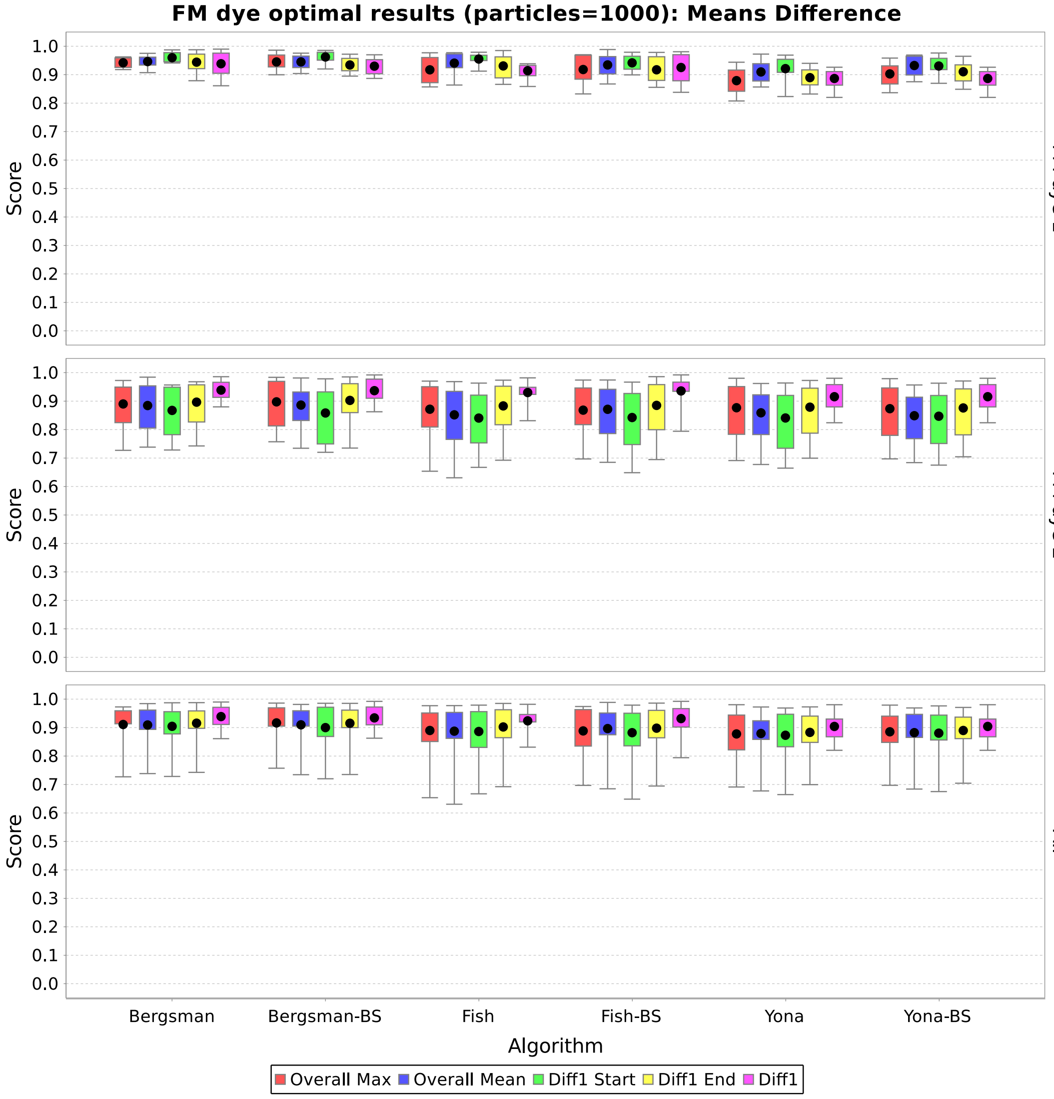

Figure B.21: Result Means Difference range values with FM dye assays. Boxes show interquartile ranges, lines show maxima and minima, and black dots show mean values for each combination of experiment, image and algorithm.

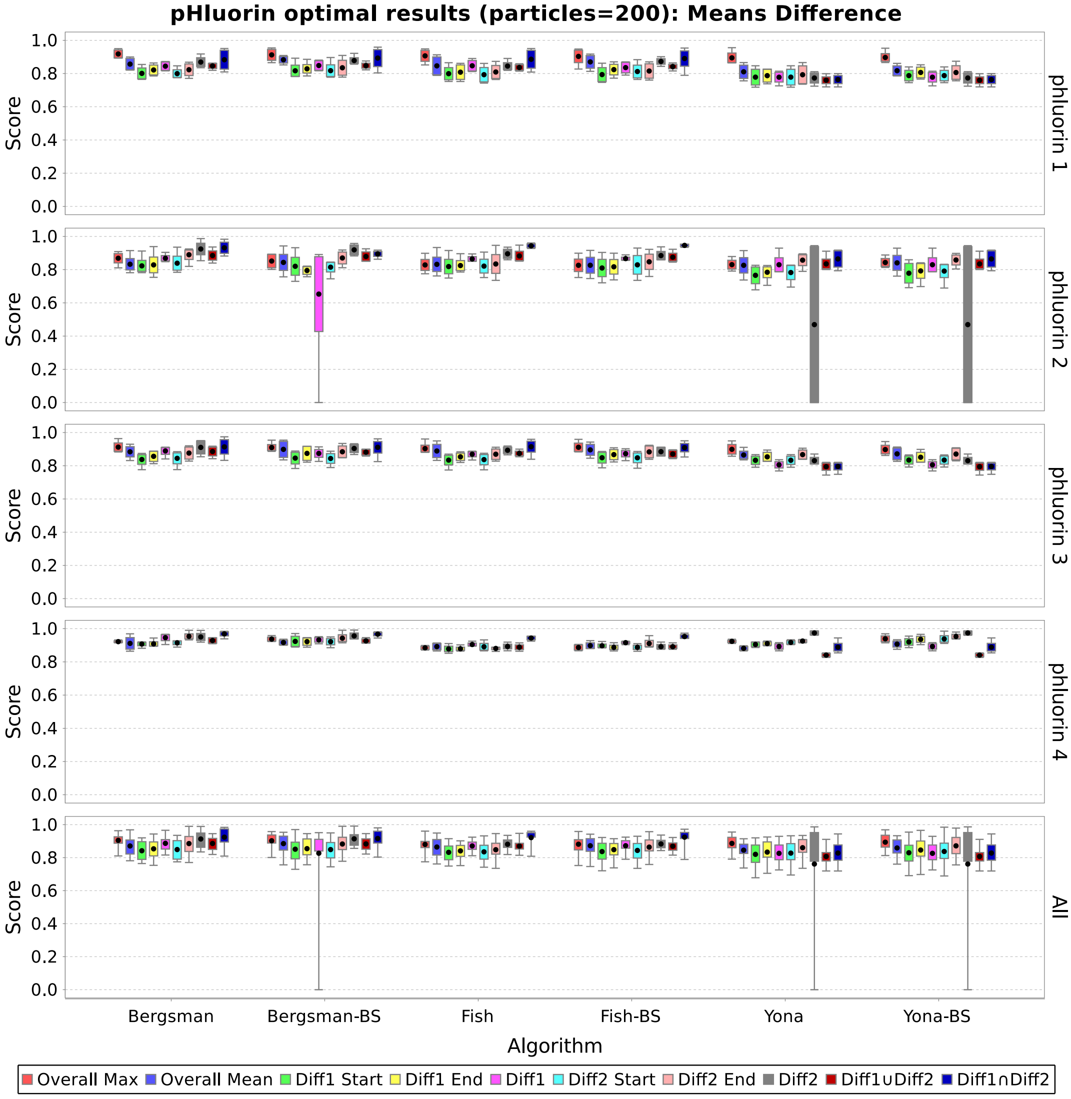

Figure B.22: Result Means Difference range values with pHluorin assays. Boxes show interquartile ranges, lines show maxima and minima, and black dots show mean values for each combination of experiment, image and algorithm.

B.12 Result: Matched Manually Segmented ROIs

Table B.12: Matched Manually Segmented ROIs for both FM dye and pHluorin experiment types broken down by algorithm and image. Each value shown is the mean (and standard deviation) of the best scoring segmentation parameter combination for each assay of that category. BS means background subtracted image.

	Bergsman		Fish		Yona	
	Non BS	BS	Non BS	BS	Non BS	BS
FM dye (particles = 1000)						
Overall Max	0.37 (0.18)	0.38 (0.18)	0.39 (0.25)	0.46 (0.32)	0.42 (0.31)	0.41 (0.3)
Overall Mean	0.34 (0.19)	0.35 (0.16)	0.46 (0.34)	0.54 (0.32)	0.56 (0.32)	0.54 (0.34)
Diff1 Start	0.26 (0.12)	0.26 (0.15)	0.35 (0.31)	0.56 (0.33)	0.37 (0.27)	0.42 (0.31)
Diff1 End	0.36 (0.18)	0.35 (0.19)	0.5 (0.34)	0.52 (0.31)	0.44 (0.31)	0.43 (0.32)
Diff1	0.33 (0.18)	0.34 (0.17)	0.35 (0.23)	0.4 (0.24)	0.24 (0.18)	0.24 (0.18)
pHluorin (particles = 200)						
Overall Max	0.69 (0.1)	0.67 (0.15)	0.74 (0.1)	0.72 (0.15)	0.51 (0.24)	0.53 (0.24)
Overall Mean	0.63 (0.09)	0.63 (0.1)	0.64 (0.18)	0.71 (0.14)	0.65 (0.21)	0.64 (0.21)
Diff1 Start	0.42 (0.12)	0.44 (0.12)	0.5 (0.15)	0.45 (0.19)	0.27 (0.22)	0.28 (0.21)
Diff1 End	0.47 (0.11)	0.45 (0.13)	0.52 (0.19)	0.58 (0.1)	0.35 (0.21)	0.36 (0.19)
Diff1	0.4 (0.22)	0.4 (0.23)	0.44 (0.22)	0.45 (0.24)	0.28 (0.17)	0.28 (0.17)
Diff2 Start	0.45 (0.17)	0.45 (0.19)	0.49 (0.2)	0.53 (0.18)	0.31 (0.25)	0.31 (0.24)
Diff2 End	0.61 (0.16)	0.65 (0.13)	0.69 (0.17)	0.71 (0.13)	0.47 (0.29)	0.47 (0.26)
Diff2	0.65 (0.17)	0.64 (0.2)	0.75 (0.16)	0.76 (0.16)	0.34 (0.27)	0.34 (0.27)
Diff1 $\cup$ Diff2	0.76 (0.13)	0.74 (0.18)	0.79 (0.13)	0.81 (0.1)	0.51 (0.21)	0.51 (0.21)
Diff1 $\cap$ Diff2	0.32 (0.22)	0.31 (0.22)	0.36 (0.2)	0.35 (0.2)	0.12 (0.12)	0.12 (0.12)

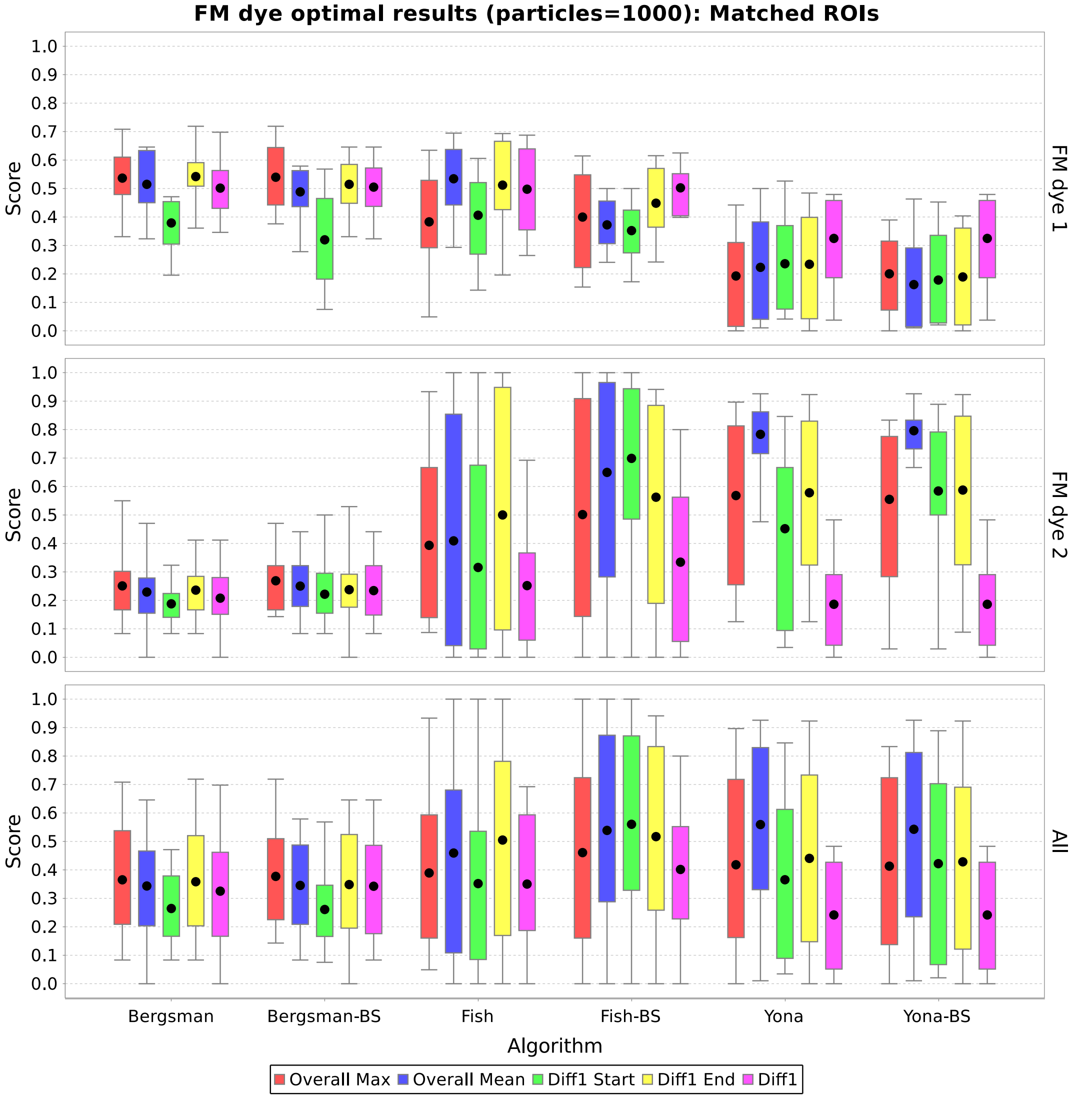

Figure B.23: Result Matched Manually Segmented ROIs range values with FM dye assays. Boxes show interquartile ranges, lines show maxima and minima, and black dots show mean values for each combination of experiment, image and algorithm.

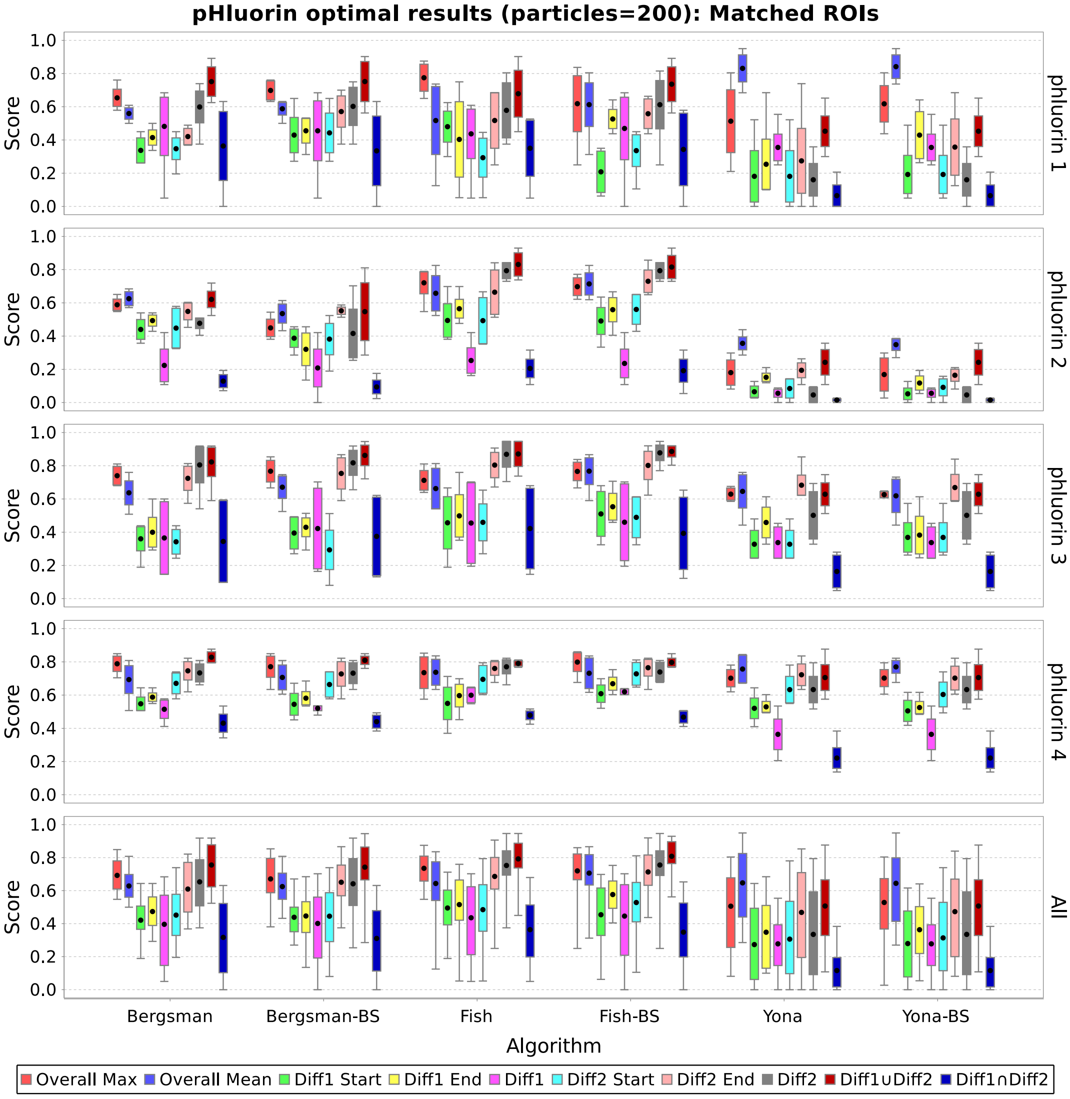

Figure B.24: Result Matched Manually Segmented ROIs range values with pHluorin assays. Boxes show interquartile ranges, lines show maxima and minima, and black dots show mean values for each combination of experiment, image and algorithm.

B.13 Result: ROI Count Score

Table B.13: ROI Count Score for both FM dye and pHluorin experiment types broken down by algorithm and image. Each value shown is the mean (and standard deviation) of the best scoring segmentation parameter combination for each assay of that category. BS means background subtracted image.

	Bergsman		Fish		Yona	
	Non BS	BS	Non BS	BS	Non BS	BS
FM dye (particles = 1000)						
Overall Max	1 (0)	1 (0.01)	0.79 (0.4)	0.7 (0.43)	0.54 (0.5)	0.53 (0.49)
Overall Mean	1 (0.01)	1 (0.01)	0.74 (0.44)	0.58 (0.49)	0.39 (0.49)	0.39 (0.49)
Diff1 Start	1 (0.01)	1 (0.01)	0.79 (0.41)	0.54 (0.51)	0.57 (0.48)	0.49 (0.5)
Diff1 End	1 (0)	1 (0.01)	0.68 (0.46)	0.6 (0.47)	0.52 (0.49)	0.52 (0.49)
Diff1	0.99 (0.01)	1 (0)	0.81 (0.36)	0.79 (0.41)	0.83 (0.36)	0.83 (0.36)
pHluorin (particles = 200)						
Overall Max	1 (0)	0.99 (0.03)	0.89 (0.27)	0.95 (0.14)	0.96 (0.12)	0.94 (0.13)
Overall Mean	1 (0.01)	1 (0.01)	0.88 (0.27)	0.94 (0.14)	0.78 (0.4)	0.77 (0.4)
Diff1 Start	1 (0)	1 (0)	0.87 (0.34)	0.98 (0.08)	1 (0.01)	0.99 (0.03)
Diff1 End	1 (0)	1 (0)	0.92 (0.25)	0.93 (0.15)	0.98 (0.05)	0.96 (0.1)
Diff1	1 (0.02)	0.94 (0.25)	0.99 (0.04)	0.97 (0.08)	0.55 (0.5)	0.55 (0.5)
Diff2 Start	1 (0.01)	1 (0)	0.93 (0.19)	0.99 (0.03)	0.95 (0.14)	0.94 (0.14)
Diff2 End	1 (0.01)	1 (0)	0.9 (0.26)	0.93 (0.16)	1 (0.01)	0.97 (0.11)
Diff2	0.99 (0.02)	0.99 (0.02)	0.99 (0.03)	0.98 (0.09)	0.55 (0.43)	0.55 (0.43)
Diff1 ∪ Diff2	0.82 (0.29)	0.78 (0.31)	0.72 (0.26)	0.68 (0.29)	0 (0)	0 (0)
Diff1 ∩ Diff2	0.71 (0.36)	0.7 (0.36)	0.77 (0.33)	0.73 (0.33)	0.31 (0.43)	0.31 (0.43)

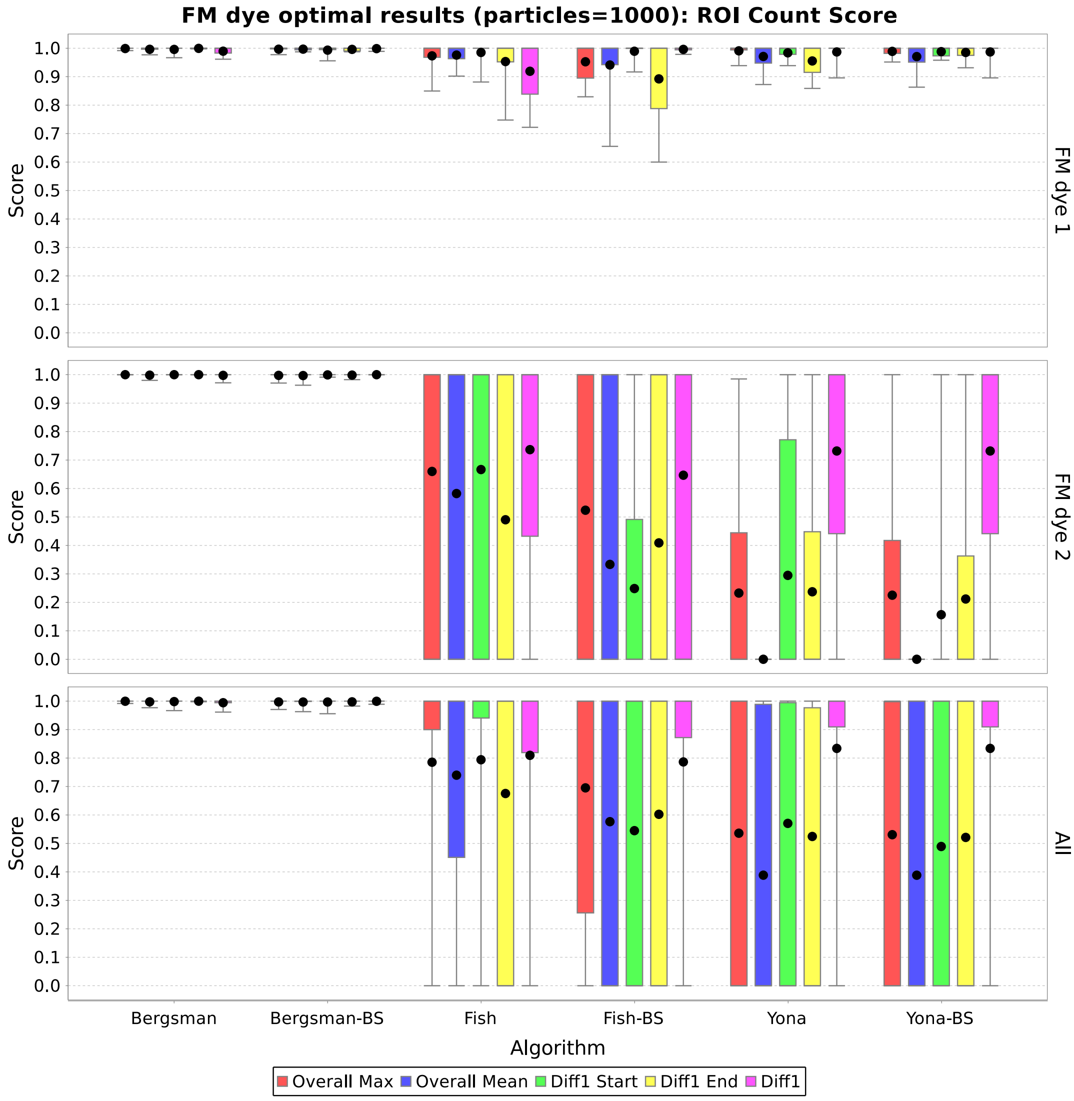

Figure B.25: Result ROI Count Score range values with FM dye assays. Boxes show interquartile ranges, lines show maxima and minima, and black dots show mean values for each combination of experiment, image and algorithm.

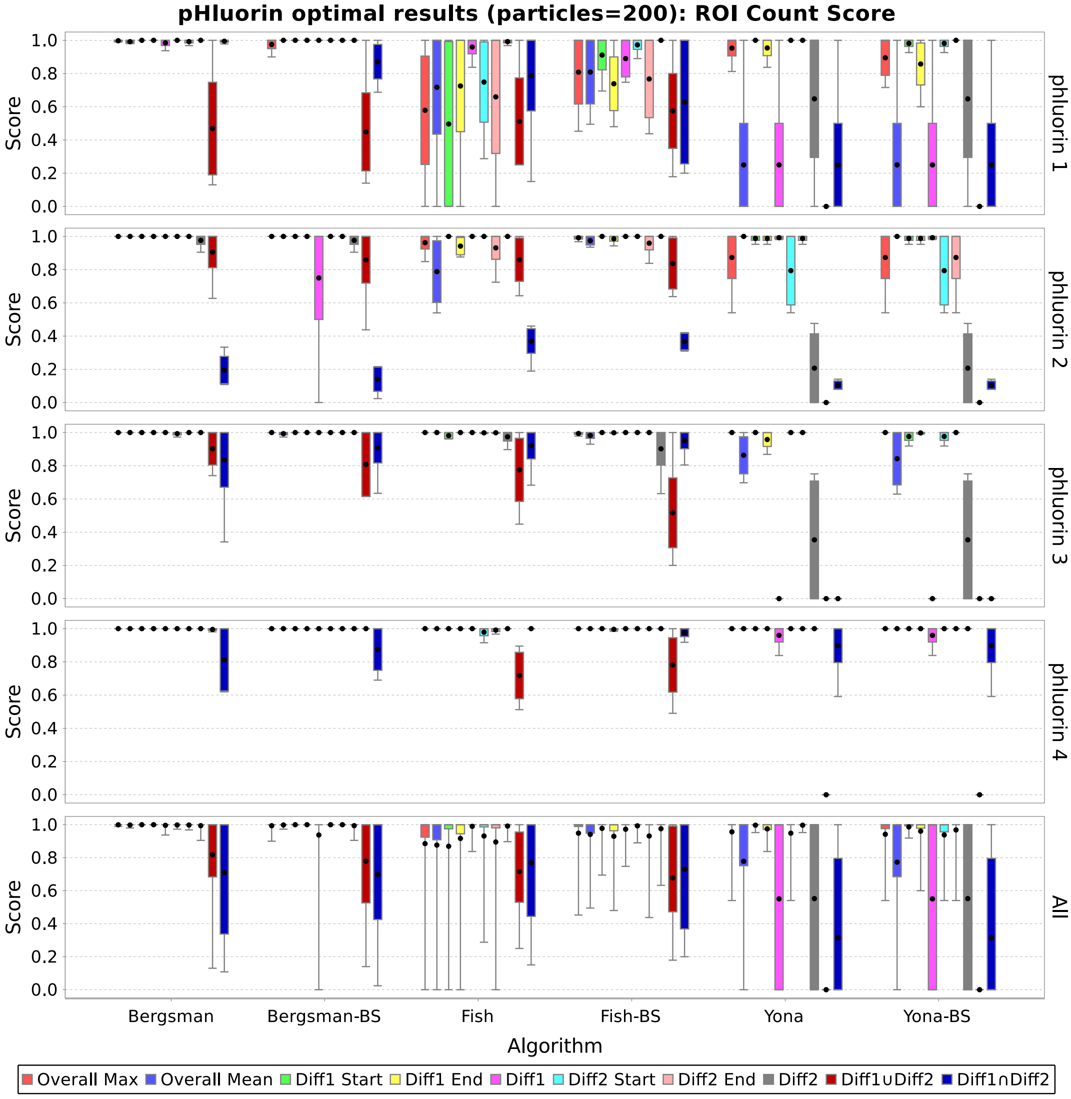

Figure B.26: Result ROI Count Score range values with pHluorin assays. Boxes show interquartile ranges, lines show maxima and minima, and black dots show mean values for each combination of experiment, image and algorithm.

B.14 Result: Total Score

Table B.14: Total Score for both FM dye and pHluorin experiment types broken down by algorithm and image. Each value shown is the mean (and standard deviation) of the best scoring segmentation parameter combination for each assay of that category. BS means background subtracted image.

	Bergsman		Fish		Yona	
	Non BS	BS	Non BS	BS	Non BS	BS
FM dye (particles = 1000)						
Overall Max	3.64 (0.39)	3.67 (0.37)	3.24 (0.54)	3.2 (0.45)	2.79 (0.55)	2.77 (0.53)
Overall Mean	3.59 (0.39)	3.59 (0.34)	3.29 (0.64)	3.13 (0.52)	2.77 (0.53)	2.74 (0.45)
Diff1 Start	3.43 (0.28)	3.42 (0.32)	3.18 (0.58)	3.09 (0.52)	2.74 (0.65)	2.7 (0.59)
Diff1 End	3.63 (0.39)	3.61 (0.38)	3.26 (0.61)	3.14 (0.51)	2.81 (0.55)	2.79 (0.51)
Diff1	3.58 (0.36)	3.62 (0.34)	3.24 (0.65)	3.31 (0.66)	3.06 (0.8)	3.06 (0.8)
pHluorin (particles = 200)						
Overall Max	4.29 (0.22)	4.23 (0.34)	4.12 (0.52)	4.22 (0.42)	3.81 (0.67)	3.84 (0.69)
Overall Mean	4.12 (0.2)	4.13 (0.22)	3.9 (0.61)	4.17 (0.42)	3.7 (0.73)	3.69 (0.72)
Diff1 Start	3.68 (0.28)	3.73 (0.29)	3.56 (0.73)	3.7 (0.53)	3.36 (0.49)	3.36 (0.49)
Diff1 End	3.8 (0.24)	3.75 (0.3)	3.71 (0.55)	3.86 (0.45)	3.48 (0.5)	3.5 (0.45)
Diff1	3.67 (0.46)	3.51 (1.03)	3.72 (0.45)	3.71 (0.49)	2.48 (0.93)	2.48 (0.93)
Diff2 Start	3.75 (0.37)	3.74 (0.42)	3.67 (0.67)	3.89 (0.42)	3.34 (0.7)	3.34 (0.68)
Diff2 End	4.1 (0.36)	4.19 (0.3)	4.01 (0.74)	4.15 (0.56)	3.79 (0.63)	3.75 (0.69)
Diff2	4.21 (0.37)	4.19 (0.45)	4.37 (0.33)	4.35 (0.33)	2.54 (1.45)	2.54 (1.45)
Diff1 $\cup$ Diff2	4.03 (0.72)	3.93 (0.72)	3.89 (0.73)	3.84 (0.65)	1.82 (0.42)	1.82 (0.42)
Diff1 $\cap$ Diff2	2.98 (1.05)	2.94 (1.08)	3.19 (1.01)	3.08 (1.03)	1.69 (0.99)	1.69 (0.99)

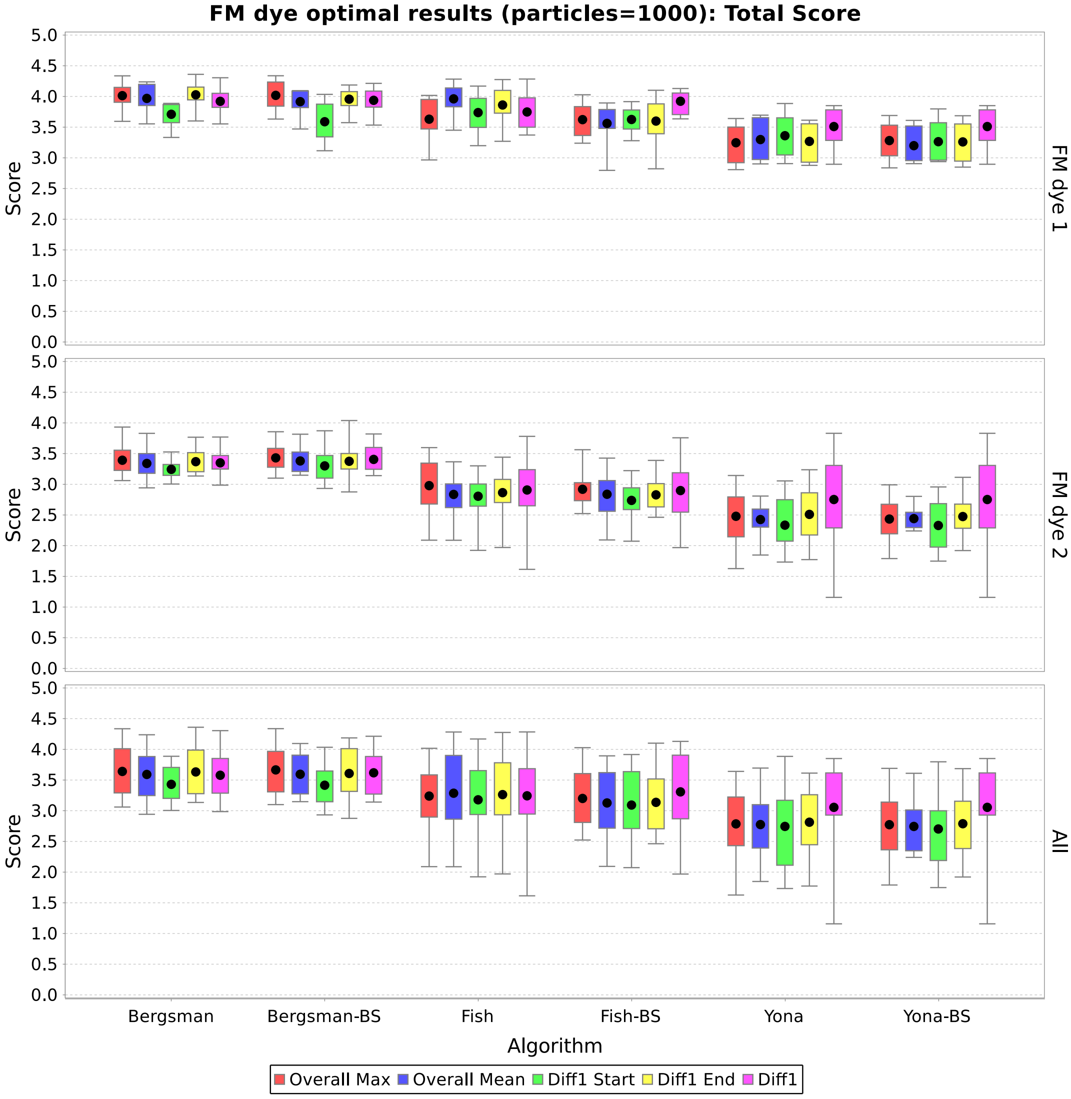

Figure B.27: Result Total Score range values with FM dye assays. Boxes show interquartile ranges, lines show maxima and minima, and black dots show mean values for each combination of experiment, image and algorithm.

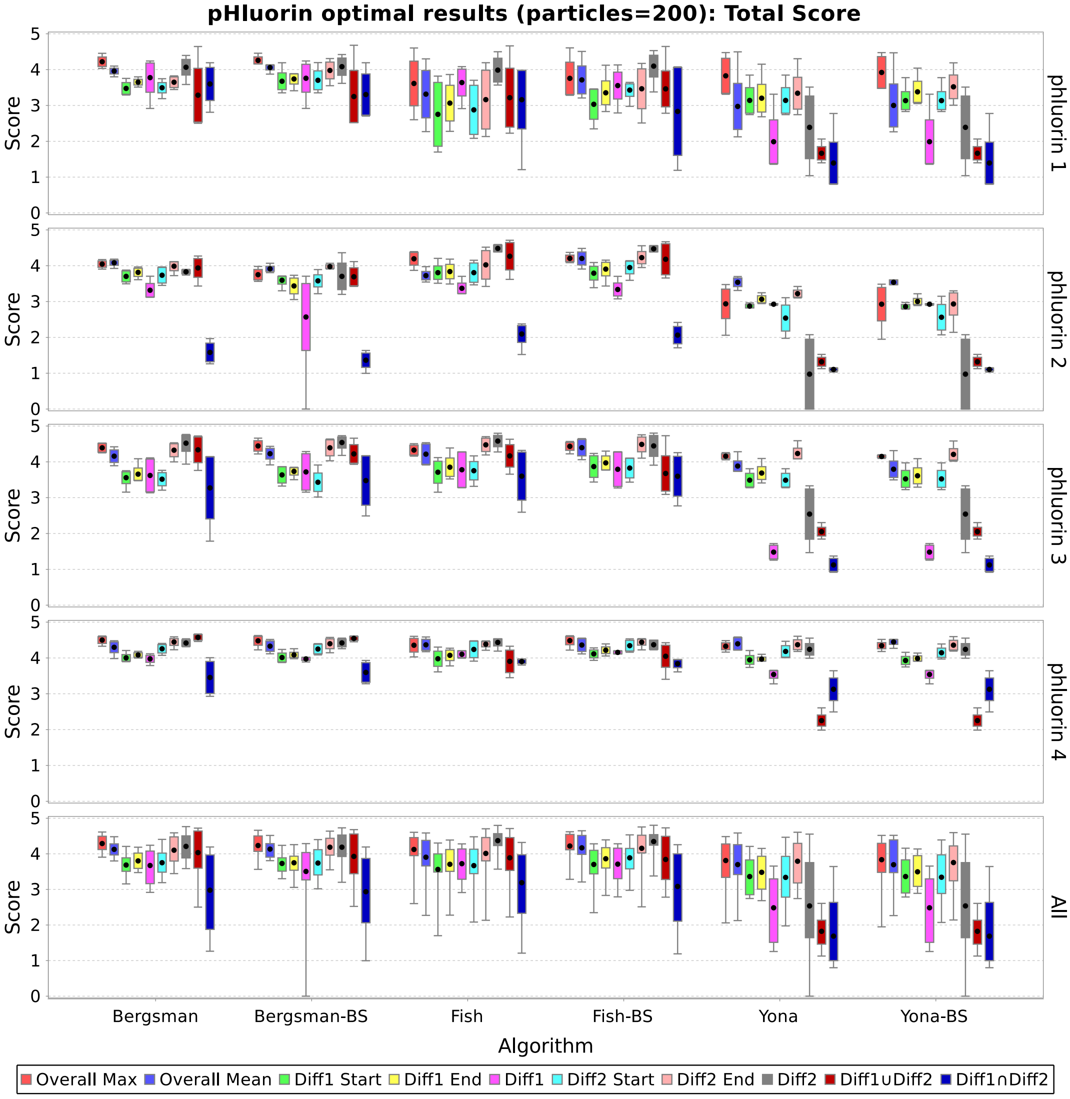

Figure B.28: Result Total Score range values with pHluorin assays. Boxes show interquartile ranges, lines show maxima and minima, and black dots show mean values for each combination of experiment, image and algorithm.

Bibliography

Agrawal, N., Nukpezah, J., and Radhakrishnan, R. (2010). Minimal mesoscale model for protein-mediated vesiculation in clathrin-dependent endocytosis. *PLoS Computational Biology*, 6(9):e1000926.

Alabi, A. and Tsien, R. (2013). Perspectives on kiss-and-run: Role in exocytosis, endocytosis, and neurotransmission. *Annual Review of Physiology*, 75:393–422.

Andrieu, C., Doucet, A., and Holenstein, R. (2010). Particle Markov chain Monte Carlo methods. *Journal of the Royal Statistical Society: Series B (Statistical Methodology)*, 72(3):269–342.

Anggono, V., Cousin, M., and Robinson, P. (2008). Styryl dye-based synaptic vesicle recycling assay in cultured cerebellar granule neurons. *Methods in Molecular Biology*, 457:333–345.

Anggono, V., Smillie, K., Graham, M., Valova, V., Cousin, M., and Robinson, P. (2006). Syndapin I is the phosphorylation-regulated dynamin I partner in synaptic vesicle endocytosis. *Nature Neuroscience*, 9(6):752–760.

Aravanis, A., Pyle, J., and Tsien, R. (2003). Single synaptic vesicles fusing transiently and successively without loss of identity. *Nature*, 423(6940):643–647.

Arendt, T. (2009). Synaptic degeneration in Alzheimer's disease. *Acta Neuropathologica*, 118(1):167–179.

Armstrong, J. and Sorokina, O. (2012). Evolution of the cognitive proteome: from static to dynamic network models. *Advances in Systems Biology*, pages 119–134.

Atluri, P. P. and Ryan, T. A. (2006). The kinetics of synaptic vesicle reacidification at hippocampal nerve terminals. *The Journal of Neuroscience*, 26(8):2313–2320.

Balaji, J. and Ryan, T. (2007). Single-vesicle imaging reveals that synaptic vesicle exocytosis and endocytosis are coupled by a single stochastic mode. *Proceedings of the National Academy of Sciences of the United States of America*, 104(51):20576–20581.

Barbuti, R., Caravagna, G., Maggiolo-Schettini, A., and Milazzo, P. (2009). On the Interpretation of Delays in Delay Stochastic Simulation of Biological Systems. *Computational Models for Cell Processes*, page 17.

Barrio, M., Burrage, K., Leier, A., and Tian, T. (2006). Oscillatory regulation of Hes1: discrete stochastic delay modelling and simulation. *PLoS Computational Biology*, 2(9):e117.

Bekkers, J. (2005). Presynaptically silent GABA synapses in hippocampus. *The Journal of Neuroscience*, 25(16):4031–4039.

Bergsman, J., Krueger, S., and Fitzsimonds, R. (2006). Automated criteria-based selection and analysis of fluorescent synaptic puncta. *Journal of Neuroscience Methods*, 152(1-2):32–39.

Betz, W., Mao, F., and Bewick, G. (1992). Activity-dependent fluorescent staining and destaining of living vertebrate motor nerve terminals. *The Journal of Neuroscience*, 12(2):363–375.

Betz, W. J., Mao, F., and Smith, C. B. (1996). Imaging exocytosis and endocytosis. *Current Opinion in Neurobiology*, 6(3):365–371.

Billings, S., Clarke, G., and Nishimune, H. (2012). ELKS1 and Ca^{2+} channel subunit $\beta 4$ interact and colocalize at cerebellar synapses. *NeuroReport*, 23(1):49–54.

Birtwistle, M. and Kholodenko, B. (2009). Endocytosis and signalling: a meeting with mathematics. *Molecular Oncology*, 3(4):308–320.

Bishop, C. M. et al. (2006). *Pattern recognition and machine learning*. Springer New York.

Cai, X. (2007). Exact stochastic simulation of coupled chemical reactions with delays. *The Journal of Chemical Physics*, 126:124108.

Caravagna, G. and Hillston, J. (2010). Modeling biological systems with delays in Bio-PEPA. *Membrane Computing and Biologically Inspired Process Calculi 2010*, page 81.

Caravagna, G. and Hillston, J. (2011). Bio-PEPAd: a non-Markovian extension of Bio-PEPA. *Theoretical Computer Science*.

Chabrier, N. and Fages, F. (2003). Symbolic model checking of biochemical networks. In *Computational Methods in Systems Biology*, pages 149–162. Springer.

Cheung, G. and Cousin, M. A. (2011). Quantitative analysis of synaptic vesicle pool replenishment in cultured cerebellar granule neurons using FM dyes. *Journal of Visualized Experiments: JoVE*, (57).

Cheung, G. and Cousin, M. A. (2012). Adaptor protein complexes 1 and 3 are essential for generation of synaptic vesicles from activity-dependent bulk endosomes. *The Journal of Neuroscience*, 32(17):6014–6023.

Cheung, G. and Cousin, M. A. (2013). Synaptic vesicle generation from activity-dependent bulk endosomes requires calcium and calcineurin. *The Journal of Neuroscience*, 33(8):3370–3379.

Cheung, G., Jupp, O., and Cousin, M. (2010). Activity-dependent bulk endocytosis and clathrin-dependent endocytosis replenish specific synaptic vesicle pools in central nerve terminals. *The Journal of Neuroscience*, 30(24):8151–8161.

Ciocchetta, F. (2009). Bio-PEPA with events. *Lecture Notes in Computer Science (including subseries Lecture Notes in Artificial Intelligence and Lecture Notes in Bioinformatics)*, 5750 LNBI:45–68.

Ciocchetta, F. and Guerriero, M. L. (2009). Modelling biological compartments in Bio-PEPA. *Electronic Notes in Theoretical Computer Science*, 227:77–95.

Ciocchetta, F. and Hillston, J. (2008). Process algebras in systems biology. *Lecture Notes in Computer Science (including subseries Lecture Notes in Artificial Intelligence and Lecture Notes in Bioinformatics)*, 5016 LNCS:265–312.

Ciocchetta, F. and Hillston, J. (2009). Bio-PEPA: a framework for the modelling and analysis of biological systems. *Theoretical Computer Science*, 410(33-34):3065–3084.

Clarke, E., Faeder, J., Langmead, C., Harris, L., Jha, S., and Legay, A. (2008). Statistical model checking in biolab: Applications to the automated analysis of t-cell receptor signaling pathway. In *Computational Methods in Systems Biology*, pages 231–250. Springer.

Clayton, E., Anggono, V., Smillie, K., Chau, N., Robinson, P., and Cousin, M. (2009). The phospho-dependent dynamin-syndapin interaction triggers activity-dependent bulk endocytosis of synaptic vesicles. *The Journal of Neuroscience*, 29(24):7706–7717.

Clayton, E. and Cousin, M. (2008). Differential labelling of bulk endocytosis in nerve terminals by FM dyes. *Neurochemistry International*, 53(3):51–55.

Clayton, E. and Cousin, M. (2009). Quantitative monitoring of activity-dependent bulk endocytosis of synaptic vesicle membrane by fluorescent dextran imaging. *Journal of Neuroscience Methods*, 185(1):76–81.

Clayton, E., Evans, G., and Cousin, M. (2008). Bulk synaptic vesicle endocytosis is rapidly triggered during strong stimulation. *The Journal of Neuroscience*, 28(26):6627–6632.

Clayton, E., Sue, N., Smillie, K., O'Leary, T., Bache, N., Cheung, G., Cole, A., Wyllie, D., Sutherland, C., Robinson, P., and Cousin, M. (2010). Dynamin I phosphorylation by GSK3 controls activity-dependent bulk endocytosis of synaptic vesicles. *Nature Neuroscience*, 13(7):845–851.

Collado-Alsina, A., Ramírez-Franco, J., Sánchez-Prieto, J., and Torres, M. (2014). The regulation of synaptic vesicle recycling by cGMP-dependent protein kinase type II in cerebellar granule cells under strong and sustained stimulation. *The Journal of Neuroscience*, 34(26):8788–8799.

Cousin, M. (2008). Use of FM1-43 and other derivatives to investigate neuronal function. *Current Protocols in Neuroscience*, pages 2–6.

Cousin, M. (2009). Activity-dependent bulk synaptic vesicle endocytosis - a fast, high capacity membrane retrieval mechanism. *Molecular Neurobiology*, 39(3):185–189.

Cousin, M. and Nicholls, D. (1997). Synaptic vesicle recycling in cultured cerebellar granule cells: Role of vesicular acidification and refilling. *Journal of Neurochemistry*, 69(5):1927–1935.

Daniels, R. W., Collins, C. A., Chen, K., Gelfand, M. V., Featherstone, D. E., and DiAntonio, A. (2006). A single vesicular glutamate transporter is sufficient to fill a synaptic vesicle. *Neuron*, 49(1):11–16.

den Otter, W. and Briels, W. (2011). The generation of curved clathrin coats from flat plaques. *Traffic*.

Denker, A., Kröhnert, K., Bückers, J., Neher, E., and Rizzoli, S. O. (2011). The reserve pool of synaptic vesicles acts as a buffer for proteins involved in synaptic vesicle recycling. *Proceedings of the National Academy of Sciences of the United States of America*, 108(41):17183–17188.

Denker, A. and Rizzoli, S. (2010). Synaptic vesicle pools: An update. *Frontiers in Synaptic Neuroscience*, (OCT).

Djurfeldt, M. and Lansner, A. (2007). Workshop report: 1st INCF workshop on large-scale modeling of the nervous system. Nature Publishing Group.

Evans, G. and Cousin, M. (2007). Activity-dependent control of slow synaptic vesicle endocytosis by cyclin-dependent kinase 5. *The Journal of Neuroscience*, 27(2):401–411.

Fange, D., Berg, O., Sjöberg, P., and Elf, J. (2010). Stochastic reaction-diffusion kinetics in the microscopic limit. *Proceedings of the National Academy of Sciences of the United States of America*, 107(46):19820–19825.

Fernández-Alfonso, T. and Ryan, T. A. (2008). A heterogeneous “resting” pool of synaptic vesicles that is dynamically interchanged across boutons in mammalian CNS synapses. *Brain Cell Biology*, 36(1-4):87–100.

Field, A., Miles, J., and Field, Z. (2012). *Discovering statistics using R*. Sage, Thousand Oaks.

Fish, K., Sweet, R., Deo, A., and Lewis, D. (2008). An automated segmentation methodology for quantifying immunoreactive puncta number and fluorescence intensity in tissue sections. *Brain Research*, 1240:62–72.

Fredj, N. B. and Burrone, J. (2009). A resting pool of vesicles is responsible for spontaneous vesicle fusion at the synapse. *Nature neuroscience*, 12(6):751–758.

Gabriel, T., García-Pérez, E., Mahfooz, K., Goñi, J., Martínez-Turrillas, R., Pérez-Otaño, I., Lo, D., and Wesseling, J. (2011). A new kinetic framework for synaptic vesicle trafficking tested in synapsin knock-outs. *The Journal of Neuroscience*, 31(32):11563–11577.

Gandhi, S. P. and Stevens, C. F. (2003). Three modes of synaptic vesicular recycling revealed by single-vesicle imaging. *Nature*, 423(6940):607–613.

Gillespie, D. (1977). Exact stochastic simulation of coupled chemical reactions. *The Journal of Physical Chemistry*, 81(25):2340–2361.

Gillespie, D., Hellander, A., and Petzold, L. (2013). Perspective: Stochastic algorithms for chemical kinetics. *Journal of Chemical Physics*, 138(17).

Gillespie, D. T. (2007). Stochastic simulation of chemical kinetics. *Annual Review of Physical Chemistry*, 58:35–55.

Gillis, K. D. (2000). Admittance-based measurement of membrane capacitance using the EPC-9 patch-clamp amplifier. *Pflügers Archiv*, 439(5):655–664.

Golightly, A. and Wilkinson, D. (2005). Bayesian inference for stochastic kinetic models using a diffusion approximation. *Biometrics*, 61(3):781–788.

Golightly, A. and Wilkinson, D. (2006a). Bayesian sequential inference for nonlinear multivariate diffusions. *Statistics and Computing*, 16(4):323–338.

Golightly, A. and Wilkinson, D. (2006b). Bayesian sequential inference for stochastic kinetic biochemical network models. *Journal of Computational Biology*, 13(3):838–851.

Golightly, A. and Wilkinson, D. (2008). Bayesian inference for nonlinear multivariate diffusion models observed with error. *Computational Statistics & Data Analysis*, 52(3):1674–1693.

Golightly, A. and Wilkinson, D. (2009). Markov chain Monte Carlo algorithms for SDE parameter estimation. *Learning and Inference for Computational Systems Biology, MIT Press*.

Golightly, A. and Wilkinson, D. (2011). Bayesian parameter inference for stochastic biochemical network models using particle Markov chain Monte Carlo. *Interface Focus*, 1(6):807–820.

Gordon, S. and Cousin, M. (2013). X-linked intellectual disability-associated mutations in synaptophysin disrupt synaptobrevin II retrieval. *The Journal of Neuroscience*, 33(34):13695–13700.

Gordon, S., Harper, C., Smillie, K., and Cousin, M. (2016). A fine balance of synaptophysin levels underlies efficient retrieval of synaptobrevin II to synaptic vesicles. *PLoS ONE*, 11(2).

Gordon, S., Leube, R., and Cousin, M. (2011). Synaptophysin is required for synaptobrevin retrieval during synaptic vesicle endocytosis. *The Journal of Neuroscience*, 31(39):14032–14036.

Graner, F. and Glazier, J. (1992). Simulation of biological cell sorting using a two-dimensional extended Potts model. *Physical Review Letters*, 69(13):2013–2016.

Granseth, B. and Lagnado, L. (2008). The role of endocytosis in regulating the strength of hippocampal synapses. *The Journal of Physiology*, 586(24):5969–5982.

Granseth, B., Odermatt, B., Royle, S. J., and Lagnado, L. (2006). Clathrin-mediated endocytosis is the dominant mechanism of vesicle retrieval at hippocampal synapses. *Neuron*, 51(6):773–786.

Harata, N., Choi, S., Pyle, J., Aravanis, A., and Tsien, R. (2006). Frequency-dependent kinetics and prevalence of kiss-and-run and reuse at hippocampal synapses studied with novel quenching methods. *Neuron*, 49(2):243–256.

Harris, K. and Sultan, P. (1995). Variation in the number, location and size of synaptic vesicles provides an anatomical basis for the nonuniform probability of release at hippocampal CA1 synapses. *Neuropharmacology*, 34(11):1387–1395.

Holderith, N., Lorincz, A., Katona, G., Rózsa, B., Kulik, A., Watanabe, M., and Nusser, Z. (2012). Release probability of hippocampal glutamatergic terminals scales with the size of the active zone. *Nature neuroscience*.

Hooke, R. and Jeeves, T. A. (1961). “Direct Search” solution of numerical and statistical problems. *Journal of the ACM*, 8(2):212–229.

Hucka, M., Finney, A., Sauro, H., Bolouri, H., Doyle, J., Kitano, H., Arkin, A., Bornstein, B., Bray, D., Cornish-Bowden, A., et al. (2003). The systems biology markup language (SBML): a medium for representation and exchange of biochemical network models. *Bioinformatics*, 19(4):524–531.

Humphrey, W., Dalke, A., and Schulten, K. (1996). VMD: Visual molecular dynamics. *Journal of Molecular Graphics*, 14(1):33–38.

Ikeda, K. and Bekkers, J. (2009). Counting the number of releasable synaptic vesicles in a presynaptic terminal. *Proceedings of the National Academy of Sciences of the United States of America*, 106(8):2945–2950.

Ikeda, K. and Bekkers, J. M. (2006). Autapses. *Current Biology*, 16(9):R308.

Iwabuchi, S., Kakazu, Y., Koh, J.-Y., and Charles Harata, N. (2014). Evaluation of the effectiveness of gaussian filtering in distinguishing punctate synaptic signals from background noise during image analysis. *Journal of Neuroscience Methods*, 223:92–113.

Kannan, M., Gross, G., Arnold, D., and Higley, M. (2016). Visual deprivation during the critical period enhances layer 2/3 GABAergic inhibition in mouse V1. *The Journal of Neuroscience*, 36(22):5914–5919.

Kavalali, E. and Jorgensen, E. (2014). Visualizing presynaptic function. *Nature Neuroscience*, 17(1):10–16.

Kim, S. and Ryan, T. (2009). Synaptic vesicle recycling at CNS synapses without AP-2. *The Journal of Neuroscience*, 29(12):3865–3874.

Kim, S. and Ryan, T. (2010). CDK5 Serves as a Major Control Point in Neurotransmitter Release. *Neuron*, 67(5):797–809.

Klingauf, J., Kavalali, E., and Tsien, R. (1998). Kinetics and regulation of fast endocytosis at hippocampal synapses. *Nature*, 394(6693):581–585.

Kokotos, A. and Cousin, M. (2015). Synaptic vesicle generation from central nerve terminal endosomes. *Traffic*, 16(3):229–240.

Kononenko, N. and Haucke, V. (2015). Molecular mechanisms of presynaptic membrane retrieval and synaptic vesicle reformation. *Neuron*, 85(3):484–496.

Kwiatkowska, M., Norman, G., and Parker, D. (2011). PRISM 4.0: Verification of Probabilistic Real-time Systems. In Gopalakrishnan, G. and Qadeer, S., editors, *Proc. 23rd International Conference on Computer Aided Verification (CAV'11)*, volume 6806 of *LNCS*, pages 585–591. Springer.

Le Novère, N., Hucka, M., Mi, H., Moodie, S., Schreiber, F., Sorokin, A., Demir, E., Wegner, K., Aladjem, M., Wimalaratne, S., et al. (2009). The systems biology graphical notation. *Nature Biotechnology*, 27(8):735–741.

Le Novère, N. and Shimizu, T. (2001). STOCHSIM: modelling of stochastic biomolecular processes. *Bioinformatics*, 17(6):575–576.

Li, C., Donizelli, M., Rodriguez, N., Dharuri, H., Endler, L., Chelliah, V., Li, L., He, E., Henry, A., Stefan, M. I., Snoep, J. L., Hucka, M., Le Novère, N., and Laibe, C. (2010). BioModels Database: An enhanced, curated and annotated resource for published quantitative kinetic models. *BMC Systems Biology*, 4:92.

Lin, M. Z. and Schnitzer, M. J. (2016). Genetically encoded indicators of neuronal activity. *Nature Neuroscience*, 19(9):1142–1153.

López-Murcia, F. J., Royle, S. J., and Llobet, A. (2014). Presynaptic clathrin levels are a limiting factor for synaptic transmission. *The Journal of Neuroscience*, 34(25):8618–8629.

Luchkina, N., Coleman, S., Huupponen, J., Cai, C., Kivistö, A., Taira, T., Keinänen, K., and Lauri, S. (2017). Molecular mechanisms controlling synaptic recruitment of GluA4 subunit-containing AMPA-receptors critical for functional maturation of CA1 glutamatergic synapses. *Neuropharmacology*, 112:46–56.

Lyles, V., Zhao, Y., and Martin, K. C. (2006). Synapse formation and mRNA localization in cultured Aplysia neurons. *Neuron*, 49(3):349–356.

Marland, J., Hasel, P., Bonnycastle, K., and Cousin, M. (2016). Mitochondrial calcium uptake modulates synaptic vesicle endocytosis in central nerve terminals. *The Journal of Biological Chemistry*, 291(5):2080–2086.

Marra, V., Burden, J. J., Thorpe, J. R., Smith, I. T., Smith, S. L., Häusser, M., Branco, T., and Staras, K. (2012). A preferentially segregated recycling vesicle pool of limited size supports neurotransmission in native central synapses. *Neuron*, 76(3):579–589.

McMahon, H. and Boucrot, E. (2011). Molecular mechanism and physiological functions of clathrin-mediated endocytosis. *Nature Reviews Molecular Cell Biology*, 12(8):517–533.

Micheva, K. D. and Smith, S. J. (2005). Strong effects of subphysiological temperature on the function and plasticity of mammalian presynaptic terminals. *The Journal of Neuroscience*, 25(33):7481–7488.

Miesenböck, G., De Angelis, D., and Rothman, J. (1998). Visualizing secretion and synaptic transmission with pH-sensitive green fluorescent proteins. *Nature*, 394(6689):192–195.

Miller, T. M. and Heuser, J. E. (1984). Endocytosis of synaptic vesicle membrane at the frog neuromuscular junction. *The Journal of Cell Biology*, 98(2):685–698.

Moraru, I., Schaff, J., Slepchenko, B., Blinov, M., Morgan, F., Lakshminarayana, A., Gao, F., Li, Y., and Loew, L. (2008). Virtual Cell modelling and simulation software environment. *Systems Biology, IET*, 2(5):352–362.

Morton, A., Marland, J., and Cousin, M. (2015). Synaptic vesicle exocytosis and increased cytosolic calcium are both necessary but not sufficient for activity-dependent bulk endocytosis. *Journal of Neurochemistry*.

Mutch, S. A., Kensel-Hammes, P., Gadd, J. C., Fujimoto, B. S., Allen, R. W., Schiro, P. G., Lorenz, R. M., Kuyper, C. L., Kuo, J. S., Bajjalieh, S. M., et al. (2011). Protein quantification at the single vesicle level reveals that a subset of synaptic vesicle proteins are trafficked with high precision. *The Journal of Neuroscience*, 31(4):1461–1470.

Nicholson-Fish, J., Kokotos, A., Gillingwater, T., Smillie, K., and Cousin, M. (2015). VAMP4 is an essential cargo molecule for activity-dependent bulk endocytosis. *Neuron*, 88(5):973–984.

Nicholson-Fish, J., Smillie, K., and Cousin, M. (2016). Monitoring activity-dependent bulk endocytosis with the genetically-encoded reporter VAMP4-pHluorin. *Journal of Neuroscience Methods*, 266:1–10.

Nunez, D., Antonescu, C., Mettlen, M., Liu, A., Schmid, S., Loerke, D., and Danuser, G. (2011). Hotspots organize clathrin-mediated endocytosis by efficient recruitment and retention of nucleating resources. *Traffic*.

Orsi, M. and W., E. J. (2011). The ELBA force field for coarse-grain modeling of lipid membranes. *PLoS ONE*, 6(12):e28637.

Pearse, B. M. (1976). Clathrin: a unique protein associated with intracellular transfer of membrane by coated vesicles. *Proceedings of the National Academy of Sciences*, 73(4):1255–1259.

Phillips, J. C., Braun, R., Wang, W., Gumbart, J., Tajkhorshid, E., Villa, E., Chipot, C., Skeel, R. D., Kalé, L., and Schulten, K. (2005). Scalable molecular dynamics with NAMD. *Journal of Computational Chemistry*, 26(16):1781–1802.

Purves, D., Augustine, G., Fitzpatrick, D., Hall, W., LaMantia, A., McNamara, J., and White, L. (2008). *Neuroscience*. Sinauer Associates.

Ramanan, V., Agrawal, N., Liu, J., Engles, S., Toy, R., and Radhakrishnan, R. (2011). Systems biology and physical biology of clathrin-mediated endocytosis. *Integr. Biol.*, 3(8):803–815.

Rizzoli, S. and Betz, W. (2005). Synaptic vesicle pools. *Nature Reviews Neuroscience*, 6(1):57–69.

Robinson, M. S., Sahlender, D. A., and Foster, S. D. (2010). Rapid inactivation of proteins by rapamycin-induced rerouting to mitochondria. *Developmental cell*, 18(2):324–331.

Roseth, S., Fykse, E., and Fonnum, F. (1995). Uptake of L-glutamate into rat brain synaptic vesicles: Effect of inhibitors that bind specifically to the glutamate transporter. *Journal of Neurochemistry*, 65(1):96–103.

Royle, S., Granseth, B., Odermatt, B., Derevier, A., and Lagnado, L. (2008). Imaging pHluorin-based probes at hippocampal synapses. *Methods in Molecular Biology*, 457:293–303.

Rozas, J. L., Gómez-Sánchez, L., Tomás-Zapico, C., Lucas, J. J., and Fernández-Chacón, R. (2010). Presynaptic dysfunction in Huntington's disease. *Biochemical Society Transactions*, 38(2):488–492.

Ryan, T., Smith, S., and Reuter, H. (1996). The timing of synaptic vesicle endocytosis. *Proceedings of the National Academy of Sciences of the United States of America*, 93(11):5567–5571.

Sankaranarayanan, S., De Angelis, D., Rothman, J., and Ryan, T. (2000). The use of pHluorins for optical measurements of presynaptic activity. *Biophysical Journal*, 79(4):2199–2208.

Sankaranarayanan, S. and Ryan, T. A. (2000). Real-time measurements of vesicle-SNARE recycling in synapses of the central nervous system. *Nature cell biology*, 2(4):197–204.

Sara, Y., Virmani, T., Deák, F., Liu, X., and Kavalali, E. T. (2005). An isolated pool of vesicles recycles at rest and drives spontaneous neurotransmission. *Neuron*, 45(4):563–573.

Schikorski, T. and Stevens, C. F. (1997). Quantitative ultrastructural analysis of hippocampal excitatory synapses. *The Journal of Neuroscience*, 17(15):5858–5867.

Schindelin, J., Arganda-Carreras, I., Frise, E., Kaynig, V., Longair, M., Pietzsch, T., Preibisch, S., Rueden, C., Saalfeld, S., Schmid, B., et al. (2012). Fiji: an open-source platform for biological-image analysis. *Nature methods*, 9(7):676–682.

Schlicht, R. and Winkler, G. (2008). A delay stochastic process with applications in molecular biology. *Journal of mathematical biology*, 57(5):613–648.

Schmitz, S. K., Hjorth, J. J., Joemai, R. M., Wijntjes, R., Eijgenraam, S., de Bruijn, P., Georgiou, C., de Jong, A. P., van Ooyen, A., Verhage, M., et al. (2011). Automated analysis of neuronal morphology, synapse number and synaptic recruitment. *Journal of neuroscience methods*, 195(2):185–193.

Schneider, C. A., Rasband, W. S., and Eliceiri, K. W. (2012). NIH Image to ImageJ: 25 years of image analysis. *Nature methods*, 9(7):671–675.

Shkurti, A., Acquaviva, A., Ficarra, E., Macii, E., Orsi, M., and Ruggiero, M. (2010). GPU acceleration of simulation tool for lipid-bilayers. In *Bioinformatics and Biomedicine Workshops (BIBMW), 2010 IEEE International Conference on*, pages 849–850. IEEE.

Smillie, K. and Cousin, M. (2011). The role of GSK3 in presynaptic function. *International Journal of Alzheimer's Disease*, 2011.

Smillie, K. J. and Cousin, M. A. (2005). Dynamin I phosphorylation and the control of synaptic vesicle endocytosis. *Biochemical Society Symposia*, (72):87–97.

Smillie, K. J. and Cousin, M. A. (2012). Akt/PKB controls the activity-dependent bulk endocytosis of synaptic vesicles. *Traffic*.

Smith, M. and Gilmore, S. (2011). Visualisation for stochastic process algebras: The graphic truth. *Lecture Notes in Computer Science (including subseries Lecture Notes in Artificial Intelligence and Lecture Notes in Bioinformatics)*, 6977 LNCS:310–324.

Sternberg, S. R. (1983). Biomedical image processing. *Computer*, 16(1):22–34.

Stewart, D., Gilmore, S., and Cousin, M. (2014). FM-Sim: Protocol definition, simulation and rate inference for neuroscience assays. *Lecture Notes in Computer Science (including subseries Lecture Notes in Artificial Intelligence and Lecture Notes in Bioinformatics)*, 8859:248–251.

Stewart, D., Gilmore, S., and Cousin, M. (2015). FM-Sim: A hybrid protocol simulator of fluorescence microscopy neuroscience assays with integrated Bayesian inference. *Lecture Notes in Computer Science (including subseries Lecture Notes in Artificial Intelligence and Lecture Notes in Bioinformatics)*, 7699:159–174.

Takamori, S., Holt, M., Stenius, K., Lemke, E. A., Grønborg, M., Riedel, D., Urlaub, H., Schenck, S., Brügger, B., Ringler, P., et al. (2006). Molecular anatomy of a trafficking organelle. *Cell*, 127(4):831–846.

Tan, T., Valova, V., Malladi, C., Graham, M., Berven, L., Jupp, O., Hansra, G., McClure, S., Sarcevic, B., Boadle, R., Larsen, M., Cousin, M., and Robinson, P. (2003). Cdk5 is essential for synaptic vesicle endocytosis. *Nature Cell Biology*, 5(8):701.

Thevenaz, P., Ruttimann, U. E., and Unser, M. (1998). A pyramid approach to subpixel registration based on intensity. *Image Processing, IEEE Transactions on*, 7(1):27–41.

Verstegen, A., Tagliatti, E., Lignani, G., Marte, A., Stolero, T., Atias, M., Corradi, A., Valtorta, F., Gitler, D., Onofri, F., Fassio, A., and Benfenati, F. (2014). Phosphorylation of synapsin I by cyclin-dependent kinase-5 sets the ratio between the resting and recycling pools of synaptic vesicles at hippocampal synapses. *The Journal of Neuroscience*, 34(21):7266–7280.

Watanabe, S., Davis, M., and Jorgensen, E. (2014). Flash-and-freeze electron microscopy: Coupling optogenetics with high-pressure freezing. *Neuromethods*, 84:43–57.

Watanabe, S., Liu, Q., Davis, M., Hollopeter, G., Thomas, N., Jorgensen, N., and Jorgensen, E. (2013a). Ultrafast endocytosis at Caenorhabditis elegans neuromuscular junctions. *eLife*, 2013(2).

Watanabe, S., Rost, B., Camacho-Pérez, M., Davis, M., Söhl-Kielczynski, B., Rosenmund, C., and Jorgensen, E. (2013b). Ultrafast endocytosis at mouse hippocampal synapses. *Nature*, 504(7479):242–247.

Whittaker, V. (1993). Thirty years of synaptosome research. *Journal of neurocytology*, 22(9):735–742.

Wilhelm, B. (2013). *Stoichiometric Biology of the Synapse*. PhD thesis, Georg August University Göttingen.

Wilhelm, B. G., Mandad, S., Truckenbrodt, S., Kröhnert, K., Schäfer, C., Rammner, B., Koo, S. J., Claßen, G. A., Krauss, M., Haucke, V., et al. (2014). Composition of isolated synaptic boutons reveals the amounts of vesicle trafficking proteins. *Science*, 344(6187):1023–1028.

Wilkinson, D. (2007). Bayesian methods in bioinformatics and computational systems biology. *Briefings in bioinformatics*, 8(2):109–116.

Wilkinson, D. (2011). *Stochastic modelling for systems biology*, volume 44. CRC press, 2nd edition.

Wojcik, S., Rhee, J., Herzog, E., Sigler, A., Jahn, R., Takamori, S., Brose, N., and Rosenmund, C. (2004). An essential role for vesicular glutamate transporter 1 (VGLUT1) in postnatal development and control of quantal size. *Proceedings of the National Academy of Sciences of the United States of America*, 101(18):7158–7163.

Wölfel, M. and Schneggenburger, R. (2003). Presynaptic capacitance measurements and Ca^{2+} uncaging reveal submillisecond exocytosis kinetics and characterize the Ca^{2+} sensitivity of vesicle pool depletion at a fast CNS synapse. *The Journal of Neuroscience*, 23(18):7059–7068.

Wu, Y., Yeh, F., Mao, F., and Chapman, E. (2009). Biophysical characterization of styryl dye-membrane interactions. *Biophysical Journal*, 97(1):101–109.

Xue, J., Graham, M., Novelle, A., Sue, N., Gray, N., McNiven, M., Smillie, K., Cousin, M., and Robinson, P. (2011). Calcineurin selectively docks with the dynamin Ixb splice variant to regulate activity-dependent bulk endocytosis. *The Journal of Biological Chemistry*, 286(35):30295–30303.

Xue, L., Sheng, J., Wu, X.-S., Wu, W., Luo, F., Shin, W., Chiang, H.-C., and Wu, L.-G. (2013). Most vesicles in a central nerve terminal participate in recycling. *The Journal of Neuroscience*, 33(20):8820–8826.

Yona, S., Katsman, A., Orenbuch, A., Gitler, D., and Yitzhaky, Y. (2011). Automatic analysis and quantification of fluorescently-labeled synapses in microscope images. In *Proceedings of SPIE - The International Society for Optical Engineering*, volume 8185.

Zhou, Z., Misler, S., and Chow, R. (1996). Rapid fluctuations in transmitter release from single vesicles in bovine adrenal chromaffin cells. *Biophysical Journal*, 70(3):1543 – 1552.